Fermilab

FERMILAB-THESIS-2000-16

A Blind Search for Supersymmetry in $p\bar{p}$ Collisions at $\sqrt{s} = 1.8$ TeV using the Missing Energy plus Multijet channel

A thesis presented

by

Maria Spiropulu

to

The Department of Physics

in partial fulfillment of the requirements

for the degree of

Doctor of Philosophy

in the subject of

Physics

Harvard University

Cambridge, Massachussetts

November 2000

A Blind Search for Supersymmetry in $p\bar{p}$ Collisions at $\sqrt{s} = 1.8$ TeV using the Missing Energy plus Multijet channel

Maria Spiropulu

Advisor: John E. Huth

Abstract

A data sample of 84.37 pb^{-1} of $p\bar{p}$ collisions at $\sqrt{s} = 1.8$ TeV recorded by the Collider Detector at Fermilab is analyzed in search of scalar quarks (squarks, $\tilde{q}$) and gluinos ($\tilde{g}$). The final state of large missing energy plus ≥ 3 jets, characteristic of hadroproduction and subsequent decays of squarks and gluinos within the minimal supersymmetry and supergravity frameworks with R-parity conservation, is used in the search. The *blind* analysis method is followed to avoid biases in the data selection. The search is negative at 95% C.L. for gluino masses below 300 GeV/c^2 for the case $m_{\tilde{q}} \approx m_{\tilde{g}}$ and 195 GeV/c^2 independent of the squark mass. Being that the limit on the gluino mass provides tight fine-tuning constraints on low-energy supersymmetry the result of this search has phenomenological implications on models with unification constraints. It also demonstrates that the missing energy plus multijet channel is a powerful probe for supersymmetry in the upcoming Tevatron Collider run.

I wish to dedicate this thesis, 7 times for each year I missed, with nostalgia

and the love I almost forgot at times

to the ancient grounds,the bright suns and the hard rains

of Greece, West Macedonia, Kastoria, Kleisoura.

With wonder of who they were to

my grandfather Markos Spiropulos and my grandmother Maria.

To my incredible beloved father George

To my mother Vasiliki, the treasure of my heart

To my beautiful and exraordinary brother Markos

For my beloved Nina who was waiting for me to go back to Greece and she no more

For my beloved grandfather Chrysostromos who was waiting too but he does no more

And for George Michail, always for George Michail.

Acknowledgments

Let me start by thanking the ones not around, that I love and admire. Thanks to George Michail for his incredible spirit. And for drawing the road map from O'Hare to Fermilab on a napkin paper and handing it it to me at 42 Oxford before my first departure with destination Batavia: I did not get lost. My aunt Nina who anxiously waited for me to finish the doctor-road and left me on the journey - many times it seemed infinite to me ; Kavafis would have been joyful and proud, I am sure. Maria Callas without whose voice my life would have been mute. Melina Merkouri for the Greek woman she was and the innumerable cigarettes she smoked. To Odysseus Elytis. To two teachers that I will never forget for their radiance in the Physics Department in Aristotle University of Thessaloniki in Greece: Mattheos Mixalodimidarkis (classical mechanics and special theory of relativity) and Dimitris Tsarouxas (differential equations). To Eugenios Pneumatikos at the Institute in Crete whose spirit was captivating and to Dimitris Ksanthopoulos : I had the chance in Thessaloniki to meet him and the transcript of this one lecture I had the chance to attend, I treasure to this day. To Karl Strauch who entered this section while I was still writing it: I met Prof. Strauch at CERN as an undergraduate and he encouraged me to go ahead and live with particle physics.

My pre-graduate-school advisors during my time at CERN : Ettore Rosso, Machi Tsirou, Stauros Katsanevas, Stephan Haider. Ferdinand Hahn for the SYBIL that became a project for me, and for precious times of silence.

Eleni Paloura for constant guidance, support and friendship since I turned twenty. Katerina Paloura for always, always being there for me ready to listen and help. Kostas Magoutis for growing together in physics at the Aristotle University of Thessaloniki.

I want to thank the Harvard High Energy group (in the order I met): Melissa Franklin for all the charm and entropy and for the love for physics that she emits, for bearing with me when I was her academic advisee and teaching assistant and for all the activity she instigated in my brain all these years. And of course for her beautiful Nica. David Kestenbaum, Thomas Baumann, Peter Hurst, Colin Jessop, Robin Coxe, Alex Samuel, Thomas Dignan, Michael Temkin, Rowan Terrel Hamilton, Bob Mattingly, Sanjib Mishra, Hitoshi Yamamoto, Gary Feldman, Richard Wilson, Jaco Konigsberg (thanks for all the CPU I borrowed), Colin Gay (thanks for good lessons), John Oliver, (thanks both for teaching me and letting me look and learn behind your back at work), Raimund Strohmer, Jorge Troconiz, Michael Schmitt and Mayda Velasco, Kevin Burkett, Robyn Madrak, Jun Masui, Stephen Bailey, Carter Hall, Ayanna Holloway, Tommaso and Maria-Rosa Dorigo and Fillipo. All the Harvard undergrads that went through Fermilab since '97 for their high energy. Caollion thank you for keeping my secrets about promises.

Mark Hill thank you for the gold angel.

Werner Riegler thanks for all the field theory arguments, the Berlin and blues outings in Chicago and for playing very loud music in the car.

Rick Haggerty (thanks for introducing me to the Irish booshmills; thanks for putting your glasses on and for checking out the squark-gluino exclusion plot ; and for all the times in the machine shop), Steve Sansone (thanks Steve for the stories and the jokes and the potato gun), Dan Hennessy, and everyone at the shop. Sarah Harder, Jack O'Kane, Nathan Felt.

Guy Sciacca, your constant help and support has been invaluable all these years. Thank you.

I want to thank the physics people at Jefferson, Sidney Coleman, Shelly Glashow

(thanks for your interest all along and the discussions on my qualifier analysis), Eric Carlson, Efthimios Kaxiras, Kostas Papaliolios (for all the greek treats too), Bert Halperin, Andrei Lesnievski, Carol Davis and Mary Lampros (thanks for all the help with the physics department work).

I wish to thank the Fermilab staff, the technical staffs of the participating institutions and the U. S. Department of Energy for supporting this work.

I spent too much time at Fermilab and not quite enough to perfect my percussion and vocal skills with the CDF band. I thank you all, Steve Hahn, Larry Nodulman, Randy and Eva Thurman-Keup, Greg Feild, Yoshi Seiya, Mike & Marie Starr and Owen Long whose playing 'whole lotta Rosie' I can never quite stop missing. Deedee Hahn and Kylie and Chad thanks for being close as family. Phil Schlabach. Al Goshaw, Bill Carithers, Franco Bedeschi, 'Elena and Lianka. Mark Kruse, Kara Hoffman, Dejan Vucinic, Tushar Shah, Petar and Anna Maksimovic, Paul Ngan and the rest of the MIT gang. Fabio Happacher and Giusy Foligno. Vaia Papadimitriou, Rocio Vilar, Juan Valls (thanks for the menthols).

Rick Colombo, Mark Leininger, Mark Schmitz and JJ Schmidt thank you for constant help. All operators at the Feynman Center. Many thanks to Steve Behrends for very usefull discussions and help with QCD. David Saltzberg many thanks for very useful discussions on the blind box and fun dinners. David Gerdes for inspiring physics-talk and Washington lessons. The exotics conveners since 1997, Kaori Maeshima, Henry Frisch, David Stuart, John Conway, Max Chertok, Ray Culbertson. Thanks to Stephan Lammel for all the SUSY advise, for the lobster and champaign dinners and for all the coffee and ice-cream breaks. Thanks to the SVX group, the Lab D crew and the Ed Barsotti group. Gino Bolla, Tamara Hawke, Paul Shepard, Jeff Spalding.

Chris Quigg thank you for providing always directions and new (extra) angles; thank you for your constant support and advise. Also Chris and Liz, thank you for your fun dinner parties. Keith Ellis, Joe Lykken (thanks for solving my differo-integrations by inspection) and Konstantin Matchev (thanks for the almost all-nighter on the blackboard). Thanks to Michael Spira for useful discussions and help. John Peoples, Mike Witherall, Bruce Chrisman and Roy Rubinstein (thanks for baring with me and my requests during my serving at the Graduate Student Association). The GSA officers. Fernanda Garcia, Durga Rajaram and Andrew Green thanks for your collaboration. Pat Lavallie, Mary Cullen, Jackie Coleman, Cynthia Sazama and Nancy Penson. Many thanks to Sharon Butler.

Thanks Andreas Korn for dragging me out of the office and for much needed help with voice recognition-ware. Cristoph Paus thanks for your list of-"do not use in a science document"-words.

Henry Frisch, Vernon Barger, Pierre Ramond, Welsley Smith and Rocky Kolb for my times in Aspen.

George Sarakinos, thanks for being there is times of extreme pain. And thanks for being so Greek. Thanks to Dr.'s Noor Kassamali and John Goldman. Joyce and Paul Gordon for including me four years in their family passover and having me read the haggada in German. Rose Frisch for extremely interesting discussions and fun lunches in Cambridge. Nirmal Daniere for being my surrogate mom in the past three years.

I want to thank J.D. Jackson for his '99 New Perspectives lecture and all his support. Jack Steinberger for good discussions about discoveries and bets.

I want to thank my godparents, Henry Frisch (thank you for your innovative spirit, your support with the analysis and you patience), Xin Wu and Andrei Nomerotski.

Avi Yagil, thanks for your smart suggestions and for not teaching me how to golf or sail.

Paolo Giromini. Fotis Ptohos, thank you for being you (and for teaching me CDF, and for standing by me around the clock, seven years already.)

Andrew [1].

George Brandenburg thank you for all the support and for making things happen when it seemed impossible. So many thanks again to the HEPL group, John and Melissa and George for always be willing to help me in the past months that RSI problems set in. A psalm for Kris Chaisangathum whose hands I borrowed to type when the RSIs went way out of control. Thanks Kris also for your advise not to use poison as a beverage. Thanks to Bill Ashmanskas for all the discussions, advise and for sharing his knowledge on pain. Kathleen Dias, Scott Turner and Ellen Tolchinski for bringing my hands back when I needed them most.

Kevin Burkett, thanks for your collaboration in the past year, your humor and your invaluable help with the thesis manuscript.

My advisor John Huth: but first John and Karen and the kids for bringing me along in their family and friends music performances, dinners, holidays at the Cape; Thank you James and Phoebe for a memorable theatrical performance one night in Newton. I want to thank John for his guidance, his constantly teaching me and for starting me off at CDF with the SVX project ; I had tons of fun and learned a huge lot working on this project. Thank you John; with million other jobs and responsibilities to tend to, you always succeeded in showing me the paths to solve problems. I am indebted to John Huth for suggesting this analysis as my thesis topic and for his persistent belief that it is possible to be done in a clear and rigorous way.

[1] Gordon you got your own section which you know why you cannot find.

Also thank you for channeling all your expertise to make the seemingly impossible task of using the difficult missing energy data sample a manageable endevour. And for your patience with me when I was confusing myself.

Many thanks to my thesis committee, John Huth, Gary Feldman and Shelly Glashow for all the help in the final times.

And my people in Greece; those that have not forgotten me in seven years of absence and those who did (also the ones I forget too). Anna Gouliamberi and Agis Kontos, Irene, Alexis Vasilis and Charis Kalaitsidis, Eleni Paloura, Katerina Paloura, George Karagiannis and Rodoula Gouliamberi, Ermioni Kontogoula, Efi Dimiropoulou, Elias Zaikos. Sofia Ksenitidou. Nikos Terzopoulos and Evi Tsakiri. My beautiful grand-mom Triantafullia. The whole family would take many pages: I thank you all. My first physics mentor Pantelis Mitsis and the ultimate math figure George Sotiriou.

Rika Michail, the bravest woman I know, thank you.

Thanks to my beloved brother Markos. Mather Vasiliki and father George: it is your doing, really. Thank you.

Contents

List of Figures

List of Tables

Chapter 1

Preface

The subject of this thesis is the rate of $\geq$3-jet events with large missing transverse energy at the Fermilab Tevatron [1] Collider. The aim of the thesis is to investigate whether Supersymmetry ([2] and References therein) production and decays of scalar quarks and gluinos contribute to this rate.

Missing energy collider data have been used for measurements of the Z boson invisible decay rates [3], the top quark cross section and searches for the Higgs boson [4, 5], and other non-Standard Model physics processes [6, 7, 8, 9].

In a detector with hermetic 4π solid angle coverage the measurement of missing energy is the measurement of neutrino energy. In a real detector it is also a measurement of energy that escapes detection due to uninstrumented regions. Jets are produced and dominate the cross section for high P_T proton antiproton scattering. QCD production (including $t\bar{t}$) and W/Z QCD associated production dominate in a sample of $\geq$3-jet events plus large missing energy. These processes are analyzed and understood with the Collider Detector at Fermilab (CDF) [10] data before narrowing the search for a supersymmetric signal with the same detection signature.

The data analysis method used is the *Blind* or *Blind Box* method. It was discussed by R. Cousins and others in the past decade and various versions and improvisations of the method have been used in different measurements and searches [11, 12, 13].

The main objective of a blind analysis is to avoid biased human decisions involving the data selection. This is achieved by insulating the signal candidate data sample until the total Standard Model background is estimated. There is an *a priori* definition of the signal candidate data sample based on the signal signature and the total background estimate and precision.

The parts of the analysis are: a) The data Pre-Selection ; designed to optate a high purity sample of large real missing energy data[1]. b) The W and Z boson QCD associated production background estimate ; the $Z(\rightarrow e^+e^-)$+jets data sample is used to normalize the theoretical rate predictions. c) The multijet QCD production background estimate; the CDF jet data samples are used to normalize the theoretical rate prediction. d) The comparisons of the total background estimates with the data in regions around the Blind Box. e) The study and probe of the supersymmetric parameter space. The hadroproduction of scalar quarks and gluinos and all their decays in minimal Supersymmetry (MSSM) with unification constraints and Supergravity (mSUGRA) frameworks [2] is used. The result of the search is negative for gluino masses below 300 GeV/c^2 for the case $m_{\tilde{q}} = m_{\tilde{g}}$, 195 GeV/c^2 for the case $m_{\tilde{q}} >> m_{\tilde{g}}$, and 570 GeV/c^2 for $m_{\tilde{q}} << m_{\tilde{g}}$ and at 95% C.L.

Chapter 2 is a brief description of the CDF detector. Chapter 3 describes the data reconstruction and samples. Chapter 4 reports the missing energy data Pre-Selection path. Chapter 5 discusses the W/Z, top and diboson Standard Model processes with

[1]The CDF Run 1B Missing Energy data sample used in already published analyses [6, 7, 8] is the product of this thesis Pre-Selection work.

large missing energy and jets in the final state. Chapter 6 discusses the QCD multijet processes. Chapter 7 is an overview of scalar quark and gluino production and decays. Chapter 8 discusses the analysis path, the sensitivity optimization for the scalar quark and gluino search and the comparisons of the total Standard Model predictions with the data around and within the Blind Box. In Chapter 9 the interpretation of the results is given. Associated with a chapter, where necessary there is an Appendix that discusses in detail or adds to the studies presented in the main body of the thesis.

Chapter 2

The Collider Detector at Fermilab

The CDF detector [10] is a multiple purpose device designed to measure $p\bar{p}$ collision properties. This thesis is concerned with the missing transverse energy and the emerging hard-scattered partons that get converted into roughly collimated *jets* of hadrons (Appendix F). The detectors that register the energy of most particles in jets are the *calorimeters*. The sum of analog signals from the calorimeters are used to trigger on the events used in this analysis. Tracking devices which measure the trajectories and momenta of charged particles are used to determine jet quality criteria in the data Pre-Selection and in all the Monte Carlo simulations. All subsystems of CDF are held together by means of the online data acquisition and trigger system. A cross sectional view of a quadrant of the CDF detector is shown in Figure 2.1.

2.0.1 The 1992-1995 Collider Run

The most recent collider run, called *Run 1*, lasted from August 1992 until July 1993 (*Run 1A*) and from January 1994 until July 1995, (*Run 1B*). The total amount of data collected during the course of the run corresponds to an integrated luminosity

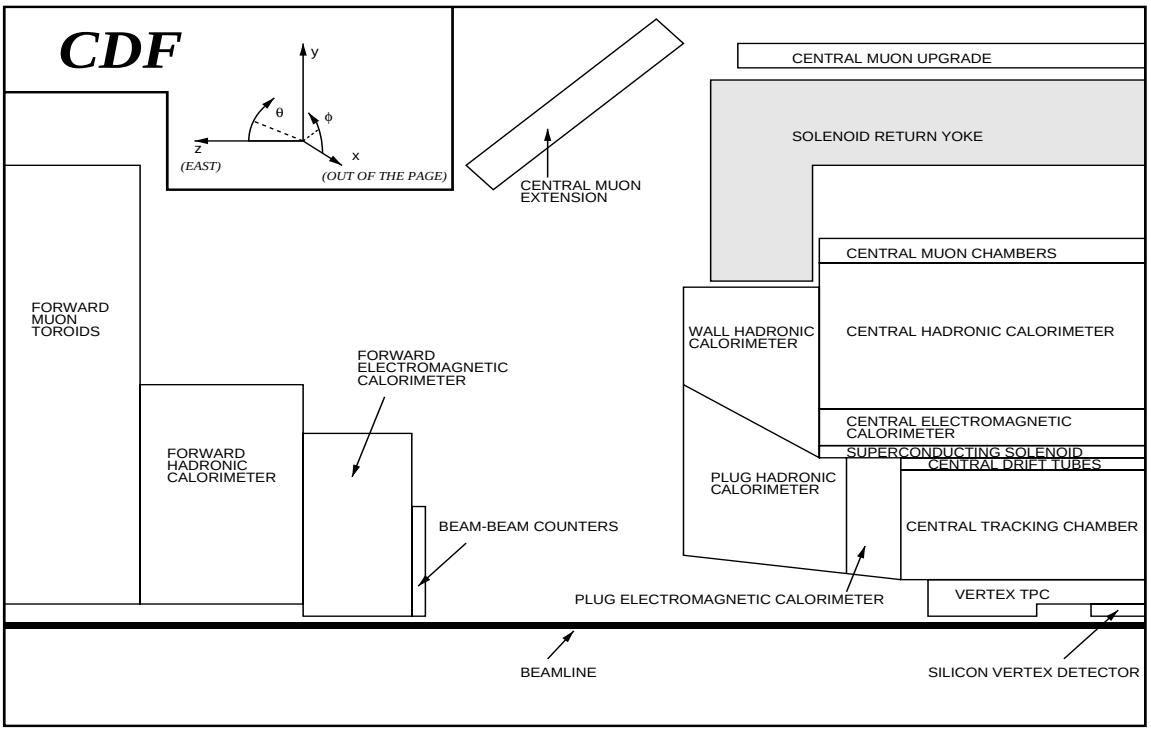

Figure 2.1: $y - z$ view of CDF.

of 109.4 ± 7.2 pb^{-1}.

The integrated luminosity, $\int \mathcal{L}$, depends on the instantaneous luminosity, $\mathcal{L}$, of the collider. The instantaneous luminosity for a $p\bar{p}$ collider is given by [14, 15]:

$$\mathcal{L} = \frac{fBN_pN_{\bar{p}}}{4\pi\sigma^2} \tag{2.1}$$

where

- f is the revolution frequency
- B is the number of proton and antiproton bunches (B = 6)
- N_p is the number of protons per bunch (typically 2×10^{11})
- $N_{\bar{p}}$ is the number of antiprotons per bunch (typically 7×10^{10})

- σ is the transverse cross sectional area of each bunch (typically 5×10^{-5} cm^2).

The highest luminosity achieved was $2.8 \times 10^{31}/\text{cm}^2 sec$ during Run 1B. Typical starting instantaneous luminosities achieved were $1.6 \times 10^{31}\text{cm}^{-2}\text{sec}^{-1}$ and $0.54 \times 10^{31}/\text{cm}^{-2}\text{sec}^{-1}$ for Run 1A and Run 1B respectively. Due to transverse spreading of the beam and collisions losses the luminosity falls exponentially.

Two planes of scintillator counters at either end of the detector, in front of the forward calorimeters are used for luminosity measurements. The counters known as beam-beam counters (BBC) are giving the hit count from particles produced during the beam crossing. The rate (number) of coincidences in these counters, divided by the effective cross section of the counters, gives the instantaneous (integrated) luminosity. The BBC cross section, σ_{BBC} is given by [16]

$$\sigma_{BBC} = \sigma_{tot} \frac{N_{BBC}^{vis}}{N_{tot}}$$

where σ_{tot} is total $p\bar{p}$ cross section as measured in CDF [17], N_{BBC}^{vis} is the BBC triggered events and N_{tot} is the total number of inelastic and elastic events. σ_{BBC} is calculated to be 51.15 ± 1.6 mb. Using σ_{BBC} the luminosity is written as:

$$\mathcal{L}(t) = -\frac{f_o}{\sigma_{BBC}} \times \ln(1 - \frac{R_{BBC}}{f_o}) \tag{2.2}$$

where f_o is the Tevatron frequency ($f_o = 286.272$ kHz) and R_{BBC} is the BBC coincidence rate. Expression 2.2 is derived by assuming Poisson distribution for the number of $p\bar{p}$ interactions per beam crossing:

$$P(n) = \exp(- < n >) \times \frac{< n >^n}{n!}$$

and measuring the probability to have at least one interaction per crossing over the total number of beam crossings

$$P = (1 - P(0)) = \frac{R_{BBC}}{f_o}$$

where $< n >$ is the average number of interactions per crossing:

$$< n >= \frac{\sigma_{BBC}\mathcal{L}}{f_o}$$

Integrating over time both parts of the luminosity equation yields the integrated luminosity, $\int \mathcal{L} dt$. Due to the high luminosity conditions during the run, the observed BBC coincidence rate does not correspond to the true collision rate. Beam gas and beam halo events contribute an additional accidental rate which depends on the luminosity of the beam. The effect is parametrized as a function of the instantaneous luminosity and is subtracted from the final integrated luminosity [16]. Using the two telescopes of beam-beam counters, the CDF luminosity is measured to an accuracy of 4.1% (3.6%) in Run 1B(1A). For Run 1B (1A) the average instantaneous luminosity is 9.1(3.3) $\times$ 10^{30} cm^{-2}sec^{-1} [18]. For a typical data set the integrated luminosity is 86.47 (19.65) pb^{-1} in Run 1B (1A) resulting in a total integrated luminosity of 106.1 $\pm$ 4.1 pb^{-1}.

Taking into account the total inelastic cross section of $\sim$ 56 mb and with a weighted average over luminosity bins (in minimum bias events) throughout Run 1B the numbers of interactions per event is shown in Figure 2.2. A careful determination of the interaction vertex is essential for the correct measurement of the energy and location of calorimeter towers contributing to the formation of jets and the measurement of the missing energy in the event. In this analysis an algorithm is developed that selects the

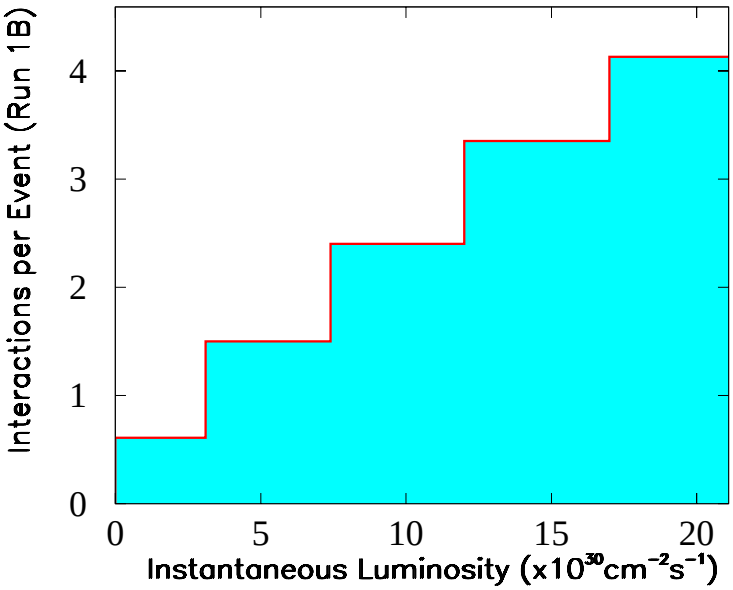

Figure 2.2: Interactions per CDF Run 1B event as a function of the instantaneous luminosity. Measured with the Minimum Bias data sample (Chapter 3).

vertex from which emerges the highest total transverse momentum of charged tracks in the event. The tracks in the three selected jets in the events are consistent with emerging from this one vertex. The danger of selecting fake three-jet events where the third jet is coming from an irrelevant source and overlaps with a two-jet event is avoided. Missmeasurments in the missing transverse energy tails are also abated.

2.0.2 The CDF Coordinates and Solid Angle Segmentation

The origin $x = y = z = 0$ is at the nominal collision point in the geometrical center of the detector. The positive z direction is the direction of the proton beam (eastward at CDF), the positive y direction is up and the positive x direction is pointing out of the rind (northward at CDF). The rest frame of the hard collision is generally boosted relative to the lab frame along the beam direction. The detector solid angle segmentation is designed to be invariant under boosts along the z direction. The angular coordinates η and ϕ are used to describe the particle kinematics and define the angular segmentation of the detector. ϕ is the azimuthal angle about the $z-$axis and $\phi = 0$ is the positive $x-$axis. η (*pseudorapidity*) is related to the polar angle θ:

$$\eta \equiv -\ln \tan \frac{\theta}{2} \tag{2.3}$$

$\eta = 0$ corresponds to the $x - y$ plane, negative η refers to the west side of the detector ($\theta < 90°$) and positive η refers to the east ($\theta > 90°$). The pseudorapidity, η, is equivalent to the *rapidity*, of a particle in the limit of $p >> m$, where p is the momentum of the particle and m its mass. The rapidity y, is defined by

$$y \equiv \frac{1}{2} \ln \frac{E + p_z}{E - p_z} \tag{2.4}$$

If y is expanded in terms of η and $\alpha = m/P_T$ where P_T is defined as $P_T = Psin\theta$,

$$y = \frac{1}{2} \ln \left(\frac{\sqrt{\cosh^2 \eta + \alpha^2} + \sinh \eta}{\sqrt{\cosh^2 \eta + \alpha^2} - \sinh \eta} \right) \sim \eta - .5\alpha^2 \tanh \eta + \mathcal{O}(\alpha^3) \tag{2.5}$$

For vanishing α it is approximately equal to η. The rapidity y of a particle transforms linearly under a boost, $y \rightarrow y + constant$. Taking the derivative shows that

segmentation in rapidity is Lorentz invariant, $dy \xrightarrow{boost} dy$. The rapidity is a function of the particle's mass and polar angle and is not used to define the angular segmentation. Pseudorapidity depends only on the polar angle and is approximately Lorentz invariant under z boosts for high P_T particles of interest to CDF. It is used to define angular segmentation. Being transverse to the z direction the ϕ is also invariant under z boosts and is the orthogonal solid angle variable.

Jets in $\eta\phi$ space are circular. Consider a point in $\eta\phi$ specified by the parton momentum vector $\vec{P}$. Around it consider a set of points with small transverse momentum relative to $\vec{P}$ (representing the decay products produced symmetrically about the parton direction). These points are modeled by adding a transverse kick to the original vector, $d\vec{P} = \Delta\theta\hat{\theta} + \sin\theta\Delta\phi\hat{\phi}$. The magnitude of the kick $|d\vec{P}|^2 = \Delta\theta^2 + sin^2\theta\Delta\phi^2$ is constant and the direction is allowed to vary. For a small kick $\sin\theta$ is constant, θ being the polar angle of $\vec{P}$. From the definition of η by differentiation, $\Delta\eta \sim -\Delta\theta/\sin\theta$. This gives the $\eta\phi$ locus of points described by the kick $d\vec{P}$

$$\Delta\eta^2 + \Delta\phi^2 \sim \Delta\theta^2/\sin^2\theta + \Delta\phi^2 = |d\vec{P}|^2/\sin^2\theta = ct \tag{2.6}$$

Jets on average have a circular P_T distribution in $\eta\phi$ space. This symmetry is used by the jet clustering algorithm. Figure 2.3 shows the CDF transverse segmentation in $\eta\phi$ space.

Transverse segmentation is adjusted radially to form *towers* which project to the nominal interaction point.

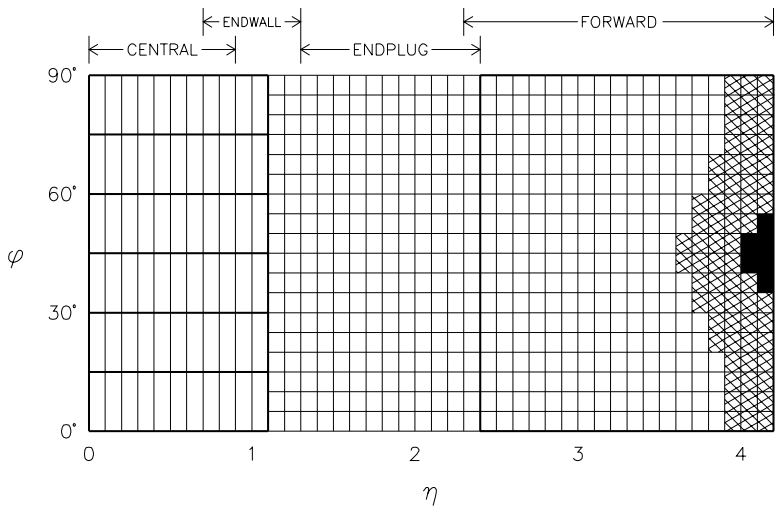

Figure 2.3: $\eta\phi$ segmentation of the CDF calorimeters. Light lines indicate the tower boundaries. Thick lines indicate component boundaries. The shaded area has no coverage.

2.1 The CDF Calorimeters

Close to 4π solid angle about the CDF interaction point is covered with both electromagnetic and hadronic shower detectors. These calorimeters are finely segmented in solid angle around the collision point and coarsely segmented radially outwards from the collision point (depth segmentation). ϕ angular coverage about the z axis is complete. Coverage in polar angle extends down to about 2° from the beam axis. There are gaps in solid angle coverage at structural boundaries. All calorimeters use *shower sampling* to measure particle energy. They are constructed of many layers of dense absorber material (steel or lead) interleaved with active scintillator material sensitive to ionization. Particles striking the absorber material undergo energy loss through their interaction with nuclei and atomic electrons. The daughter particles also interact with the absorber material giving rise to a *shower* of particles. Showers penetrate many layers of the absorber material before they exhaust their energy.

They generate a detectable signal roughly proportional to the number of particles in the shower. Each layer of the active material is said to *sample* the shower. The sum of the signals from all sampling layers is proportional to the energy of the incident particle.

The CDF calorimeters are hierarchically segmented. The polar angle coverage is divided into three regions: the *Central*, the *Plug* and the *Forward*. Each comprises of electromagnetic and hadron components. Components are constructed of many identical modules. Each module is divided transversely into *towers*. Towers are segmented in depth. Each depth of towers is read out by separate electronics channels. The beam physics conditions of the different regions dictate the design parameters. The Central region (CEM, CHA $0 < |\eta| < 1.1$) being at large polar angle to the beam is the most important to high transverse momentum objects. It also covers the largest percentage of the solid angle coverage and has the lowest energy flow. The active material is scintillator. This provides good energy resolution and adequate luminosity lifetime. Central components read each tower with two photmultiplier tubes on opposite ϕ sides. The signal balance between tubes allow a determination of ϕ of a single particle to better than 1°. The EM detectors use thin lead sheets as absorber, the HA use relatively thick steel. The thin lead sheets allow detailed sampling of electromagnetic showers while the thick steel assures containment of hadron showers. The Plug (PEM, PHA $1.1 < |\eta| < 2.2$) and Forward (FEM, FHA $2.2 < |\eta| < 4.2$) are closer to the beamline and subject to higher rates and energies. In this regions scintillating material darkens and degrades the energy measurement. The Plug and Forward cover large part of pseudorapidity. Implementation of the required transverse segmentation with scintillator is hard. Accordingly, the Plug and Forward use gas proportional chambers as an active medium. They have poorer energy resolu-

tion compared to scintillator but longer luminosity lifetime. The transverse energy resolution is approximately uniform throughout the calorimeters. Gas calorimeter transverse segmentation is accomplished with etched cathode pads. Signals from individual plane cathode pads are cabled together in depth before amplification. To aid in electron identification, the readout of the Plug and Forward EM detectors are divided in depth. The cathode pads from the first and last 15 planes of the Forward EM detector are ganged to a single amplifier as are those from the first four, middle 26 and last four Plug EM detector. The ϕ segmentation of the gas calorimeters is comparable to their η segmentation, whereas the central ϕ segmentation is more coarse. In addition to cathode pad readout, the gas calorimeters have anode plane readout of the longitudinal shower development. Anode signals are used in noise removal algorithms and in electron identification. The CHA and WHA components digitize the time of charge deposition. The resolution of these hadron TDC signals is 1 ns. They are used to remove Main Ring and cosmic ray backgrounds.

The seven components (3 EM and 4 HA) are shown in in Figure 2.1. Table 2.1 lists the design and performance parameters for each.

The missing transverse energy ($\not\!\!E_T$) is defined to be the negative of the vector sum in all calorimeter towers with $|\eta|$ <3.6. The η range is restricted because the final focusing magnets of the Tevatron obscure parts of the Forward hadron calorimeter. To be included in the sum, individual tower energies must exceed detector-dependent energy thresholds. These thresholds are 100 MeV in the CEM, CHA and WHA, 300 MeV in the PEM, 500 MeV in he PHA and FEM, and 800 MeV in the FHA.

System	η Range	$\Delta\eta \times \Delta\phi$	N_{layers}	Sampler-Absorber	$\sigma_E/\sqrt{E}$
CEM	$\lvert\eta\rvert < 1.1$	.11× 15°	30	.5 scn-.32 Pb,18 X_0	$\frac{13.7\%}{\sqrt{E_T}} \oplus 2\%$
PEM	$1.1 < \lvert\eta\rvert < 2.4$	.09× 5°	34	.7 gas-.27 Pb,18-21 X_0	$\frac{22\%}{\sqrt{E}} \oplus 2\%$
FEM	$2.2 < \lvert\eta\rvert < 4.2$	.1× 5°	30	.7 gas-.27 Pb,25 X_0	$\frac{26\%}{\sqrt{E}} \oplus 2\%$
CHA	$\lvert\eta\rvert < 0.9$	.11× 15°	32	1. scn-2.5 Fe,4.5 λ_0	$\frac{50\%}{\sqrt{E_T}} \oplus 3\%$
WHA	$0.7 < \lvert\eta\rvert < 1.3$	.11× 15°	15	1. scn-5. Fe,4.5 λ_0	$\frac{75\%}{\sqrt{E}} \oplus 4\%$
PHA	$1.3 < \lvert\eta\rvert < 2.4$	.09× 5°	20	.7 gas-5.1 Fe,5.7 λ_0	$\frac{106\%}{\sqrt{E}} \oplus 6\%$
FHA	$2.4 < \lvert\eta\rvert < 4.2$	.1× 5°	12	1. gas-10.2 Fe,7.7 λ_0	$\frac{137\%}{\sqrt{E}} \oplus 3\%$

Table 2.1: Summary of CDF calorimeter properties. The symbol $\oplus$ signifies that the constant term is added in quadrature in the resolution. Energy resolutions for the electromagnetic calorimeters are for incident electrons and photons, and for the hadronic calorimeters are for incident isolated pions. Energy is given in GeV. Thicknesses are given in radiation lengths (X_0) and interaction lengths (λ_0) for the electro-magnetic and hadronic calorimeters, respectively and in cm for the absorber and sampler material. Gas is 50% Argon, 50% Ethane with 1-4% alcohol quencher.

2.2 The CDF Tracking Detectors

Within the 1.4 Tesla magnetic field of the solenoid are three tracking chambers for charged particles. Surrounding the 1.9 cm radius beryllium beampipe is a 4 layer silicon microstrip detector (SVX) [19, 20]. which was installed in 1992. The SVX is 51 cm long and consists of two identical cylindrical modules that meet at z=0. Because $p\bar{p}$ interaction are spread along the beamline with standard deviation $\sigma \sim 30$ cm, the geometrical acceptance of the SVX is about 60%. The four layers of SVX are at distance 3., 4.2, 5.7 and 7.9 cm form the beamline. Axial microstrips with 60 μm pitch on the three inner-most layers and 55 μm pitch on the outermost layer provide precision track reconstruction in the plane transverse to the beam. The SVX single-hit resolution is measured in the data be σ=13 μm, and the impact parameter

resolution at high momentum is measured to σ=17 μm. Due to radiation damage to the SVX readout chip the performance of the SVX deteriorated over the course of the data taking period. On the innermost layer the ratio of the average analog pulse size from a particle to the noise level decreased from 9 to 6 from the beginning to the end of data taking period. For the second part of the run the SVX was replaced by a similar detector called SVX$'$ with signal to noise of 16 at the time of installation. Because of the strip geometry the SVX detector provides only 2-D information in the r-ϕ plane. Outside the SVX is an Argon-Ethane vertex drift chamber (VTX), installed in 1992 which provides tracking information up to radius of 22 cm and $|\eta|$ <3.25. The VTX is comprised of 8 octagonal module segmented into 8 wedges. The endcaps of the wedges are segmented into two sets of wires, one perpendicular to the beam and one perpendicular to the centerline. Signal are produced on the sense wires from electrons produced by the ionization of the gas when a charged particle passes through. By measuring the drift times, the position of the track is reconstructed at the r-z plane. The VTX measures the z position of the $p\bar{p}$ interaction vertex with a resolution $\sim$1 mm. Both SVX and VTX are mounted inside the Central Tracking Chamber (CTC) which is a 3.2 m long drift chamber with an outer radius of 132 cm containing 84 concentric cylindrical layers of sense wires. Sixty layers have wires parallel to the beam direction (axial wires) and provide tracking in the $r-\phi$ plane. Twenty-four layers (stereo) are tilted at $\pm 3^\circ$ with respect to the beam direction. Together the axial and stereo wires provide tracking in the $r-z$ plane. The novel feature of the chamber is the drift cell 45° tilt with respect to the radial direction which results in a purely azimuthal drift in the nominal electric and magnetic fields. The data Pre-Selection uses the CTC tracks to establish a jet quality criterion for the rejection of fake jet events. In all the Monte Carlo simulations the CTC tracks are modeled

with the appropriate degradation as measured in the data.

2.3 The CDF Muon Detectors

The Central calorimeters act as hadron absorber for the Central Muon Detector system (CMU), which consists of four layers of drift chambers located outside the CHA. The CMU covers $|\eta|$ <0.6 and is reached by muons with $P_T > 1.4$ GeV/c. In 1992, 0.6 m of steel was added behind the CMU for farther hadron absorption, and an additional four layers of drift chambers were added behind the steel. This system is the Central Muon Upgrade (CMP). Approximately 84% of the solid angle for $|\eta|$ <0.6 is covered by the CMU, 63% by the CMP and 53% by both. The coverage of the the central muon system was extended to pseudorapidity range $1. < |\eta| < 0.6$ through four free-standing conical arches which hold drift chambers for muon detection sandwiched between scintillator counters for triggering. This system is the Central Muon Extension (CMX). Approximately 71% of the solid angle for $1. < |\eta| < 0.6$ is covered by CMX. In all muon systems in the central region, the muon P_T is measured with charged tracking.

2.4 The CDF Boundary Regions (Gaps)

Due to mechanical constraints certain regions of the $\sim 4\pi$ calorimeter solid angle coverage of CDF are under-instrumented. Given the $\eta\phi$ segmentation of the calorimeter these regions are bands in either η or ϕ. In Figure 2.3 the narrow bands at constant ϕ in the Central calorimeter are due to the steel skins that separate the towers. The larger bands at constant η are due to junctions between the components. The major η gaps are :

- The 90° gap - The gap between the east and west arches of the Central calorimeter.

- The 30° gap - A region of low response where the Central and Plug calorimeters meet.

- The 10 ° gap - A region of low response at the inner edge of the Plug calorimeter (close to the beamline) plus the gap between the Plug and Forward calorimeters.

- *The chimney* - This is approximately 9 cm from the 90° gap. The region $0.77 < \eta < 1.0$, $75° < \phi < 90°$ (equivalent to two towers) is not instrumented ; it contains the cryogenic connections to the solenoidal magnet.

These regions absorb single particles without registering their full energy. A jet consists of many particles and generally only a fraction of the jet energy is lost through the gaps. Some gap regions of CDF were scanned with test beam particles, their response was mapped out and parameterizations of the longitudinal and transverse shower development in them enters the detector simulation program to model the energy loss.

The angular gap between the Plug and Forward detectors is a function of the event z-vertex position. As seen in Figure 2.1 particles originating from vertices far from the nominal detector center can pass through the hole in the Plug detector and miss the Forward detector. The importance of the limited response in the gap regions depends on the particular analysis. In analyses that do not involve large $\not\!\!E_T$, corrections can be applied to the jet energy to account for the energy lost. In this analysis an efficient jet fiducial requirement is designed based on the η of the jets, the event z-vertex and the angular correlation of the $\not\!\!E_T$ vector with the jets, to eliminate events with fake $\not\!\!E_T$ due to the gaps.

2.5 The CDF Trigger

A three level trigger system is employed at CDF to accommodate the 1 MHz of overlapping triggers in order to retain data from small cross section processes and at the same time handle efficiently the high rate of QCD dijet events. The trigger rate is successively reduced from 280 KHz Level 1 input rate to $\sim$ 10 Hz Level 3 output rate, with the output Level 3 rate being limited by the recording speed of 8 mm tape drives. The trigger complexity increases according to its level at the cost of decision time.

The Level 1 trigger

The Level 1 is the simplest and fastest of the three trigger paths. At this level the decision to accept or reject an event is based on the identification of energy clusters in the calorimeter or stubs in the muon chambers.

The energy of single trigger towers with dimensions of 15° in ϕ $\times 0.2$ in η for both the electromagnetic and hadronic calorimeters is used in the calorimeter trigger. To accommodate the high rate, a single trigger tower is required to have transverse energy exceeding a preset threshold, different for the three calorimetry regions. The single trigger tower thresholds used in Run 1A and Run 1B are summarized in Table 2.2. The high E_T threshold for the forward calorimeters (51 GeV is the highest threshold) during Run 1B, eliminated any Level 1 triggers from these detectors but it was necessary to avoid the saturation of Level 1 during very high luminosity conditions.

The single tower L1 triggers feed the L2 jet and $\not\!\!E_T$ triggers.

The Level 1 muon decision is based on a minimum P_T for the candidate muon stub. Since full tracking information is available only at the highest trigger level, the muon P_T at this trigger level is inferred by measuring the angle of incidence of the

Detector	Run 1A	Run 1B
CEM	6	8
CHA	8	12
PEM	8	11
PHA	25	51
FEM	8	51
FHA	25	51

Table 2.2: Single trigger tower E_T thresholds used at Level 1 during Run 1A and Run 1B. E_T is measured in GeV.

incoming track relative to an infinite momentum track emerging from the nominal interaction point ($z = 0$). To reduce background from accidental or uncorrelated hits, a minimum energy of 300 MeV is required in the hadron calorimeter tower associated with the muon stub.

The Level 1 trigger offers a reduction of ~ 1000 bringing the input rate to Level 2 to ~ 2 kHz, while the decision time is less than the bunch crossing time of 3.5 μs.

The Level 2 trigger

The second level of the trigger path is the stage where the decision for accepting or rejecting the largest portion of the events is made. It is a Fastbus based hardware trigger system with a decision time of $\sim$ 20 μs. The analog trigger signals from the detector components are brought to the trigger electronics. The trigger towers, defined as 15° in ϕ $\times 0.2$ units of rapidity at the first two levels of the trigger system, are summed into energy clusters by the "hardware cluster" finder, forming jet-like energy clusters. For each cluster the E_T, average ϕ, average η, and the ϕ and η widths are determined. All tower transverse energies are calculated with respect to the origin of the detector (z = 0). Tracks are reconstructed using a fast track processor (CFT). The CFT searches for tracks in the r - ϕ of the CTC and matches them to

EM clusters in the central region or muon stubs. The CFT momentum resolution is $\delta P_T/P_T = 3.5\%(\mathrm{GeV}^{-1})\mathrm{P_T}$. This procedure defines the central electron and muon Level 2 triggers.

Besides the lepton Level 2 triggers, triggers designed to collect data based on jet clusters are also implemented. The Level 2 inclusive jet triggers demand a single trigger tower above threshold at Level 1 and a cluster of electromagnetic and hadronic transverse energy in the calorimeter at Level 2. The Level 2 jet clusters are formed using a seed tower of $E_T > 3$ GeV and summing the E_T of all the contiguous to the seed towers in η and ϕ. The additional towers are required to have $E_T > 1$ GeV. Events are accepted requiring jet threshold energies above $E_T > 20$, 50, 70, and 100 GeV. The obtained data samples are referred to as *JET20, JET50, JET70* and *JET100* samples. Because of the large trigger rate, the first three jet triggers areprescaled with the JET20 having the largest prescaling factor (~ 1000)(Appendix B).

A crude estimate of the *missing transverse* energy which reflects the transverse energy imbalance in the calorimeter ($\not\!\!E_T$), attributed to non-interacting particles, is performed at Level 2. The $\not\!\!E_T$ is calculated by summing vectorially the transverse energy of all towers in the calorimeter, $\vec{\not\!\!E}_T = -\sum_{i=1}^{n} \vec{E}_T^i$, where E_T^i is the transverse energy of the i-th tower.

The `MET_35_TEX_2_NOT_GAS`, `MET_35_TWO_JETS` triggers are the two missing energy Level 2 triggers (the logical OR of these is referred to as `MET*`) used in this analysis. The first trigger requires that the highest energy cluster in the event not be a *Texas Tower* or a *gas spike* : these are large deposits of energy in the gas hadron calorimeters that cause large energy imbalance in the event and pass the missing energy trigger. The energy appears with no associated tracks or electromagnetic energy and is known

to be noise. The deposition is also spatially localized compared to real particle showers. The so called Texas Towers are caused by low energy neutrons. Neutrons are produced in a hadronic shower. Low energy neutrons have a small interaction cross section with lead and steel and they penetrate deep in the calorimeters. Low energy neutrons have a much larger cross section with hydrogen. They transfer their kinetic energy to protons in the ethane of the chamber gas. The protons lose the energy through ionization ranging out in a few centimeters of the gas. This energy generates a large calorimeter signal in a single layer and tower of the calorimeter sampler. The signal generated by neutron-induced protons is much larger than the one generated by a shower of the same energy. For instance a 1 MeV proton in the PHA deposits energy equivalent to a 28 GeV pion shower. This is a result of the calorimeter calibration. Test beam calibration constants are defined by equating the signal observed in the active medium of the calorimeter with the energy of the incident particle. Most shower energy is lost into the absorber material. The calibration extrapolates the observed signal, scaling it up to compensate for signal lost in the absorber. This calibration is necessary in all sampling calorimeters. Unlike showers, neutron-induced protons range out in the gas, depositing all their energy in the sampling medium. Interpreted using a shower-generated calibration, the scaled "energy" of this signal overestimates the true energy of the proton. The gas hadron calorimeters have the largest scaling calibration factors and are the most susceptible to this kind of noise. In addition to the Texas Towers the PHA calorimeter are afflicted with electronic cable noise. It appears in the data as a uniform signal across a 3×4 plateau of towers. In the PEM detector, spikes are caused by high voltage breakdown at the wire feedthroughs of the chamber. A similar problem in the FEM occurs at much smaller rate. In this analysis FEM clusters above 200 GeV are vetoed eliminating this noise. An algorithm

to remove gas spikes and Texas Towers is implemented as the Level 2 trigger name above indicates. The principle is to remove deposits of energy too localized to be particle showers. Remaining noise is eliminated at the data Pre-Selection. The first of the two missing energy triggers has a rate of 72 nb of which 52 nb was constant background rate. The second has a rate of 19 nb.

The Level 2 electron trigger used in this analysis requires an electromagnetic cluster of transverse energy greater than 16 GeV and a CFT track matched to it with transverse momentum $P_T > 12$ GeV/c. This trigger is used to select the $Z(\rightarrow e^+e^-) + jets$ data sample on which the normalization of the W/Z+jets predictions is based. For the muon Level 2 triggers the requirement is a CFT track with $P_T > 12$ GeV/c and pointing to within 5° of a Level 1 muon segment.

Based on the decision of Level 2 the event rate is reduced from the 2 kHz input from Level 1 down to $\sim$ 20 - 35Hz. Accepted Level 2 events are fed to the next stage of the trigger, Level 3, for final processing and decision.

The Level 3 trigger

The Level 3 trigger decision is made after full event reconstruction, including track pattern recognition and cleanup of electronic noise and gas spikes. Since the process is CPU-consuming, accepted Level 2 events are processed on a "farm" of silicon graphics processors running the full CDF reconstruction package. Each CPU has the ability of processing an event while a second one is being read in or written out to disk. The input rate is reduced by 60% with final output rate of $\sim$ 8 Hz. Loose quality criteria are applied on the leptons which are selected as output of this trigger level. The efficiency of the Level 3 trigger is $\sim$ 98% limited only by tracking pattern recognition failures. The online missing energy trigger (`EVCL_COMBINED_EXOB`) requires $\not\!\!E_T \geq$30 GeV and does not require the event to have passed the L2 missing energy triggers.

45% of the events passing the online trigger are volunteers from the JET triggers.

Chapter 3

Reconstruction - Data Samples

This chapter describes the event physics objects reconstruction with the emphasis on the missing transverse energy and jet reconstruction as well as the data samples used.

3.1 Event Reconstruction

3.1.1 Energy reconstruction

The energy in the calorimeter is measured in terms of the ADC counts of each calorimeter electronic channel. The ADC counts are converted to energy (GeV) using detector dependent scale factors determined either from specific data samples collected during the run, or from testbeam data. After suppression of noisy channels and removal of spurious sources of energy, an $\eta\phi$ array of tower energies is obtained which is further used to construct an array of transverse energies, E_T, using the polar angle θ of each tower center with respect to the event vertex. The transverse energy of each tower is $E_T = E \sin\theta$. The data are registered in one large data bank called TOWE. It lists the electromagnetic and hadronic E_T in each tower of the CDF de-

tector. In this bank an integer ($IETA - IPHI$) representation is used for the the $\eta\phi$ segmentation. The $\eta - IETA$ correspondence is given in Table 3.1.

$\|\eta\|$ range	TOWE IETA (+ -)
0-0.1308	42 43
0.1308-0.2595	41 44
0.2595-0.3841	40 45
0.3841-0.5033	39 46
0.5033-0.6163	38 47
0.6163-0.7226	37 48
0.7226-0.8225	36 49
0.8225-0.9160	35 50
0.9160-1.0036	34 51
1.0036-1.1000	33 52
1.1000-1.2000	32 53

Table 3.1: TOWE IETA, η map.

3.1.2 Jet Reconstruction

A brief summary of jet-physics is given in Appendix F. After the calorimeter data are cleaned from obvious noise sources, a *clustering* process is used to reconstruct jets. Clustering combines and simplifies the energy from separate tower energy measurements. Nearby towers are associated by an algorithm based on their proximity and energy. Clustering attempts to undo parton *fragmentation* (Appendix F). The number of jets in the event, their direction and energy is determined by the clustering. The 4-momentum (E,p) of each jet is computed assuming the energy in each tower is deposited by a massless particle striking the tower center and by summing

the 4-momenta of all the towers (i) that comprise the jet cluster:

.

$$
\begin{aligned}
E &= \sum_i (E_i^{em} + E_i^{had}) \\
p_x &= \sum_i (E_i^{em} \sin\theta_i^{em} + E_i^{had} \sin\theta_i^{had}) \cos\phi_i \\
p_y &= \sum_i (E_i^{em} \sin\theta_i^{em} + E_i^{had} \sin\theta_i^{had}) \sin\phi_i \\
p_z &= \sum_i (E_i^{em} \cos\theta_i^{em} + E_i^{had} \cos\theta_i^{had})
\end{aligned}
$$

Based on the above quantities the jet $P_T \equiv \sqrt{p_x^2 + p_y^2}$, $E_T \equiv P_T \frac{E}{P}$ and $\eta \equiv 0.5 \ln \frac{E+p_z}{E-p_z}$ are calculated. In CDF the quantity η_d, the pseudorapidity of the jet with respect to the origin of the coordinate system (x=y=z=0), is used to define the location of the jet with respect to the calorimeter regions. The jet 4-momentum calculated above is based on the raw calorimeter energies and is subject to numerous corrections. Jets which are used with the raw energy and momentum quantities are termed *uncorrected* jets. Jets are mismeasured due to a variety of effects: (a) calorimeter non-linearities, (b) reduced calorimeter response at the boundaries of the different calorimeter modules and components, (c) loss of low momentum particles inside the magnetic field, (d) energy deposition in towers outside the jet cone, (e) contribution from underlying-event or additional interactions and (f) energy loss due to muons and neutrinos. In analyses concerned with jet mass spectroscopy the jets are corrected for these effects. The correction function is a map of the detector response for different energies and pseudorapidity regions. The correction is meant to reproduce the average jet E_T correctly, not to reduce the jet fluctuations around the mean E_T. Typically the jet corrections increase the jet energy by 30%. A detailed

description of the corrections are found in references [21, ?]. Throughout this analysis raw jets are used.

The CDF jet clustering algorithm

Because fragmentation is subject to large fluctuations, no single jet looks like any other so it is not expected that the clustering will completely undo the fragmentation for every jet. A good clustering algorithm is flexible in providing an adequate jet interpretation of all events, incorporates the physical understanding of the fragmentation and the detector response and is simple and consistent. The CDF jet clustering algorithm uses a *fixed circle* method, collecting towers lying within a fixed radius in $\eta\phi$ space around a selected *seed* point. Initial seed points are selected as centers of regions of high E_T density in the calorimeters. To ensure uniform seed selection over all the detector the $\eta\phi$ segmentation is rearranged in the software: the energies of the three towers of extra ϕ segmentation of the gas calorimetry are summed together giving an effective tower size of $\sim .1 \times 15^\circ$ $\eta\phi$ over the entire detector. Effective towers containing over 1 GeV (EM+HA) of E_T are used as seeds. The seeds are pre-clustered using a simple adjacency algorithm. Seed towers are associated if they touch on a side or corner in $\eta\phi$ space. Coupled seeds towers are required to fall monotonically in energy going out from the highest energy tower to the lowest. An energy valley between groups of such conjoined towers forces pre-cluster separation. The E_T–weighted $\eta\phi$ centroid of each pre-cluster of seeds is computed and is used as the initial site for fixed circle clustering. The algorithm uses the full $\eta\phi$ segmentation of CDF. It collects towers with E_T (EM+HA) above 100 MeV inside a circle of fixed radius $\Delta R = \sqrt{\delta\eta^2 + \delta\phi^2}$. The radius is typically chosen to be 0.7 units. The center is iterated until it is matched with the E_T– weighted $\eta\phi$ centroid. The towers of

the original pre-cluster are retained during iteration regardless of whether they lay in the circle. This avoids jet formation far from the initial pre-cluster center. The iterations end when the enclosed in-the circle towers remain unchanged. The process converges within two or three iterations. Each cluster is formed independently and a calorimeter tower can be assigned to more than one cluster. In the final stage the algorithm separates the overlapping clusters. The E_T of the shared towers is computed and compared to the total E_T of the cluster. If the common towers accounts for more than 75% of the E_T of either cluster the clusters are merged into a single one. Otherwise they are separated based on an iterative process. The common towers are kept in the cluster of closest proximity in $\eta\phi$ space. The E_T weighted centroid of the separated clusters is recomputed. If the two clusters still share towers the process is repeated until the list of separated towers does not change. The single parameter of the jet algorithm is the radius. It is chosen to be 0.7 for this analysis. Clustering with different radius gives different jet energies and number of jets in an event. This ambiguity is not resolved theoretically. There is no single *right* value of the radius to use. The 0.7 value is found to give reasonable jet P_T resolution and jet angular separation. An E_T threshold of 15 GeV is required for a jet to be counted throughout this analysis.

3.1.3 Missing Transverse Energy ($\not\!\!E_T$) and Neutrino reconstruction

Neutrinos do not interact in the detector since there is not sufficient amount of material. Since the longitudinal component of the colliding partons momentum is unknown, only the transverse component of the neutrino momentum is measured.

From transverse momentum conservation, the presence of undetected neutrinos results in transverse energy imbalance in the detector which is proportional to the neutrino momentum and it is called *missing* E_T or $\not\!\!E_T$. The raw $\not\!\!E_T$, is defined as the negative vector sum of the transverse energy in the calorimeter: At Level 3, $\vec{\not\!\!E}_T$ is the vector sum of all calorimeter towers, both electromagnetic and hadronic, and is defined as

$$\vec{\not\!\!E}_T = \sum_{towers} (E_i \sin\theta_i)\hat{n}_i \tag{3.1}$$

where E_i is the energy of the *ith* tower, and $\hat{n}_i$ is a transverse unit vector pointing to the center of each tower. θ_i is the polar angle of the line pointing from $z = 0$ to the *ith* tower. The sum extends to $|\eta_d| < 3.6$, to avoid the region of the forward calorimeters that have been designed to accommodate the quadrupole focusing magnets. The magnitude of the $\not\!\!E_T$ is expressed as:

$$|\vec{\not\!\!E}_T| = \not\!\!E_T = \sqrt{(\sum_i E_T^i \cos\phi_i)^2 + (\sum_i E_T^i \sin\phi_i)^2}$$

The resolution of the $\not\!\!E_T$ depends on the response of the calorimeter to the total energy deposited in the event and therefore on the event topology. It is parametrized in terms of the total scalar E_T, termed $\sum E_T$. The resolution is measured with minimum bias events. Minimum bias events are collected requiring a coincidence of hits in both the forward and backward BBC counters. No requirements on the calorimeter energy is made. These minimum bias events are dominated by inelastic $p\bar{p}$ collisions. No significant $\not\!\!E_T$ is expected in these events. A fit to these data, yields [22]

$$\sigma(\not\!\!E_{T_x}) = -0.582 + 0.7418\sqrt{\sum E_T(GeV)}$$

The non-zero term in the expression is due to run-by-run offsets and out-of time accidental energy. For large $\not\!\!E_T$ the resolution is a function of the $\not\!\!E_T$ and the above expression is not valid.

3.1.4 Track reconstruction

Track reconstruction in CDF is performed using information from all the tracking detectors. Tracks are reconstructed by fitting the CTC hits to the three dimensional track-helix equation. The reconstruction starts by fitting hits from the CTC axial superlayers (r-ϕ plane), to a circle. The fitted circle is projected into the CTC stereo superlayers and a three dimensional five parameter fit to a track-helix is performed. For this part of the reconstruction, information from the VTX detector is also used. The five track parameters used in CDF for all track analysis are:

- *curvature*: the 2-dimensional curvature which is proportional to the transverse momentum of the track.
- *cotθ*: the cotangent of the polar angle θ.
- *impact parameter*: the distance of closest approach of the track to the interaction vertex in the transverse plane.
- z_0: the z-coordinate of the point of closest approach.
- ϕ_0: the ϕ direction of the track at the point of closest approach.

Each CTC track is then extrapolated in the SVX fiducial volume and a search for associated SVX hits is performed. Multiple scattering and ionization loss of energy in the material are taken into account during the extrapolation. The size of the search

region, *road search*, is defined based on the track parameters and their uncertainties. Every time an SVX hit is found, the track parameters, the error matrix and the road size are recalculated and a new search is performed with the new parameters. Since more points are added to the track fit, the χ^2 is recalculated and the hit assignment to the track candidate is determined according to the goodness of the fit.

3.1.5 Vertex reconstruction

The event vertex

The vertex algorithm uses tracks reconstructed in the VTX detector, to define the point of origin of the tracks. This point defines a vertex. Since there are more than one vertex present in an event, the vertex with the highest VTX hit occupancy associated with it, is the *event vertex*, also referred to as z(`VTVZ1`). An array (VTVZ array) is kept with all the vertices sorted according to the VTX hit occupancy . The event vertex, is used to determine the polar angle, θ, of each calorimeter tower. The transverse energy of each calorimeter tower is calculated according to this vertex and all algorithms making use of calorimeter towers for cluster formation or calculation of the energy imbalance in the detector, refer to this vertex.

The lepton vertex

High luminosity conditions during the run, result to more than one vertex in an event (Figure 2.2). The large number of additional vertices result in uncertainty on the choice of the event vertex. The wrong choice of the event vertex does not affect on average the kinematic characteristics of the events. On an event-by-event basis it does lead to large fluctuations . Events used in analyses that contain a high-P_T lepton *i.e.* a high-P_T track, resolve the ambiguity on the choice of vertex by using the vertex associated with the lepton track as the event vertex. This vertex is called the

z(VXPRIM).

The highest $\sum |\vec{P}_T|$ vertex

It is found that the $\not\!\!E_T$ tails are not invariant to the choice of the vertex. To determine the hard scattering vertex in an all-hadronic event a vertex finder algorithm is developed for this analysis, that selects the vertex from which emerges the highest total P_T of charged tracks in the event. All the 3-dimensional tracks with P_T over 200 MeV/c and impact parameter less than 1 cm, in the event are associated with an element of the VTVZ vertex array. The array of vertices is re-sorted according to the $\sum |\vec{P}_T|$ of the tracks extending from each vertex. The highest $\sum |\vec{P}_T|$ vertex is referred to as z(max$\sum |\vec{P}_T|$).

Jet-vertex matching algorithm

A simple jet-vertex matching algorithm is developed to assign a VTVZ vertex to each jet in the event. The jet-vertex is compared with the nominal z(VTVZ1) vertex, with the defined z(max$\sum |\vec{P}_T|$) and with the z(VXPRIM) in the JET50 data sample . The z(VXPRIM) is also compared with the z(max$\sum |\vec{P}_T|$). To assign each jet to its proper vertex:

1. Initially all the tracks of the event are being matched with some jet of cone 0.4. For each jet k there is an ensemble of tracks, which defines a set of track vertices z_0 $\{T^k\}$.

2. Each of the tracks' z_0 is assigned to the closest z(VTVZ) vertex within 5 cm. In this way, the set $\{T^k\}$ is mapped to a reduced VTVZ set of vertices $\{V\}$.

3. To decide which element of $\{V\}$ is the "jet vertex," two variables are defined:

   - Where T^k_{tot} is the total number of tracks associated with jet k and $V_l(j)$ is the number of tracks associated with each element of V, for jet k, the

vertex track occupancy $Q^k(j)$ is defined:

$$Q^k(j) = \frac{V_l(j)}{T^k_{tot}} \tag{3.2}$$

- Where PT^k_{tot} is the sum of the P_T of the total number of tracks associated with the jet k and and $PV_l(j)$ is the sum of the $|\vec{P_T}|$ of the tracks associated with each element of V then for jet k, the $\sum |\vec{P}_T|$ fraction $F^k(j)$ is defined:

$$F^k(j) = \frac{PV_l(j)}{PT^k_{tot}} \tag{3.3}$$

The highest occupancy vertex is defined as the *jet vertex*. There is less than 0.1% discrepancy in the results if the highest $\sum |\vec{P}_T|$ fraction vertex is used instead. The $z(\texttt{VTVZ1})$, $z(\texttt{VXPRIM})$, $z(\texttt{max}\sum |\vec{P}_T|)$, $z_{\texttt{jet}}(1)$ and $z_{\texttt{jet}}(2)$ (where it is implied that the jets are sorted according to their E_T) are compared. In Table 3.2 the percentage of events whose vertex difference is greater than 2.5 cm is given. The $z(\texttt{max}\sum |\vec{P}_T|$) vertex is consistent with the leading, second leading jet and $z(\texttt{VXPRIM})$ at the 1% level.

δz type	$R(\lvert\delta z\rvert > 2.5$ cm)(%)
$z(\texttt{max}\sum \lvert\vec{P}_T\rvert)$ - $z(\texttt{VTVZ1})$	12.
$z(\texttt{max}\sum \lvert\vec{P}_T\rvert)$ - $z_{\texttt{jet}}(1)$	1.
$z(\texttt{max}\sum \lvert\vec{P}_T\rvert)$ - $z_{\texttt{jet}}(2)$	1.
$z_{\texttt{jet}}(1)$ - $z_{\texttt{jet}}(2)$	1.7
$z(\texttt{VTVZ1})$ - $z_{\texttt{jet}}(1)$	11.
$z(\texttt{VXPRIM})$ - $z(\texttt{max}\sum \lvert\vec{P}_T\rvert)$	0.8

Table 3.2: Percent discrepancies between jet-vertex/event-vertex algorithms. The highest $\sum |\vec{P}_T|$ vertex is consistent with the hard collision vertex.

Figure 3.1 shows the $\not\!\!E_T$ difference between the default $\not\!\!E_T$ and the $\not\!\!E_T$ calculated with $z(\texttt{max}\sum|\vec{P}_T|)$.

To ensure that the events are reconstructed with the hard collision vertex, all data samples are re-reconstructed using the $z(\texttt{max}\sum|\vec{P}_T|\ )$ vertex.

3.1.6 Electron reconstruction

Electron reconstruction begins with a clustering algorithm to identify electron showers. An electron cluster consists of a *seed* tower and *shoulder* towers (towers adjacent to the seed). Towers with transverse electromagnetic energy of $E_T \geq 3$ GeV are considered as seed towers. Once a seed tower is found, all adjacent towers in η with $E_T \geq 0.1$ GeV are incorporated in the cluster. The algorithm continues until no more adjacent towers are added to the cluster or the cluster reaches its maximum size. The maximum of the cluster size is restricted to 3×1 in $\eta\phi$, three towers in η ($\delta\eta$=0.1), and one tower in ϕ ($\delta\phi = 15^\circ$) for central electron candidates. For the plug and forward electromagnetic calorimeters where the tower size is smaller, the maximum electromagnetic cluster size is restricted to 5×5 for the plug and 7×7 towers in $\eta\phi$ for the forward. An electromagnetic cluster is accepted if the total transverse electromagnetic energy is $E_T \geq 5$ GeV and the ratio of the energy in the hadronic component of the towers contributing to the cluster to the electromagnetic energy is less than 0.125 ($E_{had}/E_{em} \leq 0.125$). According to the jet reconstruction, an electron is reconstructed also as a jet. In the selection of the $Z(\rightarrow e^+e^-) + jets$ data sample on which the normalization of the W/Z+jets QCD predictions is based, the electrons are not counted as jets.

3.1.7 Muon reconstruction

A fit of hits observed in one of the muon detectors defines the reconstruction of a muon track segment, *stub*. The stubs are categorized according to the detector they are reconstructed at. CTC tracks are extrapolated to the muon chambers and matched to muons stubs in $r - \phi$. A muon candidate is defined when the muon stub is linked to the nearest CTC track.

3.1.8 *Bad Run* Removal

Runs associated with known detector or readout problems are removed, to ensure good quality of the datasets. This requirement removes 4% of the events in the $\not\!\!E_T$ sample[1].

3.2 Data Samples

3.2.1 The Missing Energy Sample

The Missing Energy Sample (MET sample) is the online missing energy trigger which requires $\not\!\!E_T$ $\geq$30 GeV (`EVCL_COMBINED_EXOB`) and does not require the event to have passed the L2 missing energy triggers. 45% of the data are volunteers from the jet triggers. The sample is comprised of 2517998 triggers. The total integrated luminosity of the sample is calculated using the corrected for accidentals luminosity for each data file used in the analysis and is found to be 88.6 pb^{-1} (Figure 3.2). The average cross section is $\sim$ 30 nb. After the removal of runs flagged as problematic (bad run removal) during data acquisition, the total integrated luminosity is 84.37$\pm$3.5 pb^{-1}. All the

[1]Runs flagged in the database as 15 or -1 are kept.

data and Monte Carlo samples used in this analysis are normalized to the missing energy sample luminosity. The Pre-Selection of the missing energy data sample is described in detail in Chapter 4.

3.2.2 The Inclusive Jet Data Samples

The inclusive jet samples are collected based on Level 2 triggers as discussed in Chapter 2.5. The relevant information from the trigger Table is given in Appendix B. These triggers require a cluster in the calorimeter with transverse energy above a predefined E_T threshold, termed as *trigger threshold*. Triggers with E_T thresholds set at 20, 50, 70 and 100 GeV are employed. Due to high cross sections, the first three of the above triggers are prescaled. The nominal trigger prescale factors are 1 for JET100 (un-prescaled), 1000 for JET20, 40 for JET50, and 8 for JET70. The main purpose of these triggers is to serve as control samples and samples to measure other triggers' efficiencies. Their luminosity (not necessary for non-absolute measurements) is not always accurately registered in the databases. Offline, the data samples of each jet trigger threshold are reconstructed by requiring the events to satisfy the corresponding Level 2 jet trigger. In order to reduce the noise rate, the presence of at least one SVX track is required and the samples are re-clustered using the highest $\sum |\vec{P}_T|$ vertex. Besides the above samples which are based on specific jet E_T thresholds, one additional jet trigger sample is used which requires the scalar total transverse energy, $\sum E_T$, of the event be greater than 175 GeV. This sample is referred to as SUMET175.

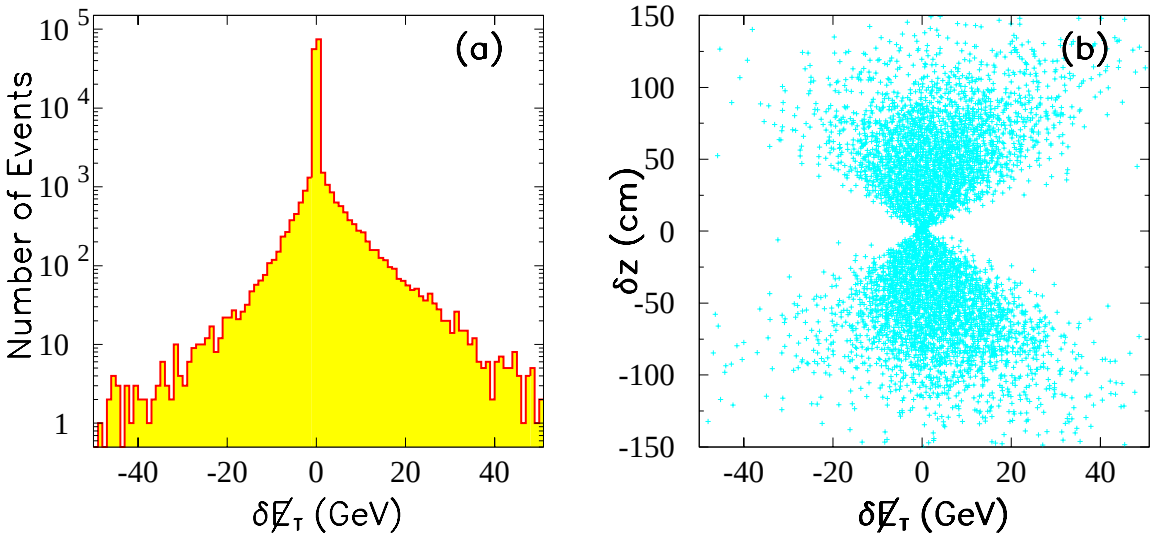

Figure 3.1: a) $\delta \not\!\!E_T$= $\not\!\!E_T$(VTVZ1)-$\not\!\!E_T$(max$\sum |\vec{P}_T|$), b) δz versus $\delta \not\!\!E_T$ for the Run 1B JET50 data.

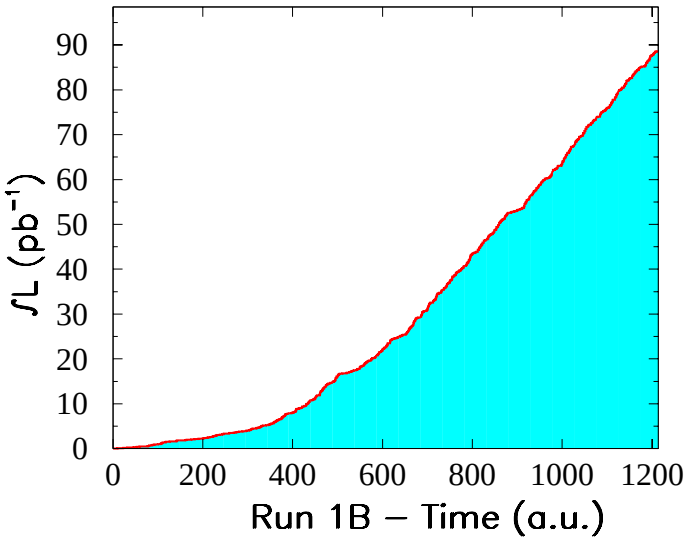

Figure 3.2: Integrated luminosity versus runtime (0 is the beginning of Run 1B) of the MET data sample.

3.2.3 JET20-JET50 Luminosity measurement

In this analysis, the JET50 and JET20 data samples are used to absolutely normalize the Monte Carlo QCD predictions. An accurate measurement of the luminosity of these datasets is necessary. The un-prescaled JET100 data sample luminosity is 86.42 pb^{-1}. This sample is used to determine the luminosity of the JET50 and JET20 data used.

JET20, JET50, JET70 independent comparison

and luminosity measurement

In Figure 3.3 the E_T of the leading jet is given for the JET20 , JET50, JET70 and JET100 samples. To form the ratio of the samples the following requirements are imposed on the leading jet: a) the jet η_d be within 1 unit of pseudorapidity, b) the jet electromagnetic fraction (EMF) to be greater than 10%, and c) at least two tracks should be present within the jet. In addition the event is required not be a bad run and to have at least one vertex within 60 cm. In Figure 3.4(1),(2),(3) the ratios of the E_T spectrum of the leading jet of the JET100 over the JET70 data sample, the JET100 over the JET50 sample and the JET50 over the JET20 sample are shown respectively. The luminosity scale factor for the prescaled samples is then given by the plateau value of the ratio of these distributions. The JET20 scale factor is derived by multiplying the JET50/JET20 with the JET100/JET50 scale factors. The results are shown in Table 3.3. The plateau is reached when the trigger in the numerator of the ratio becomes close to 100% efficient.

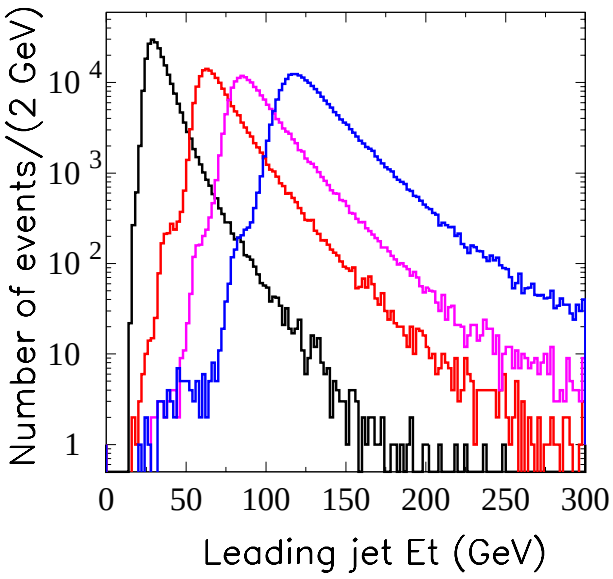

Figure 3.3: E_T of the leading jet for JET20, JET50, JET70 and JET100 data samples.

Sample	JET100	JET70	JET50	JET20
$\int \mathcal{L}$ pb^{-1}	86.42±3.46	10.8±0.8	2.35±0.12	0.0935±0.0055
Scale factor	1	8.02±0.5	36.77±1.2	926±40

Table 3.3: Independent JET100/70/50/20 sample luminosity and luminosity scale factors compared to the unprescaled JET100 sample.

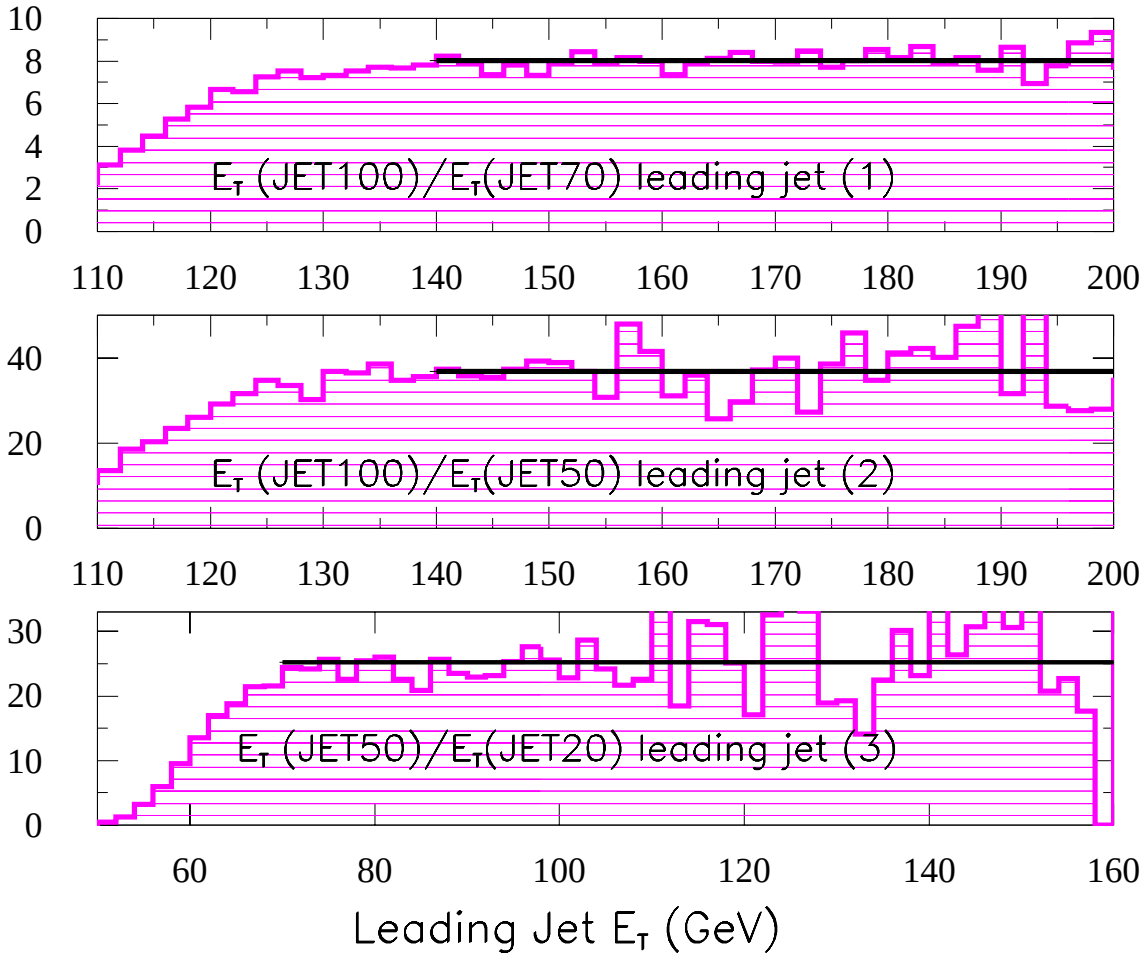

Figure 3.4: Ratio and one-parameter fit of E_T spectrum of the leading jet (1) JET100 over JET70 sample (2) JET100 over JET50 sample (3) JET50 over JET20 sample.

MET relative content in	JET100	JET70	JET50
Prescale factor	1.12±0.2	8.17±0.6	37.95±1.2

Table 3.4: JET100/70/50 prescale factors measured in the MET sample.

SUMET175 relative content in	JET100	JET70	JET50
Prescale factor	1.03±0.2	8.01±0.57	41±1.3

Table 3.5: JET100/70/50 prescale factors measured in the SUMET175 sample.

Internal measurement of the trigger prescale factors of the JET50, JET70, JET100 triggers using the MET and SUMET175 samples

It is expected the content of JET100 triggered, JET50 triggered, JET70 triggered events in the unprescaled MET and SUMET175 samples to follow the corresponding trigger Table prescale factors. This is confirmed by taking the ratio of the E_T spectrum of the leading jet in the MET sample with the E_T spectrum of the events that pass the JET100, JET70, JET50 triggers correspondingly. The results are shown in Figure 3.5 using the MET sample and Figure 3.6 using the SUMET175 . The internally measured prescale factors are shown in Table 3.4 using the MET sample and in Table 3.5 using the SUMET175 sample. To normalize the QCD predictions (Chapter 6 to the total missing energy sample luminosity the scale factors on Table 3.3 need to be multiplied by 0.97 (84.37(MET)/86.42(JET100)).

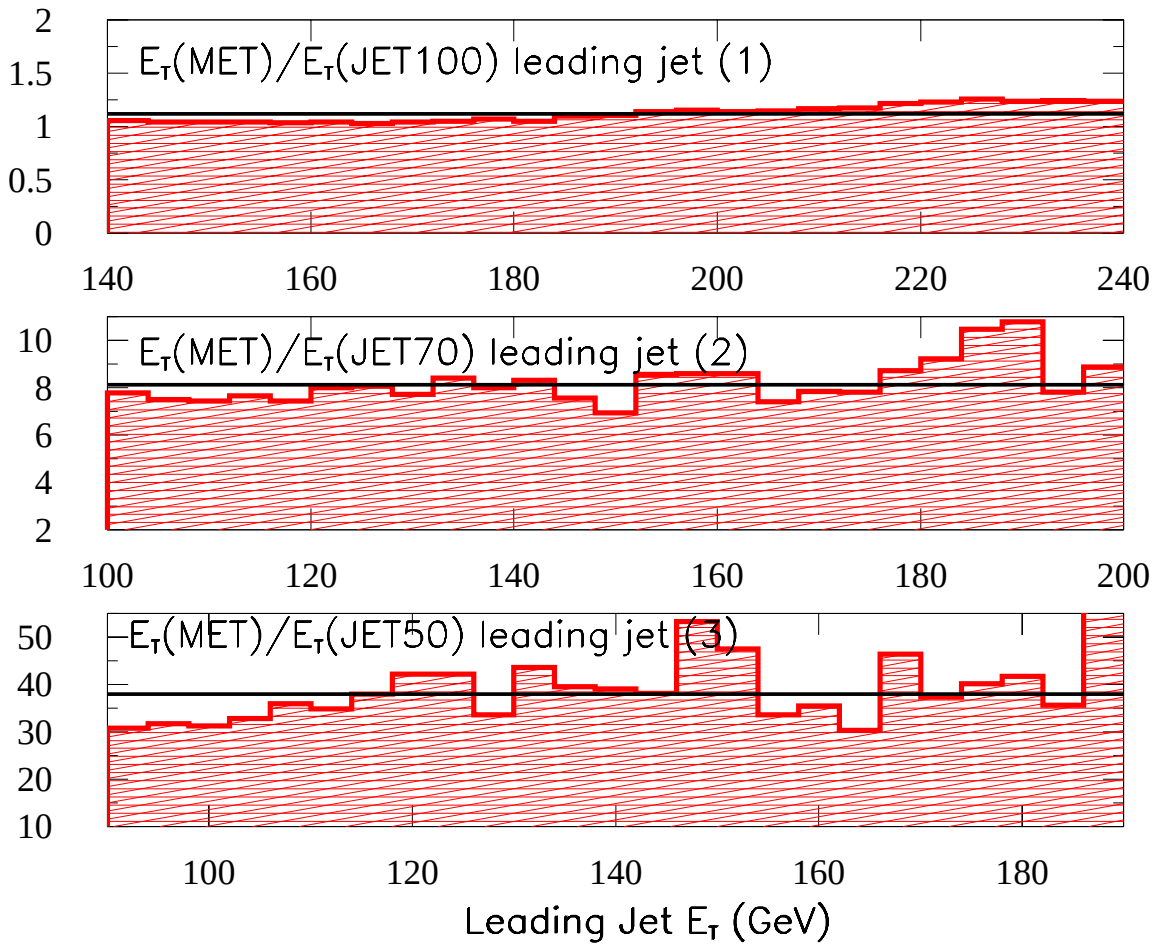

Figure 3.5: Ratio and one-parameter fit of the E_T spectrum of the leading jet in the MET sample over the E_T spectrum of those events that pass the (1) JET100 trigger (2) JET70 trigger and (3) JET50 trigger.

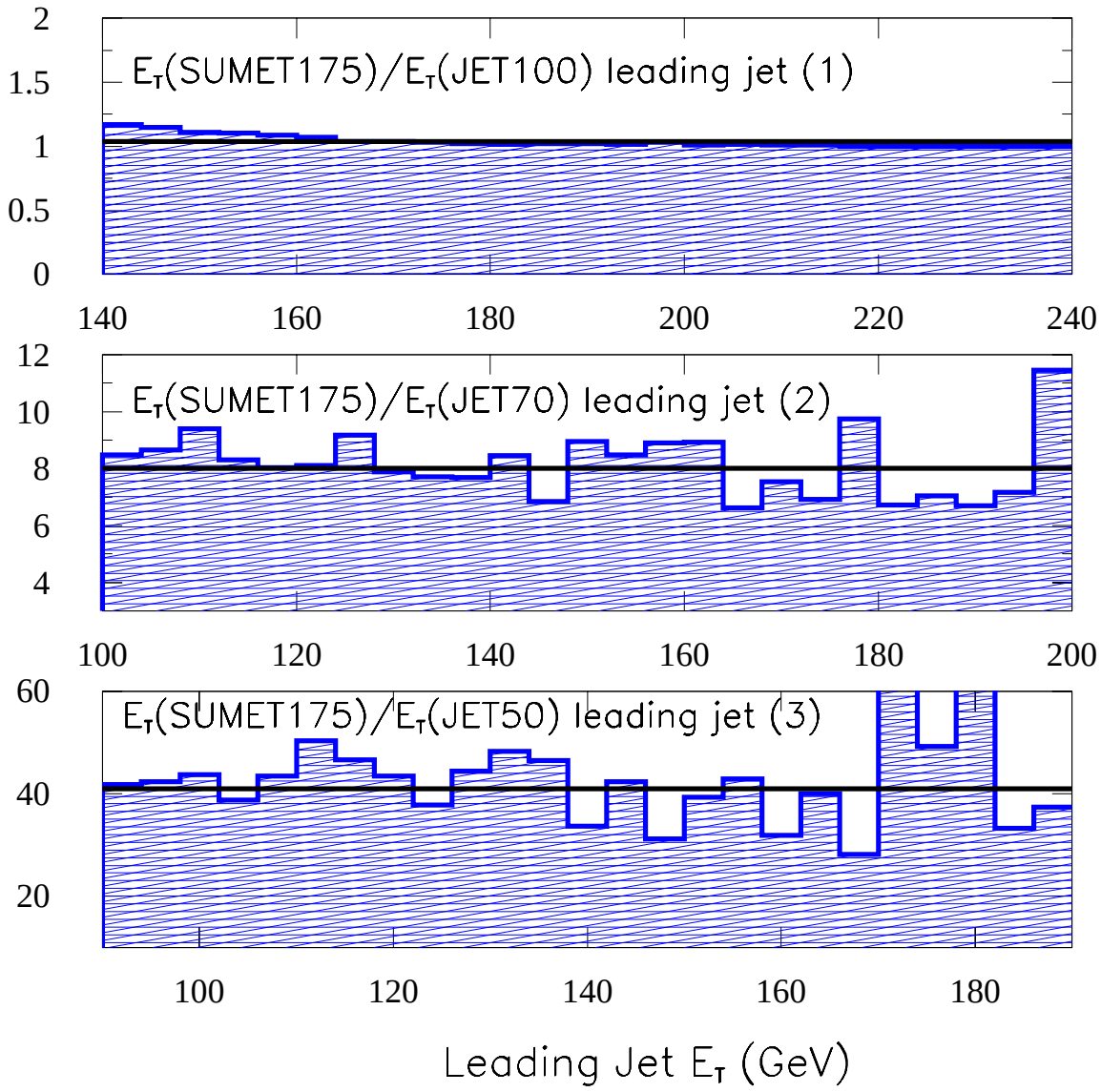

Figure 3.6: Ratio of E_T spectrum of the leading jet in the SUMET175 sample over the E_T spectrum of those events that pass the (1) JET100 trigger (2) JET70 trigger and (3) JET50 trigger.

3.2.4 The high P_T electron + jets sample

This sample is used to normalize the W/Z+jet Monte Carlo predictions. The identification of central electrons begins at the Level 1 trigger stage, requiring a CEM tower with $E_T \geq$8 GeV. At Level 2, the electromagnetic clustering is performed requiring a CEM cluster of $E_T \geq 16$ GeV. This requirement is ANDed at trigger level with the requirement of a CFT track with $P_T \geq 12\text{GeV}/c$ associated with the electromagnetic cluster. This is one of the two level 2 triggers used to accept events with high-P_T electrons. Because the CFT requirement is only $\sim 92\%$ efficient, a second trigger with the requirement $\not\!\!E_T \geq 20$ GeV in place of the CFT requirement is also used in this analysis. The last trigger is designed mainly to accept W events. The logical OR of the two triggers is found to be close to 100% efficient for W events and is used in this analysis to accept the W and Z electron events [23].

Table 3.6 summarizes the electron identification criteria used to select the high purity electron + jets sample. A brief description of the electron variables follows:

1. **Electron cluster $\mathbf{E_T} \geq$ 20 GeV.**

2. **Electron in good fiducial volume.** The central electron fiducial volume is defined by the CES strip chambers and the exclusion of uninstrumented regions. Overall the fiducial volume covers the pseudorapidity region of $|\eta| \leq 1.05$. The extrapolated track position in the CES plane is required to lie within 21 cm of the wedge center in the $r-\phi$ view, *i.e.* the electron track is required not point in a ϕ gap between wedges. The region $|\eta| < 0.05$ (90° gap) is excluded. The chimney region is also non-fiducial.

3. **E/P $<$ 1.8**. The ratio of the energy (E) measured by the calorimeter to the momentum (P) of the track as measured by the CTC is required to be close to

Transverse Energy $E_T \geq 20$ GeV
Good fiducial region
$E_{had}/E_{em} \leq 0.05$
$E/P \leq 1.8$
Lateral sharing (Lshr) ≤ 0.2
$\chi^2_{strip} \leq 10$
Track - Shower matching:
$\|\Delta(x)\| \leq 1.5$ cm, $\|\Delta(z)\| \leq 3$ cm
$\|\Delta(Z^{ele}_{vtx} - Z^{trk}_0)\| \leq 5$ cm
$\|Z^{ele}_{vtx}\| \leq 60$ cm
$Iso \leq 0.1$
Jet requirement:
0.7 hadronic jet, $E_T \geq$15 GeV, $\|\eta\| \leq 2.1$

Table 3.6: Selection criteria used in the definition of the electron + jets sample.

1. Due to *bremßtrahlung* radiation the momentum of the electron is measured lower than the energy in the electromagnetic cluster which usually contains the radiated photons.

4. $\mathbf{E_{Had}/E_{Em}} < \mathbf{0.05}$. The hadronic energy is required to be less than 5% of the electromagnetic energy associated with the electron cluster.

5. **Lateral sharing (Lshr)** $< \mathbf{0.2}$. This quantity is derived from test beam and has the functional form:

$$Lshr = 0.14 \sum_i \frac{E_i^{adj} - E_i^{prob}}{\sqrt{(0.14\sqrt{E})^2 + (\Delta E_i^{prob})^2}},$$

where E_i^{adj} is the energy (in GeV) measured in a tower adjacent to the seed tower of the electron cluster, E_i^{prob} is the energy (in GeV) expected in this tower based on strip chamber information, $0.14\sqrt{E}$ is the error on the energy estimate from calorimeter resolution and ΔE_i^{prob} is the uncertainty on the expected energy associated with a 1 cm uncertainty in the strip chamber position measurement. The LSHR allows a comparison of the lateral sharing of energy in the towers of the electron cluster to the predicted sharing based on the z position and angle of the electron shower as measured by the CES detector and a parameterization based on test beam electron data.

6. $\chi^2_{\mathbf{strip}} < \mathbf{10.}$ This quantity is derived by performing a chi-square fit of the lateral shape of the measured electron shower to the shower shape measured for electrons from a test beam.

7. **Track-shower matching variables:**

   $|\mathbf{\Delta(x)}|$ **(r-ϕ view)** < 1.5 **cm** and $|\mathbf{\Delta(z)}|$ **(r-z view)** $<$ **3.0 cm.**

   These quantities are derived comparing the shower position of the largest pulse height cluster as measured in the CES to the extrapolated position in the CES plane, of the CTC track associated with the electron cluster. A large number of fake electrons which result from overlaps of charged and neutral hadrons is removed by requiring a tight match between the track and shower position.

8. $|\delta(\mathbf{Z^{vertex}_{ele} - Z_{track}})| <$ **5.0 cm.** The electron track is required to lie within 5 cm of the event vertex.

9. $|\mathbf{Z^{ele}_{vtx}}| <$ **60 cm.** The electron vertex is required to lie within 2σ of the nominal interaction vertex (z=0). The longitudinal spread of the event vertex about the nominal interaction point is a Gaussian with a sigma of $\sigma = 26$ cm.

10. Electrons from W and Z decays are expected to be isolated from other hadronic activity in the event. The isolation is defined based on the energy surrounding the electron cluster in a cone of radius $\Delta R = 0.4$ in $\eta\phi$ space compared to the energy of the electromagnetic cluster:

$$Isolation = Iso^{ele} = \frac{E_T^{cone} - E_T^{ele}}{E_T^{ele}}, \tag{3.4}$$

where E_T^{cone} is the total energy (hadronic+electromagnetic) in a cone of radius $R = 0.4$ in $\eta\phi$ space centered about the electron direction.

Since electrons leave clusters of energy in the calorimeter, they are also reconstructed as jets according to the jet clustering algorithm. To avoid double counting of electron and jet clusters any jet matched in $\eta\phi$ with an electron cluster is not counted as a jet in the normalization program that involves $Z \to ee$+jets data.

Conversion removal

Photons produced either directly in the hard scattering or from π^0 decays can interact with the material in the detector and convert to an electron-positron pair. A conversion removal algorithm was developed to remove this type of electrons. The algorithm [24] is based on the search of an opposite sign track near the electron candidate. Two tracks are considered originating from a photon conversion if their $r - \phi$ separation at the point of conversion (the point at which the two helices are parallel in ϕ) and the difference in their polar angle, $\delta\cot(\theta)$, are close to zero. The quantity δ_{sep} is a signed quantity and it is positive if the two helices do not overlap and negative if they overlap. The quantity is symmetric around zero for real conversion pairs. For fake conversions, negative separation is the most likely configuration because fakes

$\lvert\delta(r-\phi)_{sep}\rvert \ < \ 0.3$
$\lvert\delta\cot(\theta)\rvert \ < 0.06$
$-20.0 \ < \ R_{conv} \ < \ 50.0$ cm
OR
$VTX_{occupancy} \ < \ 0.2$

Table 3.7: Criteria used to identify electrons from photon conversions.

consist of two prompt tracks arising from the interaction region. The conversion radius, defined as the distance from $x = y = 0$ to the conversion point, is required to be in the range $-20 < R_{conv} < 50$ cm. In many cases the track partner is too soft to be reconstructed and the algorithm fails. In such a case the number of VTX hits associated with the electron candidate is compared to the expected number. If the number of found hits is fewer than 20% of the expected one, the electron candidate is removed as originating from a photon conversion. Table* 3.7 summarizes the criteria used to identify and remove electrons from photon conversions. conversion electrons comprise $\sim 40\%$ of the inclusive high-P_T electron sample. The efficiency of the conversion algorithm is found to be $90.7 \pm 3.8\%$ [24].

3.2.5 Minimum Bias Data Sample

The minimum bias sample used consists of about 1383000 events taken at all instantaneous luminosity conditions across RUN 1B. The sample is used to study the underlying event (Chapter 6).

3.2.6 Monte Carlo Data Samples

The QCD associated production of W and Z bosons is generated using the VECBOS+HERPRT [25] programs. Throughout this analysis when referring to W/Z+jets Monte Carlo generation it is the VECBOS+HERPRT or equivalently the *Enhanced Leading Order* Monte Carlo implied. The QCD multijet production is generated using the 2-to-2 process of HERWIG [26] program. A brief description of these Monte Carlo event generators is given in Appendix F. The Monte Carlo PYTHIA [27] is used to generate top, di-boson and single top production. The output of the generators includes the four-vectors of all the particles which participate in the parton shower and also the appropriate indices showing the tree decay history of each particle. The information is kept in a specific data bank called *GENP*. The CDF detector simulation, QFL′ [28], uses the GENP bank and parameterization of the detector response based on testbeam measurements or tuned to the data, to create the fully simulated data banks for each event. This allows the processing and selection of simulated events to be performed in exactly the same way as in the data. For the supersymmetric signal, ISAJET (version 7.37) [29] is used. Unless otherwise stated, Monte Carlo implies the generator plus the QFL′ detector simulation.

Tracking degradation modeling

In the course of the running period the CTC performance was degraded due to aging effect. The degradation is modeled using a parameterization of the Data/QFL tracking efficiency as a function of a quality factor Q (based on the CTC hit quality and corrected for the luminosity effects) [30], [31]. The degradation algorithm discards tracks according to the expected inefficiency. After the CTC track degradation is applied, on average 90% of the Monte Carlo tracks are kept and 10% are discarded.

CTC tracking degradation is applied in all the Monte Carlo data samples of this analysis.

Chapter 4

Data Pre-Selection

This chapter describes the selection criteria towards the composition of the primary MET data sample. The purpose of the Pre-Selection is to discard fake $\not\!\!E_T$ events from obvious sources. Main Ring splash, Texas Tower, gas spikes, data acquisition noise and cosmic ray background are filtered out. For the Pre-Selection the `z(max`$\sum |\vec{P}_T|$`)` (Section 3.1.5) vertex is used and the events are re-reconstructed using this vertex.

4.1 Stage 1

4.1.1 Main Ring (MR)

The Main Ring (Appendix A.2) passes directly above CDF. Typical Main Ring transfer inefficiencies are recognized at CDF on LEGO plots (where the detector is unfolded into the $\eta\phi$ plane and the z axis indicates the tower E_T) as a blast of hadron calorimeter towers on the top and the sides of the detector (Central and End Wall regions) (Figure 4.1). In most of these events the TDC time stamp of the towers is inconsistent with the bunch crossing time. These events are out of the collision time

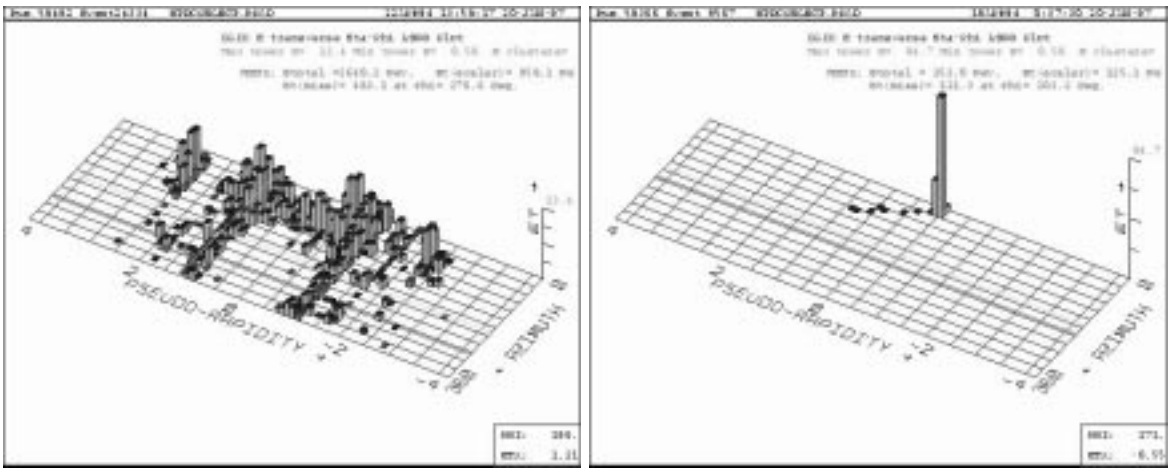

Figure 4.1: (a) Typical Main Ring and (b) Cosmic *bremßtrahlung* event at CDF.

window and are called *Out-of-Time events* [1].

4.1.2 Out-of-Time Energy Requirement

The JET50 sample (Chapter 3) is used to study the hadron TDC information and derive the requirements that rejects events whose timing is inconsistent with the beam crossing (*Xing*). The requirements for a Central Tower and an End Wall tower to be declared to be Out-of-Time are shown in Table 4.1. An event is generally flagged

[1] In the region of overlap between the CHA and the WHA the individual towers are treated separately ; dead TDCs are taken into account.

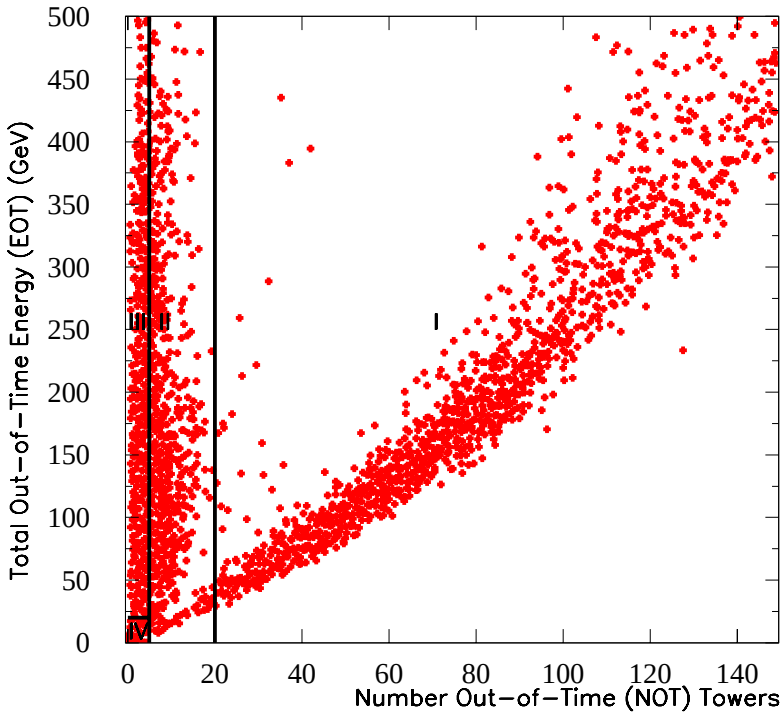

Figure 4.2: Out-of-Time Energy versus Number of Out-of-Time Towers in the JET50 data. The lines indicate the four studied sections as described in the text.

EHAD(CHA tower) $>$ 1 GeV
$\Delta t <$ -20 ns or $\Delta t >$ 35 ns
EHAD(WHA tower) $>$ 1 GeV
$\Delta t <$ -25 ns or $\Delta t >$ 55 ns

Table 4.1: Definition of CHA and WHA Out-of-Time towers

as Out-of-Time when the hadronic energy summed over all Out-of-Time towers, referred to as EOT, is greater than 8 GeV. Figure 4.2 is a plot of EOT versus the number of Out-of-Time towers (NOT) for the JET50 sample. Each event provides an entry. Two distinct regions are immediately recognized: the diagonal belt and the one along the EOT axis. The former is the Main Ring belt and the latter comprises of a mixture of MR, beam halo, cosmic and events with localized large Out-of-Time energy depositions. The high density $(EOT, NOT) = (0, 0)$ comprises of the clean in-time events. The EOT-NOT plane is quadrisected and the energy and timing of the towers in events in each of the regions is studied. The study is given at Appendix C.1.

Region I : EOT $>$ 10 GeV ; NOT $>$ 20 Identified as purely background region dominated by Main Ring splash events.

Region II: EOT $>$ 10 GeV ; 5 $<$NOT $\leq$ 20 Identified with background Main Ring events and events with large isolated energy deposition consistent with *bremß-trahlung* from cosmic ray muons.

Region III: EOT $>$ 10 GeV ; NOT $<$ 5 This Out-of-Time background region is comprised mostly from cosmic rays.

Region IV: EOT $\leq$ 10 GeV ; NOT $\leq$5 The tower topology as well as the tower hadronic and electromagnetic energy suggest that this region is the non-fake $\not\!\!E_T$ region. For the primary selection, it is determined that an EOT requirement of less than 10 GeV and an NOT requirement of less than 5 towers efficiently rejects the bulk of Main Ring and cosmic ray backgrounds. The study is repeated in the JET70 Run1B sample yielding consistent results.

4.2 Stage 1 Pre-Selection Sample

The set of requirements that are applied for the first stage of the pre-selection are shown in Table 4.2. In Table 4.3, the number of events failing each requirement is

$\not\!\!E_T \geq 35\ GeV$; $\not\!\!E_T$ using the max($\sum \vec{P}_T$) vertex
$EOT \leq 10$ GeV , $NOT \leq 5$

Table 4.2: Stage 1 Pre-Selection Requirements

shown, as well as the total number of events passing Stage 1 of the Pre-Selection.

Requirement	Number of events fail
$\not\!\!E_T$	1123734
$EOT \oplus NOT$	506241
Stage 1($\not\!\!E_T \oplus EOT \oplus NOT$)	1625603
Total passing Stage 1	892395

Table 4.3: Stage 1 Pre-Selection filtering statistics. The starting sample comprises of 2517998 events.

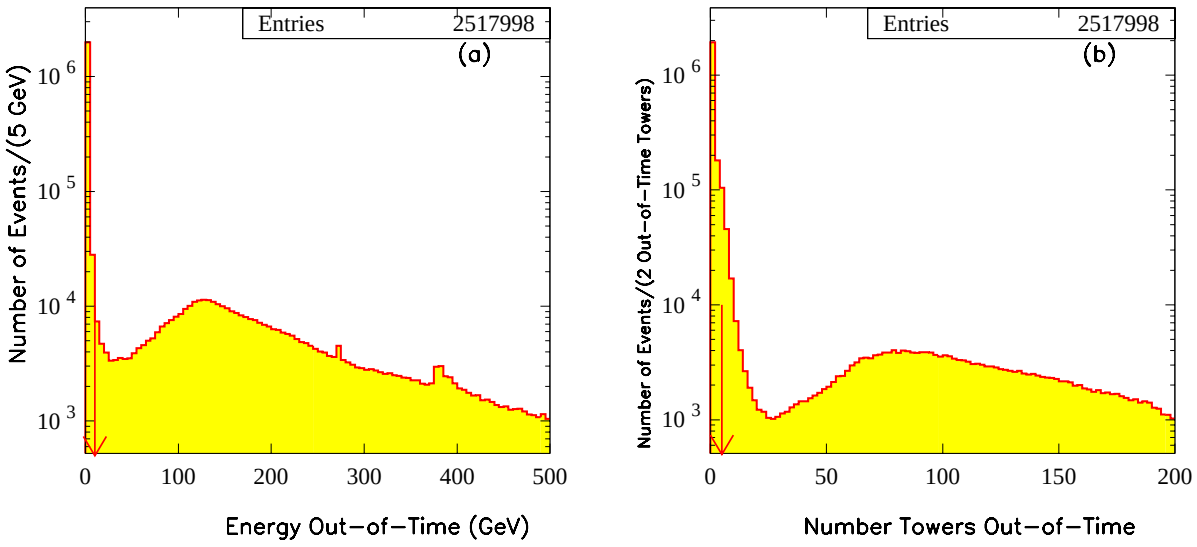

Figure 4.3: (a) Energy Out-of-Time and (b) Number of Out-Time towers for the MET sample.

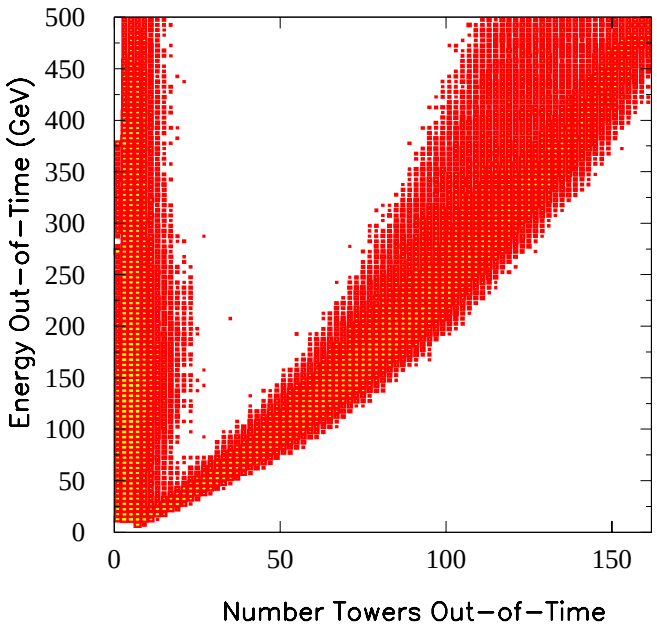

Figure 4.4: EOT-NOT plane for the MET sample events failing the Out-of-Time requirements.

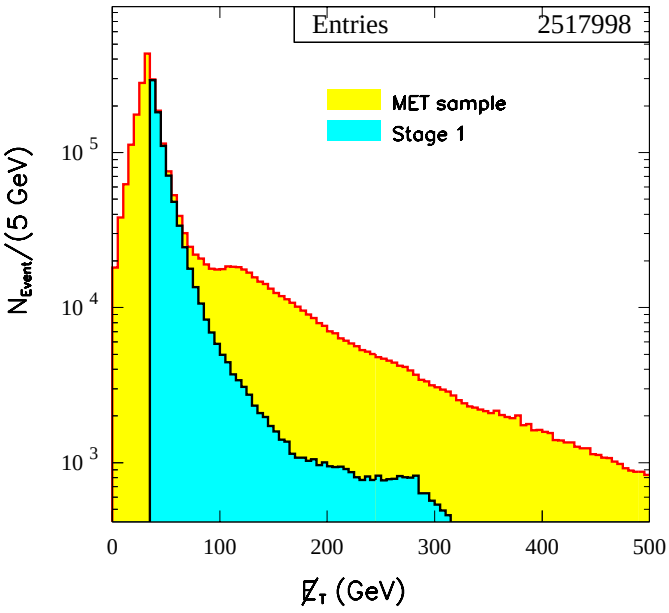

Figure 4.5: $\not\!\!E_T$ spectrum before and after Stage 1 of the Pre-Selection.

The EOT and NOT distributions are shown in Figure 4.2 for the input sample.The EOT-NOT plane for the events vetoed by Stage 1 is shown in Figure 4.2. The $\not\!\!E_T$ distributions of the Stage 1 input and output samples are shown in Figure 4.2.

4.3 Stage 2

Backgrounds that occur within the in-time window, e.g. overlap of a cosmic ray with a QCD event or Main Ring coarse overlap in time with a minimum bias event, can satisfy the requirements of Stage 1 of the Pre-Selection. To eliminate residual Main Ring and cosmic backgrounds this analysis uses jet variables, averages them over the event, defines the corresponding event variables and applies them to discriminate between real and fake jet events in the $\not\!\!E_T$ sample.

4.3.1 Event Electromagnetic Fraction

A jet is expected to have on average Electromagnetic/E_{TOT} ratio (EMF) between 0 and 1. Cosmic *bremßtrahlung* deposits energy in either the Hadronic or Electromagnetic Calorimeter, producing a jet with EMF close to 0 or to 1. Main Ring events (all-hadronic depositions) have EMF close to 0. The Event EMF (EEMF) is defined to be the E_T–weighted jet EMF sum over the whole detector:

$$EEMF = \frac{\sum_{j=1}^{N_{jet}} E_{Tj} \times EMF_j}{\sum_{j=1}^{N_{jet}} E_{Tj}} \tag{4.1}$$

where:

- N_{jet} is the number of jets of cone 0.7 with $E_T >$ 10 GeV
- E_{Tj} is the uncorrected E_T of the jth jet
- EMF_j is the EMF of the jth jet

4.3.2 Event Charge Fraction

Partons originating from a $p\overline{p}$ collision emerge from the event vertex as a spray of both charged and neutral particles which deposit energy in the calorimetry and are clustered into jets. The charged particle tracks associated with jets are reconstructed in the Central Tracking Chamber (CTC). Cosmic rays and other backgrounds do not originate from the center of the detector and may or may not pass through the CTC. Few, if any, tracks are found pointing at jets of energy associated with these backgrounds. The Event Charge Fraction is used to distinguish between real jets and

such fake jets. It is calculated by finding all the tracks pointing to each jet within a cone of 0.7 of the $\eta\phi$ centroid of the jet. Being that tracking is only available in the central calorimeter the requirement for a jet to enter into the event charge fraction variable is that its absolute pseudorapidity be less than 0.7. The Event Charge Fraction (ECHF) is defined as follows:[2]

$$ECHF = \left\langle \frac{(\sum_i^{tracks} P_{Ti})_j}{E_{Tj}} \right\rangle |^{N_{jet}} \tag{4.2}$$

- N_{jet} is the number of jets of cone 0.7 with $E_T >$ 10 GeV and $|\eta_d| < 0.7$
- E_{Tj} is the E_T of the jth jet
- $(\sum_i^{tracks} P_{Ti})_j$ is the sum of the P_T of all the tracks matched with the jet
- the average is taken over the number of central jets found

The advantage of the event variables EEMF, ECHF as defined, is that all contributions from spurious noise, not only the ones overlapping with a single jet, enter the event variable and the decision on the event. The distributions of the leading central jet charge fraction, the Event Charge Fraction, the leading jet Electromagnetic fraction and the Event Electromagnetic Fraction are given in Figure 4.6 for the JET50 data sample. The correlation of the Event Charge Fraction with the Event Electromagnetic Fraction and of each of these with the $\not\!\!E_T$ are shown in Figures 4.7 & 4.8. Stage 2 of the Pre-Selection does not intend to eliminate events containing a lepton; the events in the high tails of the EEMF and ECHF distributions will not be filtered - inevitably some fraction of background events remain in the sample. The Stage 2 Pre-Selection requirements are given in Table 4.4.

[2]Each of the 3-dimensional event tracks is matched with a central jet in $\eta\phi$. The tracks are required to be within 10 cm of the highest $\sum |\vec{P}_T|$ vertex of the event.

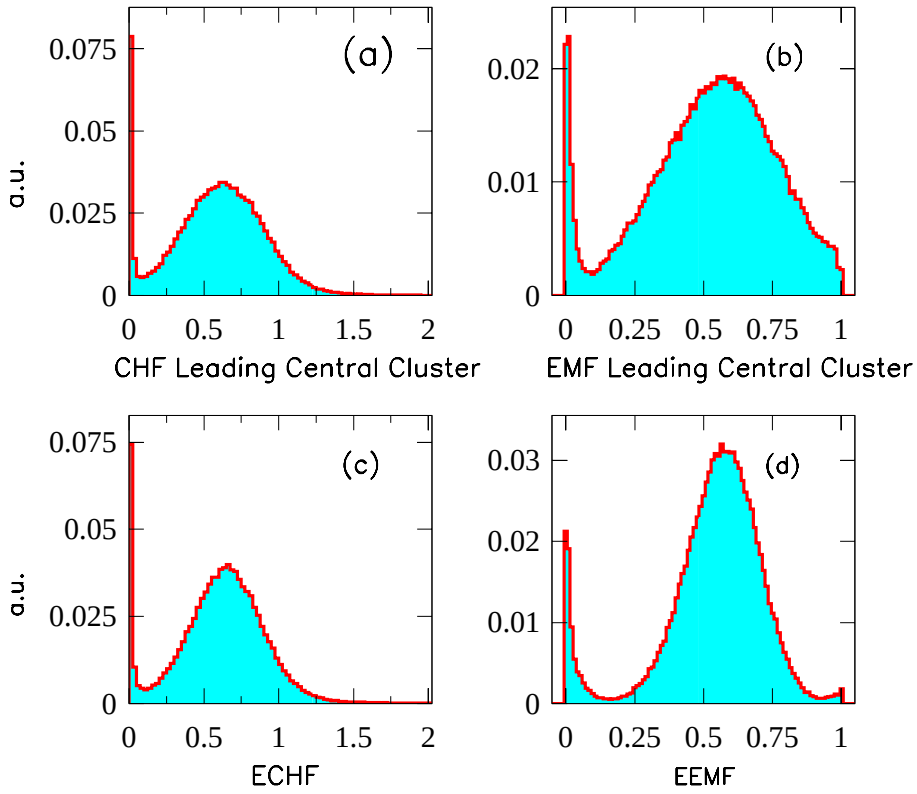

Figure 4.6: (a) Distribution of the charge fraction of the leading central jet. (b) Distribution of the Electromagnetic fraction of the leading jet. (c) Distribution of the ECHF. (d) Distribution EEMF in the JET50 sample.

Pre-Selection: Stage 2 Requirements
at least one jet with $\lvert\eta_d\rvert < 0.7$
ECHF ≥ 0.175
EEMF ≥ 0.1

Table 4.4: Stage 2 Requirements.

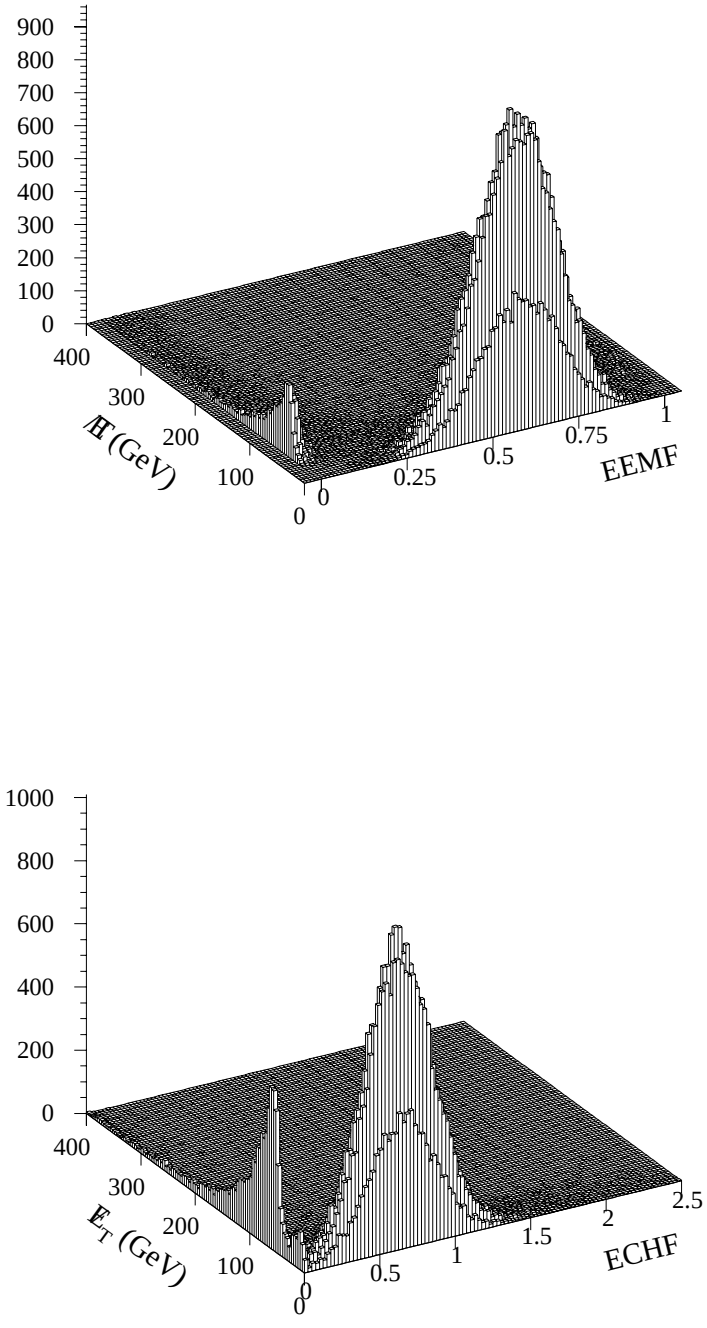

Figure 4.7: Correlation of Event Electromagnetic Fraction and Event Charge Fraction with $\not\!\!E_T$ in the JET50 sample.

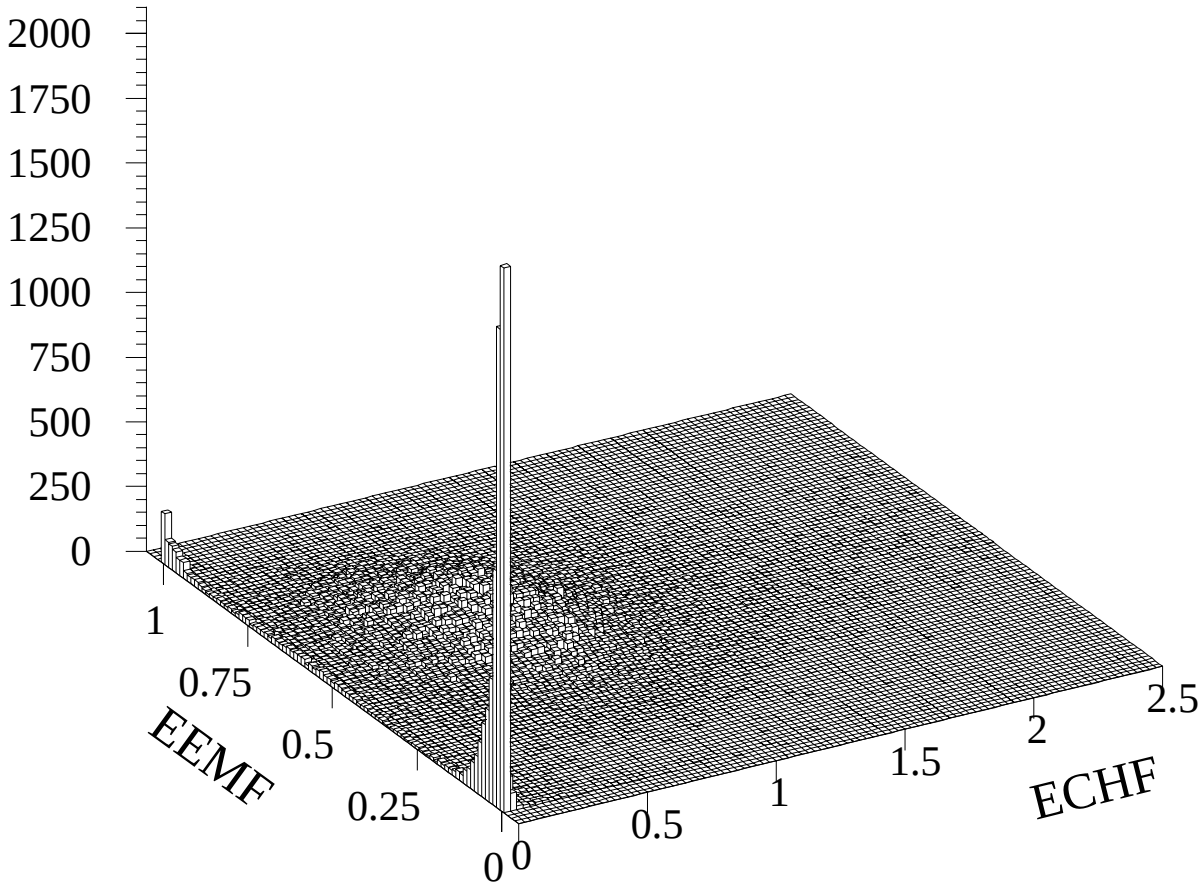

Figure 4.8: Correlation of Event Electromagnetic Fraction with Event Charge Fraction in the JET50 sample.

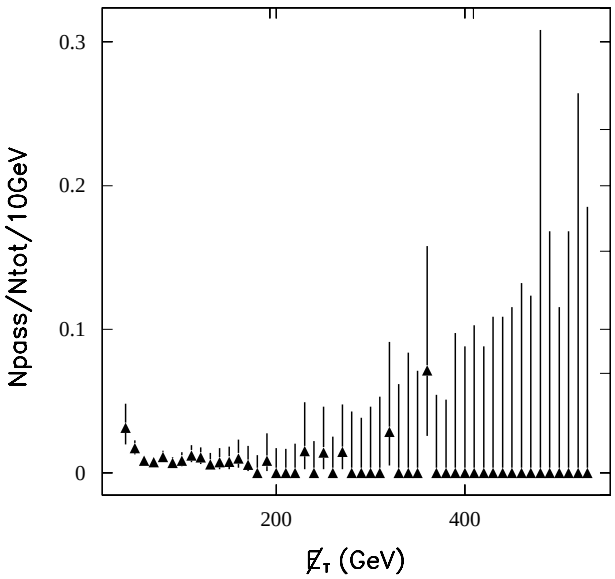

Figure 4.9: Stage 2 rejection efficiency in selected background subset of the JET50 sample.

To evaluate the rejection efficiency of the Stage 2 requirements, a subset of JET50 events with Out-of-Time energy greater than 10 GeV (this sample is purely background as discussed in Section 4.2) is used and the Stage 2 requirements are applied. Figure 4.9 displays the background rejection as a function of the $\not\!\!E_T$ in this subset: Stage 2 rejects about 99% of such background for $\not\!\!E_T$ greater than 40 GeV. Figure 4.10 shows the $\not\!\!E_T$ distribution in the JET50 sample before and after the Stage 2 requirements are applied. The EEMF, ECHF distributions of the Stage 1 output sample are given in Figure 4.11. Figure 4.12 shows the correlation between the ECHF and EEMF after the Stage 2 selection in the missing energy sample. The events at the neighborhood of EEMF= 1 and ECHF= 1 are identified to be W events by the distribution of the leading jet E_T (as discussed in Chapter 3 the clustering algorithm registers an electron cluster also as a jet cluster) in the sample before

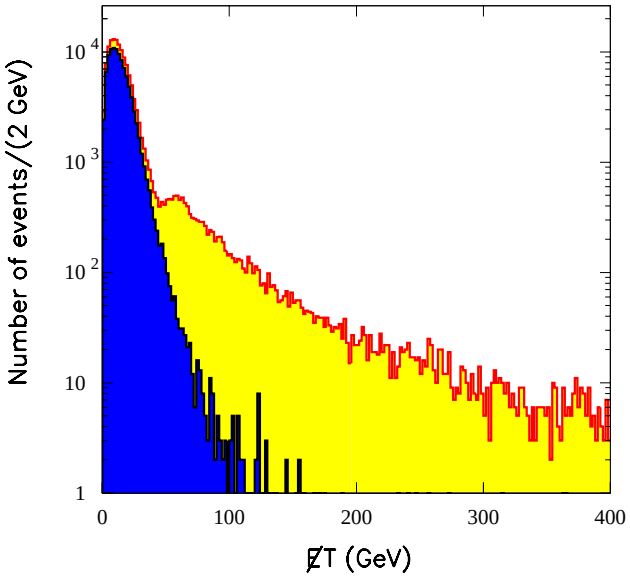

Figure 4.10: After ← before Pre-Selection Stage 2: the $\not\!\!E_T$ distribution in the JET50 sample.

and after the Stage 2 selection and the transverse mass of the leading jet with the $\not\!\!E_T$ (Figure 4.13). With no explicit lepton requirements and with efficient background reduction, the W events are identified in the $\not\!\!E_T$ sample.

4.4 Estimate of Residual Background

Figure 4.14 shows a scatter plot of the Out-of-Time energy versus the Event Charge Fraction in a subset of the MET sample before the Stage 1 requirements are applied. Events with large EOUT have small Event Charge Fraction. This plot is quadrisected and each region is studied.

- **Region 1 : EOT** > 10 **GeV ; ECHF** < 0.175

  This region is purely background. It contains the large Out-of-Time Energy

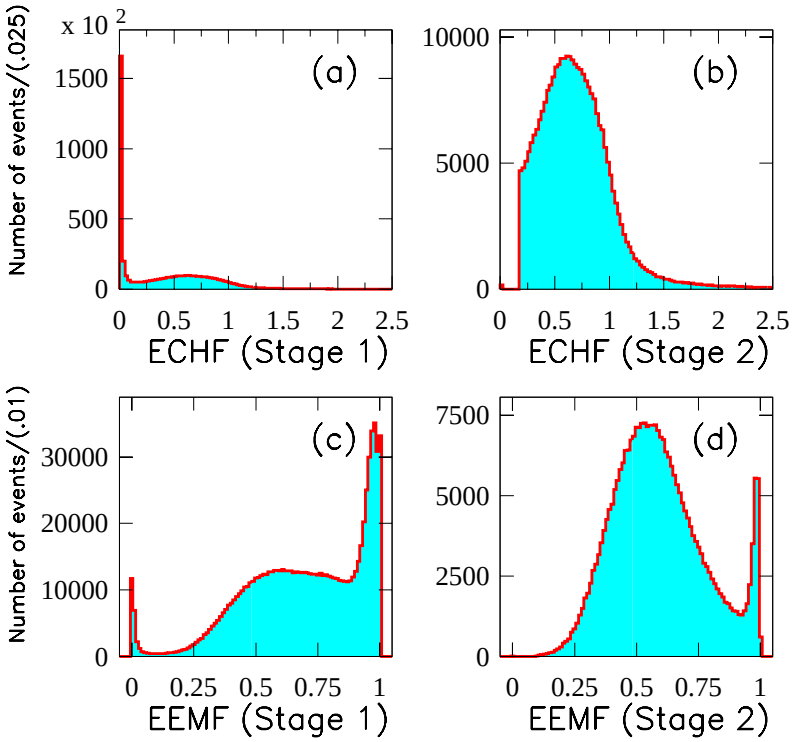

Figure 4.11: (a) Distribution of the Event Charge Fraction in Stage 1. (b) Distribution of the Event Electromagnetic Fraction in Stage 1. (c) Distribution of ECHF and (d) EEMF after Stage 2 selection in the Stage 1 sample.

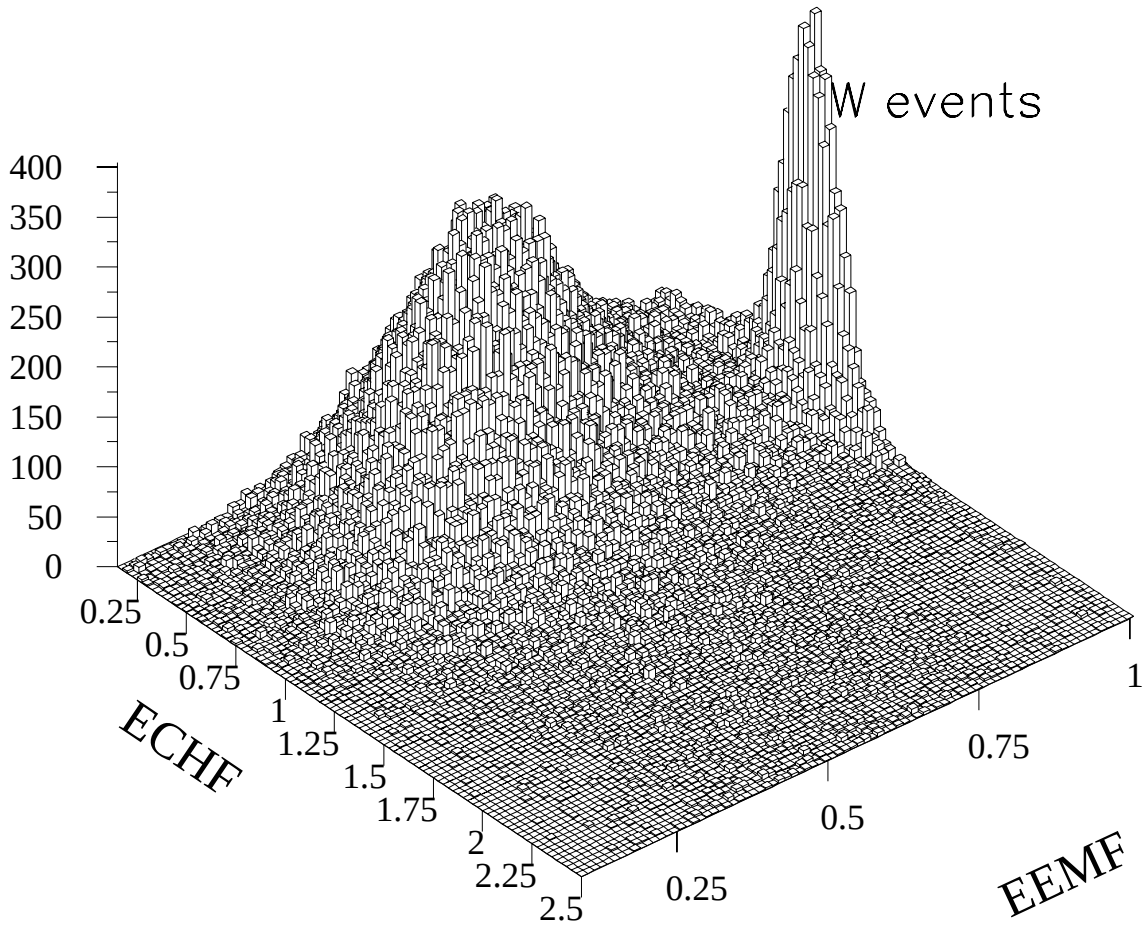

Figure 4.12: Correlation of ECHF with EEMF after Stage 2 is applied. The W events peak at around EEMF$= 1$, ECHF$= 1$.

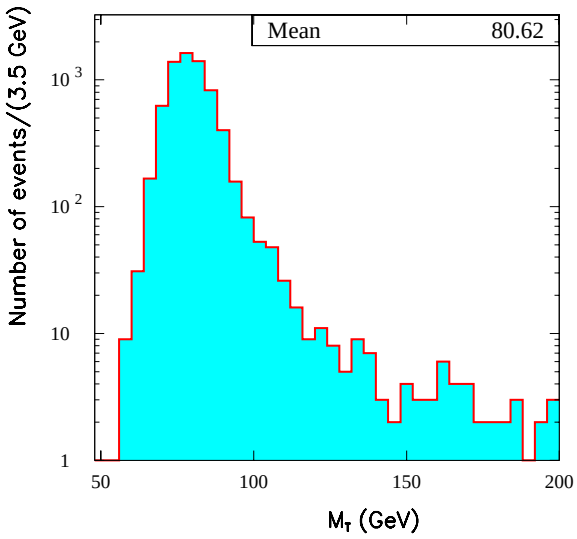

Figure 4.13: ($\not\!\!E_T$ –leading jet) transverse mass of the events falling in the W peak of Figure 4.12 after Stage 2 of the Pre-Selection.

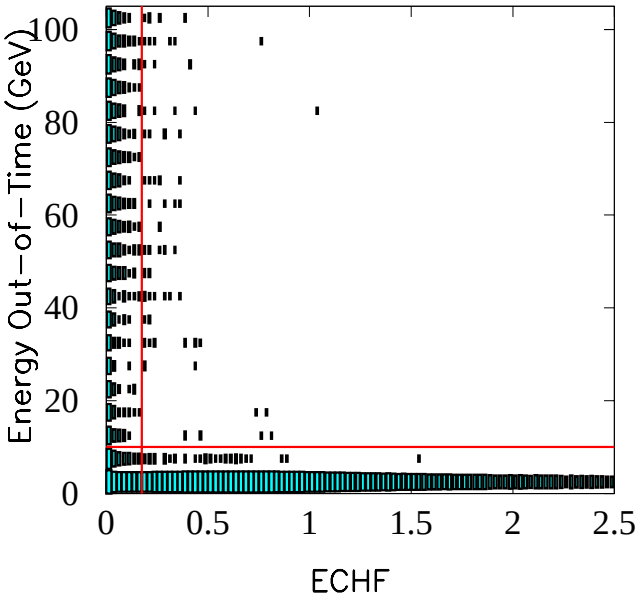

Figure 4.14: Correlation of EOUT with ECHF in the MET sample (none of the Pre-selection stages is applied). Events are required to have one central jet. The lines indicate the regions as described in the text.

events with low Event Charge Fraction.

- **Region 2 : EOT** ≤ 10 **GeV ; ECHF** < 0.175

  This region is background dominated with a small fraction of real $\not\!\!E_T$ events. It contains events with low Out-of-Time Energy and low Event Charge Fraction.

- **Region 3 : EOT** ≤ 10 **GeV ; ECHF** ≥ 0.175

  This is the real $\not\!\!E_T$ region. The residual background after the Stage 2 selection in this region needs to be estimated. Events have low Out-of-Time energy (selected by Stage 1) and high Event Charge Fraction (selected by Stage 2).

- **Region 4 : EOT** > 10 **GeV ; ECHF** ≥ 0.175

  This region is purely background. These are events with high Out-of-Time energy and acceptable Event Charge Fraction, which can arise from the overlap of an Out-of-Time cosmic event with a QCD one.

Figure 4.15 shows the ECHF in the four regions. The residual background is determined (Appendix C) to be

$$BGR_3 = (0.61 \pm .12)\% \tag{4.3}$$

less than 1% of the output sample.

4.5 Pre-Selection Output Sample

Table 4.5 shows the data reduction after Stage 2 and Figure 4.6 shows the $\not\!\!E_T$ spectrum in the stage by stage Pre-Selection reduction. *MET sample* refers to the starting online trigger sample.

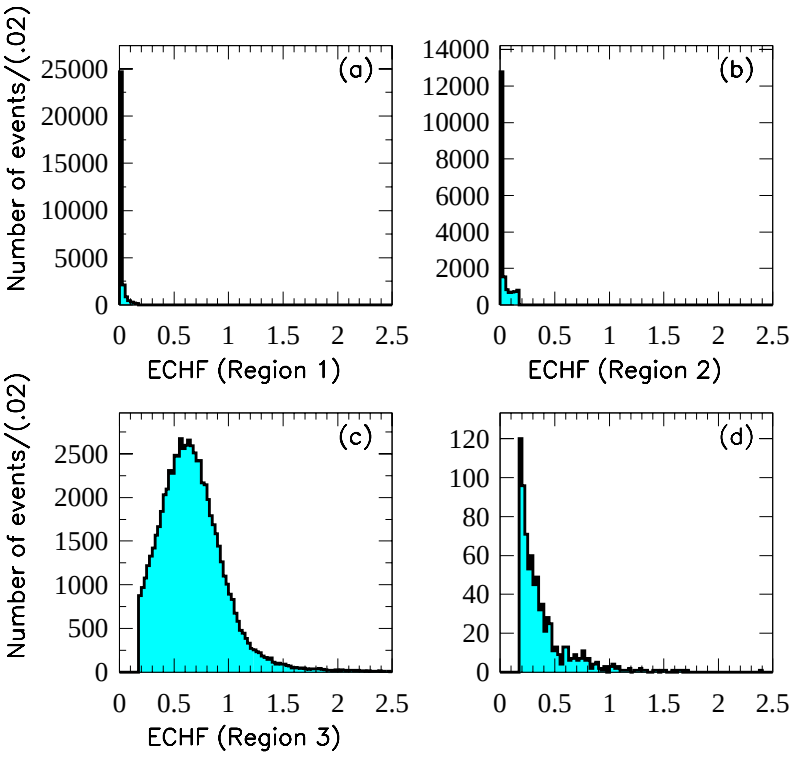

Figure 4.15: The ECHF distribution for the 4 regions defined in Figure 4.14.

Requirement	Number of Events Fail
1 central jet	372978
EEMF	24992
ECHF	591449
Total passing Stage 2	300945

Table 4.5: Statistics of the Stage 2 sample. The starting, is the Stage 1 output sample of 892394 events.

4.6 Overview

The missing energy data sample that passes the Pre-Selection is used to search for supersymmetry in the $\not\!\!E_T$+ multiple hadronic jets channel. In the next two chapters the outstanding Standard Model reactions that have the same final state (W and Z boson QCD associated production, QCD production and $t\bar{t}$ production) are analyzed and the theoretical predictions are normalized to the CDF data where possible. These are the *backgrounds* on the search for exotic physics in the $\not\!\!E_T$+multijet channel.

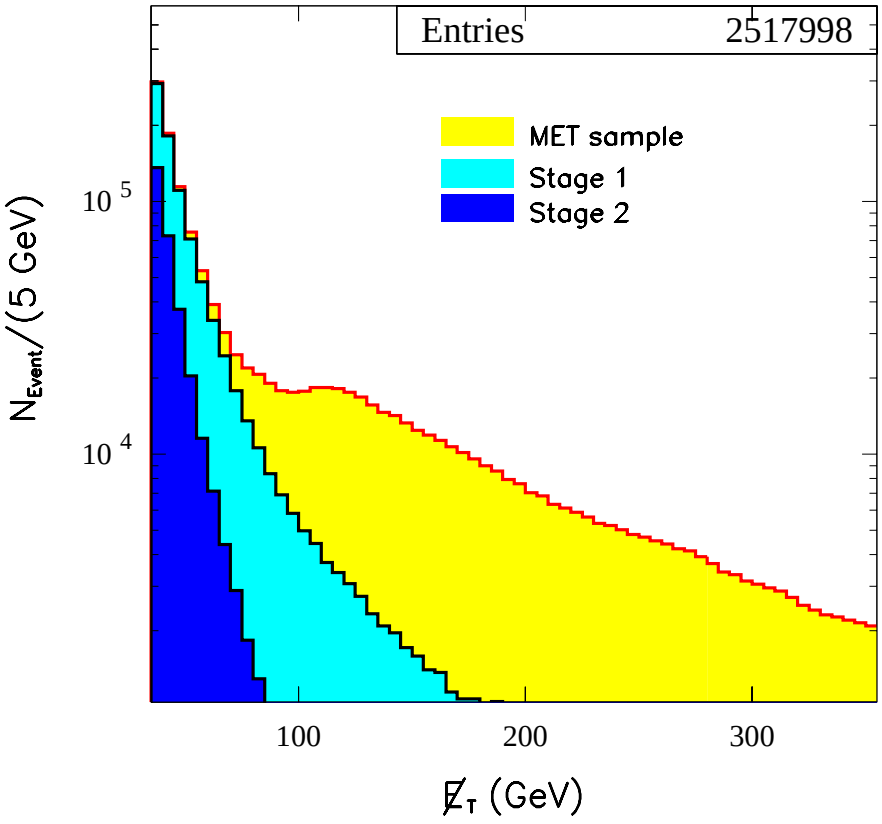

Figure 4.16: $\not\!\!E_T$ spectrum Stage 2 ⟵ Stage 1 ⟵ MET sample.

Chapter 5

Electroweak Background Components

5.1 Introduction

In $p\bar{p}$ collisions W and Z bosons can be produced in association with hadronic jets [33]. The jets are produced from the high energy partons when they hadronize after the collisions (Figure 5.1). The leading order perturbative QCD calculation for $W(Z)+ \geq N$ jets (where N is 2 and 3) is implemented in the VECBOS Monte Carlo enhanced with a coherent parton shower evolution of both initial- and final-state partons, hadronization and a soft underlying event model (VECBOS+HERPRT, Appendix F) and is normalized to the $Z(\rightarrow e^+e^-)+ \geq 2$ jets CDF data. The leading order matrix elements for the $W(Z)+N$ jet production have been computed for up to four(three) partons [34]. The jet rates, the kinematic distributions such as the boson P_T , the $\not\!\!E_T$, the jet E_T and other event topology variables are compared between the predictions and the data. The major contribution with large missing energy and

$\geq$ 3 jets in the final state is expected from a) $Z(\rightarrow \nu_i\bar{\nu}_i)+ \geq 3$ jets where i is a flavor index and b) $W(\rightarrow \tau\nu)+ \geq 2$ jets where the third jet is coming from the hadronic τ decay. A program is developed to normalize the $\geq$ 3-jets Enhanced Leading Order (ELO) calculation to the $\geq$ 3-jets bin from the $\geq$ 2-jets ELO prediction. This is directly normalized to the observed $Z(\rightarrow ee)+ \geq 2$ jets selected data sample that has negligible background and adequate statistics. To normalize the W ELO predictions the ratio $\frac{\sigma(p\bar{p}\rightarrow W\rightarrow e\nu)}{\sigma(p\bar{p}\rightarrow Z\rightarrow e^+e^-)}$ is used. Assuming lepton universality, the ELO $\geq$ 2– and $\geq$ 3–jets predictions for W and Z production and decays to all flavors are normalized to $Z(\longrightarrow e^+e^-)+ \geq 2$ jets. No absolute cross section measurement of W/Z+jets cross section is implied within the program. It is a normalization scheme of the ELO samples luminosity to the data luminosity using a well defined reference data sample. This is a technically demanding program that has the advantage of avoiding large systematic effects due to the renormalization scale, the choice of parton density functions, initial- and final-state radiation, and the jet energy scale. The systematic uncertainty is reduced to the uncertainty of the data luminosity measurement, the uncertainty on the ratio $N/(N+1)$ measurement in the data, where N is the number of jets and the uncertainty of the $\frac{W}{Z}$ ratio as a function of N in the ELO predictions.

The other electroweak background components with missing energy and multijets in the final state is the single and pair top, and diboson production and decays. To normalize the luminosity of the Monte Carlo samples used for these processes the theoretical cross section calculations are used.

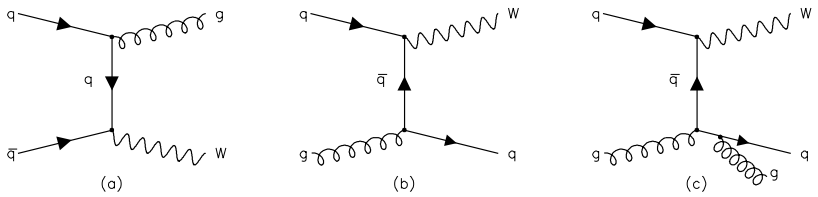

Figure 5.1: Sample of W+jet production graphs.(a) and (b) W+1jet with $q\bar{q}$ and qg initial state and (c) W+2 jets.

5.2 Z+ jets

5.2.1 The $Z(\rightarrow e^+e^-)$+ jets data and Monte Carlo

The $Z(\rightarrow ee)$+jets data sample is selected from the high P_T lepton trigger with the requirement of one 20 GeV central electron and one 15 GeV jet (not overlapping the electron). The sample is reprocessed according to the highest $\sum|\vec{P}_T|$ vertex. The Pre-Selection Stages 1 & 2 and the electron selection criteria described in Table 3.6 are applied. In addition the conversion removal algorithm described in Table 3.7 is applied. 16196 events are found before the jet requirement is applied. For the Z boson identification, a second electron is required, chosen by means of looser electron identification criteria, namely:

- electron $E_T \geq 10$ GeV
- $Iso \leq 0.2$
- $E_{had}/E_{em} \leq 0.12$

To detect the boson in the data, the invariant mass is formed

$$M_{ee} = \sqrt{(E^1_{tot} + E^2_{tot})^2 - (E^1_x + E^2_x)^2 - (E^1_y + E^2_y)^2 - (E^1_z + E^2_z)^2} \qquad (5.1)$$

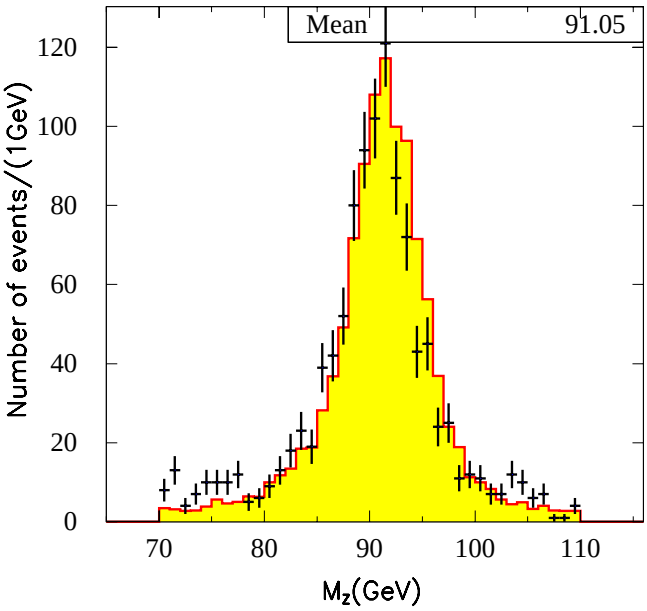

Figure 5.2: Z mass comparison $Z(\rightarrow ee)+ \geq$1 jet data and $Z(\rightarrow ee)+ \geq 1$ jet data and ELO ($\geq$ 1 jet) Monte Carlo sample. The Monte Carlo is normalized to the data.

of all pairs of electrons found in the event. The "Z pair" is considered to be that which has an invariant mass closest to the measured Z boson mass (90 GeV) and within 20 GeV. The energy of non-fiducial loose electrons in the CEM and PEM region, can be mismeasured when the electron lands close to a low response detector region. In this case, the momentum measurement is closer to to the true electron measurement [23] and the invariant mass is formed using the P_T of the second electron. The same requirements are imposed in the $Z(\longrightarrow e^+e^-)+$ jets ELO Monte Carlo simulation. 1082 are found in the mass window between 70 GeV and 110 GeV when at least one jet is required (Table 3.6). In Figure 5.3 , the inclusive and exclusive jet multiplicity for the $Z+$ jets data are shown. The $Z+N$ jets cross section is proportional to a_s^N : for each additional jet in the Z event the cross section falls by

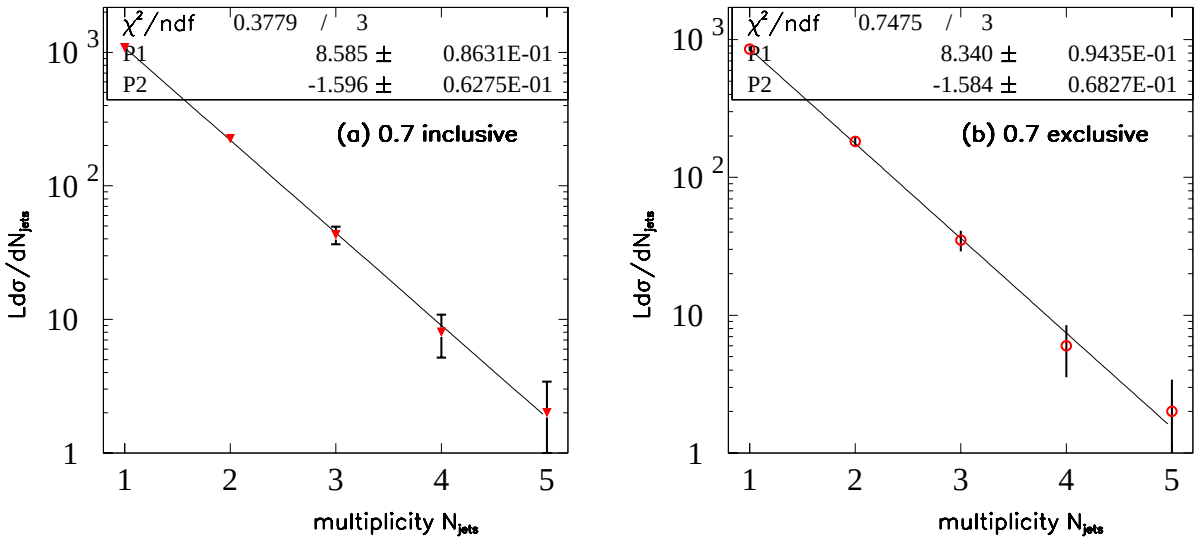

Figure 5.3: (a) Inclusive and (b) exclusive multiplicity breakdown in the $Z(\rightarrow ee)+ \geq$ 1 jet data.

a factor of a_s. The ratio (R) of the number of events in adjacent jet multiplicity bins should remain constant and be proportional to the strong coupling constant. The multiplicity breakdown in the data and the slope returned by the exponential fit is shown in Table 5.1. Given the slope for the fit the $R = \frac{dN_{events}}{dN_{jets}} = \frac{\mathcal{L}d\sigma}{dN_{jets}} = \frac{N}{N+1}$ is the above discussed ratio. A comparison of the multijet rates observed in the Z+jets

multiplicity	≥1j	≥2j	≥3j	≥4j	≥5j	$R = e^{-p2}$
N_{events}	1082	226	43	8	2	**4.93±0.31**
multiplicity	=1j	=2j	=3j	=4j	=5j	e^{-p2}
N_{events}	856	183	35	6	2	4.87±0.33

Table 5.1: Summary of the jet multiplicity breakdown (= exclusive, ≥ inclusive) in the $Z(\rightarrow e^+e^-)+ \geq 1$ jet data and extracted R. $p2$ is the value from the fits of Figure 5.3. The value from inclusive jet counting (bold) is used in this analysis.

data sample with the ones obtained from Enhanced LO Monte Carlo $Z+1,2$ and 3 jet is used to determine the renormalization and fragmentation scales in the simulation that reproduces the data. It is determined that a high renormalization/fragmentation scale ($Q^2_{renorm} = Q^2_{frag} = M_Z^2 + {P_T}_Z^2$, 0.7 cone) in the Monte Carlo reproduces the jet rates in the data [32].

The validation of kinematic variables as predicted by the Enhanced LO Monte Carlo is given in Appendix E. The $Z(\rightarrow \nu\bar{\nu})$+3 jets Monte Carlo rate is normalized to the $Z(\rightarrow e^+e^-)+ \geq 2$ jet data by means of R. The boson P_T constructed using the jet $\sum \vec{E}_T$ and the $\not\!\!E_T$ in the $Z(\rightarrow \nu\bar{\nu})+ \geq 3$ jets Monte Carlo sample, with the derived normalization is compared with the "$\nu\not\!\!E_T$", a quantity defined by vectorially adding the electron energies to the $\not\!\!E_T$ (in order to emulate the $Z(\rightarrow \nu\bar{\nu})+ \geq 3$ jets process using the electron data). The normalized $Z(\rightarrow \nu\bar{\nu})+ \geq 3$ jets Monte Carlo sample, without consideration of the lepton flavors and the branching ratio scaling, is directly compared with the electron data. Figure 5.4 shows these comparisons. The P_T of the Z boson constructed using the dielectron $\sum \vec{E}_T$ and the jet $\sum \vec{E}_T$ in the inclusive 3 jet bin in the normalized (via R) ELO $Z(\rightarrow e^+e^-)+ \geq 3$ jets Monte Carlo sample is compared with the data in Figure 5.5.) The $\not\!\!E_T$ and the $\nu\not\!\!E_T$ in the normalized (via R) $Z(\rightarrow e^+e^-)+ \geq 3$ jet ELO Monte Carlo is compared with the data in Figure 5.6.

5.3 $\frac{W}{Z}$ Ratio and Lepton Universality in the Normalization Program

The ratio $R^e_{WZ}=\frac{\sigma_W Br(W\rightarrow e\nu)}{\sigma_Z Br(Z\rightarrow ee)}$ is used to normalize the $W+ \geq N$ jets predictions (where N is 2 or 3) to the $Z(\rightarrow e^+e^-)+ \geq 2$ jet data. The lepton universality

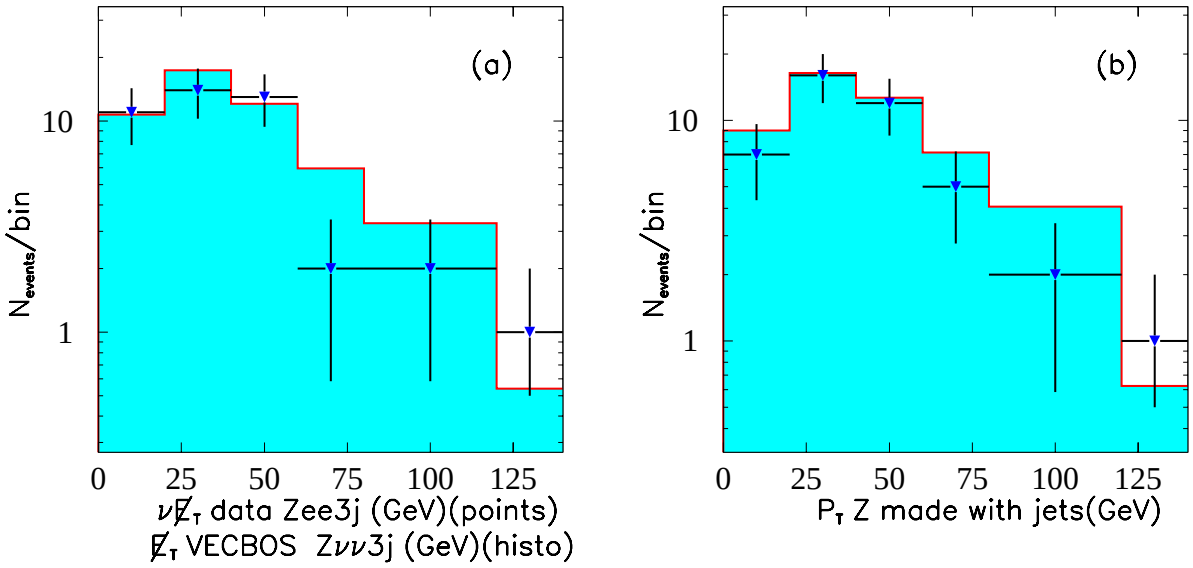

Figure 5.4: (a) $\nu\not{E}_T$ in the $Z(\rightarrow e^+e^-)+3$ jet data sample compared with the $\not{E}_T$ in the ELO $Z(\rightarrow \nu\bar{\nu})+\geq 3$ jets Monte Carlo. (b) Z P_T comparison of the same samples. The boson P_T is the jet $\sum \vec{E}_T$.

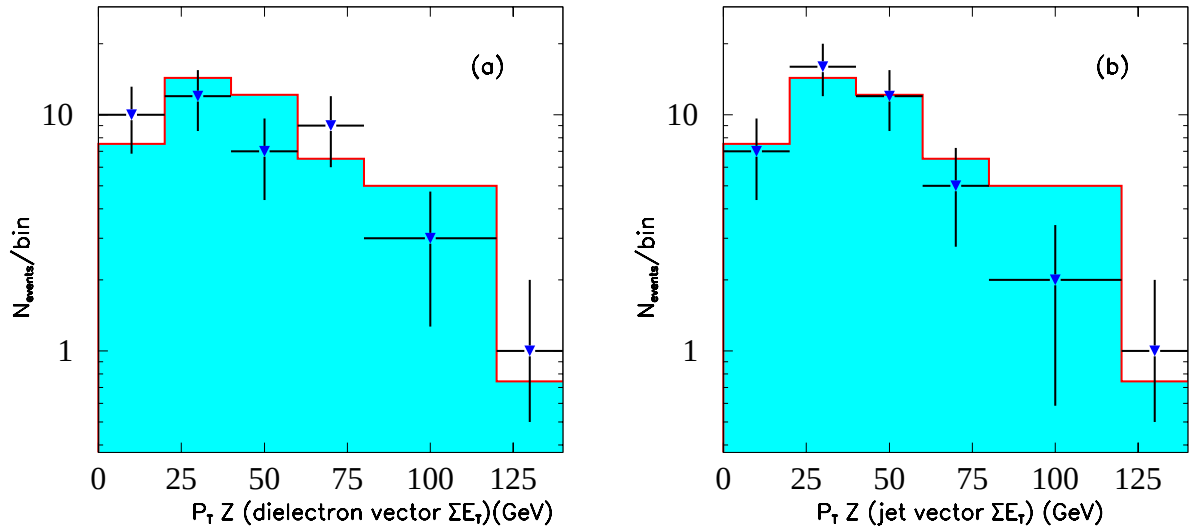

Figure 5.5: Z P_T in inclusive jet multiplicity bin 3 as predicted in $Z(\rightarrow e^+e^-)+\geq 3$jet enhanced leading order Monte Carlo compared with data. The P_T is the (a) the $\sum \vec{E}_T$ of the electrons (b) the $\sum \vec{E}_T$ of the jets.

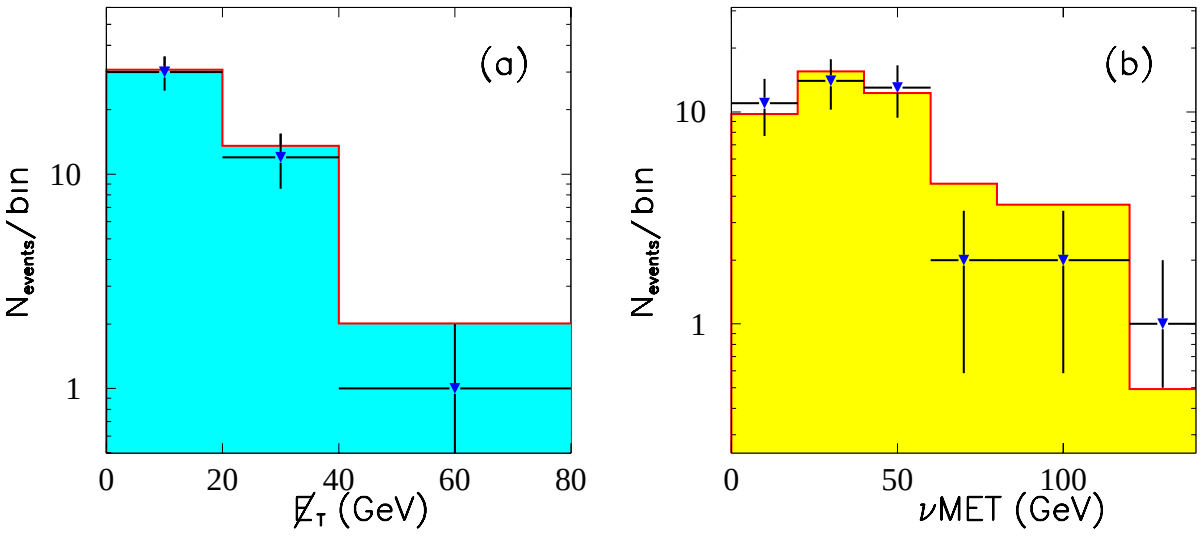

Figure 5.6: Comparison between data and normalized $Z(\rightarrow e^+e^-)+ \geq 3$ ELO Monte Carlo of the (a) $\not\!\!E_T$ and (b) $\nu\not\!\!E_T$ in the inclusive 3 jet bin.

ratio $\frac{g_e}{g_\mu}=\frac{\sigma_W Br(W\rightarrow e\nu)}{\sigma_W Br(W\rightarrow \mu\nu)}$ validates the normalization program for the $W \rightarrow \mu\nu+$ jets prediction. Assuming lepton universality for all the flavors, the normalization scheme is used for all the $W/Z+$ jets Monte Carlo predictions.

5.3.1 $\frac{\sigma_W Br(W(\rightarrow e\nu)+\geq\ 2\ jets)}{\sigma_Z Br(Z(\rightarrow ee)+\geq\ 2\ jets)}$

The ratio $\frac{W(\rightarrow e\nu)+\geq\ 2\ jets}{Z(\rightarrow ee)+\geq\ 2\ jets}$ in the data and in the Monte Carlo predictions is studied. The CDF Run 1A measurement of R^e_{WZ} in the electron channel determined $R^e_{W/Z}$ to be $10.9 \pm 0.32(stat) \pm 0.29(sys)$.

Table 5.2 summarizes the multiplicity breakdown in the data for Z and W electronic decays. Figure 5.7 shows the raw ratio N_{We}/N_{Ze} after applying the same W and Z selection in the data and ELO Monte Carlo, overlayed with the $R^e_{WZ}=\frac{N_{We}}{N_{Ze}} \times \frac{\epsilon_{Ze}*A_{Ze}}{\epsilon_{We}*A_{We}}$ as a function of the jet multiplicity, where $(\epsilon_{Ze} * A_{Ze})$, $(\epsilon_{We} * A_{We})$ are the

DATA	≥1j	≥2j	≥3j	≥4j	≥5j
$Z(\rightarrow ee)+$	1082	226	43	8	2
$W(\rightarrow e\nu)+$	5874	1442	268	53	10

Table 5.2: Summary of inclusive multiplicity breakdown in the $Z(\rightarrow e^+e^-)+ \geq 1$ jet and $W(\rightarrow e\nu_e)+ \geq 1$ jet data. The entries are number of events found.

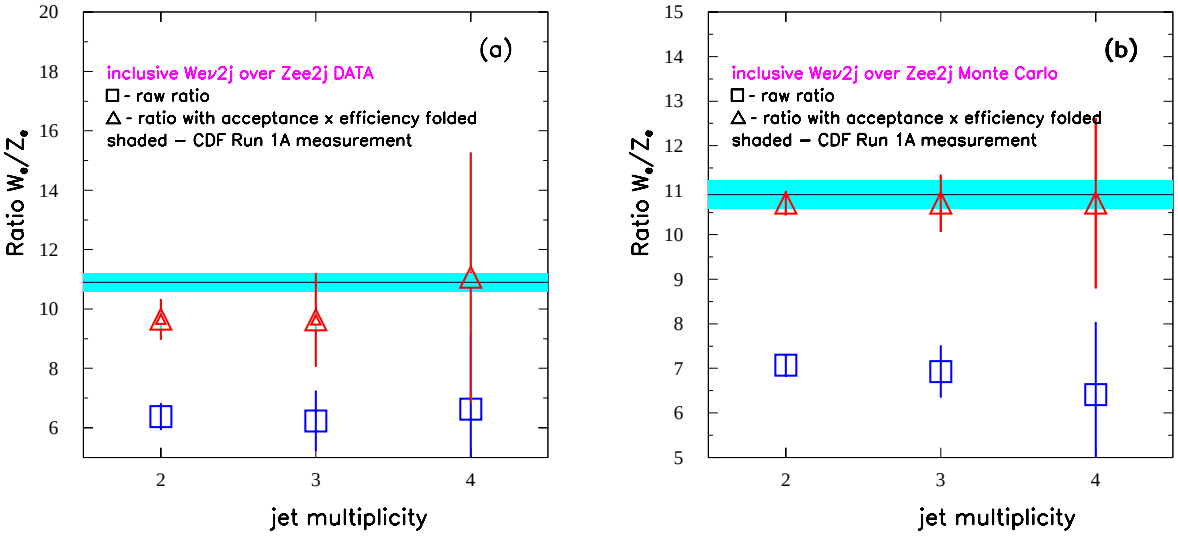

Figure 5.7: □: Raw ratio $\frac{N_{We}}{N_{Ze}}$, △: $R^e_{WZ} = \frac{N_{We}}{N_{Ze}} \times \frac{\epsilon_{Ze} * A_{Ze}}{\epsilon_{We} * A_{We}}$, (a) data, (b) Monte Carlo. The shaded band indicates the CDF measurement of the ratio.

acceptance times efficiency for the W and the Z selection respectively. The hatched band shows the CDF measurement of R in the electron channel in the inclusive zero jet bin.

5.3.2 $\frac{\sigma_W Br(W(\rightarrow e\nu)+\geq 2 \text{ jets})}{\sigma_W \text{Br}(W(\rightarrow \mu\nu)+\geq 2 \text{ jets})}$

In the Standard Model, the ratio of the coupling constants of W boson to the leptons is related to the ratio of the W branching ratios into leptons: $g_e/g_\mu = [\sigma_W Br(W \rightarrow$

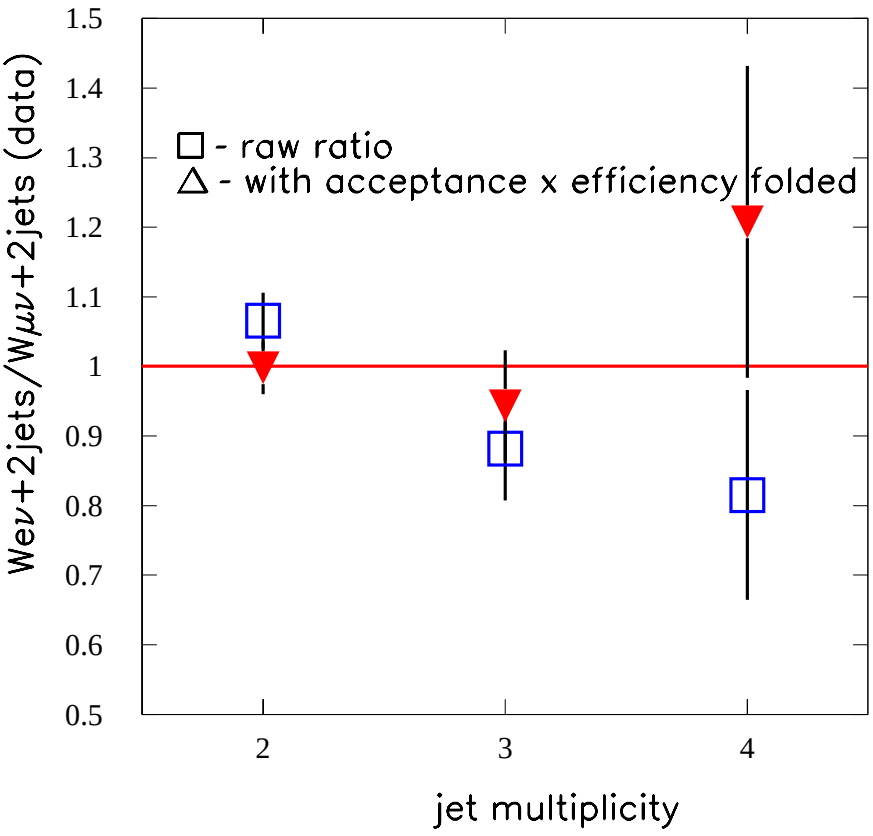

Figure 5.8: □: Raw ratio $\frac{N_{We}}{N_{W\mu}}$ in the data. △: $\frac{N_{We}}{N_{W\mu}} \times \frac{\epsilon_{W\mu} * A_{W\mu}}{\epsilon_{We} * A_{We}}$. The line at 1 is the $\frac{g_e}{g_\mu}$ Standard Model prediction.

$e\nu_e)/\sigma_W Br\ (W \to \mu\nu_\mu)]^{1/2}$. The ratio has been measured at 4% accuracy by CDF [35] to be 0.99. Figure 5.8 shows the ratio of $W \to e\nu$ over $W \to \mu\nu$ events found in the data as a function of the jet multiplicity. The line at 1 is the $\frac{g_e}{g_\mu}$ Standard Model lepton universality prediction.

5.4 Summary: $W \rightarrow \ell\nu+$ jets, $Z \rightarrow \ell\ell+$ jets ELO Monte Carlo Normalization

To normalize the vector boson Monte Carlo predictions the $Zee+ \geq 2$ jets data sample is used. It is demonstrated that the shapes of the kinematic distributions between the predictions and the data agree. The ratio $R = \frac{N}{N+1} = 4.93 \pm 0.31$, where N is the number of jets, and the $\frac{W(\rightarrow e\nu)+\geq 2j}{Z(\rightarrow ee)+\geq 2j} = 7.04 \pm 0.23$ (Figure 5.9) are used to normalize all the W/Z+jets ELO Monte Carlo samples. The ratio $\frac{W}{Z}$ in the data is within 10% of the ratio in the prediction. The ratio is lower in the data, as expected, since no background is subtracted from the W selected data sample while there is very small background in the Z data sample. The systematic effects on the $R = \frac{N}{N+1} = 4.93 \pm 0.31$ measurement is studied by fitting over the first and last three jet multiplicity bins. It is measured to be $R(1:3) = 4.899$ and $R(3:5) = 5.031$. The difference is within the uncertainty of the fit of all bins. In Table 5.3 all the VECBOS+HERPRT+QFL Monte Carlo samples used for the W/Z+jets background calculation in the missing energy plus multijet search, the VECBOS cross section (VEC σ, in pb) and luminosity (VEC $\mathcal{L}$, in pb$^-$1), the normalized VECBOS cross section (norm VEC σ, in pb) and luminosity (norm VEC $\mathcal{L}$, in pb$^-$1) and the derived normalization scale factors (s.f.) are shown.

The normalized to the data VECBOSLuminosity for $Z \rightarrow ee + 2$ jet is

$$\mathcal{L}_{Zee2j} = \frac{\mathcal{L}_{data} \times N_{Zee2j}^{MC\ found}}{N_{Zee2j}^{data}} = 834.7 \text{ pb}^{-1} \tag{5.2}$$

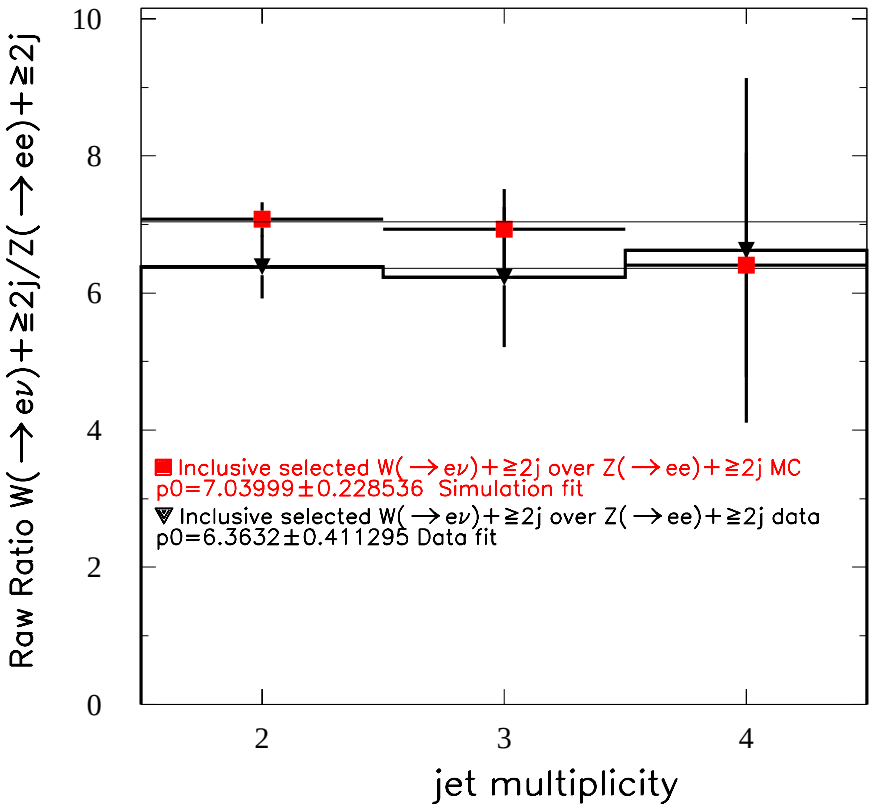

Figure 5.9: $\frac{W}{Z}$ ratio in data and Monte Carlo and the one parameter fit.

Selected Zee+ $\geq$ 2j MC events			**2236**			
Selected Zee+ $\geq$ 2j CDF events			**226**	**84.37**$\pm$4%		
MC	# GEN	VEC $\mathcal{L}$	VEC σ	norm VEC $\mathcal{L}$	norm VEC σ	s.f.
$Zee+\geq 2j$	32129	1969	16.3	834.7 $\pm$8%	38.5 $\pm$8%	0.1
$Zee+\geq 3j$	52639	11577	4.55	6740.6	38.5/**4.93***=7.8	0.0125
$Z\mu\mu+\geq 3j$	49143	10808	4.55	6300	7.8	0.013
$Z\nu_i\nu_i+\geq 3j$	63170	7012	9	494	7.8 $\times$ 6**	0.063
$Z\tau\tau+\geq 2j$	64230	3939	16.3	610	38.5	0.05
$Z\tau\tau+\geq 1j$	55052	931	59.1	290	38.5$\times$4.93	0.29
$We\nu+\geq 3j$	210350	4220.92	49.8	4213	7.8$\times$ 7.04***	0.022
$W\mu\nu+\geq 3j$	191524	3841.8	49.8	3836.6	54.9	0.024
$W\tau\nu+\geq 2j$	254057	1477.2	172	1031	38.5$\times$ 7.04	0.09

Table 5.3: Summary of the ELO Monte Carlo samples and their normalization to the data used to estimate the background in the $\not\!\!E_T$ +jets search. $^{*}R = N/(N+1)$, **Flavor and Branching ratio scaling, *** 7.04 the fitted ratio of $\frac{We\nu}{Zee}$ events. Scale factor s.f.=$\frac{METC}{normVECC}$. "# GEN" stands for the number of generated events. The values in bold indicate the normalization method.

Therefore the normalized to the data $Z \to ee + 2j$ cross section is

$$\sigma_{Zee2j} = \frac{N_{Zee2j}^{MC\ GEN}}{\mathcal{L}_{Zee2j}} = 38.5 \text{ pb} \tag{5.3}$$

Using the ratio $R = 4.93$ the derived inclusive three jet rate is

$$\sigma_{Zee3j} = \frac{\sigma_{Zee2j}}{R} = 7.8 \text{ pb} \tag{5.4}$$

The expression to derive all the normalization factors (Norm=s.f.) and their uncertainties (total, propagated statistical plus systematic in quadrature) for each sample in Table 5.3 are given below:

- $Z \to e^+e^- + \geq$ 3 jets

$$\sigma_{Zee3j} = \frac{\sigma_{Zee2j}}{R} = \frac{N_{Zee2j}^{MC\ GEN} \times 226}{\mathcal{L}_{data} \times N_{Zee2j}^{MC\ found} \times R} \tag{5.5}$$

$$\mathcal{L}_{Zee3j} = \frac{N_{Zee3j}^{MC\ GEN}}{\sigma_{Zee3j}} \tag{5.6}$$

$$Norm = \frac{\mathcal{L}_{data}}{\mathcal{L}_{Zee3j}} \tag{5.7}$$

With substitution of the expression for the normalized luminosity, the data luminosity cancels out, leaving the expression:

$$Norm = \frac{226 \times \epsilon_{Zee2j}^{-1}}{N_{Zee3j}^{MC\ GEN} \times R} \pm 9.5\% \tag{5.8}$$

where:

$$\epsilon_{Zee2j} = \frac{N_{Zee2j}^{MC\ found}}{N_{Zee2j}^{MC\ GEN}} \tag{5.9}$$

- $Z \to \mu^+\mu^- + \geq$ 3 jets

$$Norm = \frac{226 \times \epsilon_{Zee2j}^{-1}}{N_{Z\mu\mu3j}^{MC\ GEN} \times R} \pm 9.5\% \tag{5.10}$$

- $Z \to \tau^+\tau^- + \geq$ 2 jets

  The inclusive two-jet rate data is used in this case, so R does not enter:

$$Norm = \frac{226 \times \epsilon_{Zee2j}^{-1}}{N_{Z\tau\tau2j}^{MC\ GEN}} \pm 7\% \tag{5.11}$$

- $Z \to \nu\ \bar{\nu} + \geq$ 3 jets

$$Norm = \frac{226 \times \epsilon_{Zee2j}^{-1} \times \frac{3\Gamma(Z\to\nu_e\nu_e)}{\Gamma(Z\to ee)}}{N_{Z\nu\nu3j}^{MC\ GEN} \times R} \pm 9.5\% \tag{5.12}$$

- $W \to e\ \nu + \geq$ 3 jets

$$Norm = \frac{226 \times \epsilon_{Zee2j}^{-1} \times \frac{W}{Z}}{N_{We\nu3j}^{MC\ GEN} \times R} \pm 11\% \tag{5.13}$$

- $W \to \mu\ \nu + \geq$ 3 jets

$$Norm = \frac{226 \times \epsilon_{Zee2j}^{-1} \times \frac{W}{Z}}{N_{W\mu\nu3j}^{MC\ GEN} \times R} \pm 11\% \tag{5.14}$$

- $W \rightarrow \tau\ \nu + \geq\ 2$ jets

$$Norm = \frac{226 \times \epsilon^{-1}_{Zee2j} \times \frac{W}{Z}}{N^{MC\ GEN}_{W\tau\nu 2j}} \pm 11\% \tag{5.15}$$

The normalization program was re-designed to normalize the ELO predictions using the $W \rightarrow \mu\nu + \geq 2$ jet data as a reference sample and the results were consistent within 15%. This discrepancy is expected since in the W data selection, no background subtraction is performed.

The normalization program does not imply an absolute cross section normalization. Rather it is a luminosity normalization of the Monte Carlo samples using a well defined reference data sample. The conseptual design of the normalization scheme can be used in an analysis, provided that the requirements for the selection of the reference data sample, the definition of the physics objects and the generation parameters in the Monte Carlo are consistently followed.

5.5 $t\bar{t}$, Single top and diboson production

$t\bar{t}$ pairs are produced at the Tevatron via quark-antiquark annihilation or gluon fusion. A top quark decays to a W boson and a b quark. The b undergoes fragmentation and hadronization forming a jet of final state particles. In Figure 5.10 a schematic of the $t\bar{t}$ production and decays is shown. Each W can decay in any kinematically allowed pair of particles in a doublet with branching fractions $BR(W \rightarrow \ell\nu) = 1/9$ and $BR(W \rightarrow qq') = 1/3$. $\not\!\!E_T$ plus multijet final state constitutes a signature of $t\bar{t}$ production/decays which is a significant background to the search for physics beyond the standard model in this channel. The fully resummed theoretical $\sigma_{t\bar{t}} = 5.06^{+0.13}_{-0.36}$ pb for

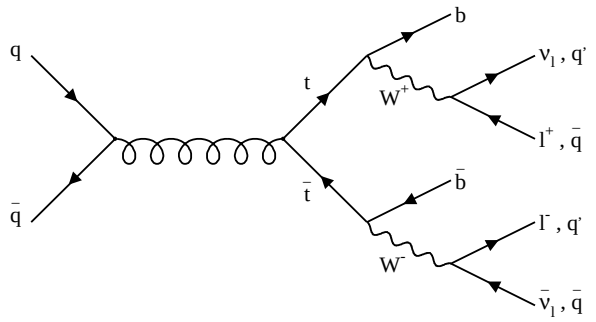

Figure 5.10: Schematic of the $t\bar{t}$ pair Standard Model decays.

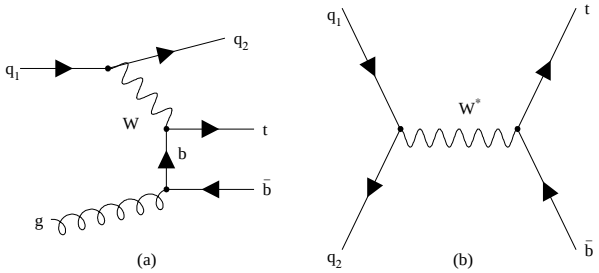

Figure 5.11: Single top production via W-gluon fusion(a) and $q\bar{q}$ annihilation(b).

$m_{top} = 175\text{GeV}/c^2$ [36] is used with total uncertainty 18% (including the uncertainty on the cross section due to the uncertainty on the top mass) is used to normalize the predictions to the data luminosity. $t\bar{t}$ events are generated using PYTHIA. Top can be produced singly via W-gluon fusion and $q\bar{q}$ annihilation (Figure 5.11) with cross section $\sigma_{Wg} = 1.7$ pb ($\pm$ 17%) and $\sigma_{W^* \to t\bar{b}} = 0.73$ pb($\pm$9%) [37]. HERWIG and PYTHIA respectively is used to generate the two single top production processes and the theoretical cross section is used to normalize to the data luminosity. The production (Figure 5.12) and subsequent decays of heavy boson pairs contribute to a final state with large missing energy and multijets. These processes are generated

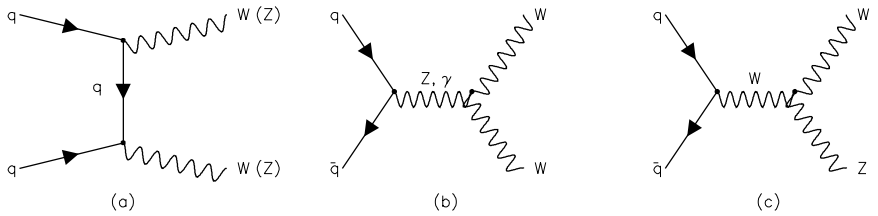

Figure 5.12: Leading order diagrams for diboson production at the Tevatron. Diagram (a) contributes to all processes. Diagrams (b) and (c) contribute to WW and WZ respectively.

using PYTHIA Monte Carlo and they are normalized to the data luminosity using the theoretical cross section calculation $\sigma(WW) = 9.5 \pm 0.7$ pb, $\sigma(WZ) = 2.6 \pm 0.3$ pb and $\sigma(ZZ) = 1 \pm 0.2$ pb [38].

Chapter 6

QCD Jet Production

A brief discussion of QCD and Jet physics is given in Appendix F. In hard parton-parton scattering, jet production (Figure 6.1) dominates the cross section. The source of missing energy in QCD jet production is the small fraction of $b\bar{b}$ and $c\bar{c}$ content (with the b and c quarks decaying semileptonically) and largely the jet mismeasurements and detector resolution. Analyses that require a measurement of the QCD multijet background use the jet data when there are extra requirements such as a b-tagged jet or a lepton. The data give a reliable estimate for the QCD background in such analyses. Comparisons between data and HERWIG QCD Monte Carlo for the ΣE_T cross section measurement at CDF [39] indicate agreement between the data and

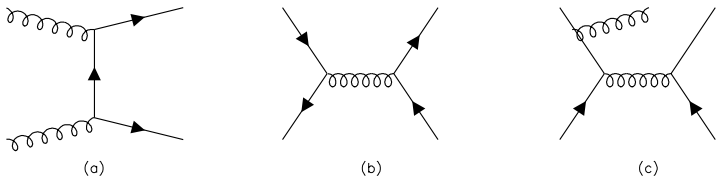

Figure 6.1: Sample of tree level jet production graphs. (a) and (b) 2-to-2 (c) 2-to-3 jets processes.

the Monte Carlo predictions. CDF studies [41] have shown adequate agreement between the b and c-tagged HERWIG QCD Monte Carlo events and their kinematic distributions with the CDF data.

In the case of the large missing energy plus multijet (≥ 3 jets) search the estimate of the QCD background is nontrivial. The missing energy trigger accepts QCD multijet events (45% of the online MET trigger are volunteers from jet triggers) and the trigger threshold is too high[1] to allow use of the low missing energy triggered data for extraction of the high missing energy spectrum. The high energy threshold jet triggered data with small or no prescale (JET70, JET100) are not suitable to extract the QCD contribution to the high $\not\!\!E_T$ tails as they themselves constitute signal candidate samples. The lower energy threshold jet triggered data with large prescales (JET20, JET50) are used in this analysis to estimate the QCD jet production contribution to the high missing energy spectrum.

Large statistics ($\sim$10 times the data) 3-jet QCD Monte Carlo samples are generated to simulate the JET20 and JET50 data samples and used to compare the shapes of the missing energy and the N-jet distribution with the data. The predictions are absolutely normalized to the data.

6.1 Hard, Semi-Hard, Soft and Multiple Scattering

The total $p\bar{p}$ cross section is the sum of the elastic and inelastic cross sections. The elastic consists of the diffractive and the "hard core" component. The latter is the one selected by the Minimum Bias trigger (Figure 6.2) which requires at least one

[1] For Run II the MET trigger is designed with a lower threshold (25 GeV) [42].

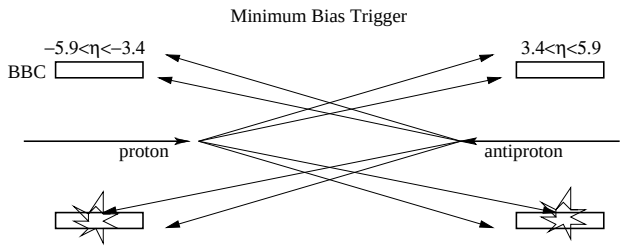

Figure 6.2: CDF Minimum Bias Trigger.

charged particle interacts with the forward and at least one interacts with the backward Beam Beam Counter (Chapter 2). The hard scattering hard core collisions correspond to large transverse momentum 2-to-2 parton-parton subprocess (Figure 6.3(a)). The soft hard core collisions shown in Figure 6.3(c) correspond to events in which no hard interaction has occured. In these events there is no large transverse momentum subprocess or short distance probing and it makes little sense to talk about partons. The proton and antiproton ooze through each other and fall apart. The hard scattering event shown in Figure 6.3(a) consists of large transverse momentum outgoing hadrons and also hadrons that originate from the break-up of the proton and antiproton (beam-beam remnants). The *underlying event* is an interesting and not very well understood object. In addition to the beam-beam remnants it contains hadrons from initial state gluon radiation and also hadrons that originate from multiple parton interactions in the same proton-antiproton collision (Figure 6.3(b)) or in different proton-antiproton collisions of the same bunch crossing (*pile-up*). For the same available energy the underlying hard scattering event has considerably higher charge particle density and transverse momentum compared to the soft collision. The soft collisions are parametrized in the different Monte Carlo generators and the hard scattering is a superposition of a hard parton-parton interaction on top of a soft minimum bias type collision. In some Monte Carlo generators multiple parton interactions

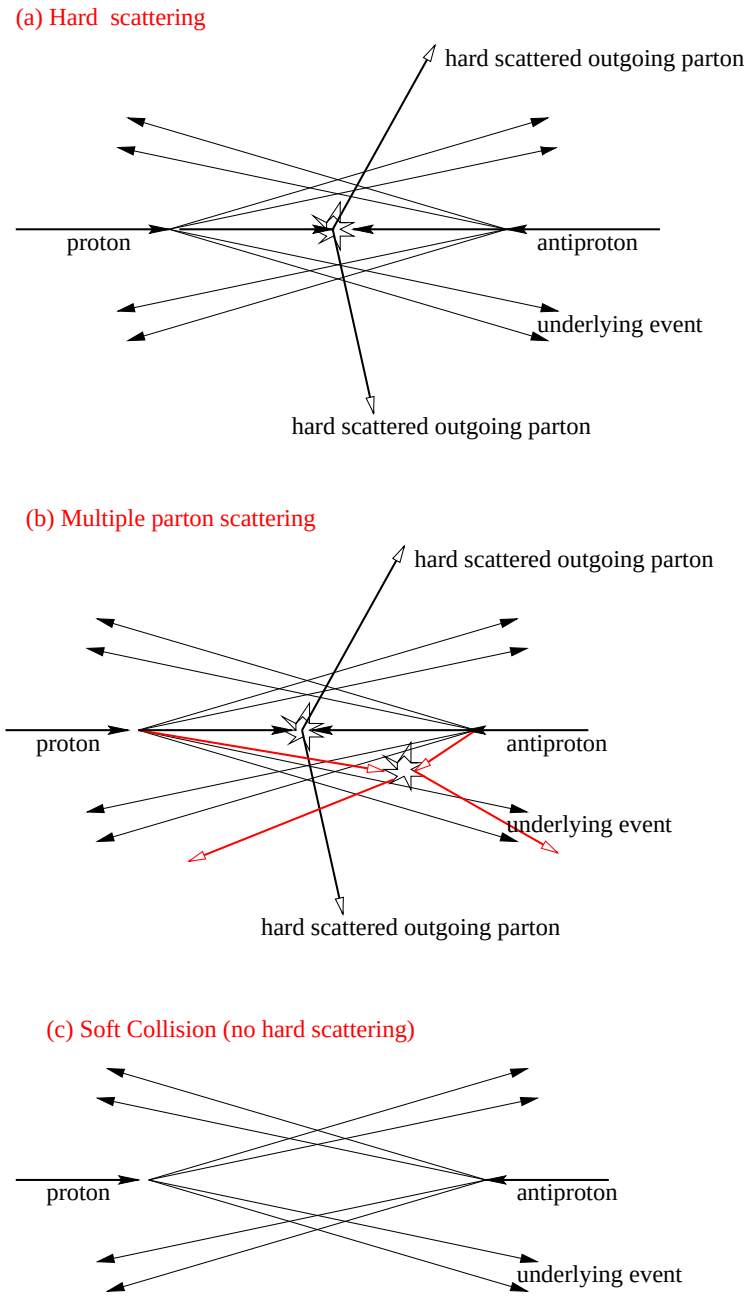

Figure 6.3: Schematic of Hard (a), Multiple (b), and Soft (c) interactions in proton antiproton collisions.

are used to enhance the activity of the underlying event. It is found [43] that none of the QCD Monte Carlo models properly describes the behavior of the underlying event. The minimum bias data sample is suitable to study the transition between soft and hard collisions and understand the contribution to the missing energy spectrum and the jet multiplicity spectrum.

The $\not\!\!E_T$, N_{jet} and N_{vert} distributions in the minimum bias event sample (Chapter 3) that was recorded throughout Run 1B and passed Pre-Selection Stages 1 & 2, are shown in Figure 6.4. The average $\not\!\!E_T$ is $\sim$7 GeV : the underlying event superimposed on the $\not\!\!E_T$ spectrum from the hard collision jet production contributes at low $\not\!\!E_T$. The jet multiplicity distribution has significant tails. The superposition of the underlying event with the hard collision promotes the event jet multiplicity by contributing hard jets or by enhancing the energy of the jets.

For a non-Standard Model signal characterized by large missing energy and a large number of high E_T jets, the underlying event does not affect the signal detection. To compare the $\not\!\!E_T$ (the whole spectrum, not only the high energy end of it) and N_{jet} distributions between the QCD 2-to-2 simulation (which has no adequate underlying event description) and the jet data, the data are required to have less than five well determined vertices so that the effect of multiple scattering in the event is moderated. The normalization is carried between the total available number of jet data (independent of the number of vertices) and the QCD Monte Carlo generated.

6.2 Comparison between data and Monte Carlo

The JET20 and JET50 data samples, after Pre-Selection Stages 1 & 2, are used. The JET20 subset $S20.nv4 \subset$ JET20 is selected to have ≤ 4 vertices (and less than

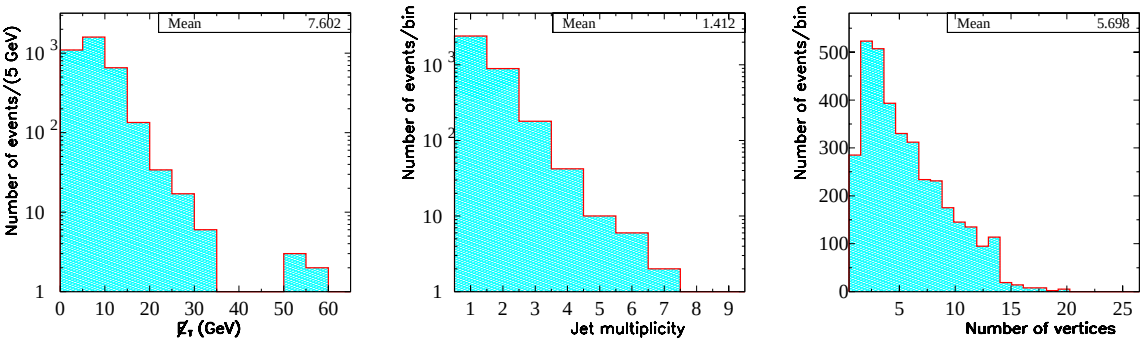

Figure 6.4: $\not\!\!E_T$, jet multiplicity, and vertex multiplicity distributions in the minimum bias sample after Pre-Selection Stages 1 & 2.

the average in the minimum bias sample – in order to moderate the effect of multiple interactions). The kinematics of the $S20.nv4$ and the JET20 sample are in agreement except the high end of the N_{jet} distribution which are affected by the extra jets of the underlying event. The kinematic distributions of the $S20.nv4$ sample and those of the QCD Monte Carlo generated according to the JET20 data sample (that passes the Pre-Selection Stages 1 & 2 and has the JET20 trigger efficiency folded in) are in agreement. The $S20.nv4$ data subset and the QCD20 Monte Carlo sample are consistently normalized to the total number of selected events in the JET20 sample and the distributions of the $S20.nv4$ data and the QCD20 Monte Carlo are directly compared. The number of vertices k that selects a $S20.nvk$ subset can be thought of as a tuning parameter according to the instantaneous luminosity during the run, the available jet data statistics, and the level of agreement with the QCD Monte Carlo. To have sufficient data statistics when comparing with the Monte Carlo, the $S20.nv4$ and $S50.nv4$ ($\subset$ JET50) subsets are selected with the requirement of the number of vertices being ≤ 4. The study is repeated for the number of vertices being ≤ 2 and the shapes of the relevant distributions are invariant. The comparison and

normalization procedure is followed in the same way for the JET50, QCD50 data and simulation samples. The QCD Monte Carlo is directly normalized to the (selected after Pre-Selection Stages 1 & 2) inclusive 3 jet JET20 and JET50 data samples. The prescales for the samples are taken into account *i.e.* since the JET20, JET50 prescales were static, the QCD samples are normalized to the total integrated luminosity of the signal candidate MET sample ($84.37\ \mathrm{pb}^{-1} \pm 4\%$).

The steps of the comparison and normalization procedure are:

- The JET20 and JET50 3-jet data samples are used after the Pre-Selection Stages 1 & 2 applied. (Chapter 4).

- Large statistics QCD20 and QCD50 HERWIG (2-to-2 process with initial- and final-state fragmentation and hadronization) 3-jet samples are generated to simulate the JET20 and JET50 triggers.

- The Monte Carlo data go through the same Pre-Selection Stages applied to the jet data.

- The JET20, JET50 measured trigger efficiencies (Appendix D) are applied to the corresponding Monte Carlo samples. For the JET20 data and QCD20 Monte Carlo samples, the E_T of the leading (trigger) jet is required to be between 45 and 70 GeV and for the JET50 data and QCD50 Monte Carlo samples the E_T of the leading (trigger) jet is required to be above 70 GeV (the regions where the JET20 and JET50 triggers are $> 90\%$ efficient).

- Each data sample is compared separately with the corresponding Monte Carlo sample.

- The trigger prescale factors as measured (Chapter 3) are applied to both the data and the Monte Carlo.

- The JET20, JET50 data and QCD20, QCD50 Monte Carlo samples are merged and the kinematics are compared. The comparisons of the kinematic distributions are shown in Figures 6.5 through 6.9.

The $\not\!\!E_T$ spectrum comparison between $S20.nv4$ jet data and QCD Monte Carlo for $3 \leq N_{jet} \leq 4$ and for $N_{jet} > 4$ (Figure 6.10) validates that the tails of the $\not\!\!E_T$ distribution are well described in the Monte Carlo and invariant to the jet multiplicity which is modulated by the vertex requirement in the data.

6.3 Jet Fiducial Requirements

6.3.1 The *Tomographic* fiducial requirement

The purpose of "tomography" selection is to precisely and with high efficiency remove primarily QCD events that fall in a known non-fiducial region and cause large missing transverse energy. In a multijet QCD event, the major source of large missing energy is energy flow from one or more jets to an uninstrumented region. The highest E_T jet is the best measured jet. When the second or third jet are grossly mismeasured because they land in an uninstrumented region, the $\not\!\!E_T$ is pulled in ϕ close to the mismeasured jet (the $\not\!\!E_T$ vector is parallel in the $r-\phi$ plane with this jet) and the pseudorapidity of this jet is consistent with a detector gap. Then, the leading well-measured jet is "back to back" in ϕ with the $\not\!\!E_T$. The mismeasured jets are concentrated in the uninstrumented regions (gaps). The energy leakage in these regions is due to the mechanical structure of the calorimetry system, shown diagrammatically in Figure

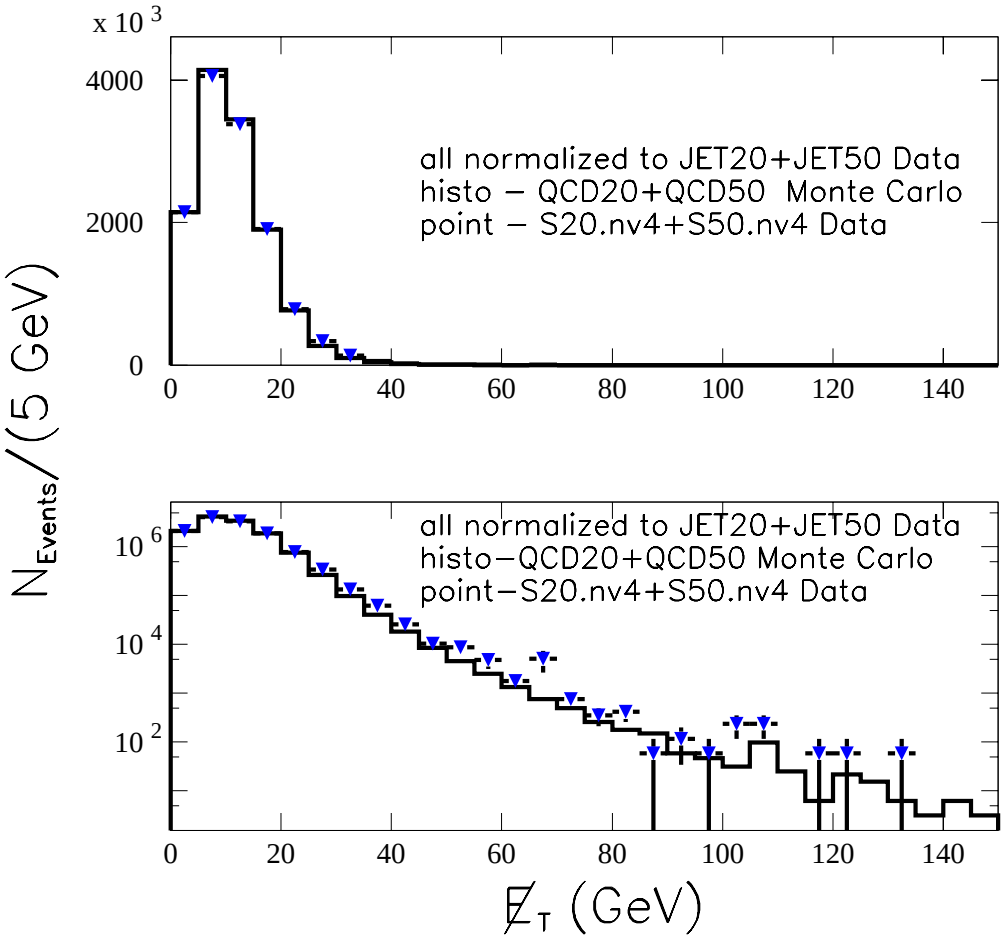

Figure 6.5: $\not\!\!E_T$ distribution in the QCD50+QCD20 Monte Carlo sample and the $S20.nv4$+$S50.nv4$ JET20+JET50 data subset. Both data and Monte Carlo are normalized to the (JET20+JET50) selected data sample with the individual prescales taken into account. ((top) linear and (bottom) log scale.)

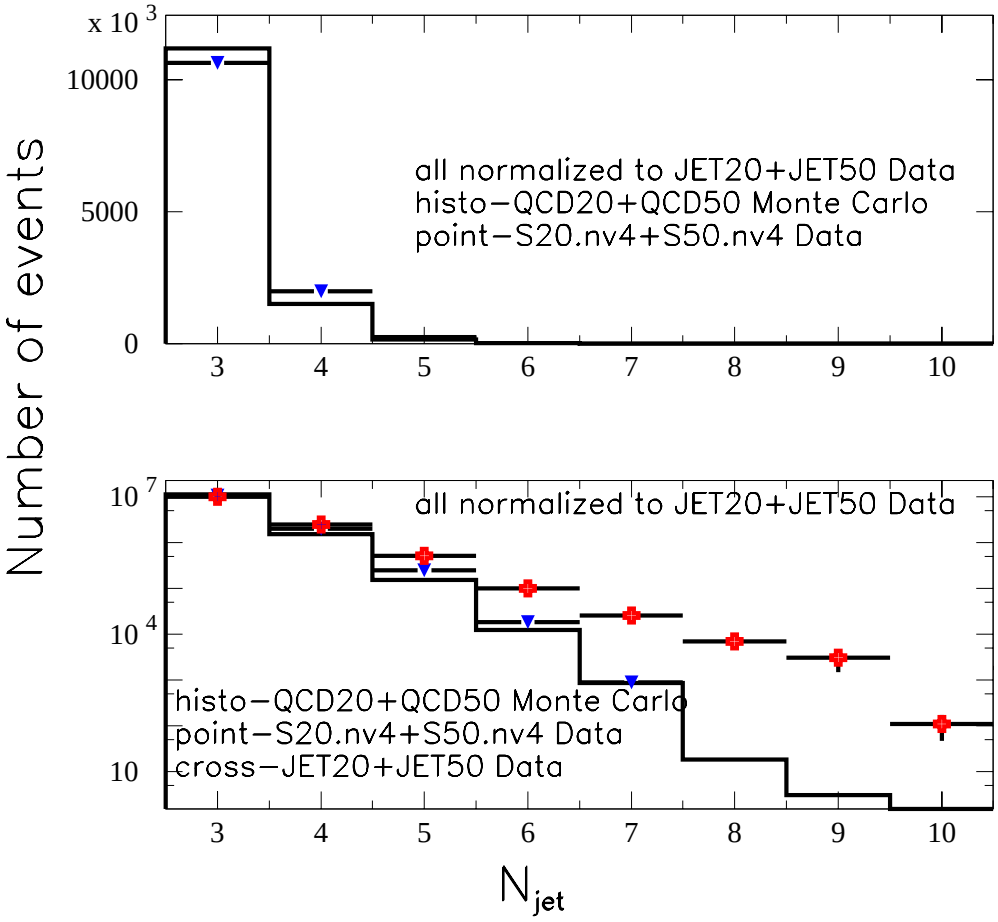

Figure 6.6: N_{jet} distributions in the QCD20+QCD50 Monte Carlo sample and the $S20.nv4$+$S50.nv4$ JET20+JET50 subset. Both data and Monte Carlo are normalized to the (JET20+JET50) selected data sample with the individual prescales taken into account. The unmodulated (crosses, no requirement on the number of vertices) JET20+JET50 N_{jet} distribution is overlayed. ((top) linear and (bottom) log scale.)

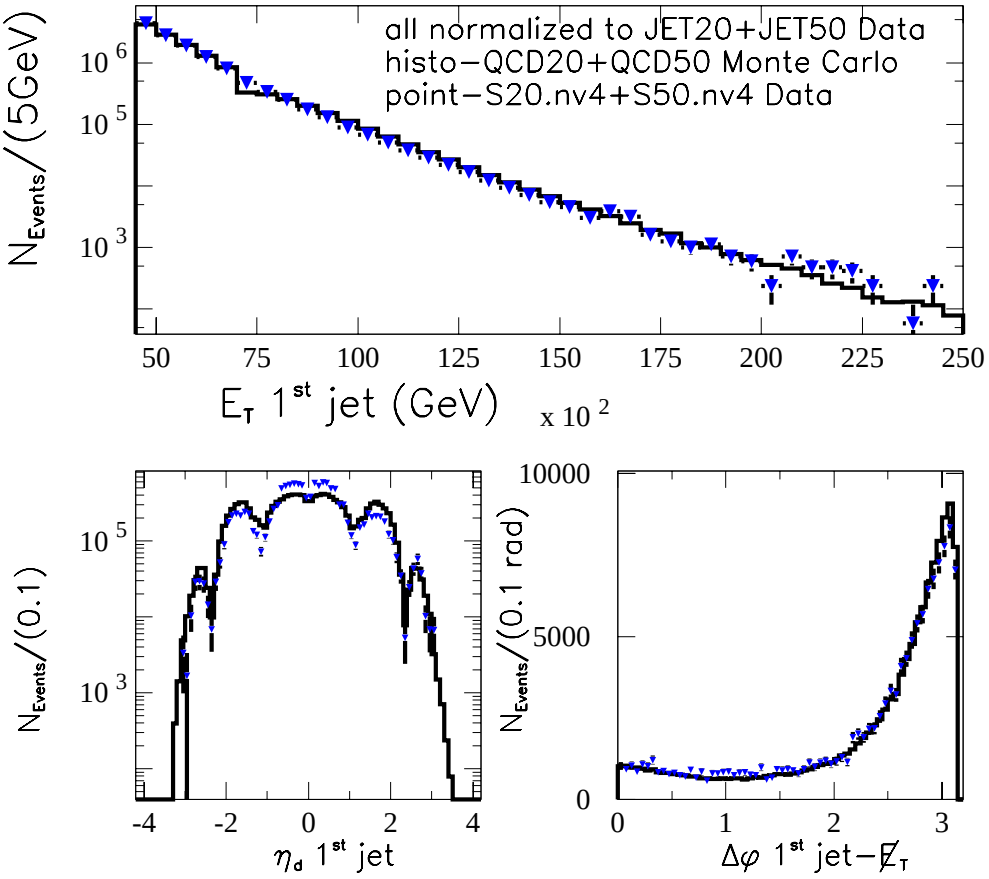

Figure 6.7: Kinematics (E_T, η_d, $\delta\phi$) of the leading jet in the QCD20+QCD50 Monte Carlo sample and the $S20.nv4$+$S50.nv4$ JET20+JET50 subset. Both data and Monte Carlo are normalized to the (JET20+JET50) selected data sample with the individual prescales taken into account.

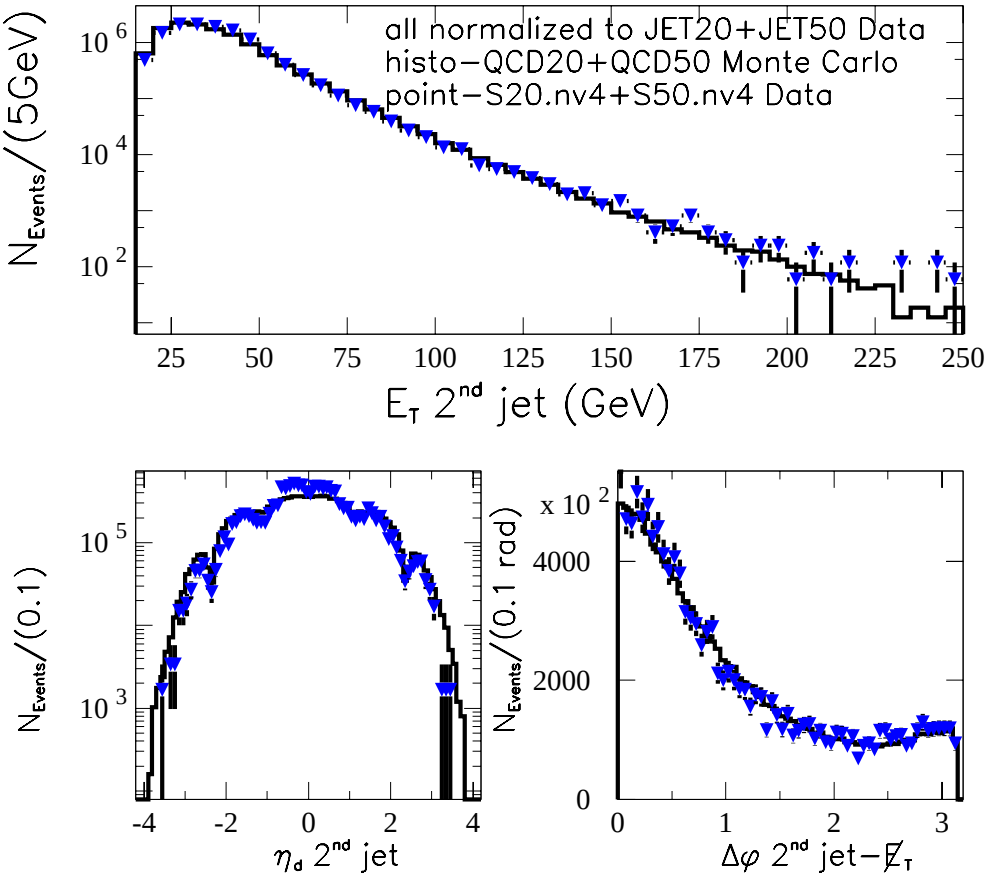

Figure 6.8: Kinematics (E_T, η_d, $\delta\phi$) of the second leading jet in the QCD20+QCD50 Monte Carlo sample and the $S20.nv4$+$S50.nv4$ JET20+JET50 subset. Both data and Monte Carlo are normalized to the (JET20+JET50) selected data sample with the individual prescales taken into account.

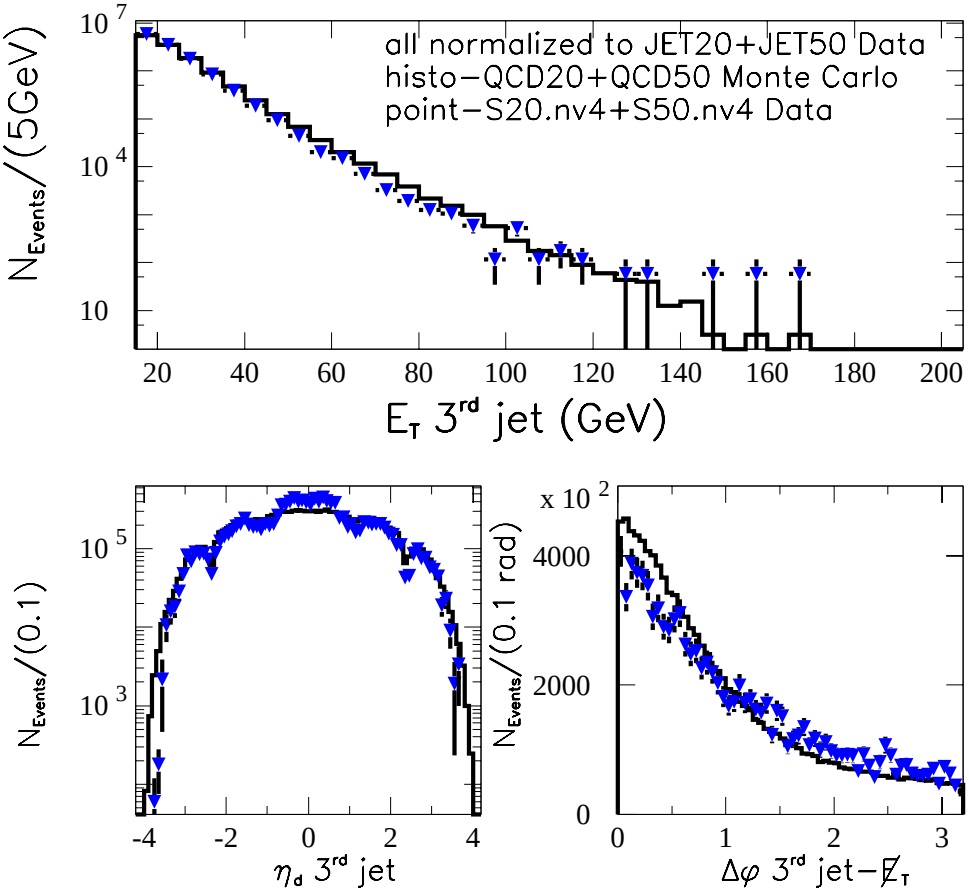

Figure 6.9: Kinematics (E_T, η_d, $\delta\phi$) of the third leading jet in the QCD20+QCD50 Monte Carlo sample and the $S20.nv4$+$S50.nv4$ JET50 subset. Both data and Monte Carlo are normalized to the (JET20+JET50) selected data sample with the individual prescales taken into account.

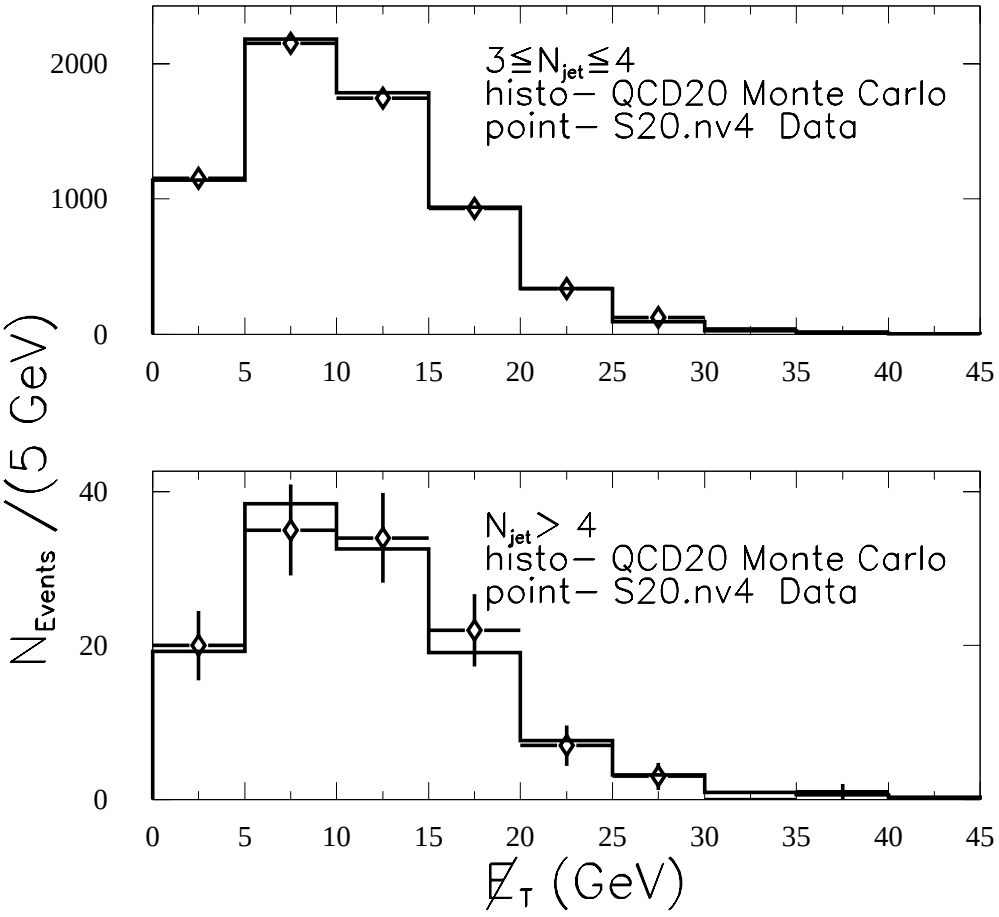

Figure 6.10: $\not\!\!E_T$ spectrum comparison between $S20.nv4$ jet data and QCD Monte Carlo for $3 \leq N_{jet} \leq 4$ (top) and for $N_{jet} > 4$ (bottom). The tails of the distribution are well described in the Monte Carlo and invariant to the jet multiplicity.

6.11. There is a gap at $\theta = 90°$ where the central arches meet. Because of this gap, jets at $\eta_d = 0$ are poorly measured. Between towers 6 and 11, energy is lost between the central arch and the end wall calorimeters. The leakage is worst between towers 9 and 11, where there is a dead region caused by the end of the solenoid and a gap at $\theta = 30°$ between the end-wall and the plug calorimeters (a discussion of the detector gaps is found in Chapter 2.4). Particles originating from vertices far from the nominal detector center can pass through the angular gap between the plug and forward detectors at $\theta = 10°$ and miss the forward detector. This region is called the "Blue Sky" region. Typically in events with large $\not\!\!E_T$ the most energetic jet (leading jet) is measured best because it lands in a fiducial region of the detector. The detector gaps appear in the η_d distribution of the first jet as dips. For the mismeasured second and third jets, the gaps are crests in the η_d distribution of the jet. This is shown in the 2-dimensional η_d versus z(vertex) and ϕ(jet) versus $\phi(\not\!\!E_T)$ graphs in Figures 6.12, 6.13, 6.14 & 6.15. The jet tomographic fiducial requirement is designed as shown pictorially in Figure 6.16. In order for a jet to be assessed non-fiducial, the η_d of the jet has to be consistent with one of the gap regions **and** the jet must be parallel in ϕ with the $\not\!\!E_T$ (within 0.5 rad). The coordinates of the non-fiducial boxes in the picture are the actual ones used in the analysis. The tomographic fiducial requirement is applied to the second and third jet.

6.3.2 2-D $\delta\phi$ requirement

The residual QCD component after the tomographic fiducial requirements on the second and third jets is displayed in the $\delta\phi_1 = |\phi_{\text{leading jet}} - \phi_{\not\!\!E_T}|$ versus $\delta\phi_2 = |\phi_{\text{second jet}} - \phi_{\not\!\!E_T}|$ plane as a strong angular correlation : the second jet is parallel with the $\not\!\!E_T$ and back to back with the first jet (Figure 6.17 & 6.18). The correlation is

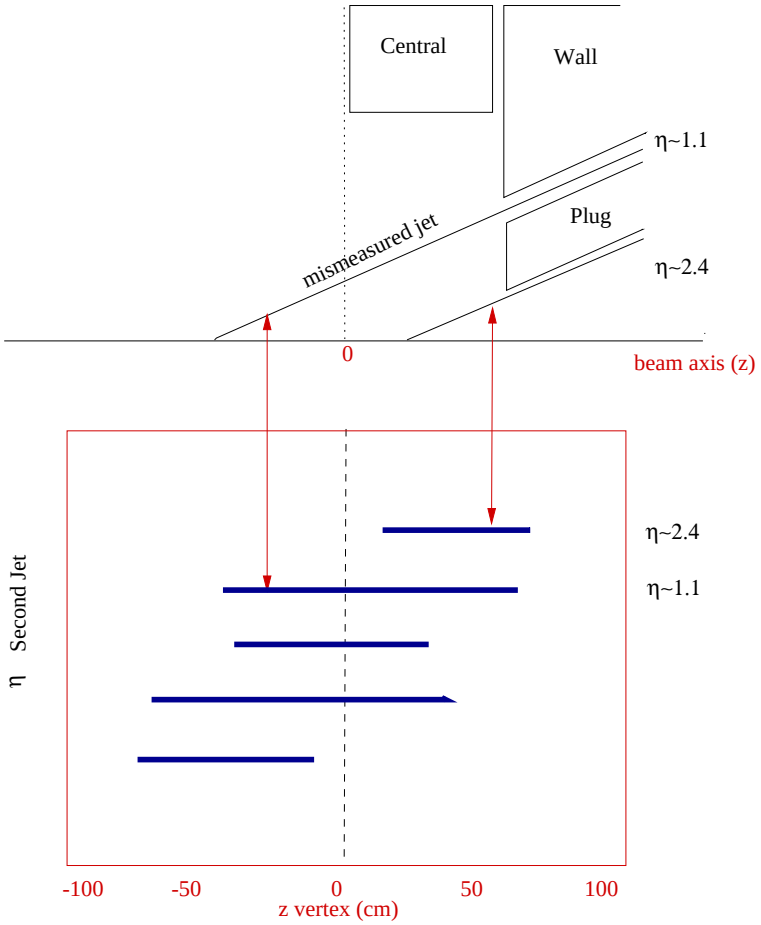

Figure 6.11: Schematic of jets pointing at the CDF boundaries and η-z vertex correlation expected.

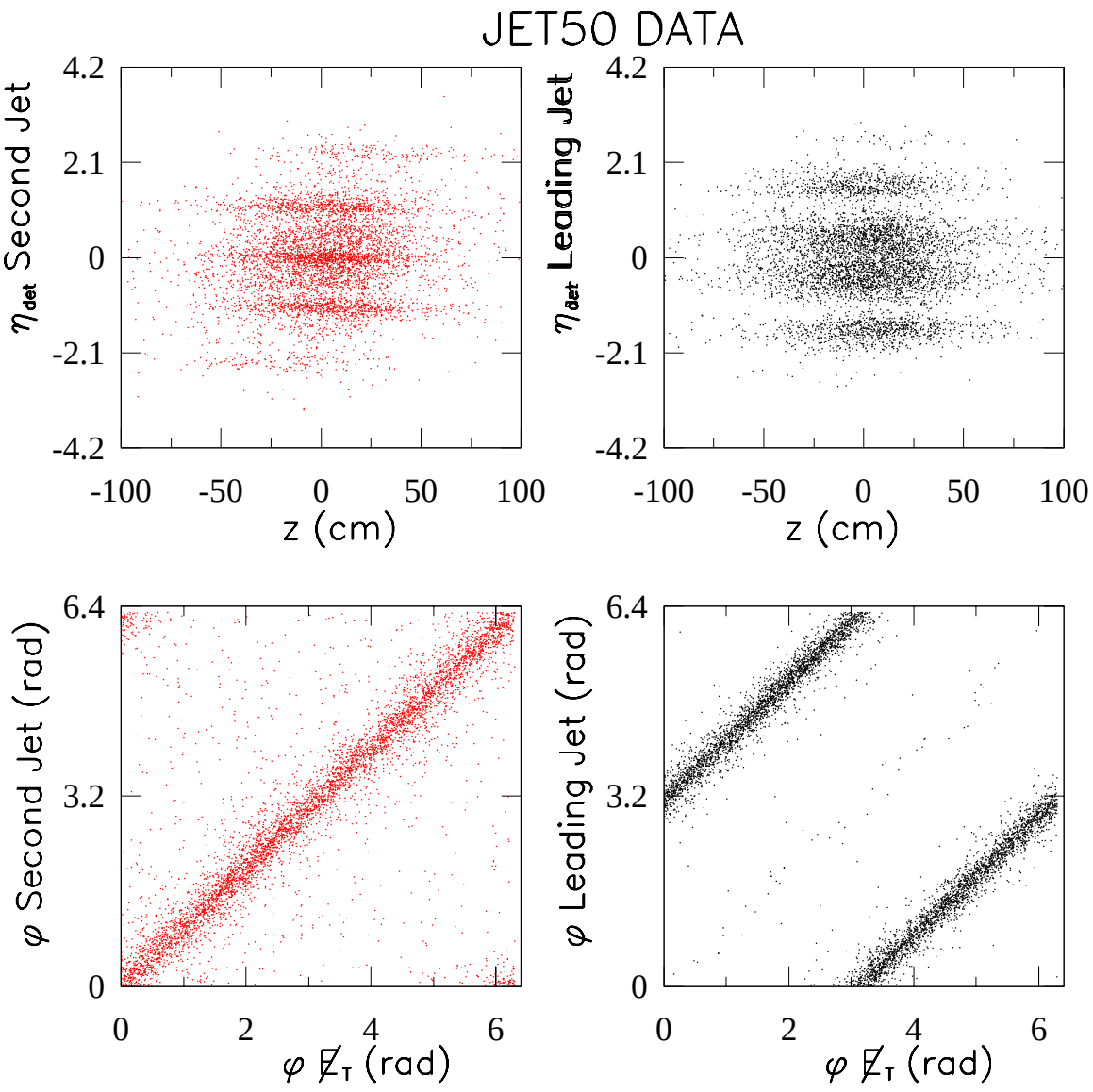

Figure 6.12: Second leading jet η_d versus z(vertex) and ϕ correlation with $\phi(\not\!\!E_T)$ (left) and the corresponding leading jet variables(right).Notice (1) in the η_d plots the higher density at the gaps for the second jet compared to the low density at the gaps for the leading jet.(2) The second jet is parallel in ϕ with the $\not\!\!E_T$ while the first jet is anti-parallel (JET50 CDF data).

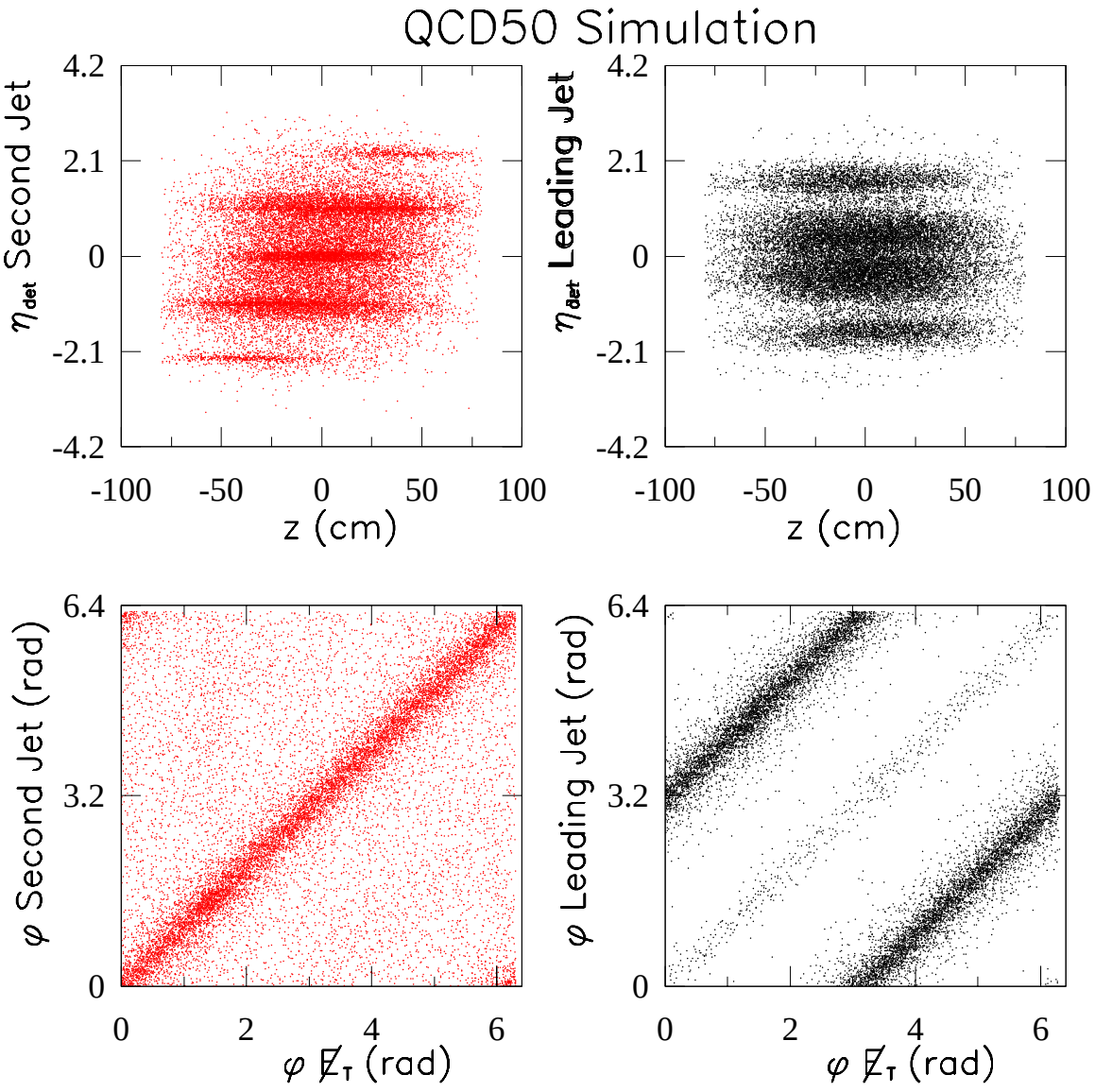

Figure 6.13: Second leading jet η_d versus z(vertex) and ϕ correlation with $\phi(\not\!\!E_T)$ (left) and the corresponding leading jet variables(right). Notice (1)in the η_d plots the higher density at the gaps for the second jet compared to the low density at the gaps for the leading jet. (2) The second jet is parallel in ϕ with the $\not\!\!E_T$ while the first jet is anti-parallel.(QCD 50 simulation.)

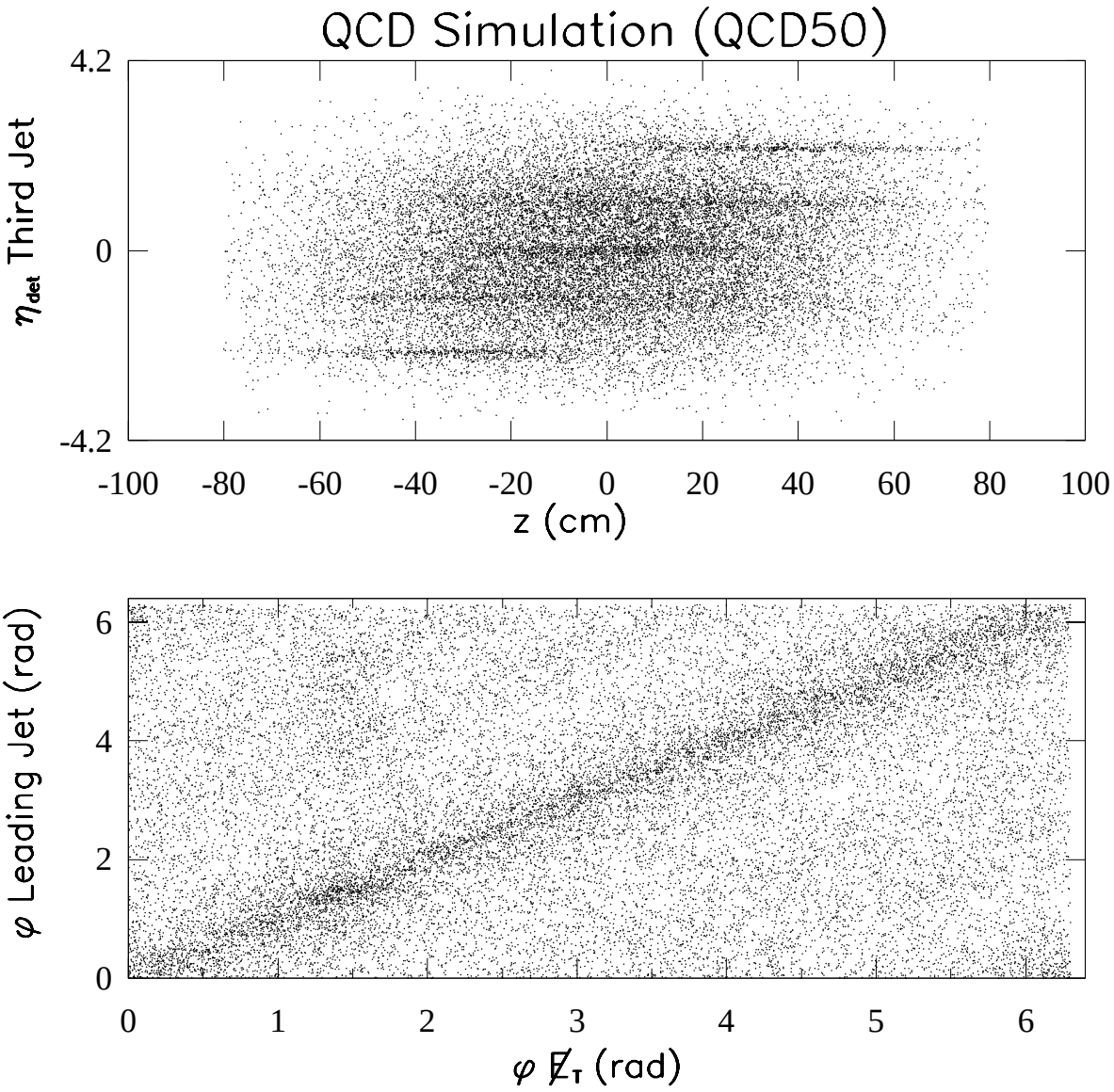

Figure 6.14: Third jet η_d versus z(vertex) and ϕ correlation with $\phi(\not\!\!E_T)$. (QCD50 simulation.)

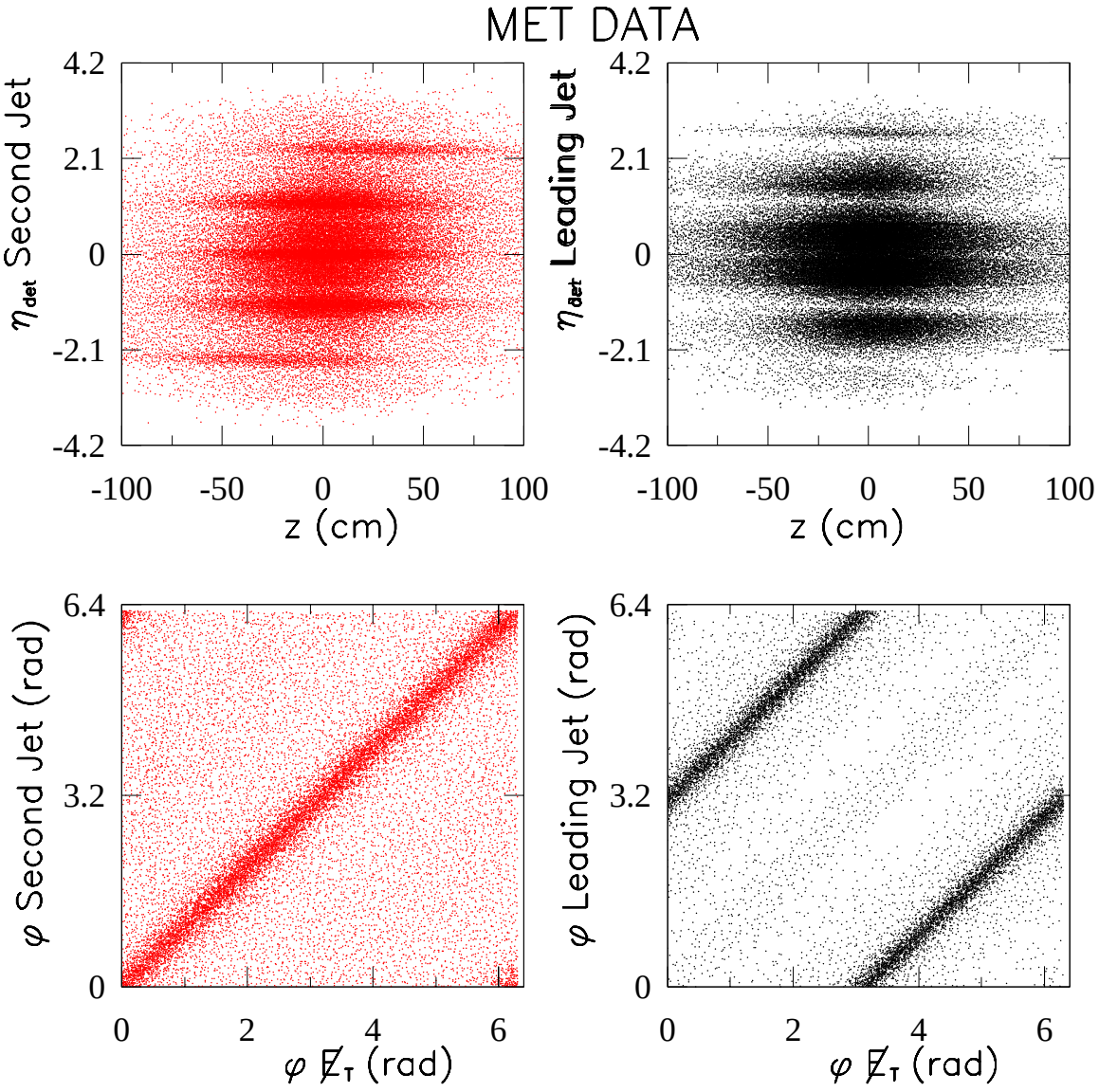

Figure 6.15: Second leading jet η_d versus z(vertex) and ϕ correlation with $\phi(\not\!\!E_T)$ (left) and the corresponding leading jet variables (right). (MET data.)

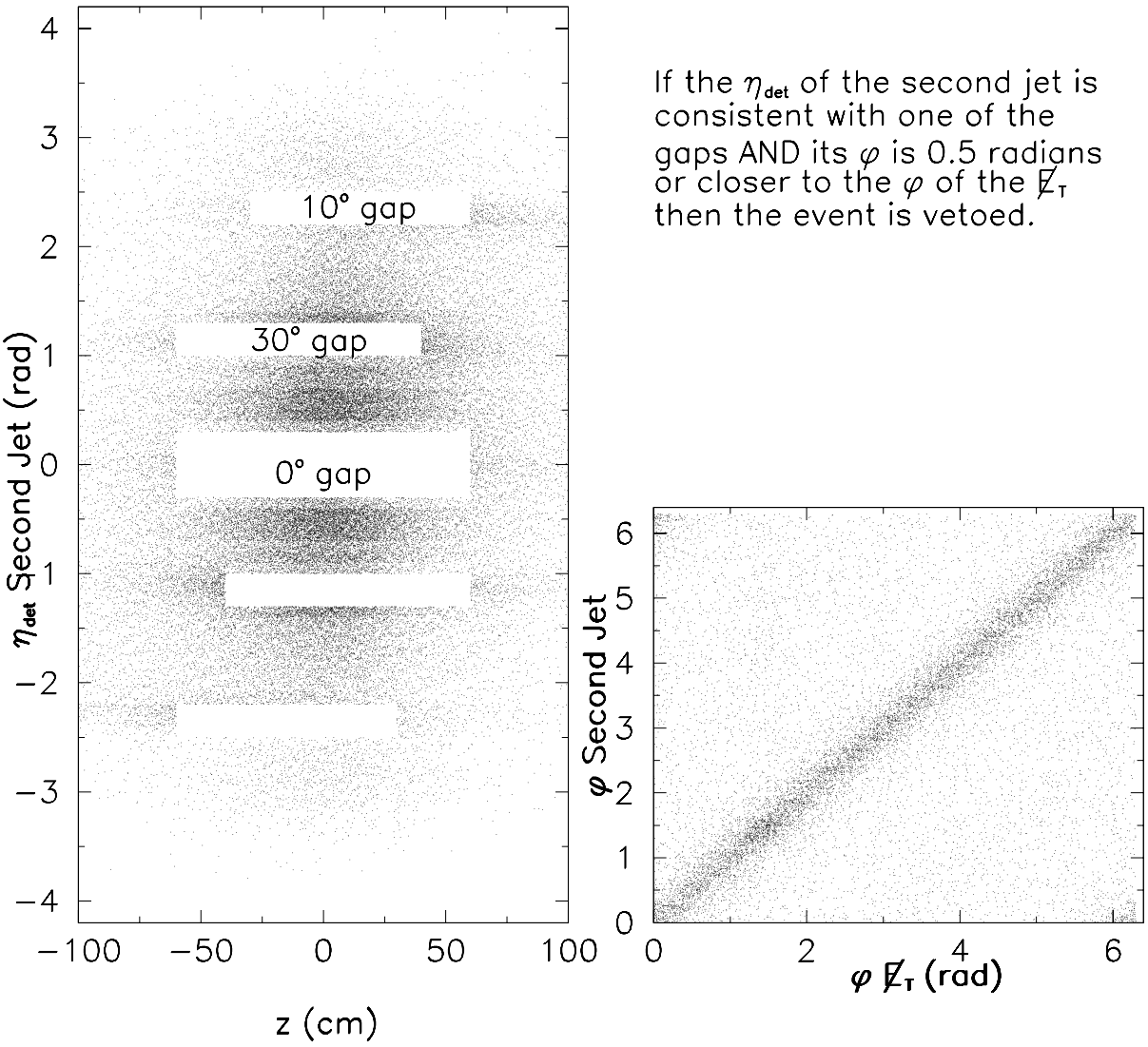

Figure 6.16: Design of the jet tomographic fiducial requirement. On the left the η_d versus z of the second jet and on the rigth the ϕ of the second jet versus the ϕ of the $\not\!\!E_T$ are shown.

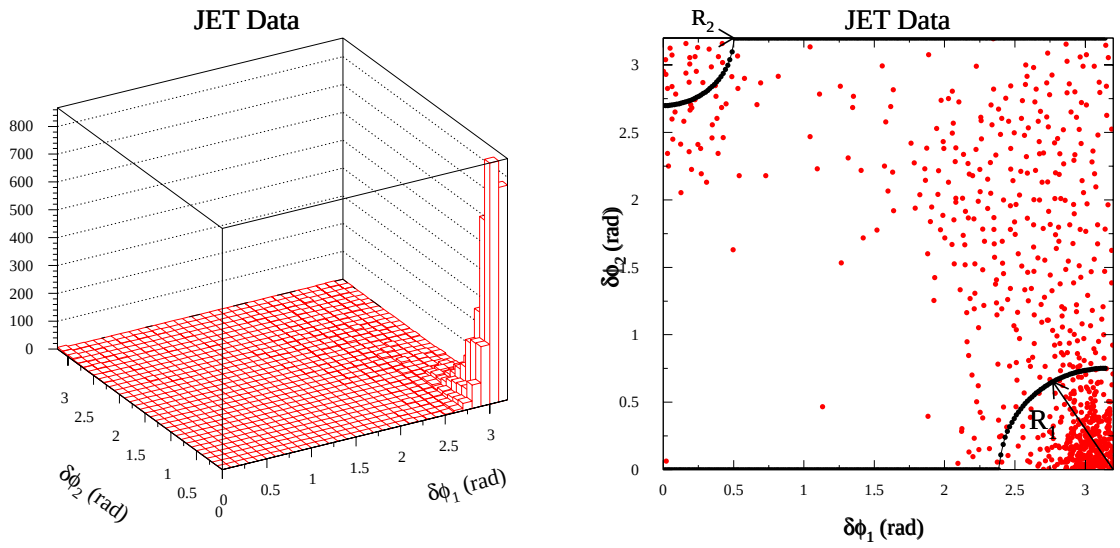

Figure 6.17: JET50 data: $\delta\phi_2$ versus $\delta\phi_1$ lego and density display showing the 2-dimensional requirement applied.

quantified with the variables:

$$R_1 = \sqrt{\delta\phi_2^2 + (\pi - \delta\phi_1)^2}, \qquad R_2 = \sqrt{\delta\phi_1^2 + (\pi - \delta\phi_2)^2} \tag{6.1}$$

Figure 6.20 shows the simultaneous optimazation of for R_1 and R_2 using the signal/background ratio in one SUSY signal point. (Figure 6.19; the signal Monte Carlo is discussed in Chapter 7). The outcome of of the optimization requires that $R_1 \geq 0.75$ and $R_2 \geq 0.5$.

6.3.3 QCD normalization

The total number of events in the data and Monte Carlo are shown in Table 6.1. In the same table, the number of events after the fiducial tomographic requirement and the 2-Dimensional $\delta\phi$ requirements both in the data and in the Monte Carlo are

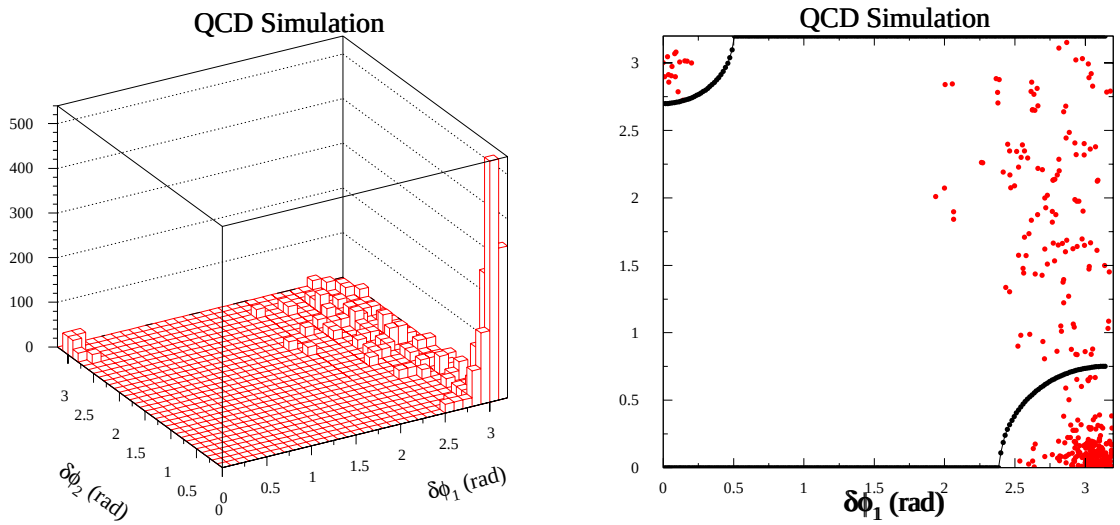

Figure 6.18: QCD50 Simulation: $\delta\phi_2$ versus $\delta\phi_1$ lego and density display showing the 2-dimensional requirement.

given. The derived scale factor (s.f.$_{QCD}$) shown in Figure 6.21 is stable after the Pre-Selection and the fiducial path. In Figure 6.21 the scale factor is shown as a function of $\not\!\!E_T$ after the Pre-Selection and after both fiducial requirements. The fitted value s.f.$_{QCD} = 0.087 \pm 7\%$ (one-parameter fit) is used. Together with the prescale factor and the luminosity correction, the normalization factor applied to the QCD Monte Carlo is $n.f. = 0.087 \times 36.77 \times 0.975 = 3.12 \pm 7.7\%$. Since the QCD simulation is absolutely normalized to the data, there is no systematic uncertainties due to the jet energy scale, the Q^2 or the parton distribution functions. The systematic uncertainty on the QCD background enters in the shape of the $\not\!\!E_T$ tails due to the jet energy resolution, which is discussed in the following section.

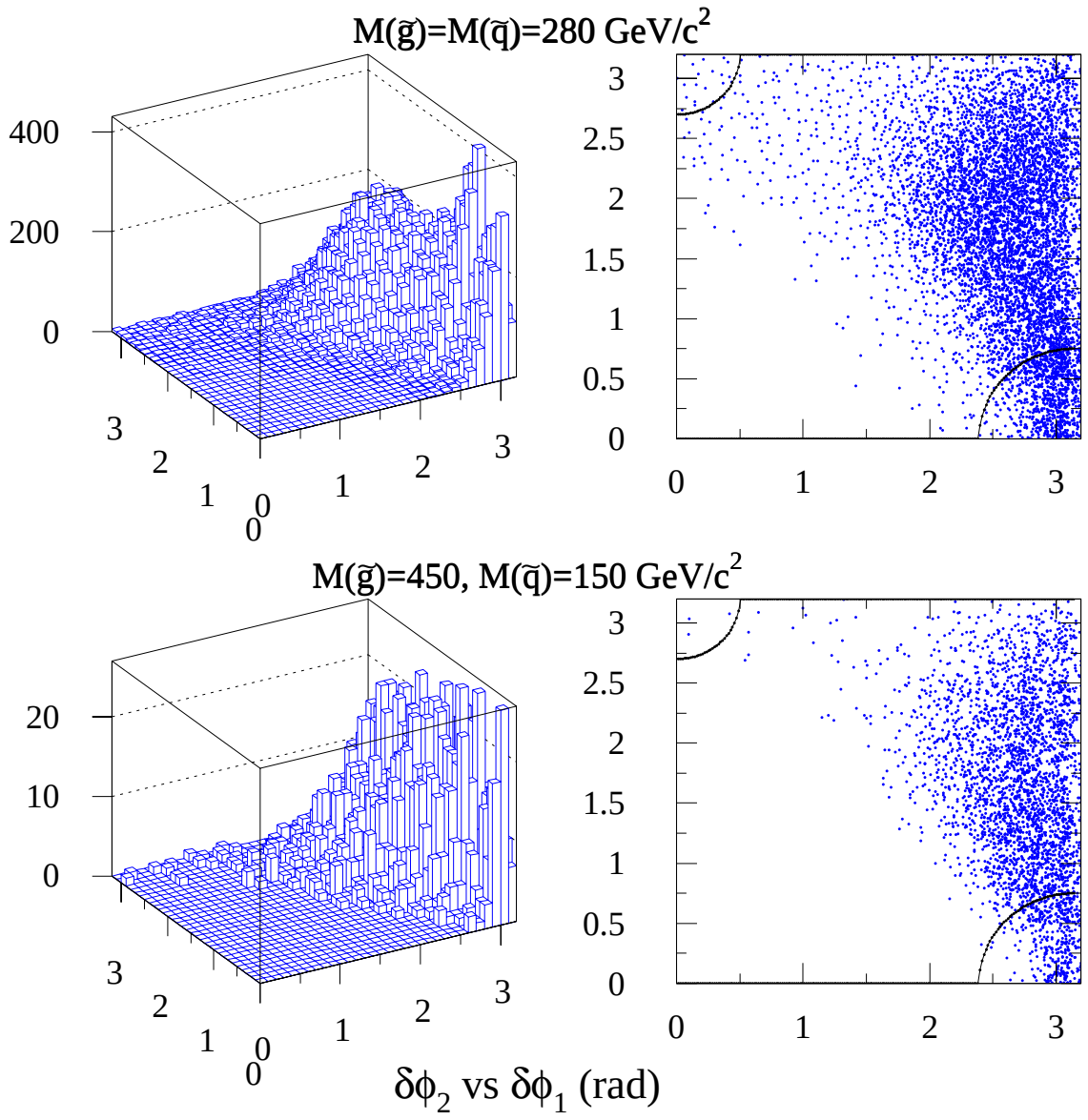

Figure 6.19: Signal Simulation: (up) $m_{\tilde{g}} \approx m_{\tilde{q}}$ =280 GeV/c^2 (down) $m_{\tilde{g}}$ =450 GeV/c^2 $m_{\tilde{q}}$ =150 GeV/c^2. $\delta\phi_2$ versus $\delta\phi_1$ lego and density display showing the 2-d $\delta\phi$ requirement.

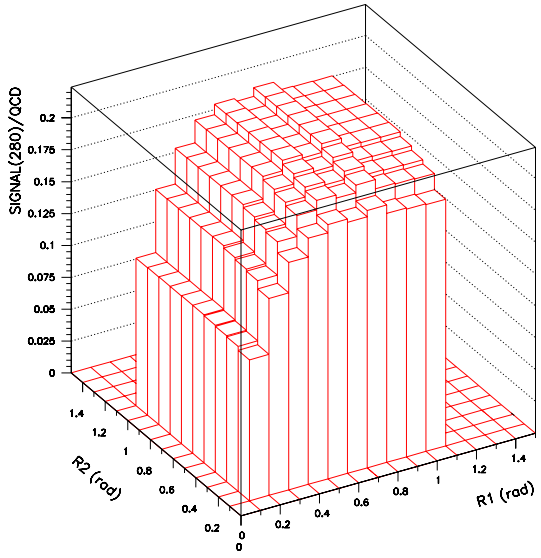

Figure 6.20: R_2, R_1 simultaneous optimization using the ratio Signal/Background for one SUSY point.

Path	JET50	MC50	s.f.$_{QCD}$	$\pm$
	N_{events}			
Pre-Selection	48318	539051	0.0896	4E-03
tomographic fiducial	34701	387542	0.0895	5E-03
2-d $\delta\phi$ fiducial	18809	214569	0.0876	7E-03
prescale	**36.77**$\pm$1.2			
Luminosity correction	0.975			

Table 6.1: Measurement of the stability of the normalization scale factor between jet data and QCD Monte Carlo after the Pre-Selection and the two fiducial requirements.The leading jet is required to be$\geq$70GeV.

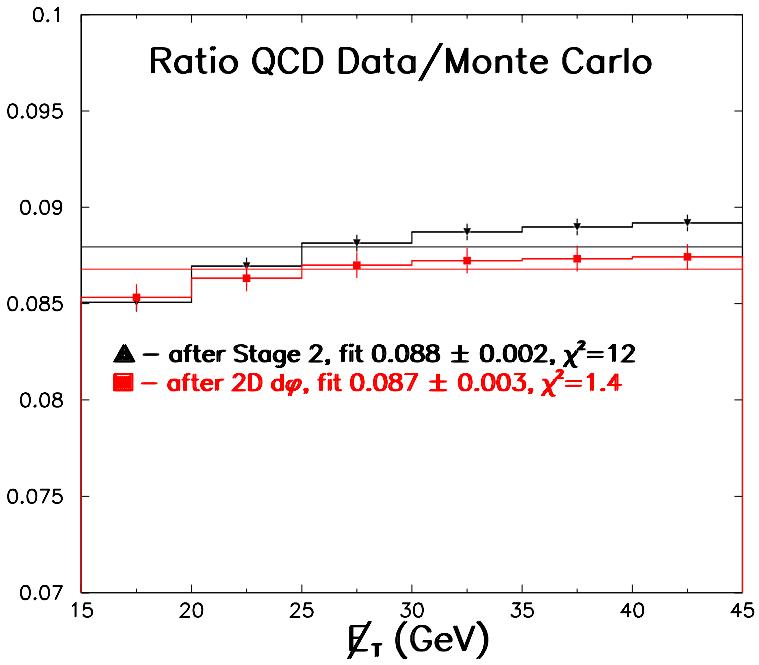

Figure 6.21: QCD Data/Monte Carlo ratio as a function of the $\not\!\!E_T$ after Stage 2 of the Pre-Selection and after the tomographic and 2-d $\delta\phi$ fiducial selection. The lines are one-parameter fits.

Resolution Functions

The shape of the tails of the $\not\!\!E_T$ distribution depends on the response of the CDF detector to jets, *i.e.*, on the the calorimeter energy response and resolution, the uninstrumented regions in the calorimeter (both the ϕ boundaries between modules in the central calorimeter and η boundaries between the central, end wall, plug and forward calorimeters) and fluctuations in the amount of the underlying event falling within the jet cone. Jets of a given "predetector" energy are smeared by a Gaussian function, due to calorimeter resolution, modified by downward and upward-going tails (the result of uninstrumented regions and underlying event respectively). The ratio of measured to true E_T is shown in Figure 6.22 [44] for central jets of true energy 150, 50 and 10 GeV. Energy lost in the uninstrumented regions of the detector generates the downward tail. The underlying event energy in the jet cone produces the upward tail. At low E_T , the upward-going tail is prominent as jet energies approach the level of overlapping energy from the underlying event. At high E_T the downward-going tail is significant. At 50 GeV the two tails are approximately equivalent.

The effect of the jet resolution is studied as follows: in the 2-to-2 QCD Monte Carlo sample (after the Pre-Selection Stages 1 & 2, the fiducial requirement for the second and third jet and the leading jet $E_T > 70$ GeV requirement are applied), the two outgoing partons at the generator level are matched in $\eta - \phi$ with two detector reconstructed jets. The detector simulation implements the response functions (Gaussian + two exponentials). In Figure 6.23, the $\Delta E_T = {E_T}^{measured} - {E_T}^{parton}$ is plotted for the two matched parton-jet pairs. The distribution is fit with two Gaussians and has an exponential downward going tail. The two Gaussians are a result of the fact that in the histogram contains jets from the whole parton energy spectrum landing in the whole η_d region of the detector. The detector response of jets in the

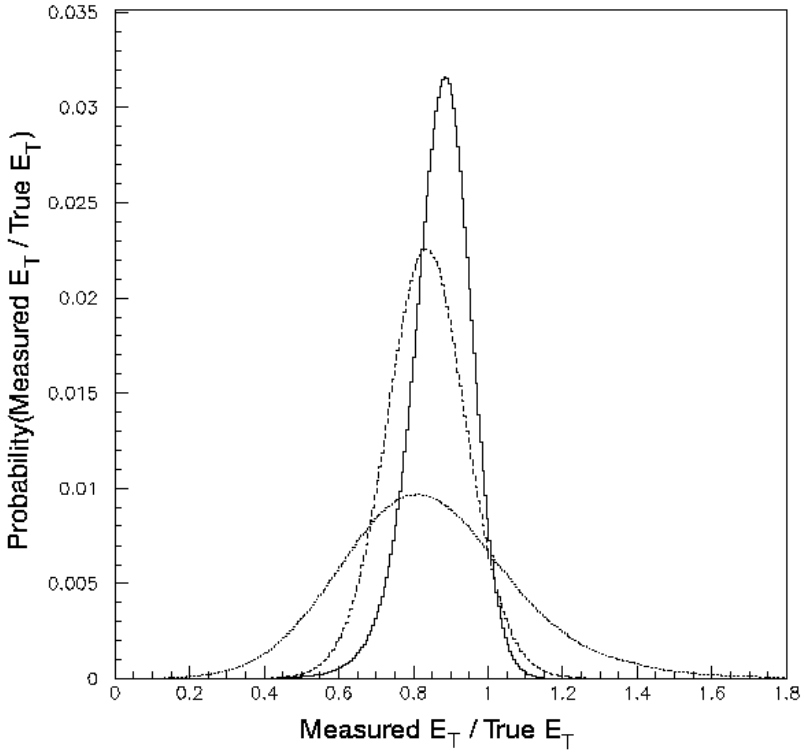

Figure 6.22: The ratio of measured to true jet E_T for jets with a true E_T of 150 GeV (solid), 50 GeV (dashed) and 10 GeV(dotted). The measured E_T is the result of smearing the true E_T by a parameterization of the detector response. [44]

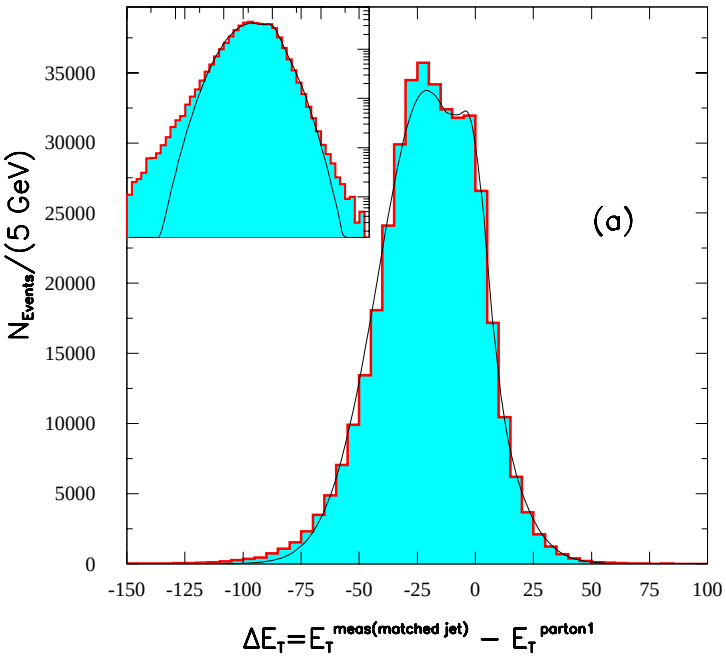

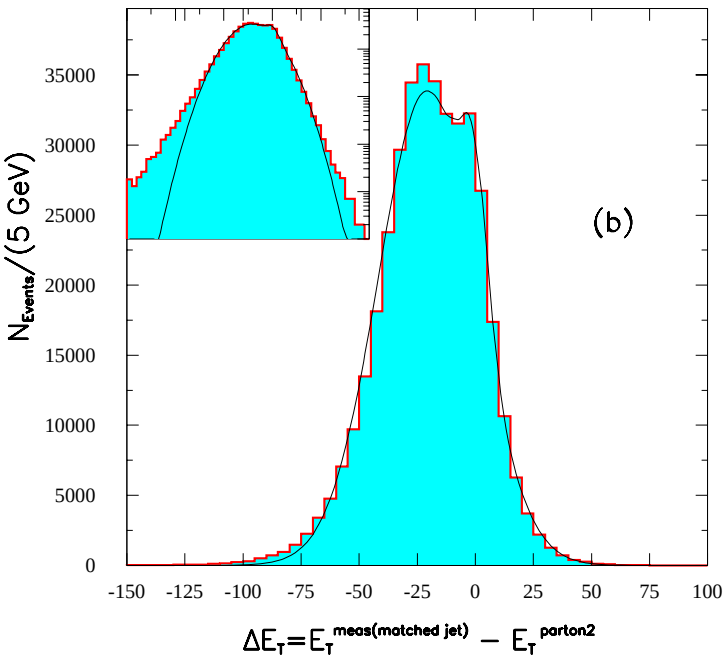

Figure 6.23: $\Delta E_T = {E_T}^{measured} - {E_T}^{parton}$ (a) matched reconstructed jet with outgoing parton 1, (b) matched reconstructed jet with outgoing parton 2.

plug and forward calorimeters is qualitatively similar to the central but the RMS of the distributions are 10-20% larger. The aim is to extract the effect of the response for the under-measured jets. Events with jets falling in the downward exponential tail contribute to the tails of the $\not\!\!E_T$ distribution. For two case studies, 20% (30%) of the events in the downward-going tails are weighted such that they contribute 20% (30%) more in the sample. For the observed jets that are not matched with any of the two outgoing partons, 20% (30%) of the events in the high energy tail of each measured jet E_T distribution are weighted such that they contribute 20% (30%) less in sample. In this manner, the weight of events with grossly under-measured jets is increased (*i.e.*, the downward-going exponential is exaggerated) and the weight of events with very high, well- or over-measured jets (those not matched with a parton) is decreased.

The original $\not\!\!E_T$ distribution spectrum and the one after the weighing scheme is applied are shown in Figure 6.24. The inset zooms in the $\not\!\!E_T$ region above 70 GeV. The ratio of the original $\not\!\!E_T$ distribution over the ones resulting from the 20% and 30% cases gives the positive systematic uncertainty as a function of the $\not\!\!E_T$. The result is shown in Figure 6.24. The average of the two studies for $\not\!\!E_T$=70 GeV is taken as the systematic uncertainty (12%) due to the jet energy resolution.

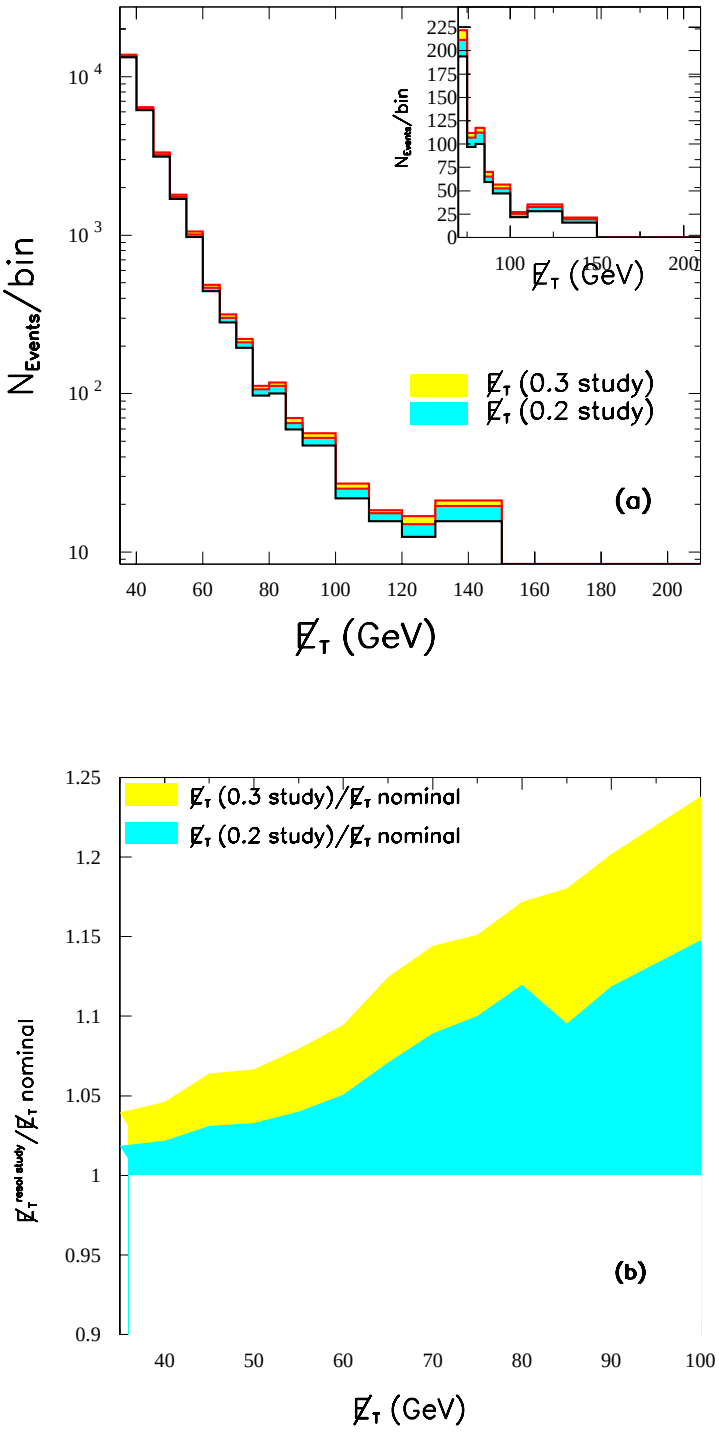

Figure 6.24: QCD simulation (a) $\not\!\!E_T$ nominal spectrum. Overlayed is the spectrum resulting from the 20% and 30% study. The inset is zooming in the region above 70 GeV. (b) The ratio of the $\not\!\!E_T$ after the two studies over the nominal $\not\!\!E_T$ spectrum.

Chapter 7

Squarks and Gluinos

7.1 Introduction

The Standard Model [45] accurately describes all physical phenomena [46] down to scales of $\sim 10^{-16}$ cm. There are many possible ways of extending the Standard Model down to smaller length scales. These include extra gauge interactions, new matter, new levels of compositeness, and supersymmetry (SUSY) [2]. Supersymmetry does not explain the Standard Model but it provides a robust extension to it which is in good agreement with all experimental data. There are various ways to link SUSY with the Standard Model. For simplicity the *minimal* construction is used. This is written in terms of the most general effective Lagrangian for the minimal extension of the Standard Model which is invariant under SUSY transformations up to *soft-breaking* terms.[1]

In Appendix G a brief overview of motivation for SUSY and the minimal construction can be found. The minimal extension of the Standard Model with unbro-

[1]Soft breaking terms generally implies mass terms of $\mathcal{O}(electroweak)$.

ken SUSY (MSSM) is a simple model with fewer free parameters than the Standard Model despite the large number of new fields. It is in the breaking of SUSY that the number of parameters becomes large, but it is only in the breaking of SUSY that the model can attempt to describe nature as observed. In the Standard Model the field content along with the gauge symmetries serve to provide a number of accidental symmetries such as the baryon number B and lepton number L. These also serve to forbid flavor-changing neutral currents (FCNC) arising from Yukawa couplings in loops. The MSSM does not have these properties. The most general MSSM would have the proton decay with a weak-interaction lifetime and large FCNC's. B and L conservation can be postulated in the MSSM by adding a new symmetry which has the effect of eliminating the possibility of B and L violating terms. This new symmetry is called (also Appendix G) "R-parity" [48] where s is the spin:

$$R = (-1)^{3(\mathrm{B-L})+2s} \tag{7.1}$$

and does not allow fast proton decay.

One recurring feature in SUSY is the question of "naturalness" which is the problem besetting the Higgs sector of the Standard Model and provides a reason for low energy supersymmetry [49, 50]. It involves the understanding of small numbers or ratios, such as the ratio of the electroweak to the Planck scale in terms of approximate symmetries. The role of radiative corrections is very important because even if the ratio of two couplings or two masses could be chosen far from unity at tree level, without some approximate symmetry there would be no reason for the ratio to persist beyond tree level. The chiral symmetry of the Standard Model fermions is a classic example of this phenomenon: an approximate symmetry protects the fermion masses

from receiving corrections proportional to heavy mass scales. Without SUSY there is nothing like a chiral symmetry to protect scalar masses from heavy mass scales. With SUSY the chiral symmetry in the fermionic sector protects the scalars too. The naturalness criterion measures the sensitivity of the weak scale to variations of the SUSY parameters at a fundamental scale, for example the GUT scale. In the literature many measures of naturalness have been studied [50, 51, 52, 53, 54] and although a precise absolute measure of fine-tuning is nonsensical, relative fine-tuning can be helpful in selecting, based on the experimental limits, certain models and regions of the parameter space over others. A general result based on the above studies is that the superpartners of the first two generations can be much heavier than the weak scale [2] without extreme fine-tuning in the absence of universality (the hypothesis that all sleptons and squarks have the same mass at the GUT scale). On the other hand, the gluino and the third generation scalars must remain at the electroweak scale and in general should be ≤ 400 GeV/c^2. The subject of fine-tuning will be revisited in Chapter 9 in the context of the interpretation of the results of this analysis.

7.2 Minimal SUSY Particle Content

In the MSSM there are 32 [56] distinct masses corresponding to undiscovered particles. Assuming that the mixing of first- and second-family squarks and sleptons is negligible, the mass eigenstates of the MSSM are listed in Table 7.1. A complete set of Feynman rules for the interactions of these particles with each other and with the Standard Model quarks, leptons, and gauge bosons can be found in References [57, 58].

[2] This solves the problem of FCNCs while at the same time satisfies the naturalness constraints [51, 53, 55].

Name	Spin	R	Mass Eigenstates	Gauge Eigenstates
Higgs bosons	0	$+1$	$h^0\ H^0\ A^0\ H^\pm$	$H_u^0\ H_d^0\ H_u^+\ H_d^-$
squarks	0	-1	$\widetilde{u}_L\ \widetilde{u}_R\ \widetilde{d}_L\ \widetilde{d}_R$ $\widetilde{s}_L\ \widetilde{s}_R\ \widetilde{c}_L\ \widetilde{c}_R$ $\widetilde{t}_1\ \widetilde{t}_2\ \widetilde{b}_1\ \widetilde{b}_2$	$\widetilde{u}_L\ \widetilde{u}_R\ \widetilde{d}_L\ \widetilde{d}_R$ $\widetilde{s}_L\ \widetilde{s}_R\ \widetilde{c}_L\ \widetilde{c}_R$ $\widetilde{t}_L\ \widetilde{t}_R\ \widetilde{b}_L\widetilde{b}_R$
sleptons	0	-1	$\widetilde{e}_L\ \widetilde{e}_R\ \widetilde{\nu}_e$ $\widetilde{\mu}_L\ \widetilde{\mu}_R\ \widetilde{\nu}_\mu$ $\widetilde{\tau}_1\ \widetilde{\tau}_2\ \widetilde{\nu}_\tau$	$\widetilde{e}_L\ \widetilde{e}_R\ \widetilde{\nu}_e$ $\widetilde{\mu}_L\ \widetilde{\mu}_R\ \widetilde{\nu}_\mu$ $\widetilde{\tau}_L\ \widetilde{\tau}_R\ \widetilde{\nu}_\tau$
neutralinos	1/2	-1	$\widetilde{\chi}_1^0\ \widetilde{\chi}_2^0\ \widetilde{\chi}_3^0\ \widetilde{\chi}_4^0$	$\widetilde{B}^0\ \widetilde{W}^0\ \widetilde{H}_u^0\ \widetilde{H}_d^0$
charginos	1/2	-1	$\widetilde{\chi}_1^\pm\ \widetilde{\chi}_2^\pm\ \widetilde{\chi}_3^\pm$	$\widetilde{W}^\pm\ \widetilde{H}_u^+\ \widetilde{H}_d^-$
gluino	1/2	-1	$\widetilde{g}$	$\widetilde{g}$
gravitino/ goldstino	3/2	-1	$\widetilde{G}$	$\widetilde{G}$

Table 7.1: The Minimal Supersymmetric Standard Model particles.

In the minimal supergravity models (mSUGRA) (where SUSY breaking is mediated through gravitational interactions to the physical sector of the theory [2]) it is assumed that the gauge couplings unify at a GUT scale and that supersymmetry breaking occurs with universal soft breaking terms that are related to the electroweak scale using the Renormalization Group (RG, [59, 60] and Appendix G). The parameters of the model are M_0^2 (the common scalar mass at the GUT scale), $M_{1/2}$, (the common gaugino mass at the GUT scale), A_0 (the common soft trilinear coupling at the GUT scale), μ (the Higgsino mass mixing parameter), and B_0 (the soft bilinear coupling at the GUT scale). After evolving the soft terms down to the electroweak scale using the Renormalization Group equations and requiring that the scalar potential gives correct electroweak symmetry breaking, the $|\mu|$ and B_0 can be traded for one parameter $\tan\beta$ (the ratio of the Higgs vacuum expectation values at the electroweak scale) and the remainder parameter is the sign of μ. To a reasonable approximation, the entire mass spectrum in minimal supergravity models is determined

by only five unknown parameters: M_0^2, $M_{1/2}$, A_0, $\tan\beta$, and sign(μ). Such a scenario provides a favorite mechanism for SUSY breaking mediation: It simplifies the MSSM spectrum, it has a small number of input parameters, it is automatic in the sense that any theory that connects gravity to a supersymmetric field theory would seemingly have to include supergravity, and at lowest order it produces the kind of universal masses necessary to solve FCNC problems.

In this analysis when mSUGRA is used the average mass of the $\tilde{q}$ of the first two families and sbottom is taken to be the degenerate $m_{\tilde{q}}$. Explicitly top squark production gets zero weight in the analysis and the cross section calculation reflects this. The reason is that the top squark mass is expected to be lower that the first two generation scalar quarks because of mixing effects. Alternative search signatures involving b and c quark tagging are used for stop searches [6]. Although the scalar bottom also has this feature, particularly for high values of $\tan\beta$ it is analyzed within mSUGRA so that the analysis can be directly compared with previous results that used the same model and assumptions.

In a more flexible MSSM model also used in this analysis, grand unification constraints are assumed in the neutralino and chargino masses. The scalar particle soft masses are input parameters and the physical masses are slightly different because of other contributions and mixings for third generation sparticles. The input parameters are $m_{\tilde{g}}$, μ, A, $\tan\beta$, and the soft squark masses $m_{\tilde{q}_i}$, the slepton masses $m_{\tilde{\ell}_i}$ and the squark and slepton mixing parameters $A_{t(b)(\tau)}$. When this model is used the third family squark production (both scalar top and bottom) is getting zero weight in the analysis and the calculation of the production cross section reflects this. This is to avoid third generation mixing effects. Generally in the standard minimal supersymmetry scenarios with R-Parity conservation [2]:

- The Lightest Supersymmetric Particle (LSP) is the lightest neutralino $\widetilde{\chi}_1^0$.
- The gluino is heavier than the lighter neutralinos and charginos. [3]
- The squarks of the first and second families are nearly degenerate and heavier than the sleptons.
- The squarks of the first two families cannot be lighter than about 0.8 times the mass of the gluino in minimal supergravity models. This is why the mSUGRA model is used above the diagonal in the $m_{\widetilde{q}} - m_{\widetilde{g}}$ mass plane and the MSSM is used below the diagonal.
- The lighter stop $\widetilde{t}_1$ and the lighter sbottom $\widetilde{b}_1$ are probably the lightest squarks.
- The lightest charged slepton is probably a stau $\widetilde{\tau}_1$.
- The lightest neutral Higgs boson h^0 should be lighter than about 150 GeV, and may be much lighter than the other Higgs scalar mass eigenstates A^0, $H^{\pm}$, H^0 [61].

7.2.1 The gluino

The gluino is a color octet fermion, so it cannot mix with any other particle in the MSSM, even if R-parity is violated. In minimal supergravity models the gluino mass parameter M_3 is related to the other two gaugino mass parameters M_1 (bino) and M_2 (wino) (by equation (G.24))

$$M_3 = \frac{\alpha_S}{\alpha} \sin^2 \theta_W M_2 = \frac{3}{5} \frac{\alpha_S}{\alpha} \cos^2 \theta_W M_1 \tag{7.2}$$

[3] This is true in the case of the "standard" gaugino mass relation $M_1/g_1^2 \simeq M_2/g_2^2 \simeq M_2/g_2^2 \simeq M_{1/2}/g_{GUT}^2$, (Equation Appendix G.24).

where θ_W is the standard EWK Weinberg angle, at any RG scale. For $\alpha_S = 0.118$, $\alpha = 1/128$, $\sin^2\theta_W = 0.23$, the rough prediction is that

$$M_3 : M_2 : M_1 \approx 3.3 : 1 : 0.5 \tag{7.3}$$

at the electroweak scale. It is suspected that the gluino should be much heavier than the lighter neutralinos and charginos. For more precise estimates, the fact that the parameter M_3 is a running mass with an implicit dependence on the RG scale Q is taken into account. The gluino is a strongly interacting particle and M_3 runs quickly with Q [Equation. (G.22)]. A useful physical quantity is the RG scale-independent mass $m_{\tilde{g}}$ at which the renormalized gluino propagator has a pole. Including one-loop corrections to the gluino propagator due to gluon exchange and quark-squark loops, the pole mass is given in terms of the running mass by [62]

$$m_{\tilde{g}} = M_3(Q)\Big(1 + \frac{\alpha_S}{4\pi}[15 + 6\ln(Q/M_3) + \sum A_{\tilde{q}}]\Big) \tag{7.4}$$

where

$$A_{\tilde{q}} = \int_0^1 dx\, x \ln[x m_{\tilde{q}}^2/M_3^2 + (1-x)m_q^2/M_3^2 - x(1-x)]. \tag{7.5}$$

The sum in equation (7.4) is over all 12 squark-quark supermultiplets, and effects due to squark mixing are neglected. Requiring $m_{\tilde{g}}$ to be independent of Q in equation (7.4) reproduces the one-loop RG equation for $M_3(Q)$ in equation (G.22). The correction terms proportional to α_S in expression (7.4) can be quite significant because the gluino is strongly interacting, with a large group theory factor [the 15 in expression (7.4)] due to its color octet nature, and because it couples to all the squark-quark pairs. There are similar corrections which relate the running masses of

all the other MSSM particles to their physical masses. These have been evaluated at one-loop order in Reference [63].

7.2.2 The squark and slepton mass spectrum

From the RG analysis in mSUGRA, analytical expressions can be obtained for the squark and slepton mass parameters when the corresponding Yukawa couplings are negligible (*i.e.* for the first two generations). For a GUT universal scalar mass M_0 and gaugino mass $M_{1/2}$ at the scale the expressions for the squark and slepton masses are [64]:

$$m_{\tilde{f}}^2 = M_0^2 + \sum_{i=1}^{3} f_i M_{1/2}^2 + (T_{3,\tilde{f}} - e_{\tilde{f}} \sin^2 \theta_w) M_Z^2 \cos 2\beta \ , \tag{7.6}$$

where the f_i are (positive) constants [65] that depend on the evolution of the gauge couplings. There is a contribution f_i from each interaction of the $SU(3)\times SU(2)\times U(1)$ of the Standard Model. $T_{3,\tilde{f}}$ is the SU(2) quantum number and $e_{\tilde{f}}$ is the electromagnetic charge of the sfermion.

The squark mass spectrum of the third generation is more complicated because the effects of the third generation Yukawa couplings need not be negligible and there can be substantial mixing between the left and right top squark fields (and left and right bottom squark fields for large $\tan\beta$) so that the mass eigenstates are linear combinations of the left and right sfermion fields.

The relations for the sleptons at the scale M_{EW} which determine the mass eigen-

states are given by (notation from Table G.3),:

$$m^2_{L_{1,2}} \simeq m^2_{L_3} \simeq M_0^2 + 0.5 M_{1/2}^2 \,; \qquad m^2_{\bar{e}_{1,2}} \simeq m^2_{\bar{e}_3} \simeq M_0^2 + 0.15 M_{1/2}^2 . \tag{7.7}$$

The only Yukawa coupling that might be important in the evolution of the slepton masses is the tau Yukawa coupling when $\tan\beta \geq 40$. In that case, the third generation slepton mass parameters also receive non–negligible contributions in their running which can modify the above expressions. If M_0 and $M_{1/2}$ are of the same order of magnitude, physical slepton masses are dominately given by M_0. The $\tilde{\nu}$ mass is fixed by a sum rule

$$m^2_{\tilde{\nu}_\ell} = m^2_{\tilde{\ell}_L} + M_W^2 \cos 2\beta \ , \tag{7.8}$$

which follows directly from $SU(2)$ gauge symmetry.

The squark mass parameters have a stronger dependence on the common gaugino mass $M_{1/2}$ because of color. For the first and second generation squarks, the left– and right–handed soft SUSY–breaking parameters at M_{EW} are given approximately by (notation from Table G.3):

$$m^2_{Q_{1,2}} \simeq M_0^2 + 6.3 M_{1/2}^2 \,; \qquad m^2_{\bar{u}_{1,2}} \simeq M^2_{\bar{d}_{1,2}} \simeq M_0^2 + 5.8 M_{1/2}^2 \,. \tag{7.9}$$

In general, the squarks are heavier than the sleptons and the lightest neutralino and chargino. The first and the second generation squark soft SUSY–breaking parameters have the same value for squarks with the same quantum numbers since the contributions from the Yukawa couplings is negligible. A detailed analysis of the SUSY mass spectra at the weak scale can be found in Reference [65] and References therein.

$\widetilde{q}\overline{\widetilde{q}}$ production:	$q_i + \bar{q}_j \longrightarrow \widetilde{q}_k + \overline{\widetilde{q}}_l, \quad g + g \longrightarrow \widetilde{q}_i + \overline{\widetilde{q}}_i$
$\widetilde{q}\widetilde{q}$ production:	$q_i + q_j \longrightarrow \widetilde{q}_i + \widetilde{q}_j$ and $c.c.$
$\widetilde{g}\widetilde{g}$ production:	$q_i + \bar{q}_i \longrightarrow \widetilde{g} + \widetilde{g}, \quad g + g \longrightarrow \widetilde{g} + \widetilde{g}$
$\widetilde{q}\widetilde{g}$ production:	$q_i + g \longrightarrow \widetilde{q}_i + \widetilde{g}$ and $c.c.$

Table 7.2: Hadroproduction of squarks and gluinos.

7.3 Squark and Gluino Production

The hadroproduction of squarks and gluinos in leading order (LO) proceeds through the partonic reactions in Table 7.2.

The chiralities of the squarks $\widetilde{q} = (\widetilde{q}_L, \widetilde{q}_R)$ are not noted explicitly. The indices i–j indicate the flavors of the quarks and squarks. Also charge-conjugated processes ($c.c.$) are possible, related to the $\widetilde{q}\widetilde{q}$ and $\widetilde{q}\widetilde{g}$ production. The Feynman diagrams corresponding to these partonic reactions are displayed in Figure 7.1. The momenta of the two partons in the initial states are denoted by k_1 and k_2, those of the particles in the final states by p_1 and p_2. The production of squark-antisquark final states requires quark-antiquark 7.1(a) or gluon-gluon 7.1(b) initial states. Squark pairs are only produced from quark-pair 7.1(c) initial states. Gluino pairs are produced from quark-antiquark 7.1(d) and gluon-gluon 7.1(e) initial states. The squark-gluino final states are produced from quark-gluon 7.1(f) intitial states.

The relative yields of $\widetilde{q}\overline{\widetilde{q}}$, $\widetilde{q}\widetilde{q}$, $\widetilde{g}\widetilde{g}$ and $\widetilde{q}\widetilde{g}$ final states in $p\bar{p}$ collisions at the Tevatron are shown for a set of mass parameters in Figure 7.2. The relative yields depend strongly on the mass ratio $m_{\widetilde{q}}/m_{\widetilde{g}}$. If squarks are lighter than gluinos, the valence partons give the dominant yield of squark-antisquark/squark-squark pairs. If the gluinos are the lighter of the two species, their production is the most copious. The

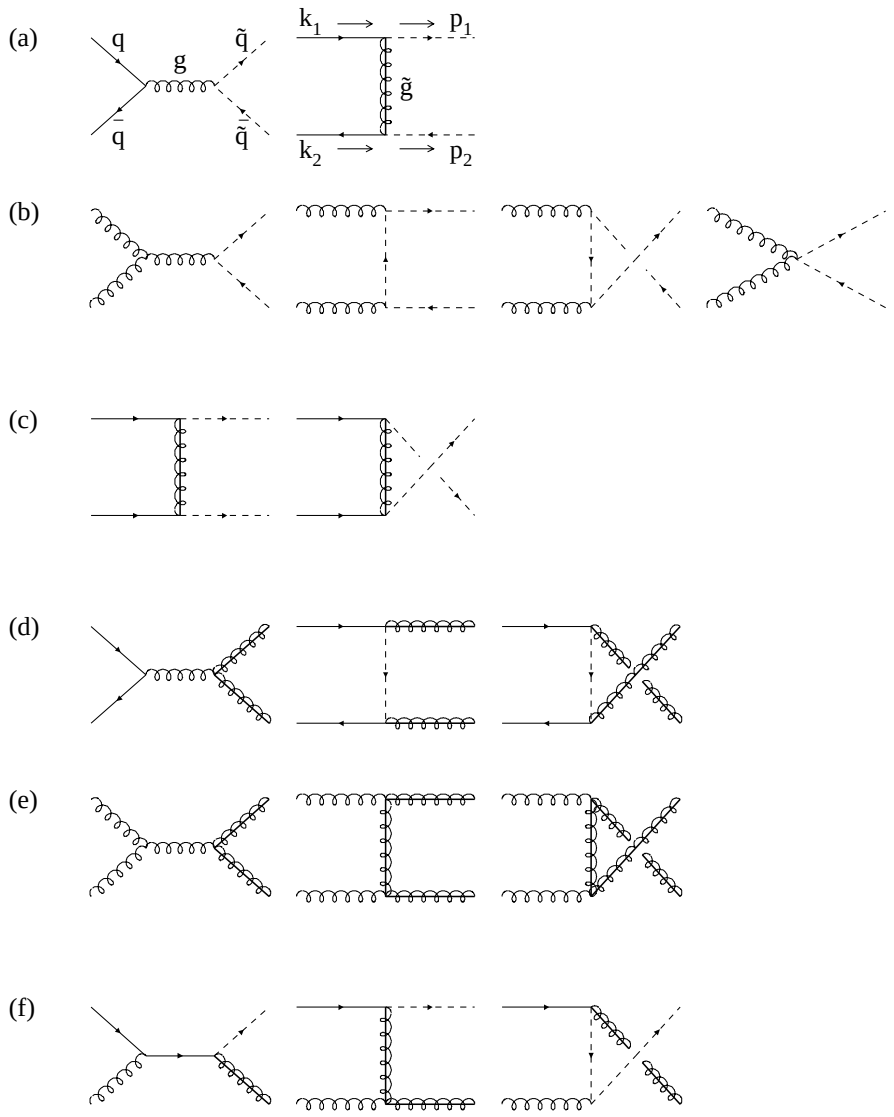

Figure 7.1: Feynman diagrams for the production of squarks and gluinos in lowest order. The diagrams without and with crossed final-state lines [e.g.in (b)] represent t- and u-channel diagrams, respectively. The diagrams in (c) and the last diagram in (d) are a result of the Majorana nature of gluinos. Note that some of the above diagrams contribute only for specific flavors and chiralities of the squarks [66].

relative yields of $\tilde{q}\bar{\tilde{q}}$, $\tilde{q}\tilde{q}$, $\tilde{g}\tilde{g}$ and $\tilde{q}\tilde{g}$ final states for all the signal points generated for this analysis are given in Appendix G. The virtual (one-loop) amplitudes include self-energy corrections, vertex corrections, and box diagrams. For the virtual particles inside loops the complete supersymmetric QCD spectrum is used: gluons, gluinos, all quarks, and all squarks. The divergences in the virtual corrections are regularlized by performing the calculations in $n = 4-2\epsilon$ dimensions [66]. These divergences consist of ultraviolet, infrared (IR), and collinear divergences (also called mass singularities) and are included in the next-to-leading order (NLO) calculation. The NLO evaluation of squark and gluinos production includes also the corrections from real-gluon radiation which are obtained from the LO partonic reactions by adding a gluon to the final state:

$q_i + \bar{q}_j \longrightarrow \tilde{q}_k + \bar{\tilde{q}}_l + g, \qquad g + g \longrightarrow \tilde{q}_i + \bar{\tilde{q}}_i + g$

$q_i + q_j \longrightarrow \tilde{q}_i + \tilde{q}_j + g, \qquad q_i + \bar{q}_i \longrightarrow \tilde{g} + \tilde{g} + g$

$g + g \longrightarrow \tilde{g} + \tilde{g} + g, \qquad q_i + g \longrightarrow \tilde{q}_i + \tilde{g} + g$

The charge-conjugate final states, which are not given explicitly, are included in the hadronic cross-section calculation [66]. A representative set of Feynman diagrams, contributing to the real-gluon amplitude, is given in Figure 7.3. The momenta of the initial-state partons are denoted by k_1, k_2, while the particles in the final states carry momenta p_1, p_2, and k_3. There are partonic reactions that are only realized in next-to-leading order of the SUSY-QCD perturbative expansion which involve final states with an additional massless (anti)quark. In such reactions, explicit particle poles arise in the allowed phase space that require the isolation of on-shell squark and gluino production and the subtraction of the poles [66]. Reactions that involve the radiation of a massless (anti)quark are :

$g + \bar{q}_j \longrightarrow \tilde{q}_k + \bar{\tilde{q}}_l + \bar{q}_i, \qquad q_i + g \longrightarrow \tilde{q}_k + \bar{\tilde{q}}_l + q_j$

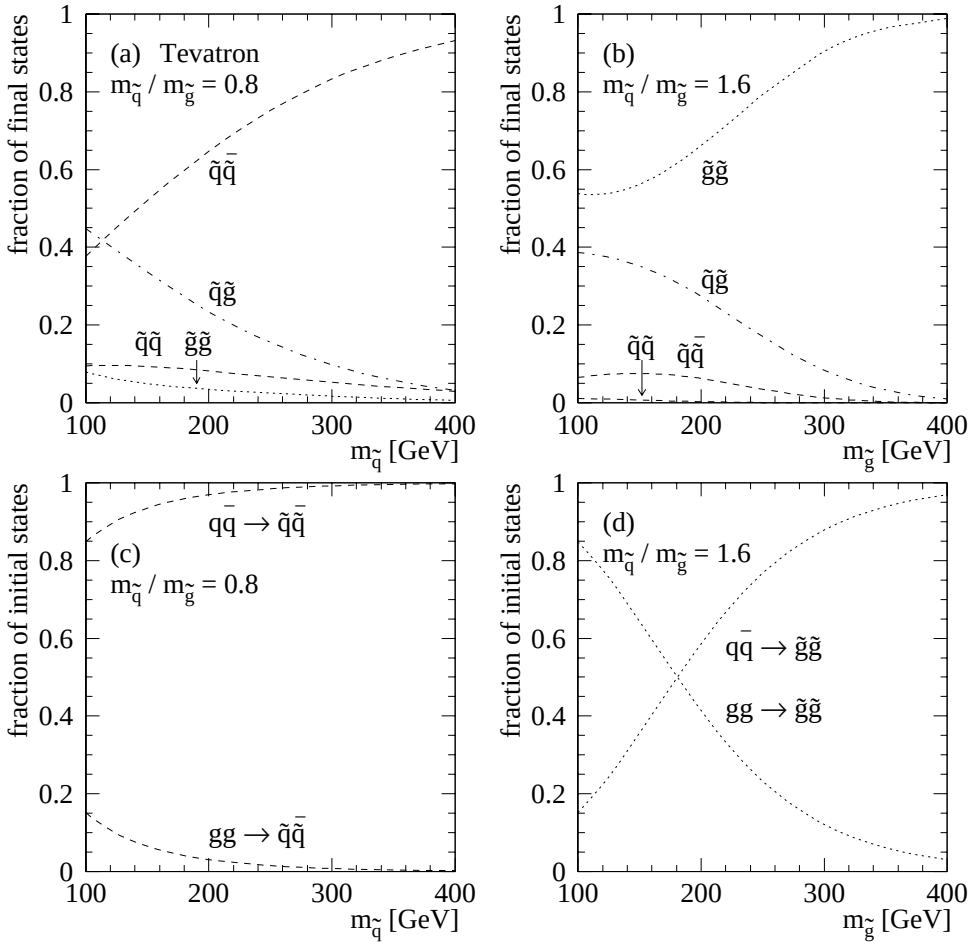

Figure 7.2: The relative yields of squarks and gluinos in the final states at the Tevatron. The mass ratio $m_{\tilde{q}}/m_{\tilde{g}}$ is chosen to be (a) 0.8 and (b) 1.6. Also shown are the leading parton contributions for (c) $\tilde{q}\bar{\tilde{q}}$ and (d) $\tilde{g}\tilde{g}$ final states. Parton densities: GRV 94 [67], renormalization and factorization scale $Q = m_{\tilde{q}}$ for squarks, $Q = m_{\tilde{g}}$ for gluinos, and $Q = (m_{\tilde{q}} + m_{\tilde{g}})/2$ for squark–gluino pairs.[66]

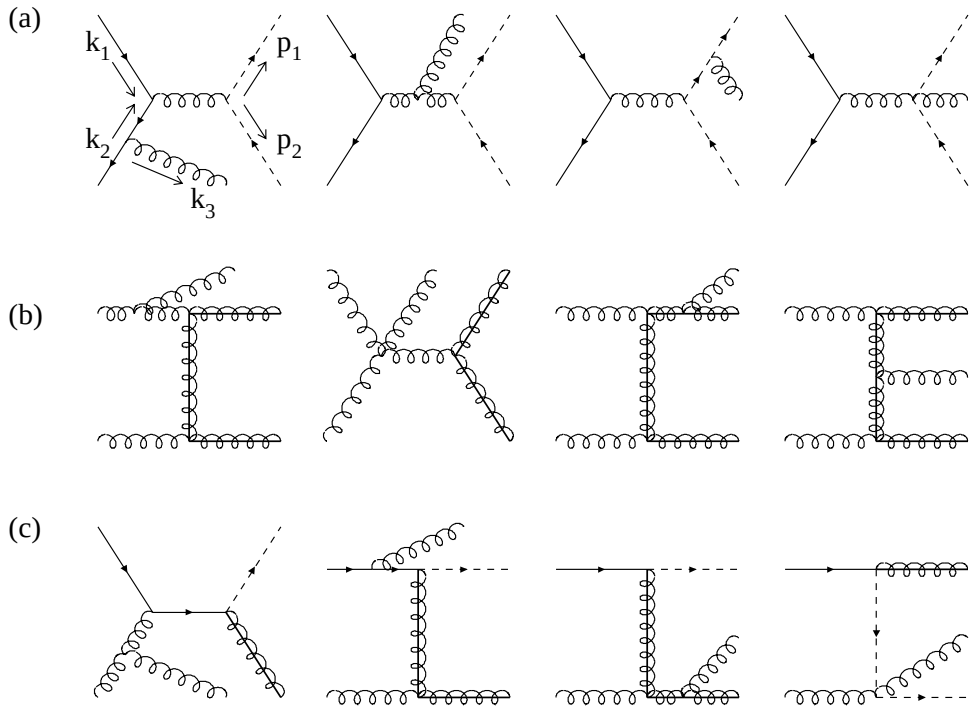

Figure 7.3: A representative set of Feynman diagrams corresponding to real-gluon radiation: (a) squark–antisquark production, (b) gluino-pair production and (c) squark–gluino production (c)[66].

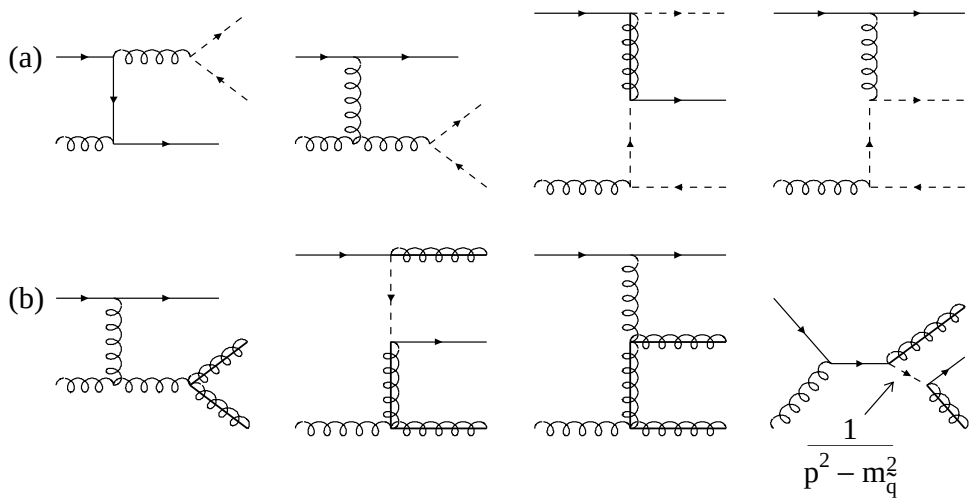

Figure 7.4: Selected set of Feynman diagrams for subprocesses that involve additional massless quarks in the final state. (a) Squark-antisquark production, and (b) gluino–gluino production [66].

$$q_i + g \longrightarrow \tilde{q}_i + \tilde{q}_j + \bar{q}_j, \qquad g + \bar{q}_i \longrightarrow \tilde{g} + \tilde{g} + \bar{q}_i$$

$$q_i + g \longrightarrow \tilde{g} + \tilde{g} + q_i, \qquad g + g \longrightarrow \tilde{q}_i + \tilde{g} + \bar{q}_i$$

$$q_i + \bar{q}_j \longrightarrow \tilde{q}_k + \tilde{g} + \bar{q}_l, \qquad q_i + q_j \longrightarrow \tilde{q}_k + \tilde{g} + q_l.$$

In Figure 7.4 some selected Feynman diagrams for (a) the squark-antisquark-quark final state and (b) the gluino-gluino-quark final state. The momenta of the initial-state partons are denoted by k_1, k_2, while those of the particles in the final states are denoted by p_1, p_2, and k_3. In the next to leading order calculation of the squark, gluino production cross section the renormalization scale (Q) dependence is reduced by a factor of 2.5-4 compared with leading-order calculations [66] (for different $\frac{m_{\tilde{q}}}{m_{\tilde{g}}}$ ratios), and the theoretical predictions of the cross-sections are stable. The shape of the differential distributions in transverse momentum and rapidity of one of the outgoing squarks or gluinos is hardly affected by the NLO corrections [66]. In this analysis the PROSPINO [69] next-to-leading-order calculator is used for the production cross section considering the five light mass-degenerate quark flavors (using mSUGRA). In

the MSSM analysis where only the first two-family light quark flavors are used the cross section is calculated by subtracting [68] the sbottom related production cross section [4].

7.3.1 Decays

A brief qualitative overview of the decay patterns of sparticles in the MSSM, assuming that R-parity is exactly conserved is given. The possible decays of neutralinos, charginos, sleptons, squarks, and the gluino are discussed. The lightest neutralino $\widetilde{\chi}_1^0$ is the Lightest Supersymmetric Particle, and all decay chains end up containing the $\widetilde{\chi}_1^0$ in the final state.

7.3.2 Squark decays

If the decay $\widetilde{q} \to q\widetilde{g}$ is kinematically allowed, it will always dominate, because the quark-squark-gluino vertex has QCD strength. Otherwise, the squarks can decay into a quark plus neutralino or chargino: $\widetilde{q} \to q\widetilde{\chi}_i^0$ or $q'\widetilde{\chi}_i^{\pm}$. The direct decay to the LSP $\widetilde{q} \to \widetilde{\chi}_1^0$ is always kinematically favored, and for right-handed squarks it can dominate because $\widetilde{\chi}_1^0$ is mostly bino. The left-handed squarks may strongly prefer to decay into heavier charginos or neutralinos instead, *i.e.* $\widetilde{q} \to q\widetilde{\chi}_2^0$ or $q'\widetilde{\chi}_1^{\pm}$, because the relevant squark-quark-wino couplings are much bigger than the squark-quark-bino couplings. Squark decays to higgsino-like charginos and neutralinos are less important, except in

[4] The calculation for stop production is used for sbottoms. The sbottom mass is taken to be equal to the squark masses of the first 4 flavors and zero mixing angle is used. The cross sections for $\widetilde{b}_1$ and $\widetilde{b}_2$ pair production are calculated. (dominantly produced from light $q\bar{q}$ and gg initial states). This sum is subtracted from the cross sections for squark-antisquark production of PROSPINO(with 5 flavors). This is sufficiently precise since contributions of the b densities of the proton compared to the light parton densities can be neglected (which also means that sbottom-sbottom and sbottom-gluino production is suppressed numerically, since these require b densities in the initial states).

the cases of stops and sbottoms which have sizeable Yukawa couplings. The gluino, chargino or neutralino resulting from the squark decay will in turn decay, and so on, until a final state containing $\widetilde{\chi}_1^0$ is reached. This can result in very numerous and complicated decay chain possibilities called cascade decays.

7.3.3 Gluino decays

The decay of the gluino can only proceed through an on-shell or a virtual squark. If two-body decays $\widetilde{g} \to q\widetilde{q}$ are open, they will dominate, because the relevant gluino-quark-squark coupling has QCD strength. Since the top and bottom squarks can easily be much lighter than all of the other squarks, it is quite possible that $\widetilde{g} \to t\widetilde{t}_1$ and/or $\widetilde{g} \to b\widetilde{b}_1$ are the only available two-body decay mode(s) for the gluino, in which case they will dominate over all others. If instead all of the squarks are heavier than the gluino, the gluino will decay only through off-shell squarks, so $\widetilde{g} \to qq'\widetilde{\chi}_i^0$ and $qq'\ \widetilde{\chi}_i^\pm$. The squarks, neutralinos and charginos in these final states will then decay as discussed next, so there are very many competing gluino decay chains. These cascade decays can have final-state branching fractions that are individually small and quite sensitive to the parameters of the model.

7.3.4 Neutralino and chargino decays

Each neutralino and chargino contains at least a small admixture of the electroweak gauginos $\widetilde{B}$, $\widetilde{W}^0$ or $\widetilde{W}^\pm$ *i.e.* $\widetilde{\chi}_i^0$ and $\widetilde{\chi}_i^\pm$ inherit couplings of weak interaction strength to (scalar, fermion) pairs. If sleptons or squarks are sufficiently light, a neutralino or chargino will decay into lepton+slepton or quark+squark (antiparticles implied too). Since sleptons are probably lighter than squarks, the lepton+slepton final states are more likely. A neutralino or chargino may also decay into any lighter neutralino or

chargino plus a Higgs scalar or an electroweak gauge boson, because they inherit the gaugino-higgsino-Higgs and $SU(2)_L$ gaugino-gaugino-vector boson couplings of their components. So, the possible two-body decay modes for neutralinos and charginos in the MSSM are:

$\widetilde{\chi}_i^0 \to Z\widetilde{\chi}_j^0, \quad W\widetilde{\chi}_i^{\pm}, \quad h^0\widetilde{\chi}_j^0, \quad \ell\widetilde{\ell}, \; \nu\widetilde{\nu}, \quad [A^0 \; \widetilde{\chi}_j^0 \quad , \; H^0\widetilde{\chi}_j^0, \quad H^{\pm}\widetilde{\chi}_i^{\pm}, \; q\widetilde{q}];$

$\widetilde{\chi}_i^{\pm} \to W\widetilde{\chi}_j^0, \quad Z\widetilde{\chi}_1^{\pm}, \quad h^0\widetilde{\chi}_1^{\pm}, \quad \ell\widetilde{\nu}, \; \nu\widetilde{\ell}, \quad [A^0\widetilde{\chi}_1^{\pm}, \quad H^0\widetilde{\chi}_1^{\pm}, \quad H^{\pm}\widetilde{\chi}_j^0, \quad q\widetilde{q}']$

using a generic notation ν, ℓ, q for neutrinos, charged leptons, and quarks. The final states in brackets are the less kinematically-plausible ones. (h^0 is required to be light and it is the most likely of the Higgs scalars to appear in these decays.) For the heavier neutralinos and charginos ($\widetilde{\chi}_3^0$, $\widetilde{\chi}_4^0$ and $\widetilde{\chi}_2^{\pm}$), one or more of the decays above is likely to be kinematically allowed. If all of these two-body modes are kinematically forbidden for a given chargino or neutralino, especially in the case of $\widetilde{\chi}_1^{\pm}$ and $\widetilde{\chi}_2^0$ decays then the three-body decays $\widetilde{\chi}_1^0 \to ff\widetilde{\chi}_j^0$, $\widetilde{\chi}_i^0 \to ff'\widetilde{\chi}_i^{\pm}$, $\widetilde{\chi}_i^{\pm} \to f\, f'\widetilde{\chi}_j^0$ and $\widetilde{\chi}_2^{\pm} \to ff'\widetilde{\chi}_1^{\pm}$ are expected through the same (but now off-shell) gauge bosons, Higgs scalars, sleptons, and squarks that appear in the two-body decays. f is generic notation for a lepton or quark, with f and f' belonging to the same $SU(2)_L$ multiplet.

7.3.5 Slepton decays

Sleptons have two-body decays into a lepton and a chargino or neutralino, because of the gaugino admixture of the latter. The two-body decays $\widetilde{\ell} \to \ell\widetilde{\chi}_i^0$, $\widetilde{\ell} \to \nu\widetilde{\chi}_i^{\pm}$, $\widetilde{\nu} \to \nu\widetilde{\chi}_i^0$, and $\widetilde{\nu} \to \ell\widetilde{\chi}_i^{\pm}$ are of weak interaction strength. The direct decays $\widetilde{\ell} \to \ell\widetilde{\chi}_1^0$ and $\widetilde{\nu} \to \nu\widetilde{\chi}_1^0$ are (essentially[5]) always kinematically allowed if $\widetilde{\chi}_1^0$ is the LSP. If

[5] An exception occurs if the mass difference $m_{\widetilde{\tau}_1} - m_{\widetilde{\chi}_1^0}$ is less than m_τ

the sleptons are sufficiently heavy, then the two-body decays to charginos and heavier neutralinos can be important, especially $\widetilde{\ell} \to \nu\widetilde{\chi}_1^{\pm}$, $\widetilde{\ell} \to \ell\widetilde{\chi}_2^0$, and $\widetilde{\nu} \to \ell\widetilde{\chi}_1^{\pm}$. The right-handed sleptons do not have a coupling to the $SU(2)_L$ gauginos, so they typically prefer the direct decay $\widetilde{\ell}_R \to \ell\widetilde{\chi}_1^0$, if $\widetilde{\chi}_1^0$ is bino-like. The left-handed sleptons may prefer to decay to charginos and heavier neutralinos (if it is kinematically possible and if the $\widetilde{\chi}_1^{\pm}$ and $\widetilde{\chi}_2^0$ are mostly wino) rather than directly to the LSP. This is because the slepton-lepton-wino interactions are proportional to the $SU(2)_L$ gauge coupling g, whereas the slepton-lepton-bino interactions are proportional to the much smaller $U(1)_Y$ coupling g'.

7.3.6 Kinematics

In Figure 7.5 the signal points generated for this analysis are shown in the $m_{\widetilde{q}}$–$m_{\widetilde{g}}$ plane. The plane is loosely divided into four regions A,B,C and D as indicated. For the points shown on Table 7.3 the following distributions are presented in Figures 7.6 through 7.13:

- The $\not\!\!E_T$ at the generator level (calculated vectorially from the E_T of the two $\widetilde{\chi}_1^0$ and all neutrinos in the final state) overlayed with the $\not\!\!E_T$ after the detector simulation.
- The $H_T = E_{T2} + E_{T3} + \not\!\!E_T$ where 2, 3 indicate second and third most energetic jets in the event.
- The jet multiplicity N_{jet}.
- The isolated track multiplicity[6], N_{trk}^{iso}.

[6]The definition of an isolated track is found in Table 8.3

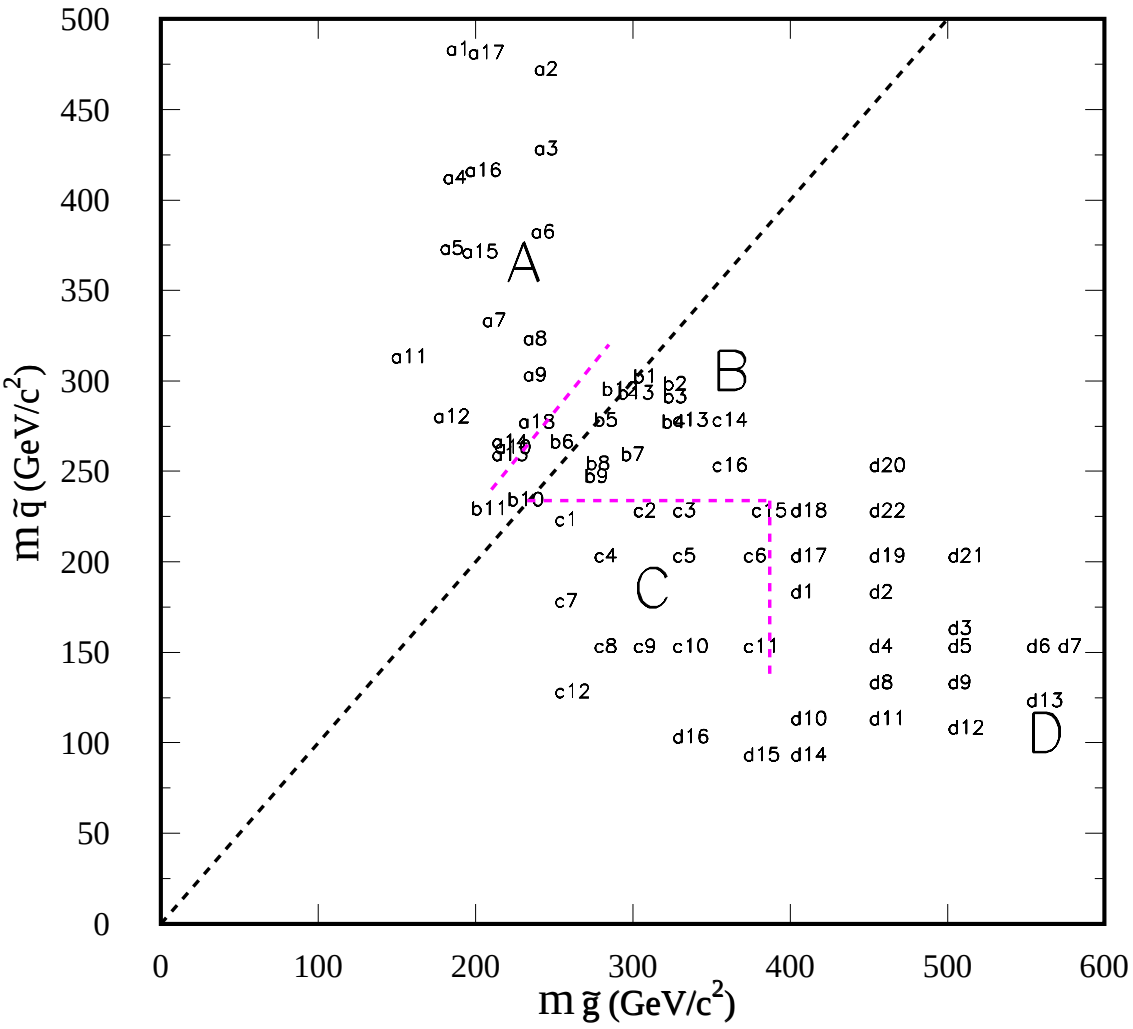

Figure 7.5: Studied Signal Points in $m_{\tilde{q}} - m_{\tilde{g}}$ mass plane and outline of signal regions A, B, C, D.

index	$m_{\tilde{q}}$ (GeV/c^2)	$m_{\tilde{g}}$ (GeV/c^2)	$m_{\tilde{\chi}_1^0}$ (GeV/c^2)	σ_{NLO} pb	region
a16	413	193	25	6.9	A
b1	299	300	44	0.78	B
c15	225	375	53	3.44	C
d6	150	550	86.3	20.9	D

Table 7.3: Representative Signal Points generated according to mSUGRA (analysis regions A, B) and MSSM (analysis regions C,D).

- The $E_{T\,1,2}$ and $\eta_{1,2}$ for the leading and second leading jets in the event.
- The (detector) $\not\!\!E_T$, H_T compared with the $\not\!\!E_T$, H_T from the $Z(\rightarrow \nu\nu)$+ jets and $W(\rightarrow \tau\nu)$+ jets background simulations.

From Figures 7.6 through 7.13 and the summary of the means of the different kinematic/topology distributions, the following observations are made:

- The $\not\!\!E_T$ at the generator level and the $\not\!\!E_T$ smeared by the CDF detector are in good agreement.
- The mean $\not\!\!E_T$ varies in the parameter space up to a factor of 2 and is higher close to the diagonal in the $m_{\tilde{q}} - m_{\tilde{g}}$ plane. It is obvious that the MET sample trigger efficiency threshold of 70 GeV which drives the $\not\!\!E_T$ requirement for the analysis, will affect the signal detection efficiency mostly at regions A and D. In Figures 7.14 through 7.16 the E_T of the two LSPs in the final state (at generation level) as well as their δ_ϕ is shown. It is notable that in region D the lower $\not\!\!E_T$ observed is due to the LSPs being produced "back to back" resulting in missing energy partial cancellation.
- In all the regions there are always ≥ 3 jets detected with the number of jets

becoming smaller when $\frac{m_{\tilde{g}}}{m_{\tilde{q}}} >> 1$

- In all the regions the number of high P_T isolated tracks is close to 0 with the highest close to the diagonal where cascade decays are expected to contribute.

- In all the regions the two leading jets are very energetic with the region where $\frac{m_{\tilde{g}}}{m_{\tilde{q}}} >> 1$ having the less energetic ones. The η_d distributions the two leading jets (and the third although not shown here) indicates that they are mostly central.

- The mean H_T does not vary by more than 1.5 across the regions. In the comparisons with the major $Z \rightarrow \nu\nu+ \geq 3$ jets and $W \rightarrow \tau\nu+ \geq 2$ jets Standard Model processes H_T shows a good discrimination, even when the $\not\!\!E_T$ does not.

- It is not shown here but in comparisons of the $\not\!\!E_T$ and H_T in all the representative SUSY points with $t\bar{t}$ Monte Carlo very little or no discrimination is observed. Kinematically $t\bar{t}$ is very similar to the SUSY signal searched for, and is expected to be a large background in the analysis. (The $\not\!\!E_T$+ multijet channel can be used to directly measure the $t\bar{t}$ cross section.)

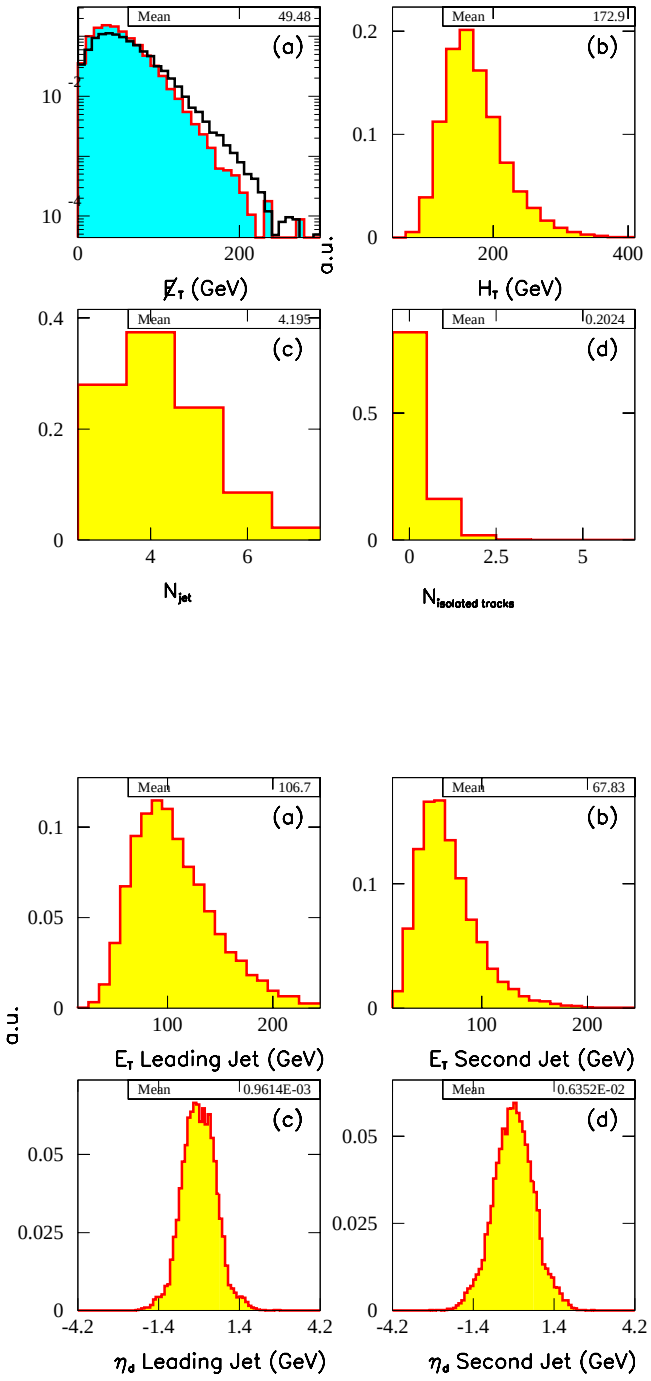

Figure 7.6: Top: (a) $\not\!\!E_T$ generated (histo) and after the detector simulation (shade) (b) H_T (c) N_{jet}, (d) N_{trk}^{iso}. Bottom: (a), (c)E_T, η leading jet (b), (d) E_T, η second jet. $m_{\tilde{q}} = 413, m_{\tilde{g}} = 193$ GeV/c^2 (point a16.)

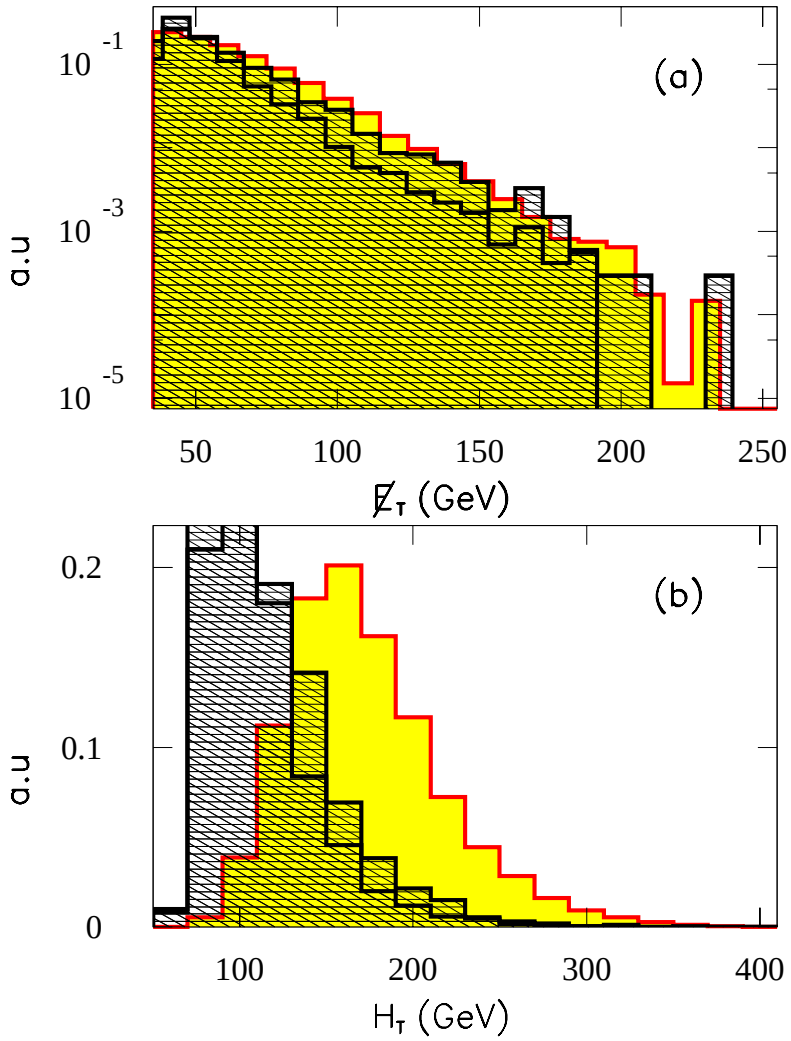

Figure 7.7: (a) $\not\!\!E_T$, (b) H_T signal (shaded) overlayed with $Z(\rightarrow \nu\nu)$+ jets and $W(\rightarrow \tau\nu)$+ jets background simulations (hatched). $m_{\tilde{q}} = 413, m_{\tilde{g}} = 193$ GeV/c^2. (point a16.)

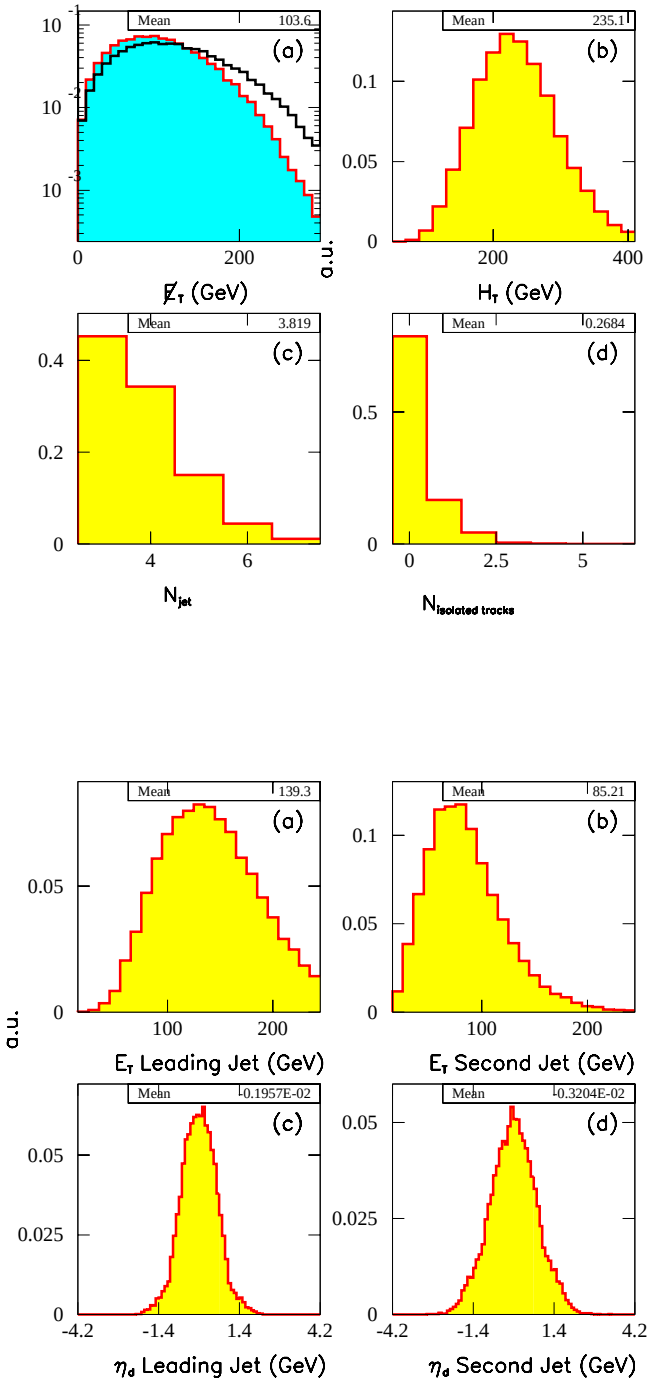

Figure 7.8: Top: (a) $\not\!\!E_T$ generated (histo) and after the detector simulation (shade) (b) H_T (c) N_{jet}, (d) N_{trk}^{iso}. Bottom: (a), (c) E_T, η leading jet (b), (d) E_T, η second jet. $m_{\tilde{q}} = 299, m_{\tilde{g}} = 300$ GeV/c^2. (point b1.)

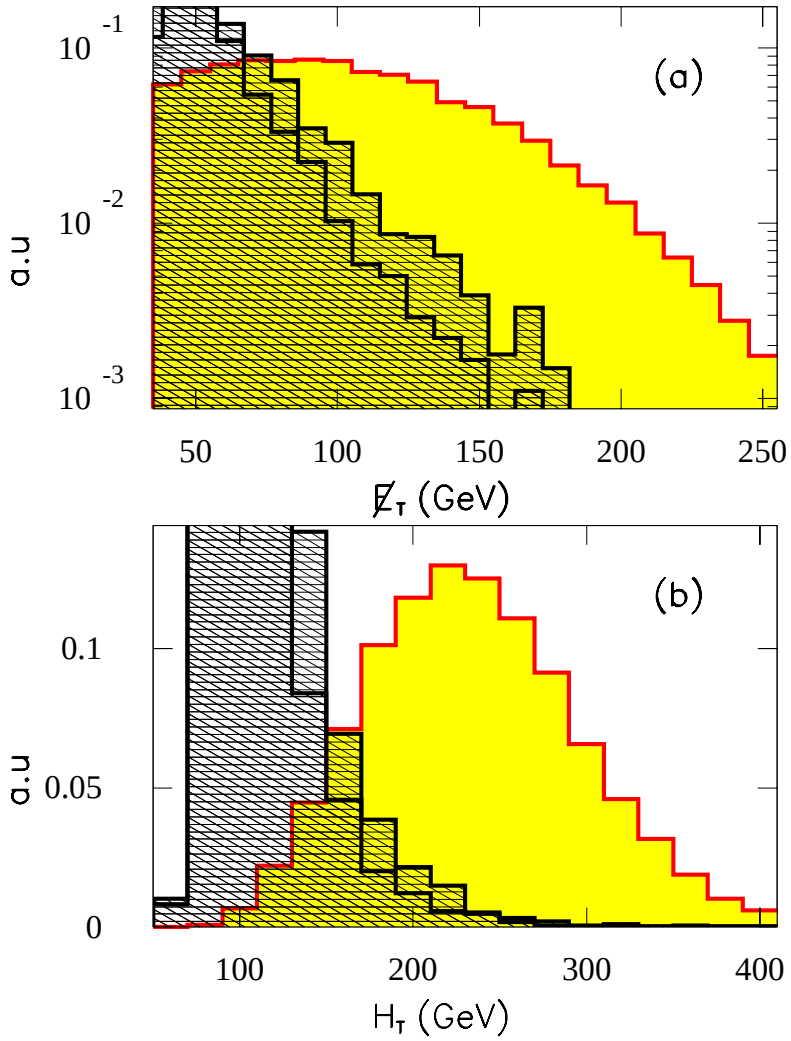

Figure 7.9: (a) $\not{E}_T$,(b) H_T signal (shaded) overlayed with $Z(\rightarrow \nu\nu)$+ jets and $W(\rightarrow \tau\nu)$+ jets background simulations (hatched). $m_{\tilde{q}} = 299$, $m_{\tilde{g}} = 300\text{GeV/c}^2$. (point b1.)

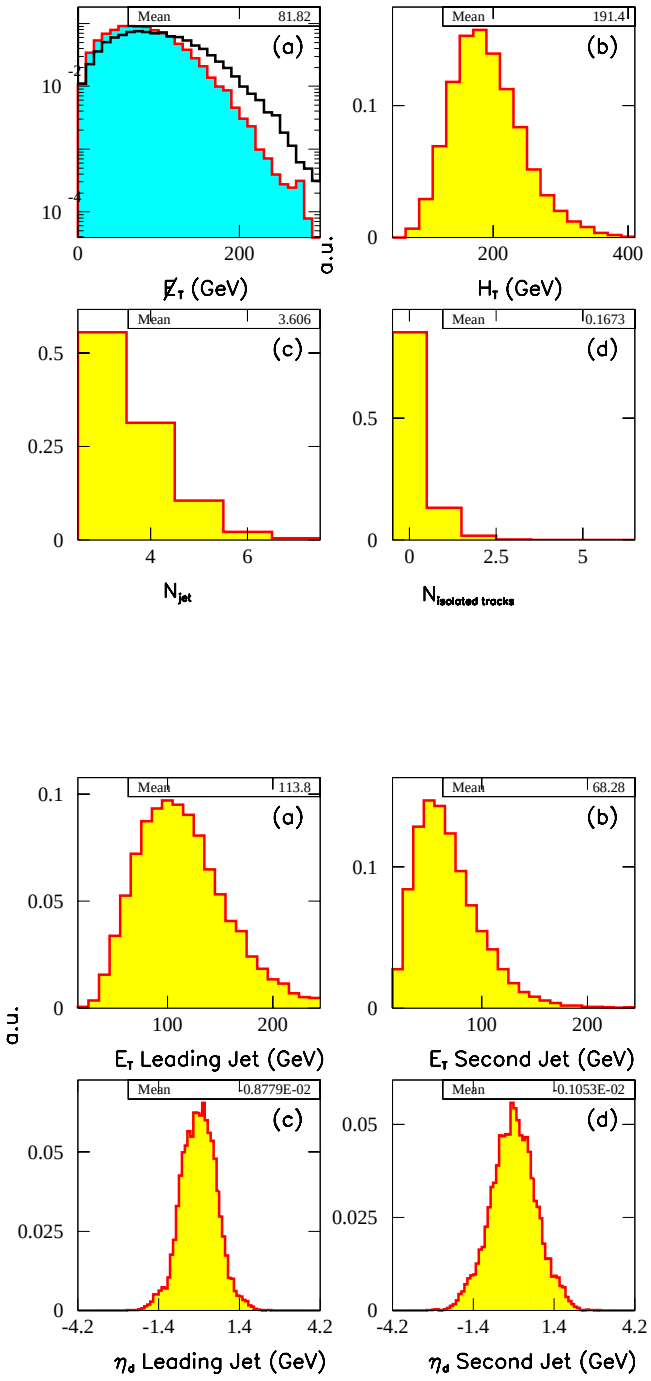

Figure 7.10: Top: (a) $\not\!\!E_T$ generated (histo) and after the detector simulation (shade) (b) H_T (c) N_{jet}, (d) N_{trk}^{iso}. Bottom: (a), (c) E_T,η leading jet (b),(d) E_T, η second jet. $m_{\tilde{q}} = 225, m_{\tilde{g}} = 375$ GeV/c^2 (point c15.)

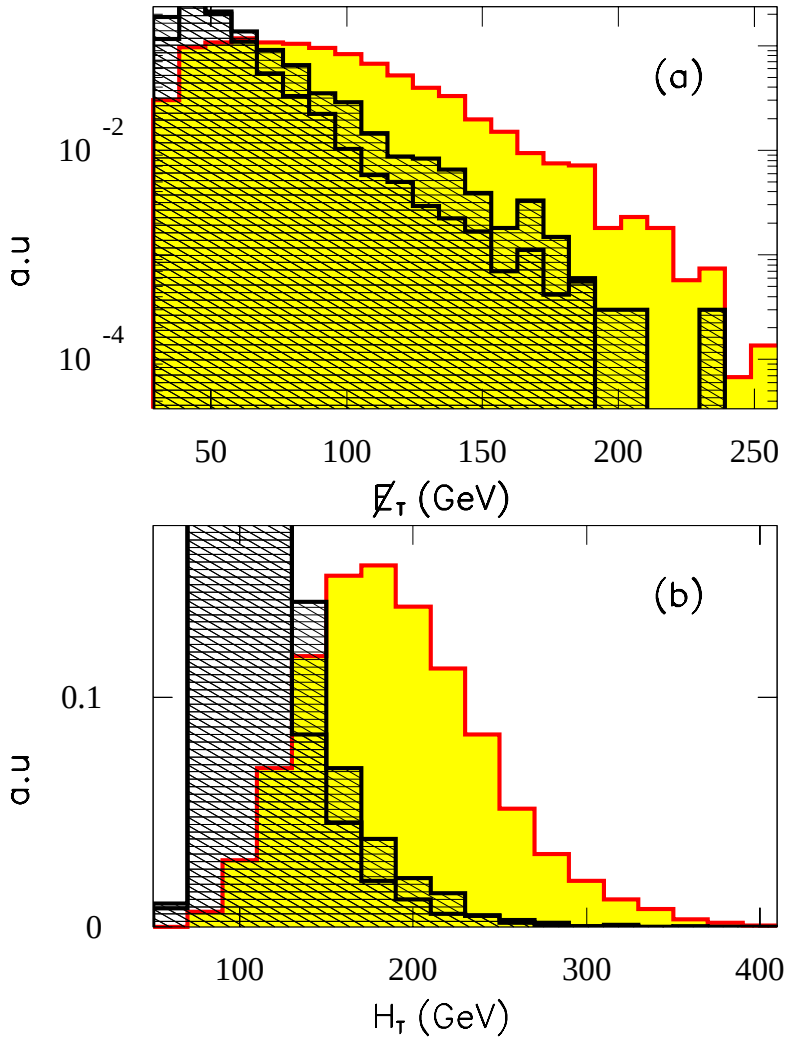

Figure 7.11: (a) $\not\!\!E_T$,(b) H_T signal (shaded) overlayed with $Z(\rightarrow \nu\nu)$+ jets and $W(\rightarrow \tau\nu)$+ jets background simulations (hatched). $m_{\tilde{q}} = 225, m_{\tilde{g}} = 375$ GeV/c^2. (point c15.)

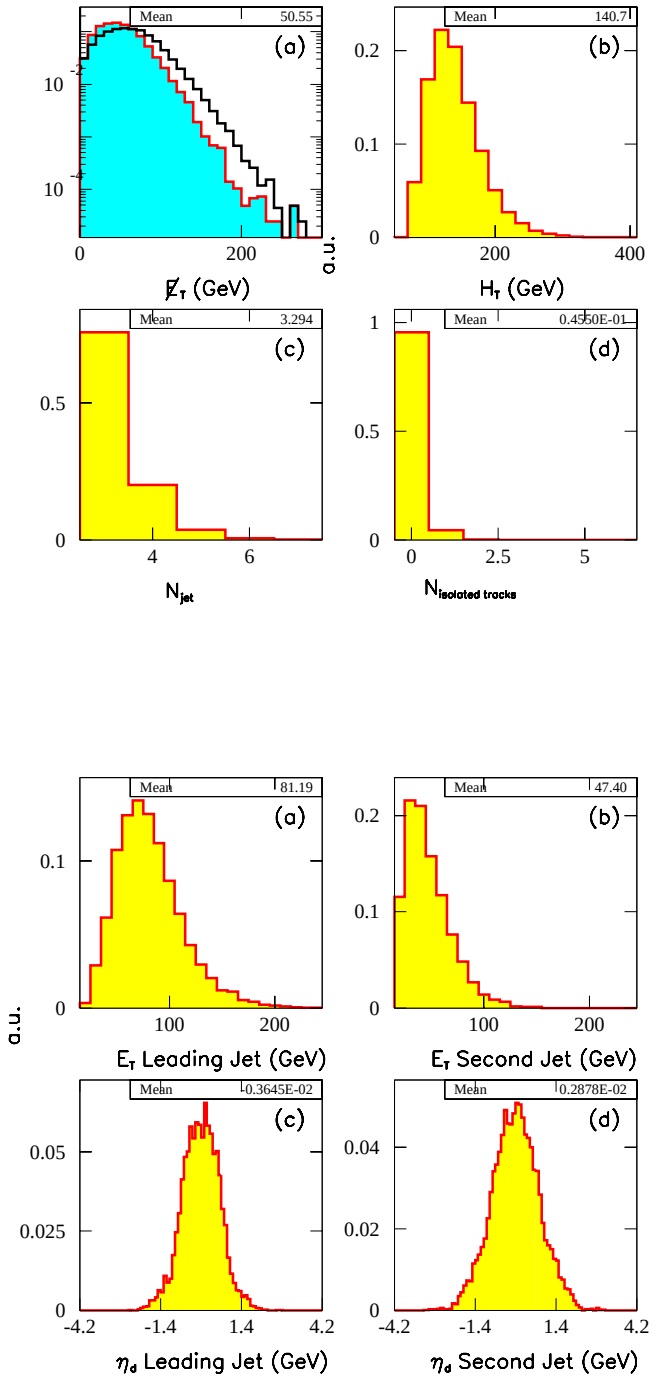

Figure 7.12: Top: (a) $\not\!\!E_T$ generated (histo) and after the detector simulation (shade) (b) H_T (c) N_{jet}, (d) N_{trk}^{iso}. Bottom: (a), (c) E_T, η leading jet (b), (d) E_T, η second jet. $m_{\tilde{q}} = 150, m_{\tilde{g}} = 550$ GeV/c^2. (point d6.)

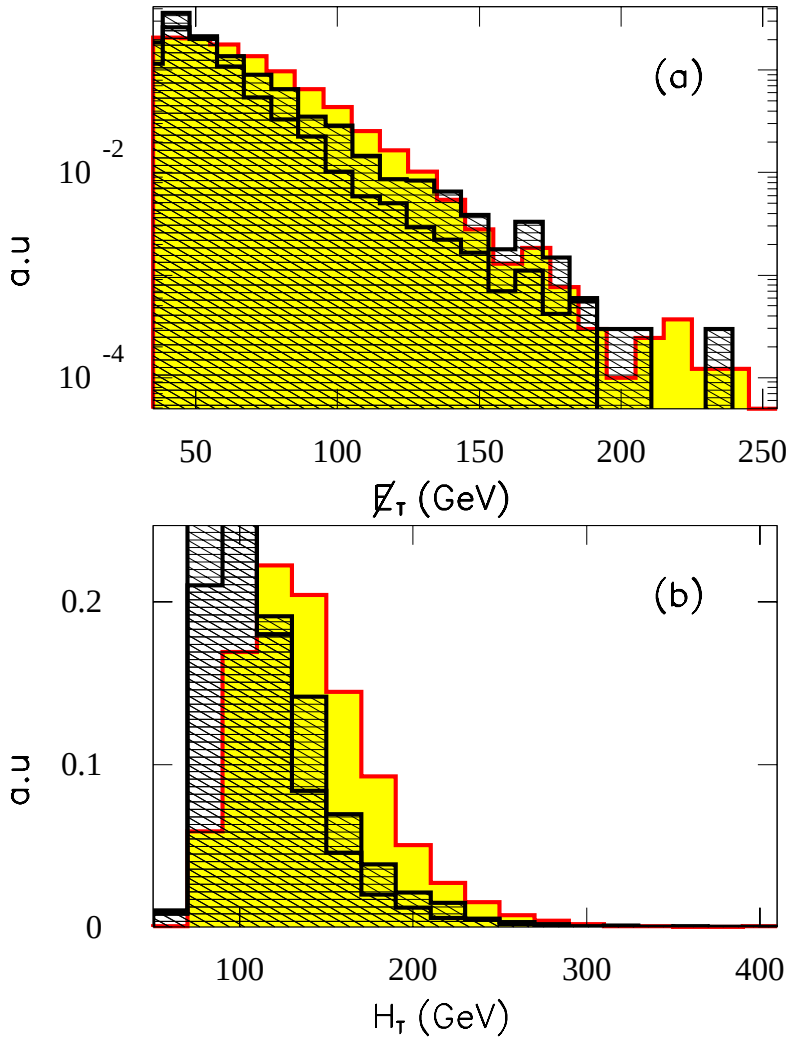

Figure 7.13: (a) $\not\!\!E_T$,(b) H_T signal (shaded) overlayed with $Z(\rightarrow \nu\nu)$+ jets and $W(\rightarrow \tau\nu)$+ jets background simulations (hatched). $m_{\tilde{q}} = 150, m_{\tilde{g}} = 550$ GeV/c^2. (point d6.)

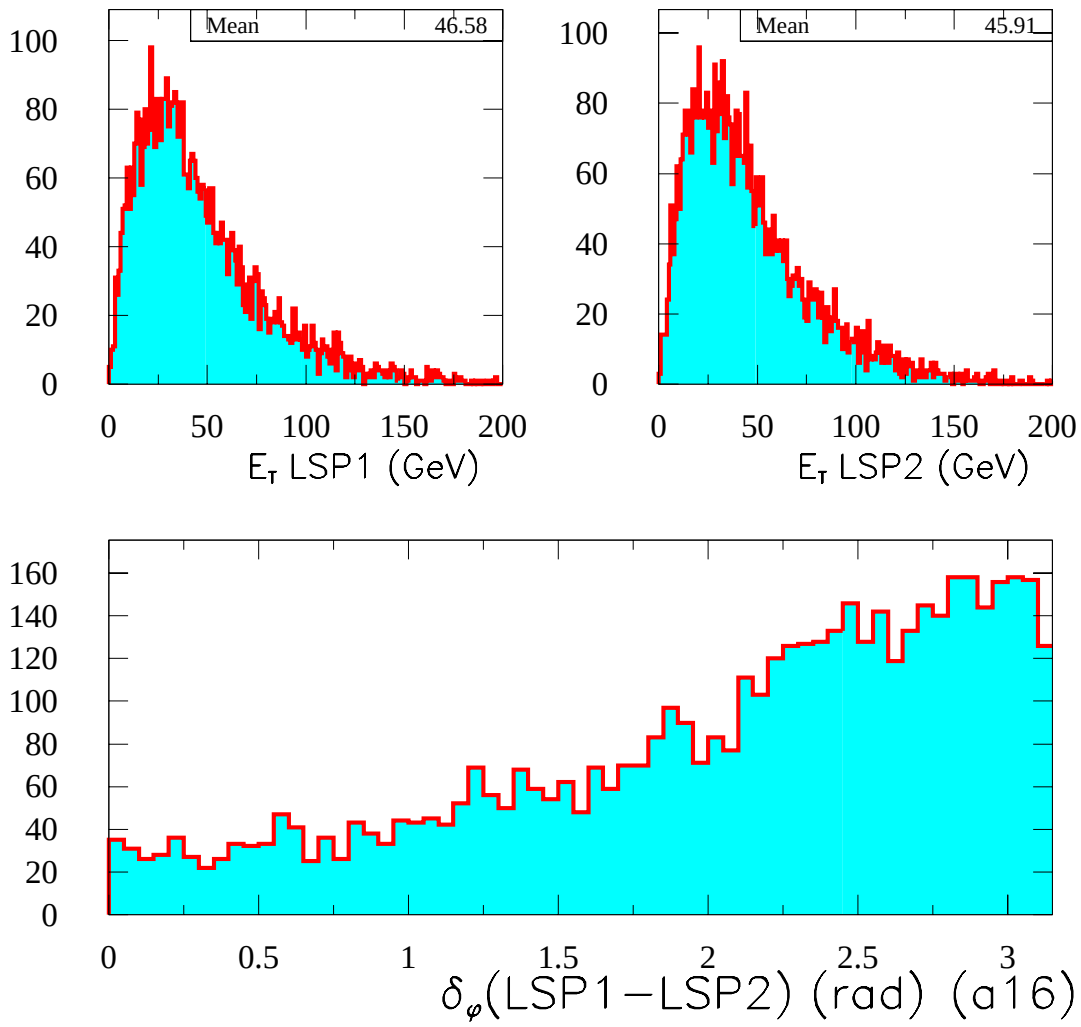

Figure 7.14: E_T distribution of the two LSPs in the final state (at generation level) and their δ_ϕ distribution. (point a16.)

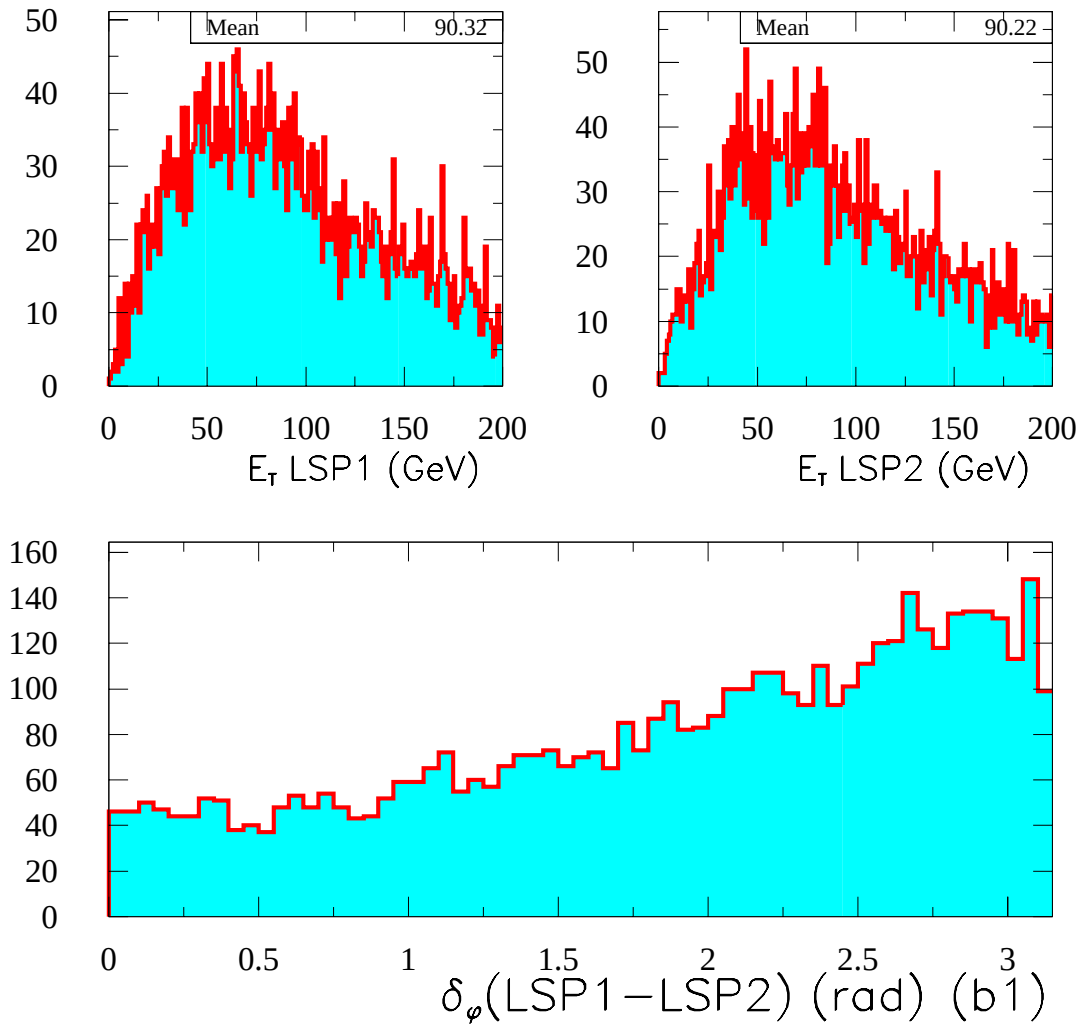

Figure 7.15: E_T distribution of the two LSPs in the final state (at generation level) and their δ_ϕ distribution. (point b1.)

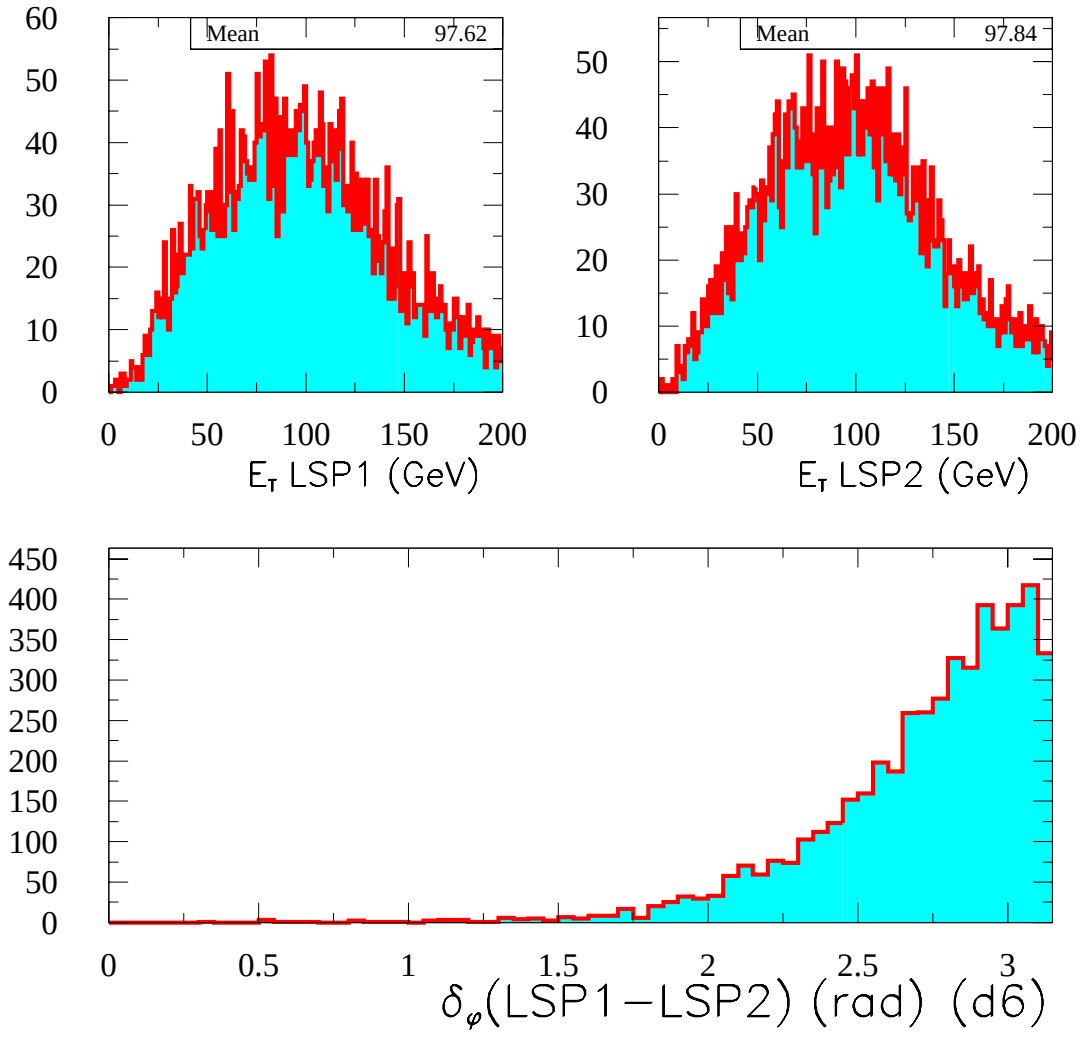

Figure 7.16: E_T distribution of the two LSPs in the final state (at generation level) and their δ_ϕ distribution. (point d6.)

index	a16	b1	c15	d6
$m_{\tilde{q}}$ (GeV/c^2)	413	299	225	150
$m_{\tilde{g}}$ (GeV/c^2)	193	300	375	550
$< \not\!\!E_T >$ (GeV/c^2)	50	103	81	50.5
$< H_T >$ (GeV)	173	235	190	141
$< N_{jet} >$	4.2	3.8	3.6	3.2
$< N_{trk}^{iso}$	0.2	0.27	0.16	0.05
$< E_{T1} >$ (GeV)	106	139	113	81
$< E_{T2} >$ (GeV)	70	85	68	47
region	A	B	C	D

Table 7.4: Representative Signal Points generated according to mSUGRA (analysis regions A, B) and MSSM (analysis regions C, D). Means of kinematic distributions.

Chapter 8

The Analysis

The data Pre-Selection (Chapter 4) and the jet fiducial requirements discussed in Chapter 6 are designed to retain a high purity in real missing energy sample referred to as the *signal candidate sample*. This data sample is not used in the determination of the analysis search path which is discussed in this chapter. In the *missing energy plus multijet* search the large missing energy comes from the two LSPs in the final states of the squark and gluino decays as discussed in Chapter 7. The three or more hadronic jets come from the hadronic decays of the $\widetilde{q}$, $\widetilde{g}$. There can be leptons from cascade decays of squarks and gluinos. This analysis does not explicitly identify and veto leptons. To reduce the large background contribution mainly from $W(\rightarrow \ell\nu) + jets$ and $t\bar{t}$ production, an *indirect lepton veto* scheme is applied as is discussed in Section 8.2.

Three variables are used to define the signal candidate region (blind box): the $\not\!\!E_T$, the H_T and the Isolated Track Multiplicity N_{trk}^{iso}. The requirements are shown in Table 8.1. The missing energy requirement for the definition of the box is motivated by the missing energy Level 2 trigger efficiency (Appendix D). The H_T requirement

$\not\!\!E_T \geq 70$ GeV
$H_T \geq 150$ GeV
$N_{trk}^{iso}=0$

Table 8.1: Selection criteria used in the definition of the signal candidate region (blind box).

is motivated by the discrimination power between the signal and the background as demonstrated in Chapter 7. The N_{trk}^{iso} requirement increases the sensitivity of the search for all-hadronic final states by significantly reducing the W/Z+jets, $t\bar{t}$ backgrounds while at the same time retaining the signal cascade decays where a lepton is produced close to a jet (non-isolated lepton). The rest of the analysis path is based on the kinematics and aims at high sensitivity to the signal. There are seven neighboring spaces around the box (by reversing the requirements which define it). One additional space is defined by reversing the $\not\!\!E_T$ and H_T requirements independent of the presence of an isolated track.

Once the analysis path is completely defined the missing energy data are compared with the Standard Model predictions in the neighboring spaces. These are the comparisons around the box and they serve as validation of the Standard Model estimates before examining the data in the signal candidate region (this is referred to as "opening the box") and comparing the predictions with the data. To increase the sensitivity in the different regions of the SUSY parameter space, four regions are defined in the $m_{\tilde{q}} - m_{\tilde{g}}$ plane (Chapter 7) and the H_T and $\not\!\!E_T$ variables are optimized for representative points belonging to each region. The analysis selection path requirements and number of events passing each stage are shown in Table 8.2 and figure 8.1. In the following each requirement is discussed.

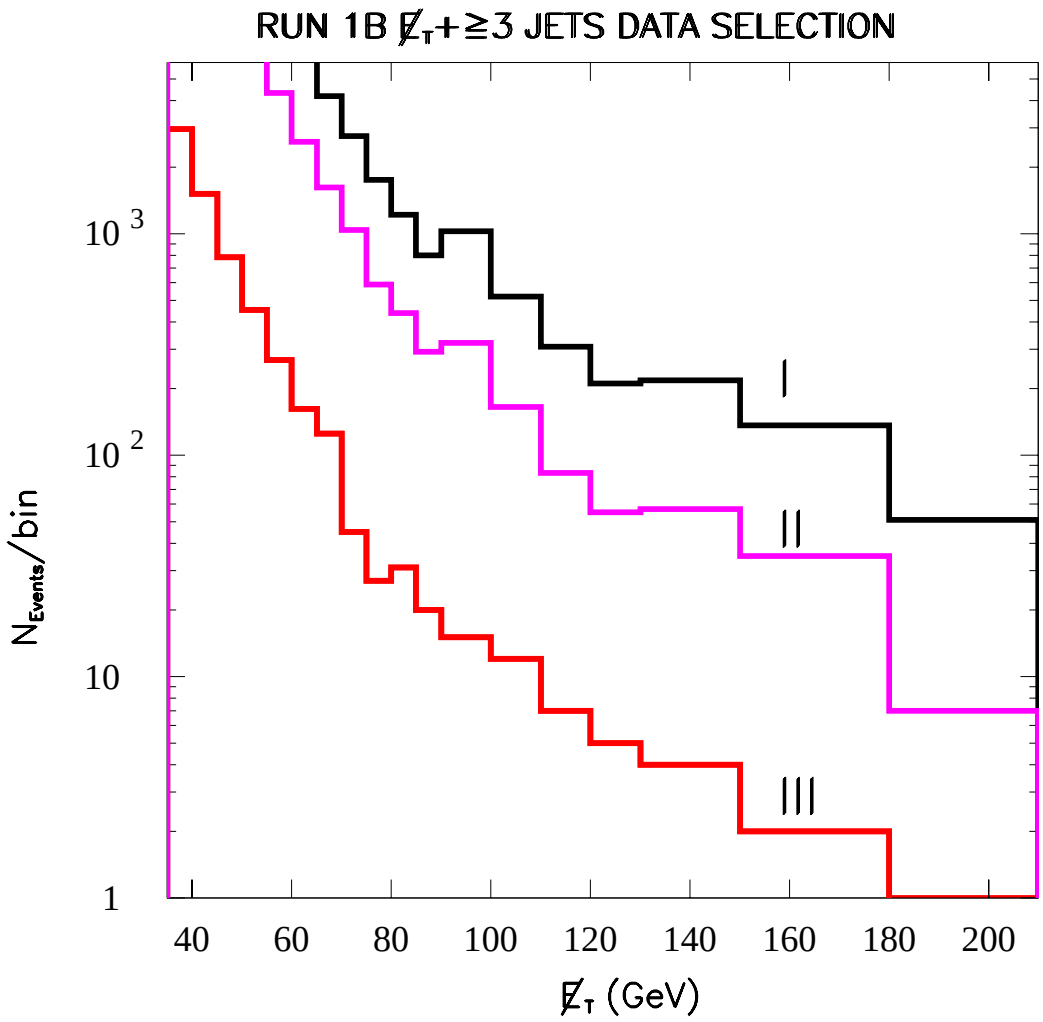

Figure 8.1: Data $\not\!\!E_T$ spectrum for different stages of the analysis path. (I) Pre-Selection and jet fiduciality, (II) ≥3 jets, (III) $E_T(1)$≥70 GeV, $E_T(2)$≥30 GeV, (IV) Indirect Lepton Veto (as in Table 8.2).

Requirement	Number of Events passing
Pre-Selection and Bad Run veto	286728, **(I)**
N_{jet} $\geq$3 (cone .7,$E_T \geq$ 15 GeV)	107509,**(II)**
Fiduciality fiducial 2nd,3rd jet 2-D $\delta\phi$	 57011 23381
BOX data removed	
$E_T(1) \geq$70GeV $E_T(2) \geq$30GeV $\lvert\eta_d\rvert$(1 *or* 2 *or* 3) $<$ 1.1	 6435,**(III)**
EMF(1),EMF(2)$\leq$ 0.9 L2 trigger	6013 4679
$\delta\phi_{min} \geq$ 0.3	2737

Table 8.2: The data selection path for the $\not\!\!E_T$ $+\geq$ 3 jets search. The $\not\!\!E_T$ spectrum for stages I, II, III is shown in figure 8.1.

8.1 Analysis Requirements

8.1.1 E_T Leading Jet, Second Leading Jet, $\not\!\!E_T$, H_T

The leading jet $E_T \geq$70 GeV requirement is motivated by the JET50 L2 trigger efficiency (Appendix D) and was suggested by the comparisons of the data and predictions around the box where threshold effects were present. In the different points of the SUSY parameter space (Chapter 7) the leading jet (second leading) jet are very energetic and the 70(30) GeV requirement is efficient. Examples of the ratio $N_{signal}/\sqrt{N_{background}}$, where $N_{background}$ is the total number of predicted Standard Model events, for different points in the parameter space as a function of the jet E_T (leading and second leading) , the $\not\!\!E_T$ and the H_T (for the box definition) are given in Appendix Hand typical means are given in Table 7.4. The requirement of

at least one of the three most energetic to be central is motivated by the signal jets being central (Chapter 7).

8.2 Indirect Lepton Veto

The two most energetic jets are required not be purely electromagnetic. This requirement eliminates events with high energy electrons in the final state. Events that have one or more high P_T isolated tracks are also vetoed. Track isolation is used (for example [70, 71]) as a powerful criterion in τ selection. In this analysis it is used as an indirect lepton veto requirement (aiming at reducing high P_T electrons, muons and taus).

The requirements for a track to be counted as isolated are given in Table 8.3. The

If a (3-D) track is found with $P_T \geq 10$ GeV/c,
$d_0 \leq 0.5cm$, $\lvert z_0 - z_{primary} \rvert < 5$ cm and the
ΣP_T of all tracks (with $d_0^i \leq 1$ cm) around the
high-P_T track in a cone of $DR = \sqrt{(\delta\eta)^2 + (\delta\phi)^2} = 0.4$
is $\Sigma P_T \leq 2$ GeV/c then it is counted in
the number of isolated tracks, N_{trk}^{iso}, in the event.

Table 8.3: Definition of track isolation

two requirements constitute what is referred to as "indirect lepton veto" requirements and are shown in Table 8.4. This indirect lepton veto mechanism is validated in the W data and Monte Carlo and the JET50 data and Monte Carlo (Appendix H).

EMF(1),(2)$\leq$0.9
N_{trk}^{iso}=0

Table 8.4: Indirect lepton veto requirements.

8.3 $\delta\phi_{min}$ variable

A significant improvement of the signal to background ratio is achieved by requiring a minimum $\delta\phi$ between the $\not\!\!E_T$ and any jet E_T in the event. This variable is used to eliminate residual QCD events with mismeasured jets. (In most of the events the closest jet to the $\not\!\!E_T$ is (still after the fiducial requirements) the second jet). The optimized value is found to be $\delta\phi_{min} \geq 0.3$ rad for an event to be accepted. The optimization study for $\delta\phi_{min}$ is given in Appendix H.

8.4 Summary of Standard Model processes with $\not\!\!E_T + \geq 3$ jets in the final state

The Standard Model processes with large missing energy and multijets in the final state are discussed in detail in Chapters 5 & 6. Here they are briefly summarized.

- Z+jets : QCD associated Z production with $Z \to ee$, $Z \to \mu\mu$, $Z \to \tau\tau$, $Z \to \nu\nu$. Residual contributions from $Z \to ee(Z \to \mu\mu)$ occurs where one electron(muon) is lost in an uninstrumented or in a high η_d region. In $Z \to \tau\tau$ decays there is $\not\!\!E_T$ from the semileptonic decays of the τ lepton but the branching ratio for all-hadronic decays is much larger and little contribution is expected. The most significant and irreducible background component is

expected from the $Z \to \nu\nu$ process. The hadronic decays of the Z (three times the rate of all the leptonic decays) contribute $\not\!\!E_T$ in the same ways QCD does. This background is accounted for in the overall QCD background estimate since the predictions are normalized to the JET data.

- W+jets : QCD associated W production with $W \to e\nu$, $W \to \mu\nu$, $W \to \tau\nu$ has a large $\not\!\!E_T$ +jets contribution. Again the contribution from the hadronic decays of the W is accounted for in the overall QCD background. For the W+jets and Z+jets backgrounds the ELO (VECBOS+HERPRT+QFL) Monte Carlo simulation is used and all the channels are normalized using the $Z \to ee + 2$ jets data as described in detail in Chapter 5.

- top, single top : In $t\bar{t}$ production a W from a top decay can decay semileptonicaly and contribute to the high $\not\!\!E_T$ tails. We use PYTHIA to simulate $t\bar{t}$ production with all inclusive top decays. For the normalization to the data luminosity the theoretical calculation $\sigma(t\bar{t}) = 5.1\ pb \pm 18\%$ (which is consistent with the CDF $t\bar{t}$ [72] cross section) is used . HERWIG and PYTHIA Monte Carlo programs are used to simulate single top production via W-gluon fusion and W* production respectively. The theoretical cross sections $\sigma(tq') = 1.7$ pb $\pm 15\%$ and $\sigma(bt) = 0.73$ pb $\pm 9\%$ [36] are used to normalize the samples.

- dibosons : For WW, WZ, ZZ production PYTHIA is used For the normalization, the theoretical cross sections calculation for each diboson process: $\sigma(WW) = 9.5 \pm 0.7$ pb, $\sigma(WZ) = 2.6 \pm 0.3$ pb and $\sigma(ZZ) = 1 \pm 0.2$ pb [38] are used.

- QCD : The QCD background is generated with HERWIG and normalized to the CDF jet data as discussed in Chapter 6.

Bin number	Description	EWK	QCD	All	Data
1	$\not\!\!E_T \geq$70,$H_T \geq$150,$N_{trk}^{iso} > 0$	13.9	6.26	20.2±4.7	10
2	$\not\!\!E_T \geq$70,$H_T <$150,$N_{trk}^{iso} = 0$	2.3	6.26	8.6±4.5	12
3	35$<\not\!\!E_T <$70,$H_T >$150,$N_{trk}^{iso} = 0$	1.95	134.6	136.5±27.8	134
4	$\not\!\!E_T >$70,$H_T <$150,$N_{trk}^{iso} > 0$	1.73	0	1.73±0.3	2
5	35$<\not\!\!E_T <$70,$H_T >$150,$N_{trk}^{iso} > 0$	13.95	9.39	23.34±5.7	24
6	35$<\not\!\!E_T <$70,$H_T <$150,$N_{trk}^{iso} = 0$	4.9	413.16	418.1±68.8	410
7	35$<\not\!\!E_T <$70,$H_T <$150,$N_{trk}^{iso} > 0$	3.3	28.17	31.4±10.2	35
8	$\not\!\!E_T >$70,$H_T >$150,$N_{trk}^{iso} = 0$	35.3	40.69	76.02±12.8	?
9	35$<\not\!\!E_T <$70,$H_T <$150	8.2	441.3	449.5±72	445

Table 8.5: Comparison of the Standard Model prediction and the data in the neighboring to the blind box spaces. Bin 8 is the blind box. Also refer to the summary plot 8.3.

8.5 Comparison between data and predictions around the blind box

In Figure 8.2 the blind box and its neighboring spaces is schematically shown. The blind box is open-ended on the high $\not\!\!E_T$ and H_T sides. In addition to the spaces pictured a ninth bin is considered by reversing the $\not\!\!E_T$ and H_T requirements independent of N_{trk}^{iso}. The prediction in each of these bins is compared with the data. In the following the bin indexing is kept as in Figure 8.2. Figure 8.3 and Table 8.5 show the summary of the comparison between the predictions and the observed data around the blind box. *EWK* refers to the sum of W/Z+jets, diboson, $t\bar{t}$, and single top processes. The uncertainty includes all the systematic components. In Tables 8.6 & 8.7 the breakdown of the each component of the background prediction is given. Absent is the $Z \to \tau\tau$+ jets component which is found to be negligible.

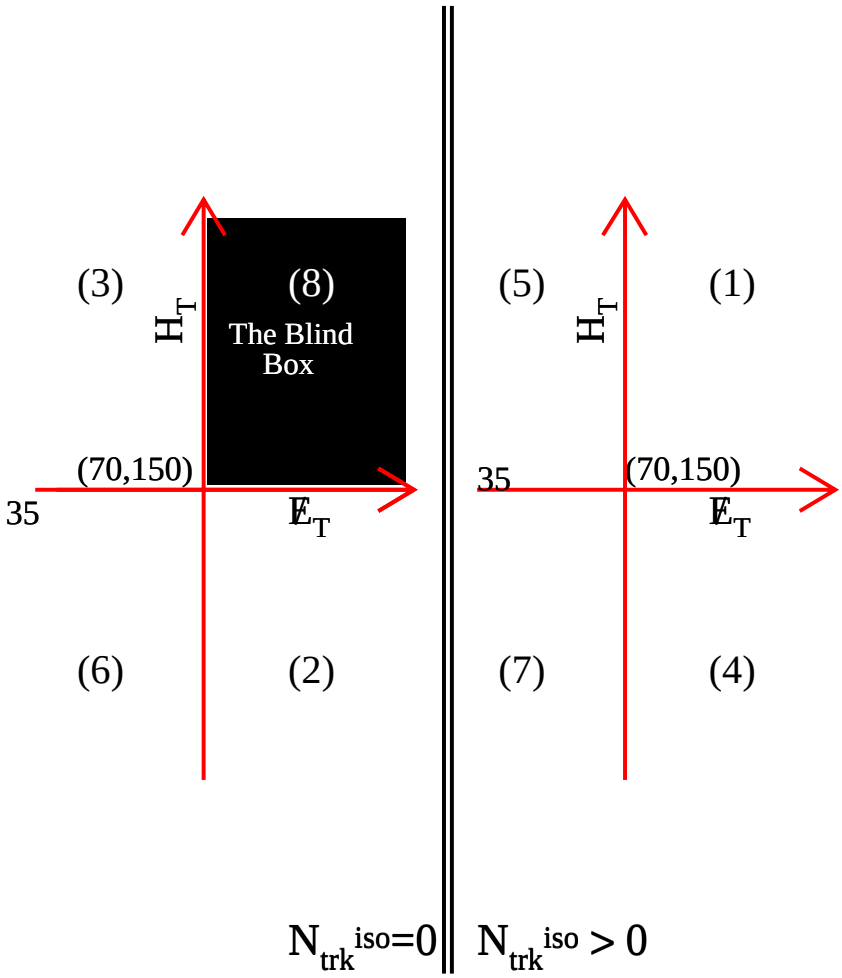

Figure 8.2: Schematic of blind box and the regions outside the box where the Standard Model background predictions are compared to the data.

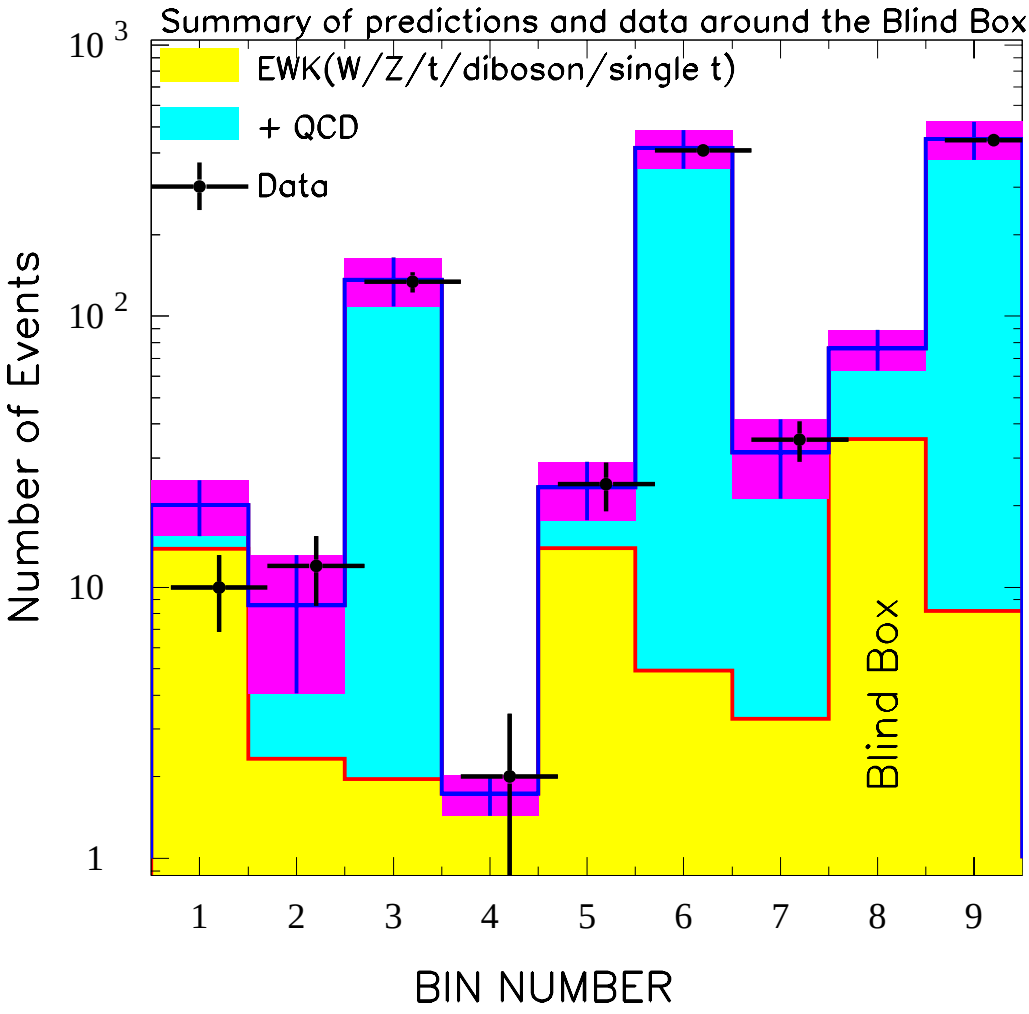

Figure 8.3: Comparison of Standard Model predictions and data in the bins around the blind box (bin 8). Also refer to the summary Table 8.5.

Bin	$Z \to \nu_i \bar{\nu}_i$	$Z \to e^+e^-$	$Z \to \mu^+\mu^-$
1	0.13±0.09 (2)	0.04±0.02 (3)	1.08±0.15 (83)
2	0.7±0.2 (11)	- (0)	- (0)
3	0.44±0.17 (7)	- (0)	- (0)
4	- (0)	- (0)	0.117±0.04 (9)
5	0.06±0.06 (1)	0.08±0.03 (6)	1.17±0.16 (90)
6	1.39±0.32 (22)	0.03±0.02 (2)	0.08±0.03 (6)
7	0.13±0.09 (2)	0.04±0.02 (3)	0.14±0.05 (11)
8	12.66±1.5 (201)	- (0)	0.22±0.06 (17)
9	1.5±0.3 (24)	0.06±0.03 (5)	0.22±0.06 (17)
Bin	$W \to e\nu_e$	$W \to \mu\nu_\mu$	$W \to \tau\nu_\tau$
1	1.65±0.27 (75)	2.9±0.4 (119)	2.61±0.57 (29)
2	0.2±0.07 (9)	0.24±0.08 (10)	1.±0.32 (11)
3	0.3±0.09 (15)	0.22±0.08 (9)	0.27±0.16 (3)
4	0.28±0.09 (13)	0.45±0.12 (19)	0.63±0.25 (7)
5	3.65±0.5 (166)	2.±0.33 (84)	2.34±0.54 (26)
6	1.±0.18 (45)	0.5±0.12 (19)	1.±0.33 (12)
7	0.6±0.14 (28)	0.67±0.15 (28)	0.9±0.3 (10)
8	4.±0.56 (182)	3.36±0.5 (140)	7.02±1.16 (78)
9	1.6±0.27 (73)	1.13±0.2 (47)	1.98±0.48 (22)

Table 8.6: Breakdown of $W/Z+$ jets component of the Standard Model background. The number in the parenthesis is the Monte Carlo entries that pass the requirements of the corresponding bin. Multiplied by the scale factor (last column "s.f.") of Table 5.3 they yield the normalized numbers tabulated here.

Bin	WW	WZ	ZZ
1	0.31±0.05	0.05±0.01	0.01±0.004
2	0.04±0.02	0.004±0.002	0.004±0.001
3	0.02± 0.01	0.007±0.007	0.002±0.001
4	0.007±0.007	0.005±0.003	0.002±0.001
5	0.12±0.03	0.04± 0.009	0.01± 0.003
6	0.05± 0.02	0.007±0.004	0.007±0.003
7	0.06± 0.02	0.007±0.004	0.003±0.002
8	0.56± 0.08	0.22± 0.03	0.14± 0.03
9	0.11± 0.03	0.01± 0.005	0.01± 0.003
Bin	$t\bar{t}$	single $t(Wg)$	single $t(W^*)$
1	5.04±0.94	0.03±0.01	0.09±0.02
2	0.17±0.03	0.006±0.004	0.006±0.004
3	0.64± 0.12	0.009±0.005	0.02±0.008
4	0.21± 0.04	0.006±0.004	0.009±0.005
5	4.2± 0.78	0.1± 0.02	0.153±0.02
6	0.75± 0.14	0.03±0.01	0.05±0.01
7	0.65± 0.12	0.026± 0.009	0.033±0.01
8	6.86± 1.3	0.09± 0.02	0.19± 0.03
9	1.4± 0.27	0.06± 0.01	0.09± 0.02

Table 8.7: Breakdown of diboson, $t\bar{t}$ and single top component of the Standard Model background.

Regions	$\not\!\!E_T$,H_T(GeV)	Standard Model prediction
A/D	90,160	32.7 $\pm$ 6.7
B	110,230	3.7 $\pm$ 0.5
C	110,170	10.6 $\pm$ 1

Table 8.8: $\not\!\!E_T$, H_T optimized requirements for four regions in the $m_{\tilde{q}} - m_{\tilde{g}}$ plane.

8.6 Shapes around the box

The Standard Model predicted $\not\!\!E_T$, H_T, N_{jet} and the leading jet E_T distributions are compared with the data in all the bins around the box. Bin 9 (QCD dominated) and bin 5 ($\sim$50% EWK - 50% QCD) are presented in Figures 8.4 & 8.5 respectively. The comparisons in all other bins are found in Appendix H.

8.7 $m_{\tilde{q}}$ - $m_{\tilde{g}}$ analysis regions

In Chapter 7 the $m_{\tilde{q}} - m_{\tilde{g}}$ plane is divided into four general regions : (A) above the diagonal ($m_{\tilde{q}} \gg m_{\tilde{g}}$, mSUGRA, 5 degenerate $\tilde{q}$) (B) above and around the diagonal ($m_{\tilde{q}} \sim m_{\tilde{g}}$, mSUGRA, 5 degenerate $\tilde{q}$) (C) below and around the diagonal ($m_{\tilde{q}} < m_{\tilde{g}}$, MSSM, 4 degenerate $\tilde{q}$) (D) below the diagonal ($m_{\tilde{q}} \ll m_{\tilde{g}}$, MSSM, 4 degenerate $\tilde{q}$). (Figure 7.5). Representative points of each region are used to optimize the $\not\!\!E_T$, H_T requirements for increased sensitivity to the signal . The optimization curves are given in Appendix H and the results in Table 8.8. Regions A and D are optimized for the same set of ($\not\!\!E_T$,H_T) requirements.

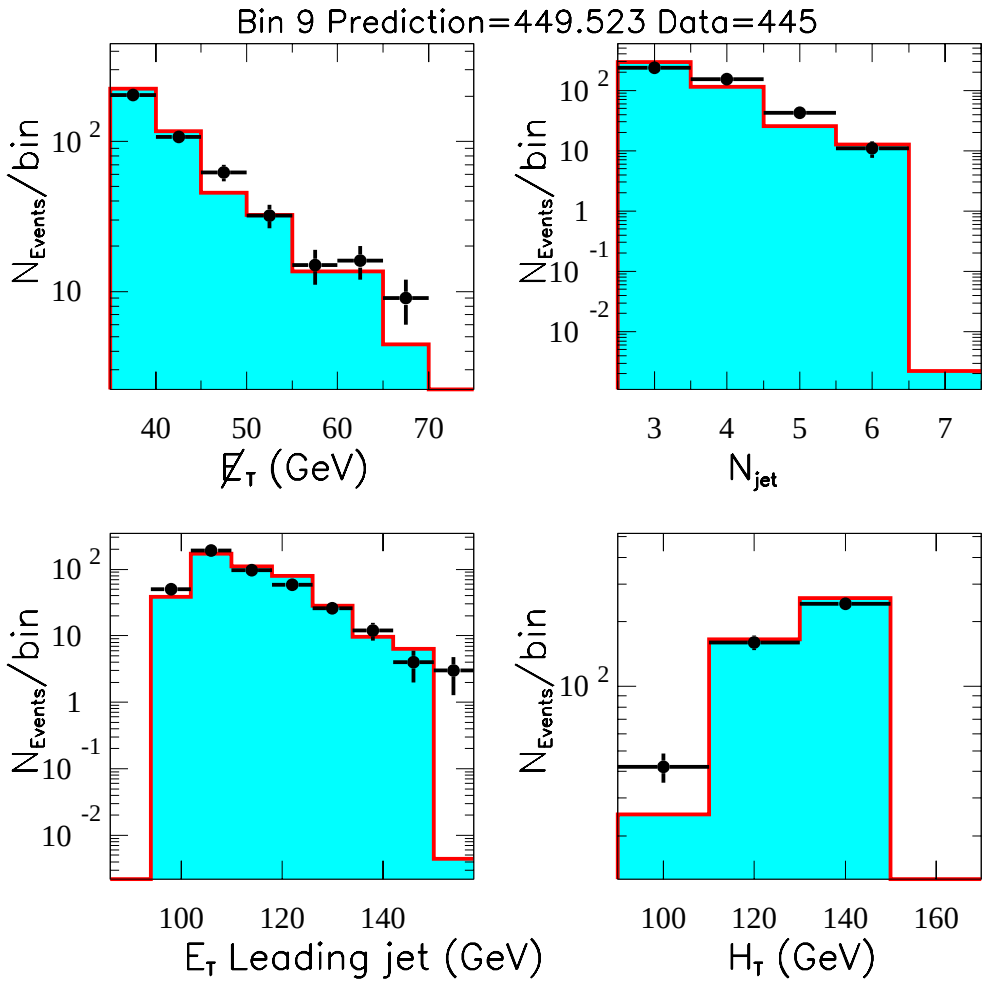

Figure 8.4: Comparison of Standard Model prediction and data in bin 9 (QCD dominated). The histogram is the Standard Model predictions and the points are the data observed.

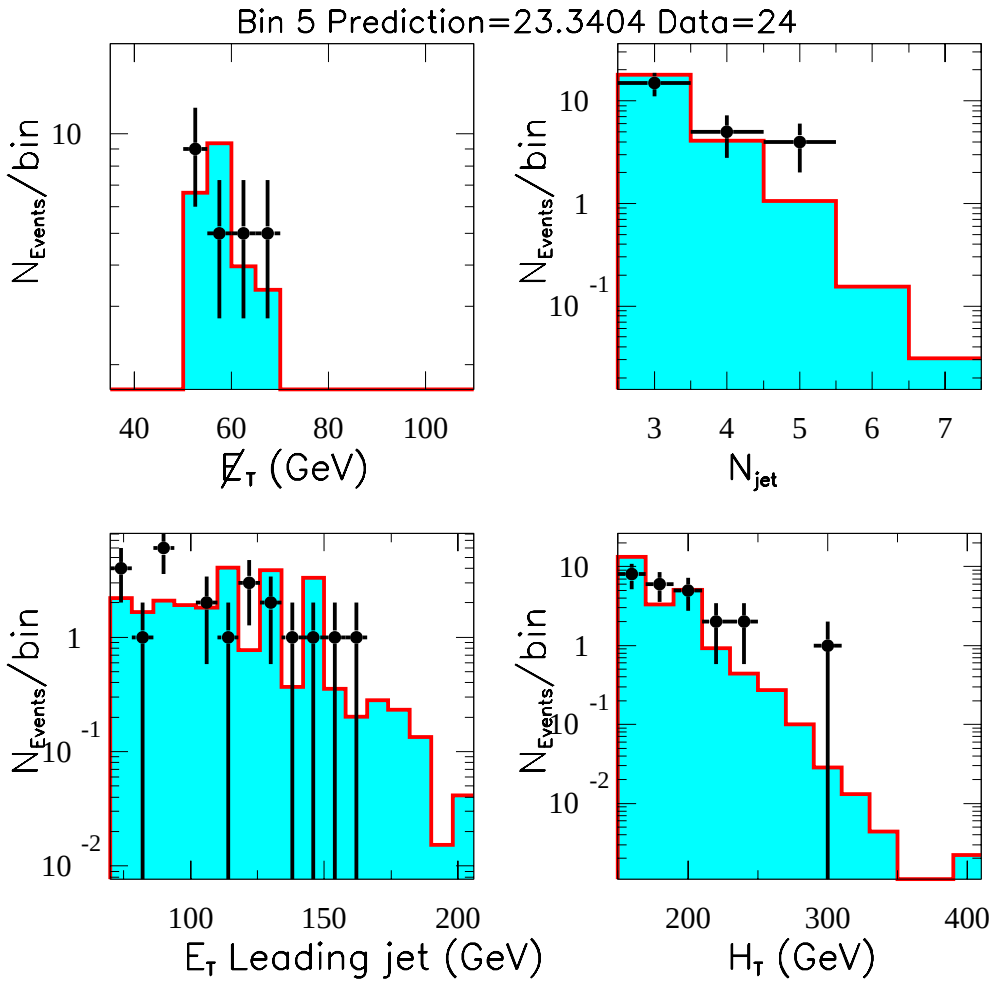

Figure 8.5: Comparison of Standard Model prediction and data in bin 5 (∼50%-50% EWK-QCD). The histogram is the Standard Model predictions and the points are the data observed.

box/region	Expected	Observed
BOX	76 ± 12.8	74
A/D	32.7 ± 6.7	31
B	3.7 ± 0.5	5
C	10.6 ± 1	14

Table 8.9: $\not\!\!E_T$ H_T optimized requirements for the four regions in the $m_{\tilde{q}} - m_{\tilde{g}}$ plane.

8.8 Box results

The blind box and sub-boxes corresponding to $m_{\tilde{q}} - m_{\tilde{g}}$ regions A, B, C, D defined by the optimized $\not\!\!E_T$ and H_T requirements are opened and the observations are given in Table 8.9. There is no significant discrepancy from the Standard Model predictions. In the next chapter the interpretation of the results are given in the SUSY parameter space based on the number of events observed and the number of events expected (counting experiment). The kinematic distributions may be used and the result of the search can be derived in terms of a likelihood function. The shapes of the kinematic variables are examined in this analysis to validate the background Monte Carlo using the data but a likelihood approach is not attempted to extract the result (the results are not expected to differ, however a more careful study of the systematic uncertainties in the shapes of the distributions are necessary and the calculation of the limit becomes significantly more complicated). When higher order QCD jet and QCD associated vector boson production is implemented in the Monte Carlo and larger data samples are available to normalize the predictions, the use of the shapes of the kinematic distributions can be used to increase the sensitivity of the search (Run II). The kinematic distributions for the box and the sub-boxes corresponding to the A/D, B, C regions are given in Figures 8.6, 8.7, 8.8, & 8.9. In Figure 8.10

an event passing all the analysis requirements is displayed.

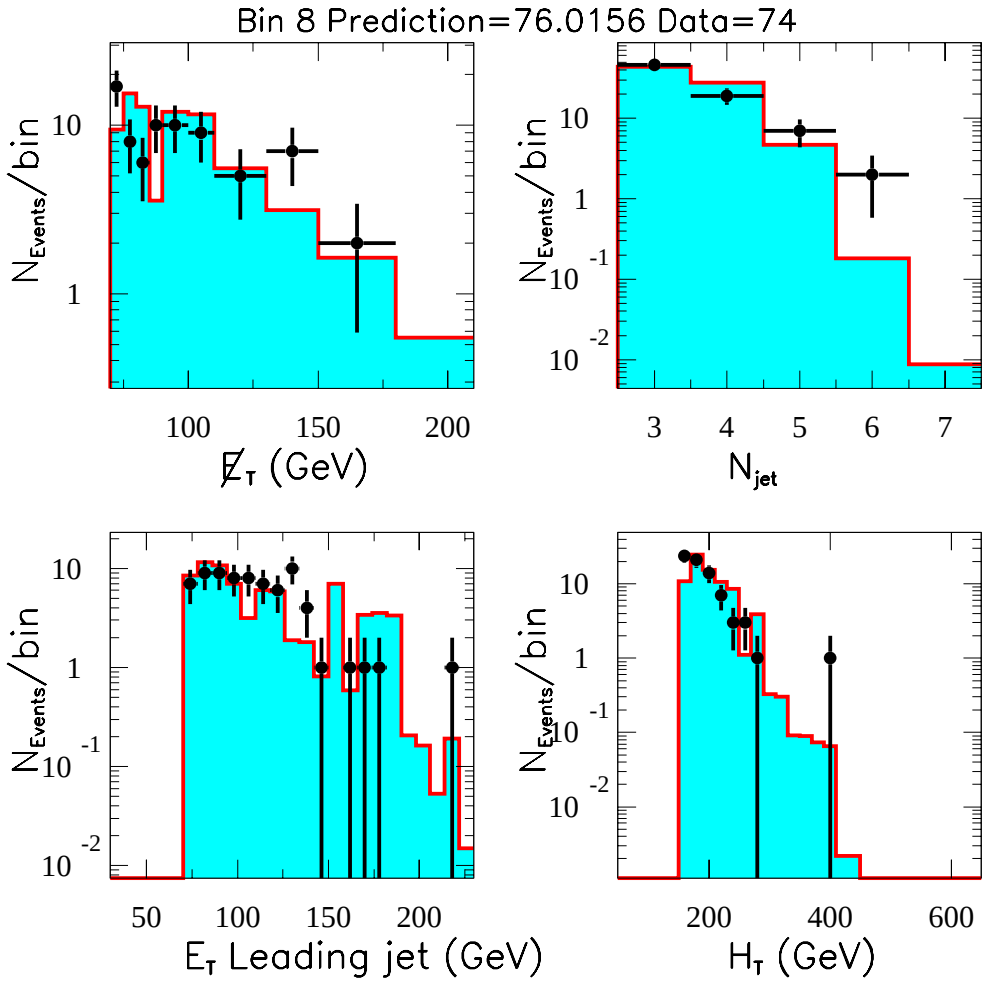

Figure 8.6: Comparison of Standard Model prediction and data in the blind box. The histogram is the Standard Model predictions and the points are the data observed.

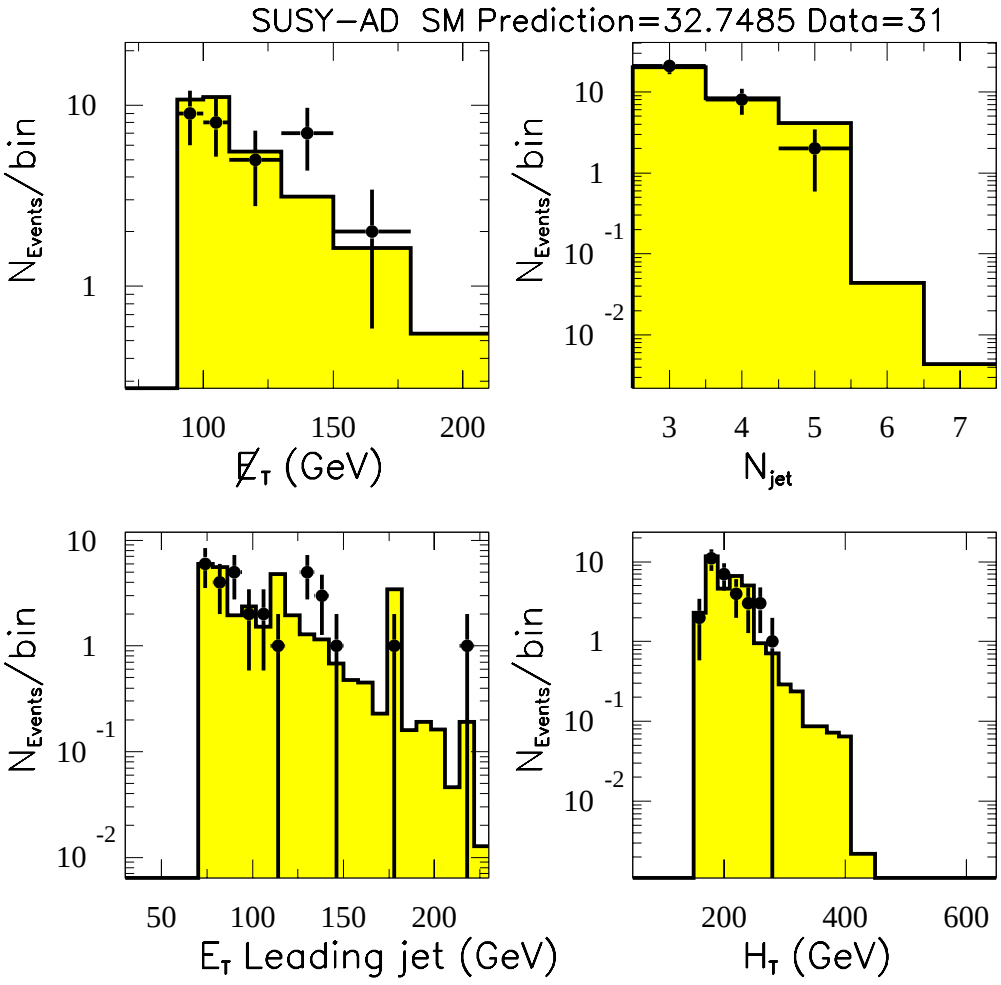

Figure 8.7: Comparison of Standard Model prediction and data in the sub-box optimized for $m_{\tilde{q}}-m_{\tilde{g}}$ regions A and D. The histogram is the Standard Model predictions and the points are the data observed.

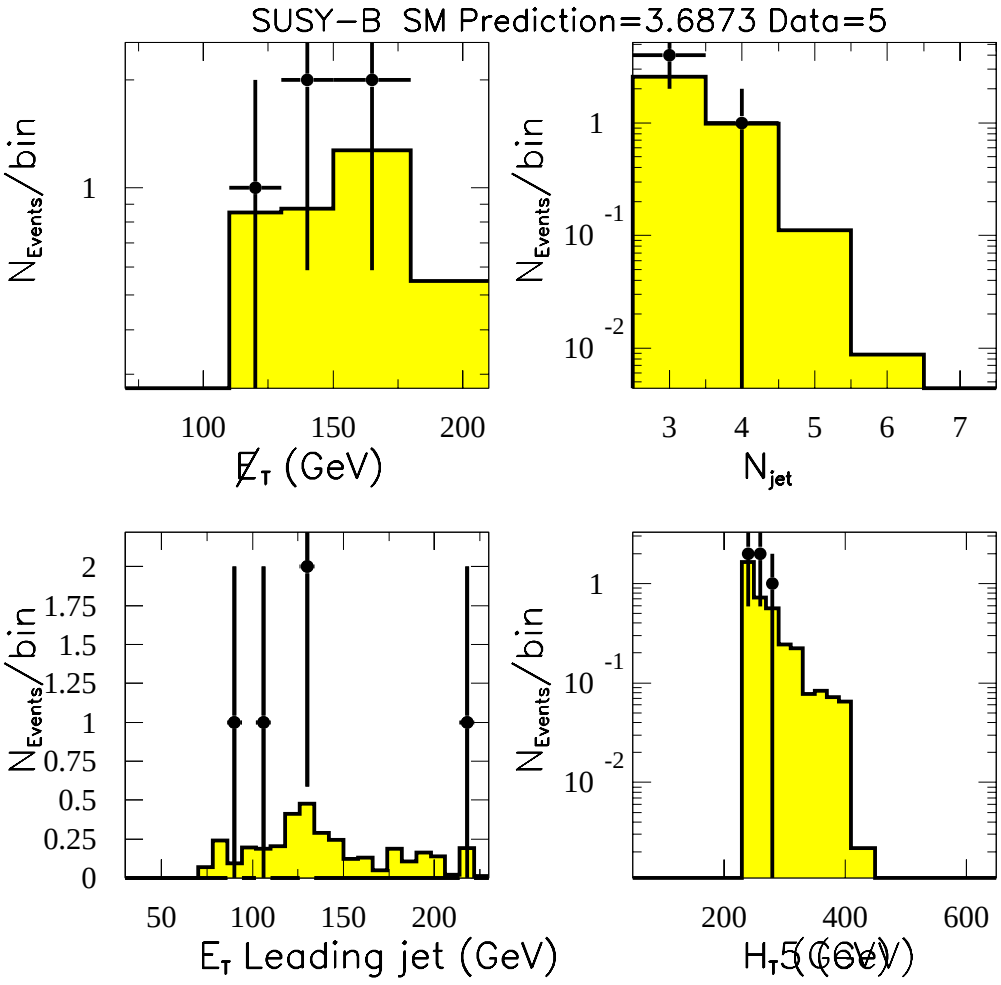

Figure 8.8: Comparison of Standard Model prediction and data in the sub-box optimized for $m_{\tilde{q}} - m_{\tilde{g}}$ region B. The histogram is the Standard Model predictions and the points are the data observed.

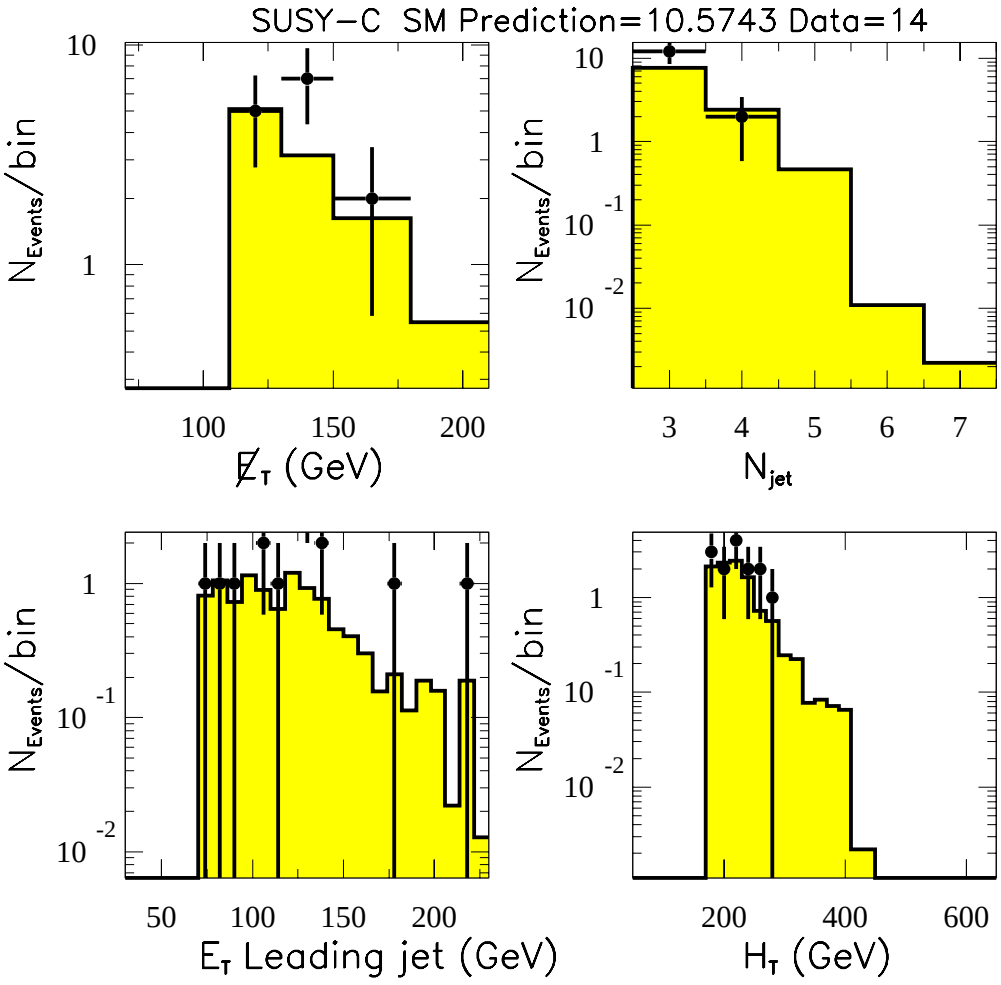

Figure 8.9: Comparison of Standard Model prediction and data in the sub-box optimized for $m_{\tilde{q}} - m_{\tilde{g}}$ region C. The histogram is the Standard Model predictions and the points are the data observed.

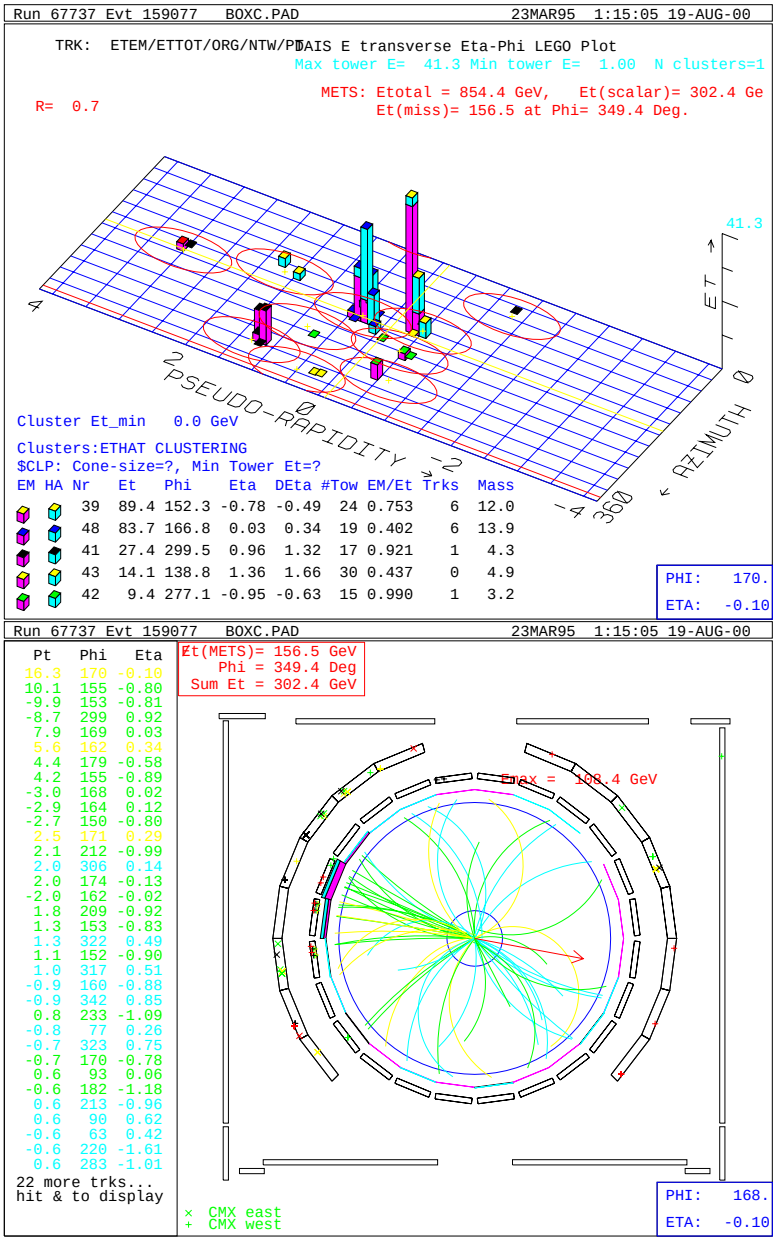

Figure 8.10: (Top) LEGO (Bottom) CTC Event Display of candidate event.

Chapter 9

Interpretation of the results

Based on the observations, the Standard Model expectations and the relative total systematic uncertainty on the signal acceptance in the four analysis regions a 95% C.L. limit is set on the $m_{\tilde{q}} - m_{\tilde{g}}$ plane. For the signal points generated with mSUGRA (regions A and B) the limit is interpreted also in the $M_0 - M_{1/2}$ plane.

9.1 Systematic Uncertainties on the Signal Acceptance

9.1.1 Choice of Q^2 Scale

The Q^2 scale enters in the structure functions, the matrix element and the backward evolution prescription for generating the initial state radiation. In Chapter 7 the dependence of the $\tilde{q}$, $\tilde{g}$ production cross section is discussed. For the relative uncertainty on the signal acceptance the nominal ISAJET Q^2, where $\hat{s}$, $\hat{u}$, $\hat{t}$ are the Mandelstam

variables,

$$Q_0^2 = (\frac{2\hat{s}\hat{t}\hat{u}}{\hat{s}^2 + \hat{t}^2 + \hat{u}^2}) \tag{9.1}$$

is varied between ($Q^2 \times 2$ and $Q^2 \div 2$) for representative signal points. The systematic uncertainty is taken to be the maximum change in the signal acceptance from the nominal scale.

9.1.2 Structure Function

The choice of the structure function affects the total cross section as discussed in Chapter 7. It also affects the development of the parton shower in the initial state radiation. The nominal structure function used in all signal points generation is the MRSA$'$ [73]. The systematic uncertainty is taken to be the average change in the signal acceptance when the CTEQ3L [74] and MRSD0$'$ [75] structure functions are used.

9.1.3 Gluon Radiation

The effect of gluon radiation is studied in ISAJET by varying the parton virtuality cut-off (t_c, `CUTJET [29]` in the generator). The nominal value for t_c^2 is $(6GeV)^2$. This is varied between $(4.2GeV)^2$ and $(8.5GeV)^2$ ($\pm 30\%$). The maximum change in the signal acceptance compared to the nominal value is taken to be the systematic effect from gluon radiation.

9.1.4 Calorimeter Response (Jet Energy Scale)

The calorimeter response is calibrated at dedicated test beams and *in situ* during the collider runs as discussed in Chapter 3. These calibrations are used to set

the response in the detector simulation and to determine the absolute energy scales applied to the data during the event reconstruction. In this analysis all the jets in the signal events are rescaled by $\pm 10\%$ and the average change in the signal acceptance is the systematic uncertainty.

9.1.5 Trigger Efficiency

The parameterization of the L2 MET* trigger efficiency (discussed extensively in Appendix D) is folded in the signal simulation. A 2% systematic uncertainty is used based on the different methods and samples used to measure the trigger efficiency.

9.1.6 Monte Carlo Statistics

The detection acceptance is $\mathcal{A} = N_{pass}/N_{gen}$ with N_{gen} the number of generated events and N_{pass} the number of events satisfying all the analysis requirements. The statistical uncertainty in $\mathcal{A}$ is

$$\delta\mathcal{A}^{stat} = \sqrt{\frac{\mathcal{A}(1-\mathcal{A})}{N_{gen}}} \tag{9.2}$$

This is $< 0.2\%$ for all the signal points generated.

9.1.7 Overall relative uncertainty $\sigma_{\mathcal{A}}$ on the signal acceptance

In Table 9.1 the individual components of the relative systematic uncertainty on the signal acceptance is given for representative signal points. Table 9.2 shows the combined components and Table 9.3 the overall relative uncertainty on the signal acceptance for each region in the $m_{\tilde{q}} - m_{\tilde{g}}$ plane. For region C the maximum between region and B and D is taken.

ind	a16	a14	b13	b4	d18	d6
% CTEQ3M	4.55	6	4	5.5	4.5	4
% MRSD0P	9	1	7	2.5	1	5.5
% $(t_c - 30\%)$	9	5.5	2.5	2.5	1.5	3
% $(t_c + 30\%)$	12.5	6	3	4	3	3
% $(2 \times Q^2)$	6	4.5	7	1	2	4
% $(Q2 \div 2)$	5.5	6.5	3.5	5.5	4	9
% (JET+10%)	6.5	3.5	3.5	2.5	3	6
% (JET-10%)	3	3.5	8.5	10	3	2

Table 9.1: Components of systematic uncertainty (%) on signal acceptance. The first raw contains the index of the signal point used. The raws labeled CTEQ3M and MRSD0P contain the uncertainty due to the corresponding PDFs. The t_c raws contain the uncertainty due to gluon radiation. The Q^2 raws contain the uncertainty due to the variation of the renormalization scale and the JET raws due to the jet energy scale variation.

ind	a16	a14	b13	b4	d18	d6
% <PDFs >	6.5	3.5	5.5	4	3	5
% max(Radiation)	12.5	6	3	4	3	3
% $max(Q^2)$	6.5	6.5	5.5	5.5	4	9
% <JET>	4.5	3.5	6	6	3	4
% Trigger	2					
% MC stat.	<0.2					

Table 9.2: Combined components of relative systematic uncertainty (%) on signal acceptance. The <PDFs> raw is the mean variation due the two PDFs, max(Radiation) is the maximum variation of the two t_c values, the $max(Q^2)$ is the maximum variation of the two scales, the <JET> is the mean of the jet energy scale variation, the Trigger is the variation due to the MET trigger efficiency, the MC stat. is the Monte Carlo statistics.

	A	B	C	D
$\sigma_{\mathcal{A}}\%$	15	11	11	10

Table 9.3: Overall uncertainty $\sigma_{\mathcal{A}}$ on the signal acceptance for the four signal regions.

9.2 Results

9.2.1 Calculation of the limit

Given n_0 the integer number of observed events and μ the number of expected events, the Poisson probability P for observing n_0 is:

$$P(n_0;\mu) = \frac{\mu^{n_0}\exp^{-\mu}}{n_0!} \tag{9.3}$$

The value of μ is the one to be determined. The upper limit N(real) on the number of expected events is defined as μ for which there is some probability to observe n_0 or fewer events. The confidence level (C.L.) of the upper limit is $1-\epsilon$ where ϵ is the sum over the Poisson probabilities:

$$\epsilon = \sum_{n=0}^{n_0} P(n;\mu) \tag{9.4}$$

To calculate N the μ is varied until ϵ is found for the desired C.L. and N is then μ. If the expected background is μ_B and if μ_B is know precisely, then the upper limit on the number of signal events N represents the value μ_S. mu_S is the mean number of signal events expected for which the probability $1-\epsilon$ that in a random experiment more than n_0 events are observed and $n_B \leq n_0$ where n_B is the number of background events observed. Then

$$\epsilon = \frac{\sum_{n=0}^{n_0} P(n;\mu_B+N)}{\sum_{n=0}^{n_0} P(n;\mu_B)} \tag{9.5}$$

According to the PDG [76] this results in a conservative upper limit in that for some true μ_S the probability of obtaining $N > \mu_S$ exceeds on average $1-\epsilon$. Or equivalently

Box	MET,HT	Expected	Observed	$N_{95\%C.L.}$.
A	90,160	32.7 ± 6.7	31	17.7
B	110,230	3.7 ± 0.5	5	7.4
C	110,170	10.6 ± 1	14	11.9
D	90,160	32.7 ± 6.7	31	17.3

Table 9.4: $N_{95\%C.L.}$ upper limit on the number of signal events

if the true μ_S exceeds N there is a probability smaller than ϵ that more than n_0 events would be observed and have $n_B \leq n_0$. Assuming that the value μ_B is known with an overall (statistical plus systematic) Gaussian uncertainty of σ_B and the overall signal acceptance $\mathcal{A}$ is known to within $\sigma_{\mathcal{A}}$, the Poisson upper limit N on μ_S for which more than n_0 events would be observed and $n_B \leq n_0$ is found by [77]

$$\epsilon = \frac{\sum_{n=0}^{n_0} \frac{1}{\sqrt{2\pi\sigma_N^2}} \int_0^\infty \int_0^\infty P(n; \mu'_B + \mu'_S) e^{-\frac{(\mu_B - \mu'_B)^2}{2\sigma_B^2}} e^{-\frac{(N - \mu'_S)^2}{2\sigma_N^2}} d\mu'_B d\mu'_S}{\sum_{n=0}^{n_0} \int_0^\infty P(n; \mu_B) e^{-\frac{(\mu_B - \mu'_B)^2}{2\sigma_B^2}}} \tag{9.6}$$

where $\sigma_N = N\sigma_{\mathcal{A}}/\mathcal{A}$. An *a priori* Gaussian distribution of the true values of μ_S and μ_B with width given by the signal and background overall uncertainties is assumed. The integral is performed by generating large ensemble of pseudo-experiments and varying the expected number of signal and background about their nominal values according to a Gaussian distribution. The expected number of signal and background events are chosen from the Gaussian and Poisson distributed numbers of generated signal (n_s) and background (n_B). For the trials that $n_B \leq n_0$ the fraction f in which $n_B + n_S > n_0$ is the confidence level for a given N. N is varied until the desired C.L. is obtained. The 95% C.L. upper limit on the number of signal events ($N_{95\%}$) for the

three analyses (A/D, B, C) of the $\tilde{q}$, $\tilde{g}$ signal is given in Table 9.4.

9.3 The Limit

The information for all the signal points generated is given in Tables 9.5 & 9.6. Figures 9.1 & 9.2 show the 95% C.L. limit in the $m_{\tilde{q}} - m_{\tilde{g}}$ and $M_0 - M_{1/2}$ planes respectively (CDF 1B, this analysis). The result of the search is negative at 95% C.L. for gluino masses below 300 GeV/c^2 for the case $m_{\tilde{q}} = m_{\tilde{g}}$, 195 GeV/$c^2$ for the case $m_{\tilde{q}} >> m_{\tilde{g}}$, and 570 GeV/$c^2$ for $m_{\tilde{q}} << m_{\tilde{g}}$. In Figure 9.1 also the results from previous searches are shown: UA1 ([78]), UA2 ([79]), LEP I ([80]), LEP II ([83]), CDF 89 ([84]), D0 ([85]) and CDF 1A ([86]). The region indicated as $m_{\tilde{q}} < m_{\tilde{\chi}_1^0}$ is excluded because the squark is lighter than the LSP. In Figure 9.2 the D0 result [87] is also shown. The region indicated as EWKSB is excluded because there is no electroweak symmetry breaking.

9.4 Discussion

9.4.1 Gluino mass and fine-tuning

As discussed in Chapter 7 although the notion of naturalness and fine-tuning [49] is not very well defined, it is unavoidable since it is the fine-tuning in the Standard Model that motivates low-energy supersymmetry and supports the projection that superpartners should be found before or at the LHC. Many measures and studies of fine-tuning have appeared in the literature [50, 51, 52, 53, 54].

In a model-independent analysis [89], naturalness constraints are weak for some superpartners, *e.g.* the squarks and sleptons of the first two generations. In widely

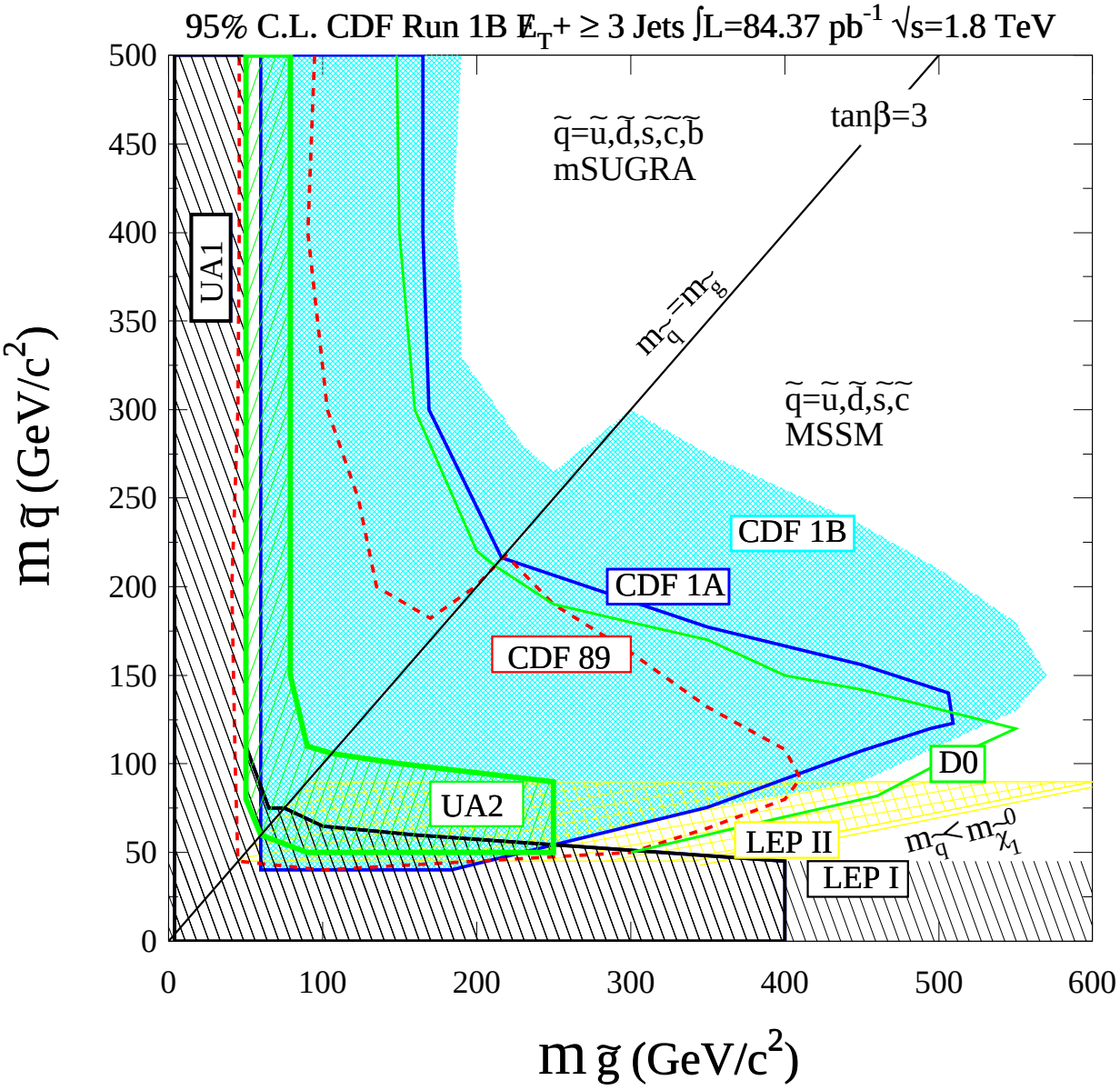

Figure 9.1: 95% C.L. Limit curve in the $m_{\tilde{q}}$ − $m_{\tilde{g}}$ plane. Results from previous searches are shown: UA1 ([78]), UA2 ([79]), LEP I ([80]), LEP II ([83]), CDF 89 ([84]), D0 ([85]) and CDF 1A ([86]). The region indicated as $m_{\tilde{q}} < m_{\tilde{\chi}_1^0}$ is excluded because the squark is lighter than the LSP.

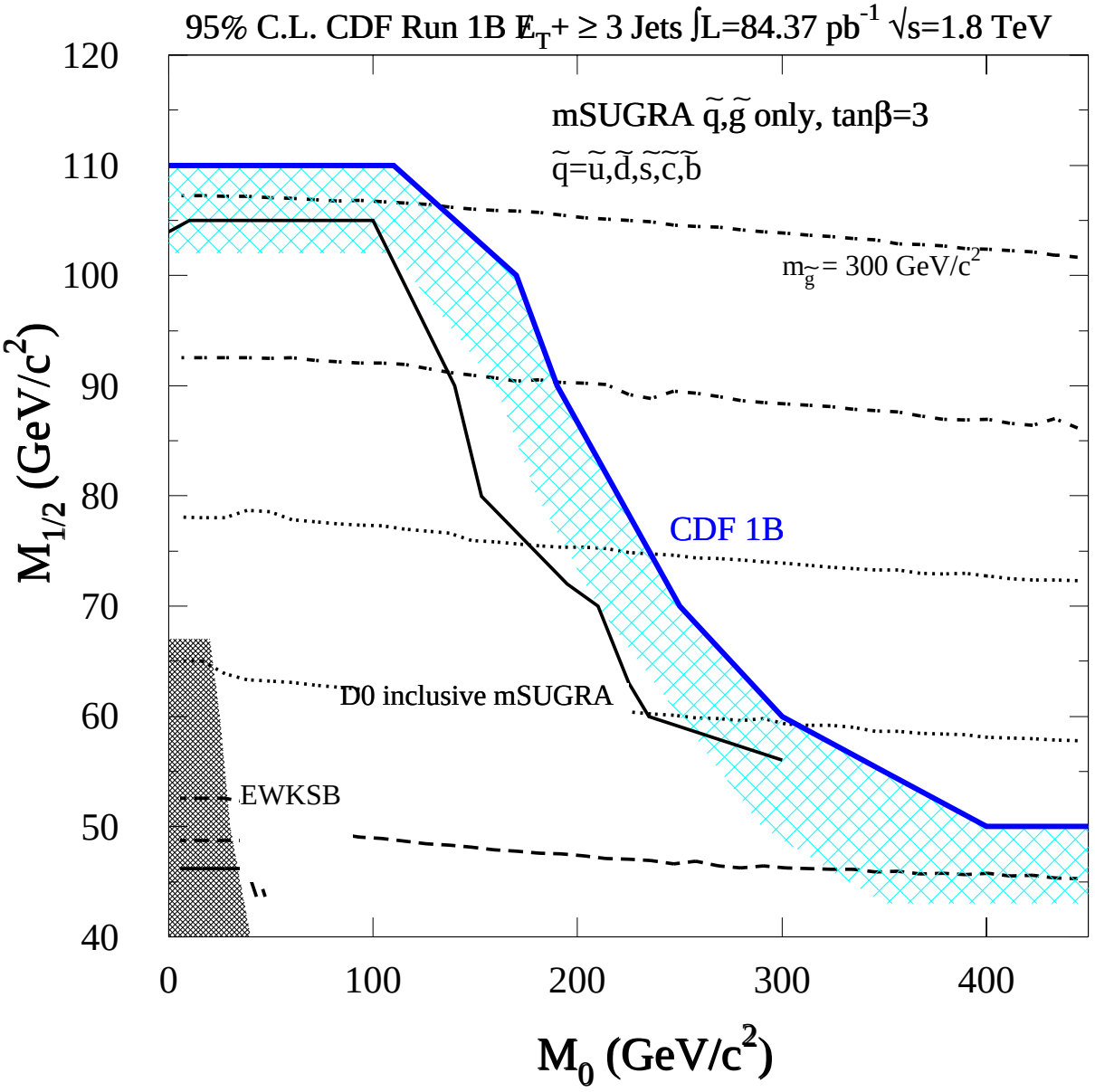

Figure 9.2: 95% C.L. Limit curve in the $M_{1/2}$ – M_0 plane. The D0 result [87] is shown. The region indicated as EWKSB is excluded because there is no electroweak symmetry breaking. The dotted and dashed lines are the iso-gluino mass curves.

ind	M_0	$M_{1/2}$	$m_{\tilde{q}}$	$m_{\tilde{g}}$	$m_{\tilde{\chi}_1^0}$	σ_{NLO}	BOX	A/B	$\mathcal{A}$	SUSY
	GeV/c^2					pb	N_{events}		$\times 100\%$	
a1	470	50	480	181	23	11.9	46.09	19.16	0.02	x
a2	450	70	469	237	31	1.41	12.6	6.75	0.06	$\surd$
a3	400	70	425	237	31	1.32	12.6	6.91	0.06	$\surd$
a4	400	50	409	179	23	11.99	48.5	20.86	0.02	x
a5	350	50	370	177	23	12.65	50.1	22.81	0.02	x
a6	350	70	370	235	31	1.4	13.4	7.34	0.06	$\surd$
a7	300	60	330	204	27	4.6	32.5	16.74	0.04	$\surd$
a8	270	70	320	230	32	2.09	21.2	12.1	0.07	$\surd$
a9	250	70	300	230	32	2.51	26.3	15.72	0.07	$\surd$
a10	210	65	260	212	30	6.32	59.4	34.3	0.06	x
a11	300	40	310	146	19	48.64	101.5	45.5	0.01	x
a12	250	50	277	173	23	17.28	83	38.6	0.03	x
b1	170	100	299	300	44	0.78	15.6	7.65	0.10	$\surd$
b2	110	110	295	319	48	0.74	13.76	7.36	0.11	$\surd$
b3	90	110	288	319	48	0.87	14.57	8.63	0.09	x
b4	0	110	274	318	48	1.24	16.8	8.87	0.08	x
b5	150	90	275	275	40	1.72	30.3	12.64	0.08	x
b6	170	90	263	247	40	3.16	46.43	14.9	0.06	x
b7	50	100	256	292	44	2.3	30.48	13.8	0.07	x
b8	110	90	251	270	40	3.11	51.6	20.74	0.08	x
b9	90	90	244	269	40	3.7	54.13	20.45	0.06	x
b10	150	70	231	220	32	8.83	105.88	26.43	0.04	x
b11	70	60	226	197	28	14.65	112.03	17.06	0.02	x
b12	190	90	292	280	40	1.14	23	10.05	0.09	x
b13	161	97	290	290	43	1.1	19.9	8.9	0.09	x
a13	200	65	256	210	30	7.	65.5	37	0.06	x
a14	200	67	263	210	30	6.4	61.7	36	0.07	x
a15	350	55	368	191	25	7.2	38.2	18	0.03	x
a16	400	55	413	193	25	6.9	35.	16	0.03	$\surd$
a17	470	55	478	195	25	6.9	32.6	15	0.03	$\surd$
a18	210	70	274	227	31	3.7	41	24.9	0.08	x

Table 9.5: Signal Points generated according to mSUGRA (analysis regions A,B). x stands for excluded at 95% C.L. and $\surd$ for allowed. M_0, $M_{1/2}$ are the common scalar and gaugino masses, $m_{\tilde{q}}$, $m_{\tilde{g}}$ are the scalar quark and gluino masses at the electroweak scale, $m_{\tilde{\chi}_1^0}$ is the LSP mass and σ_{NLO} is the cross section. $\mathcal{A}$ is the signal acceptance in the analysis region A or B correspondingly. In the column "BOX" the number of events in the general blind box is given for each point.

ind	$m_{\tilde{q}}$	$m_{\tilde{g}}$	$m_{\tilde{\chi}_1^0}$	μ	A_t	σ_{NLO}	BOX	BOXC/D	$\mathcal{A}$	SUSY
	GeV/c^2					pb	N_{events}		$\times 100\%$	
c1	220	250	37	-800	-500	7.6	114.3	52.15	0.08	x
c2	225	300	46	-800	-500	4.67	73.6	34.	0.09	x
c3	225	325	50.6	-800	-500	4.13	63.9	29.5	0.08	x
c4	200	275	42	-800	-500	10.4	132.9	51.6	0.06	x
c5	200	325	50	-800	-500	8.14	96.9	36	0.05	x
c6	200	370	57.7	-800	-1000	6.92	57.1	22.5	0.04	x
c7	175	250	40	-800	-500	24.11	234.1	71.04	0.03	x
c8	150	275	42.2	-800	-500	43.2	227.6	59.7	0.02	x
c9	150	300	46.2	-800	-500	38.45	178.7	47.2	0.01	x
c10	150	325	50	-800	-500	34.76	143.7	37.2	0.01	x
c11	150	370	57.7	-800	-1000	30.27	82.2	24.5	0.01	x
c12	125	250	38.3	-800	-500	109	315.4	70.1	0.008	x
c13	275	325	49.	-800	-500	1.13	23	13.7	0.14	$\surd$
c14	275	350	53.	-800	-500	1.	19.8	11.7	0.14	$\surd$
c15	225	375	58	-800	-500	3.44	49.2	21.8	0.07	x
c16	250	350	53.6	-800	-500	1.9	34.3	18	0.11	x
d1	180	400	62.2	-800	-500	11.24	68.33	40.6	0.04	x
d2	180	450	70.4	-800	-1000	9.98	36.7	23.3	0.03	x
d3	160	500	78.3	-800	-1000	16.51	49.7	27.7	0.02	x
d4	150	450	70.3	-800	-1000	25	68.7	39	0.02	x
d5	150	500	78.3	-800	-1000	22.72	59.2	33.8	0.02	x
d6	150	550	86.3	-800	-1000	20.9	38.9	20.6	0.012	x
d7	150	570	89.5	-800	-1000	20.3	34.2	18.3	0.01	x
d8	130	450	70	-800	-1000	49.4	74	36.5	0.008	x
d9	130	500	78	-800	-1000	45.2	48	25.3	0.006	x
d10	110	400	62	-800	-1000	117	94.6	54.3	0.002	x
d11	110	450	70	-800	-1000	107	52.9	24.5	0.003	x
d12	105	500	77	-800	-1000	123	25	11.5	0.001	$\surd$
d13	120	550	86	-800	-500	61.7	22.2	10.5	0.002	$\surd$
d14	90	400	62	-800	-1000	288.6	57.3	31.7	0.002	x
d15	95	370	57.3	-800	-1000	239	109	64.9	0.004	x
d16	100	325	50	-800	-500	211.7	169.2	86.2	0.006	x
d17	200	400	62	-800	-500	6.4	60.86	38.4	0.07	x
d18	225	400	70	-800	-500	3.2	42.6	29.6	0.11	x
d19	200	450	70	-800	-500	5.6	45.6	28.7	0.06	x
d20	250	450	70	-800	-500	1.4	23.3	17.4	0.14	$\surd$
d21	200	500	70	-800	-500	5.1	35.1	21.4	0.05	x
d22	225	450	72	-800	-500	2.82	85.86	24.84	0.11	x

Table 9.6: Signal Points generated according to MSSM (analysis regions C,D). x stands for excluded at 95% C.L. and $\surd$ stands for allowed.

considered scenarios with scalar mass unification at a high scale, such as minimal supergravity, it is assumed that the squark and slepton masses must be $\lesssim$1 TeV/c^2. This bound places all scalar superpartners within the reach of present and near future colliders. This assumption is re-examined [54] in models with strong unification constraints and the squarks and sleptons are found to be natural even with masses above 1 TeV/c^2. Furthermore by relaxing the universality constraints the naturalness upper limits on supersymmetric particles increase significantly [51] without extreme fine-tuning. This suppresses sparticle mediated rare processes and the problem of SUSY flavor violations is ameliorated. The fine-tuning due to the chargino mass is found to be model dependent [53]. With or without universality constraints the gluino remains below 400 GeV/c^2 [51]. In fact, as it is pointed in [53] the tightest constraints on fine-tuning come from the experimental limits on the lightest CP-even Higgs boson and the gluino for a number of supersymmetry models. It is then those two key particles that are within reach of the present (Tevatron, LEP) colliders. These results follow from the observation that fine-tuning is mainly dominated by M_3, the gluino mass parameter at the electroweak scale, and this dominant contribution can be partly canceled by negative contributions from other soft parameters as can be seen from the expansion of the Z mass in terms of the input parameters and for fixed $\tan\beta = 2.5$ [53] :

$$M_Z^2 = -1.7\mu^2(0) \; + \; 7.2M_3^2(0) \; - 0.24M_2^2(0) \; + \; 0.014M_1^2(0) + ... \qquad (9.7)$$

The required cancellation is easier if $M_3(0)(= m_{\tilde{g}})$ is not large (or alternatively if M_2

is increased for a given M_3). Using the results of this analysis on the gluino mass

$$M_3 \gtrsim 300 \rightarrow \frac{7.2 M_3^2}{M_Z^2} \gtrsim 80. \tag{9.8}$$

A similar relation is derived using the LEP limits on the chargino $m_{\widetilde{\chi}_1^+} \gtrsim 100$ GeV/c^2 [90, 91] that points to the consideration of gaugino mass non-unification with a lighter gluino. The main effect of a relatively light gluino is the enhancement of the missing energy plus multijet signal with a lepton veto since for a given chargino mass not yet excluded, the $\widetilde{g}\widetilde{g}$ cross section is enhanced and the gluino cascade decays through charginos are suppressed (fewer leptons are produced in the final state [65, 92]).

9.4.2 The $\not\!\!E_T$ trigger for RUN II

The $\not\!\!E_T$ trigger drives a number of analyses and the need for a carefully designed $\not\!\!E_T$ trigger for the Run II luminosity environment is evident. A few of the physics processes that are studied with a data sample triggered by large energy imbalance are the following:

- **Vector boson** production and leptonic decays. Although there is a dedicated $\not\!\!E_T$ plus lepton trigger for the study of the W boson, W QCD associated production remains a crucial background for a number of searches beyond the Standard Model and the $\not\!\!E_T$ plus jets trigger provides a good sample to study these processes. For Z production and decay, the $\not\!\!E_T$ sample provides a dataset to measure directly the $Z \rightarrow \nu\bar{\nu}$ + jets cross section. Furthermore again, the Z boson QCD associated production is a background to many searches.

- **top quark** production and decay to a $W + b$. The $\not\!\!E_T$ trigger provides an alternate dataset to measure the top cross section.

- Associated **Higgs**-W and Higgs-Z production. The $\not\!\!E_T$ combined with a b quark tagging or a tau lepton tagging trigger can provide a highly efficient triggering scheme for the discovery of the Higgs boson.

- Beyond the Standard Model searches. To mention a few, the $\not\!\!E_T$ trigger can be used to search for:

  - **Supersymmetric partners**: In R-Parity conserving supersymmetric scenarios the LSP escapes the detector and appears as energy imbalance. Examples are squark and gluino searches, scalar top and scalar bottom quark (utilizing an additional heavy flavor tag) searches.

  - **Gravitino**: In Gauge Mediated Supersymmetry Breaking scenarios that incorporate gravity the Lightest Supersymmetric Particle is the gravitino – the spin 3/2 partner of the graviton. The gravitino goes undetected and produces energy imbalance [8].

  - **Leptoquarks**: The leptoquark decays to a quark and a neutrino [7] resulting in large $\not\!\!E_T$.

  - CHArged Massive Particles (**CHAMPS**): These are long-lived massive particles that if they are penetrating enough can go undetected and cause energy imbalance [93].

  - **Gravitons**: In Kaluza-Klein-type theories of extra dimensions [94] the graviton can be produced in high energy hadron collisions and escapes to the extra spatial dimensions resulting in energy imbalance [95, 96].

The specifications of the $\not\!\!E_T$ trigger for RUN II are determined using the Run 1B data [42]. The main feature of the trigger is the lower Level 2 $\not\!\!E_T$ threshold (25 GeV compared to 35 GeV in Run 1B).

Appendix A

The Fermilab Tevatron Collider

A.1 Introduction

The predicted high mass of the W and Z bosons inspired the development of high energy $p\bar{p}$ colliders. In the mid 1970s, conventional fixed target machines at Fermilab and CERN produced a maximum center of mass energy of 30 GeV much less than 80 or 90 GeV required for a W or a Z. The center of mass energy of e^+e^- colliders was not adequate either. The ISR at CERN had a center of mass energy of 63 GeV, but it was a proton-proton machine and even with an increase in energy the probability of finding a high-x antiquark in either proton with which to produce a W or Z was very small . The alternative was to collide protons with antiprotons. The valence quarks from each beam could produce a weak boson and the beams could be accelerated by the same lattice of magnets which would be cost effective. At the time, the technology for producing, storing and reaccelerating antiprotons was in early development and the possibility of generating sufficient luminosity to observe the W and Z bosons seemed remote.

A.2 Stochastic Cooling

The major obstacle to producing high intensity antiproton beams is phase space density. When a beam of protons strikes a production target the yield of antiprotons is relatively low and covers a large volume of the phase space. It is necessary in order to cool the antiprotons, to pack them densely in the phase space. Stochastic cooling developed by Simon van der Meer [88, 97] and his colleagues at CERN was one of the most significant technological developments toward high intensity antiproton beams. In the case of a single particle the basic idea is illustrated in Figure A.1.

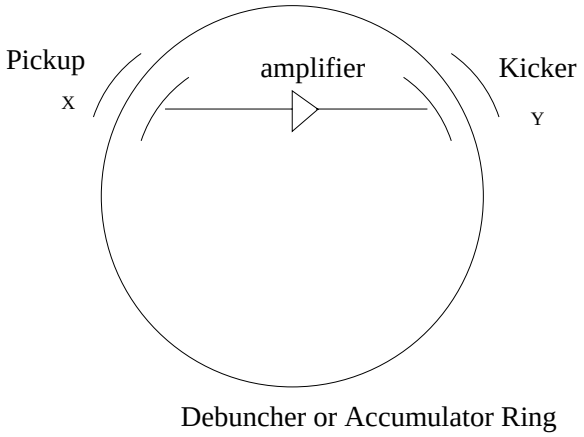

Figure A.1: Naive Stochastic Cooling.

If the radial position of a particle at position X is slightly off, a sensor picks it up and sends a correcting pulse across the ring to point Y. In the case of a beam of 10^7 protons, cooling is more complicated. The sensor will not sample single particles. And according to Liouville's Theorem the phase space of a system of particles cannot change at the presence of conservative forces such as the magnetic kickers employed in an accelerator. The size of the beam in Energy, time called longitudinal and in $p_x,\ p_y$

called transverse emittance remain the same as the system propagates. Stochastic cooling is better examined in the time domain. The phase of each particle to the ideal revolution frequency is corrected by a sensor-kicker system. Each particle contributes to its own correction and tends to change its motion coherently. The other particle's contribution to the motion of a single particle is "heating", a kind of random walk process with the sign of the contribution depending on the relative phase and the net effect goes as the square root of the number of other particles. The coherent cooling effect is proportional to the correction while the heating effect goes as the square root of the correction and there is always a gain such that the coherent correction dominates the heating.

Two kinds of stochastic cooling are employed in the storage of antiprotons *The Betatron cooling* [101] which is a damping of the particles transverse motion . A small transverse emittance is important to get large numbers of antiprotons in the beam and high luminosity. A parallel plate pickup detects the position of a sample of particles with non-zero transverse dispersion, runs the correcting signal across a chord of a circle (as in the naive one particle example) to a point of zero dispersion and gives the particle the correct transverse momentum. *Longitudinal cooling* decreases the energy spread of the beam. It is used in the Accumulator to pack antiprotons in a very small region of the phase space which is described by a core energy and a narrow width. There two basic cooling techniques, both employed at Fermilab, the Palmer and the Filter cooling. The Palmer cooling is similar to Betatron cooling. The correction signal however corrects the energy with a longitudinal boost. The Palmer technique is used in the Accumulator to cool the antiprotons from the Debuncher down to a core energy. If T is the revolution time of a particle with the desired energy, in any given cycle, the signal picked up by the sensor delayed by the ideal

period of revolution and subtracted from itself gives the correction. If the result is zero, the particle has ideal mean energy and no kick is applied. Otherwise depending on the sign the kicker will increase or decrease its energy. This is the technique to keep the antiprotons at the desired core energy when they are cooled down into a stack. A more detailed discussion on stochastic cooling can be found in References [98, 100, 99].

A.3 The Cycle

Figure A.2 is an aerial view of the Tevatron [102] and the principal accompanying machines.

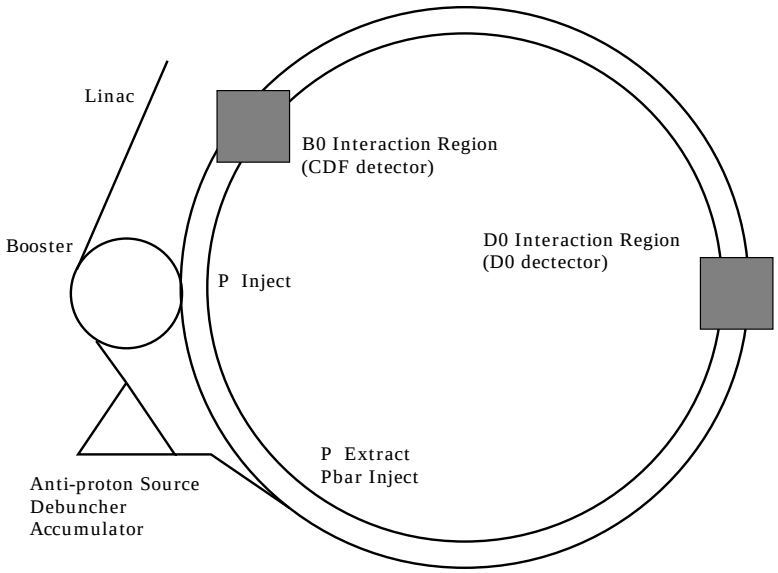

Figure A.2: The Tevatron Complex.

The proton beam begins as hydrogen anions which are accelerated to about 50 MeV in the Cockroft-Walton accelerator. They go into the Linac where they are

accelerated to about 500 MeV. The beam is injected to the Booster which brings the beam energy up to 8 GeV. From the Booster, protons are transferred to the Main Ring which brings them to 500 GeV and injects them to the Tevatron, a ring of superconducting magnets which lies below the Main Ring (apart form detours near the collision areas). At least 10^{12} antiprotons must be produced and stored. Production begins at the Main Ring. A bunch of protons from the Booster in injected in the Main Ring, brought to 120 GeV. In order that the antiprotons which they will produce have the correct longitudinal emittance, an RF manipulation, know as bunch rotation is needed. The RF field in the Main Ring is lowered adiabatically and the energy spread of each beam shrinks. It is then quickly raised to its initial value. The bunches begin synchrotron oscillation in the mismatched buckets. Since the spread in energy E, δE times the spread in time t, δt is a constant (Liouville's Theorem), the δt will be at a minimum after a quarter cycle of synchrotron oscillation at which point the beam is extracted and focused on a tungsten target. Groups of anti-protons produced mainly at small angles with respect to the initial bin direction and having a mean momentum of 10 GeV are magnetically focused by a current pulsed lithium lens and injected into the Debuncher ring. Their energy spread is about 2%, too large for the acceptance of the Accumulator. Their short time spread produced by the bunch rotation in the Main Ring is exchanged for a smaller energy spread by further rotating them in the Debuncher. The resultant bunch length is the entire length of the Debuncher. In order to match the beam emittance to the acceptance of the accumulator, the Debuncher ring also reduces the beam's transverse emittance with two seconds of Betatron cooling.

The beam is then transferred to the Accumulator, whose primary function is to cool and store large numbers of anti-protons in small phase space characterized by a

a core energy and a very narrow spread. Anti-protons enter the Accumulator with a high momentum and are longitudinally cooled into the core, a process known as *stacking*, which takes about two hours per bunch. As one batch of anti-protons heads for the core, new bunches arrive. Cooling is most rapid at the outer edge of the stack where new anti-protons arrive with each cycle and old batches must be removed. Because the gradient of the energy density seen by the batch changes as it cools down towards the core, the amplifier response must vary with energy. In the course of three to four hours, the anti-proton energy density grows to more than 10^5 $\bar{p}$/eV.

When a sufficient number of anti-protons has been stored and all transfer systems have been checked, the injection of anti-protons into the Tevatron, known as *shot*, begins. The injection cycle starts as about ten bunches of protons are extracted from the Booster and injected into the Main Ring. They are accelerated to 150 GeV. The batches in the Main Ring are *cogged*: the RF is adjusted so that they are at the proper radius. The bunches are than *coalesced*, the ten odd bunches are turned into one. Coalescing involves some of the techniques used in the anti-proton production cycle. The RF field is lowered, which lowers $\delta E/E$ for each bunch. A much lower frequency field is turned on, and the mismatched beam rotates in phase space for a quarter-cycle in the larger bucket until its time spread is at minimum, whereupon the high frequency field is quickly turned back on and captures most of the protons in a single bucket. This bunch is injected into the Tevatron. Two others follow. When the protons are in place, a fraction of the anti-proton store is moved in a bunch from the stack and accelerated to an extraction orbit. Another RF system of the same frequency as the one holding the bunch together, but of higher voltage, is then turned on and shortens the bunch. The RF is raised and the one large bunch is broken into nine smaller bunches, which are extracted from the accumulator and are

injected into the Main Ring. There, they are treated as the protons before them, and are injected into the Tevatron between the proton bunches.

Once both anti-proton and proton bunches are in, the magnets' currents are ramped to the top, and the two beams are accelerated to 900 GeV and stored. To increase the CDF luminosity, the low-β quadrupoles at both ends of the B0 collision hall are activated, a process known as *squeezing*. The frequencies of the two RF systems, which act on protons and anti-protons separately, are adjusted, advancing or retarding the beams so that the center of collision is at the nominal CDF vertex. From time to time, there is one final step, that of beam *scraping*, which eliminates some of the halo from errant protons and anti-protons.

A.4 Main Ring Operation

The Main Ring during Run 1B was used in three different modes: proton acceleration from 8 GeV to 120 GeV for antiproton production, proton acceleration from 8 GeV to 150 GeV with coalescing and cogging for Tevatron injection and antiproton acceleration from 8 GeV to 150 GeV with coalescing and cogging for Tevatron injection. In the first two modes the Main Ring accepts beam from the Booster and in the third mode from the antiproton source. In all of these operating modes the performance during Run 1B exceeds that of previous runs. In the cycles of the Main Ring operation which are used to fill the Tevatron for collider operations, there is particle loss from injection through transition energy and the total loss is about 20%. A few percent (<3%) of particles are lost between 20 GeV and 150 GeV. The proton loss during cogging and coalescing is about 25% due to the limited momentum aperture at flat-top. The average transfer efficiency through the Main Ring during antiproton

production cycle is at best 80%, whereas the average transfer efficiency of coalesced proton and antiproton bunches are 50% and 70% respectively. During Run 1B there was a coalescing upgrade which resulted in an increase in proton transfer efficiency and a subsequent decrease in the percentage of protons in satellite bunches. The typical satellite bunches after the coalescing upgrade have intensities less than 2% of the central bunch intensity compared with 8-12% before. The result is considerable reduction in background due to parasitic collisions.

Appendix B

QCD Level 2 Trigger Requirements

B.1 L2 Missing Energy Triggers

TRIGGER MET_35_TEX_2_NOT_GAS

```
SELECT MISSING_ET
CUT MISSING_ET_SQUARED >= 1225.  (GeV**2)
SELECT CALOR_CLUSTER
CUT NUMBER_OF_CALOR_CLUSTERS >= 1
SELECT TEXAS_FILTER ! Cut out "Texas Towers"
CUT HIGH_ET_JET_MIN_EM_ET >= 2.0 (GeV)
SELECT SINGLE_CLUSTER_CUT ! Leading cluster not gas cal.
PARAMETER CLUSTER_TYPE = 1 !  highest Et
PARAMETER CLUSTER_QUANTITY = 17 !  Yseed
PARAMETER COMPARE_TYPE = 5 !  >
CUT THRESHOLD = 15 !  (0-15 are plug and frwd West)
SELECT SINGLE_CLUSTER_CUT
```

```
PARAMETER CLUSTER_TYPE = 1 !  highest Et
PARAMETER CLUSTER_QUANTITY = 17 !  Yseed
PARAMETER COMPARE_TYPE = 6 !  <
CUT THRESHOLD = 26 !  (26-41 are plug and fwd East)
```

TRIGGER MET_35_TWO_JETS

```
SELECT MISSING_ET CUT MISSING_ET_SQUARED >= 1225.  (GeV**2)
SELECT CALOR_CLUSTER
CUT NUMBER_OF_CALOR_CLUSTERS >= 2
SELECT SINGLE_CLUSTER_CUT ! Leading cluster not forward:
PARAMETER CLUSTER_TYPE = 1 !  highest Et
PARAMETER CLUSTER_QUANTITY = 17 !  Yseed
PARAMETER COMPARE_TYPE = 5 !  >
CUT THRESHOLD = 9 !  (0-9 are forward West)
SELECT SINGLE_CLUSTER_CUT
PARAMETER CLUSTER_TYPE = 1 !  highest Et
PARAMETER CLUSTER_QUANTITY = 17 !  Yseed
PARAMETER COMPARE_TYPE = 6 !  <
CUT THRESHOLD = 32 !  (32-41 are forward East)
SELECT SINGLE_CLUSTER_CUT ! 2nd leading cluster not forward
PARAMETER CLUSTER_TYPE = 2 !  2nd highe
PARAMETER CLUSTER_QUANTITY = 17 !  Yseed
PARAMETER COMPARE_TYPE = 5 !  >
CUT THRESHOLD = 9 !  (0-9 are forward West)
SELECT SINGLE_CLUSTER_CUT
```

```
PARAMETER CLUSTER_TYPE = 2 !  2nd highest Et
PARAMETER CLUSTER_QUANTITY = 17 !  Yseed
PARAMETER COMPARE_TYPE = 6 !  <
CUT THRESHOLD = 32 !  (32-41 are forward East)
SELECT SINGLE_CLUSTER_CUT ! Cut on Et of leading cluster
PARAMETER CLUSTER_TYPE = 1 !  highest Et
PARAMETER CLUSTER_QUANTITY = 1 !  EM Et
PARAMETER COMPARE_TYPE = 5 !  >
CUT THRESHOLD = 1 !  (0-9 are forward West)
SELECT SINGLE_CLUSTER_CUT ! Cut on Et of2nd leading cluster
PARAMETER CLUSTER_TYPE = 2 !  2nd highest Et
PARAMETER CLUSTER_QUANTITY = 1 !  EM Et
PARAMETER COMPARE_TYPE = 5 !  >
CUT THRESHOLD = 1 !  (0-9 are forward West)
```

B.2 L2 JET20, JET50, JET70, JET100 triggers

TRIGGER JET_20_TEX_0_PRE_25_V2

```
PREREQUISITE L1_4_PRESCALE_40
EXECUTE LEVEL2_PRESCALING
PARAMETER PRESCALE_FACTOR = 25
SELECT JET1
PARAMETER ET_THRESHOLD >= 20.  (GeV)
CUT NUMBER_OF_JETS_1 >= 1
SELECT TEXAS_FILTER ! Cut out "Texas Towers"
```

```
   CUT HIGH_ET_JET_MIN_EM_ET >= 0.5 (GeV)
```

TRIGGER JET_50_V3

```
   PREREQUISITE L1_4_PRESCALE_40
   SELECT JET1
   PARAMETER ET_THRESHOLD >= 50.  (GeV)
   CUT NUMBER_OF_JETS_1 >= 1
```

TRIGGER JET_70

```
   EXECUTE LEVEL2_PRESCALING
   PARAMETER PRESCALE_FACTOR = 8
   SELECT JET1
   PARAMETER ET_THRESHOLD >= 70.  (GeV)
   CUT NUMBER_OF_JETS_1 >= 1
```

TRIGGER JET_100

```
   EXECUTE LEVEL2_PRESCALING
   PARAMETER PRESCALE_FACTOR = 1
   SELECT JET1
   PARAMETER ET_THRESHOLD >= 100.  (GeV)
   CUT NUMBER_OF_JETS_1 >= 1
```

B.3 L2 SUMET Trigger

TRIGGER TOTAL_ET_175_CLUSTER_SUM

```
   SELECT TOTAL_CLUSTER_ET_1
```

```
CUT TOTAL_ET >= 175.  (GeV)
```

Appendix C

Data Pre-Selection Studies

C.1 Tower Timing and Energy Study

The requirements for a Central Tower and an End Wall tower to be declared to be Out-of-Time are shown in Table C.1. Δt is considered relative to the beam crossing

EHAD(CHA tower) $>$ 1 GeV
$\Delta t <$ -20 ns or $\Delta t >$ 35 ns
EHAD(WHA tower) $>$ 1 GeV
$\Delta t <$ -25 ns or $\Delta t >$ 55 ns

Table C.1: Definition of CHA and WHA Out-of-Time towers

(taken to be 0 ns). The broader in-time window for the End Wall TDC's is due to problems in calibration of the End Wall TDC's and the poorer timing resolution. The 1 GeV threshold removes long tails in the time distribution and ensures the

TDCs efficiency. The TDCs are enabled approximately 150 ns after the calorimetry becomes active. The result is that the TDCs do not register energy deposited during this 150 ns interval. These are called *no-hit* TDCs [103]. When there is hadronic energy deposited in a tower and no TDC information, the energy is recorded in this 150 ns interval when the ADC is registering but the TDC is not, *i.e.*, in a cosmic ray or Main Ring event. These towers are also declared to be Out-of-Time. The time distributions for Central and End Wall towers above 1 GeV are given respectively in Figures C.1 & C.2. In these plots each tower above 1 GeV provides an entry. The distribution extends from -150 to 600 ns. The TDCs are enabled from -50 ns to 650 ns. The discrepancy is due to the removal of cable and other delays amounting to $\approx$100 ns.

Region I : EOT $>$ 10 GeV ; NOT $>$ 20 In Figure C.3 the tower IETA (a) (Chapter 3, Table 3.1), IPHI (b) and IETA versus IPHI (c) for the events falling in this region is shown. The Main Ring splashing onto the central top six wedges and the End Walls of CDF is observed. In the 2-dimensional plot C.3(c), the two uninstrumented chimney region towers are also observed. The structure is the same as the Main Ring event LEGO display of Figure 4.1 of Chapter 4. Figure C.4(a) shows the electromagnetic tower energy, Figure C.4(b) the hadronic tower energy and Figure C.4(c) shows the timing of the towers falling in this region (Δt with respect to the beam crossing). The hadronic energy tails and large timing tails are identified as being populated by Main Ring events.

Region II: EOT $>$ 10 GeV ; 5 $<$NOT $\leq$ 20

The tower IETA and IPHI topology is different from the previous region. From the

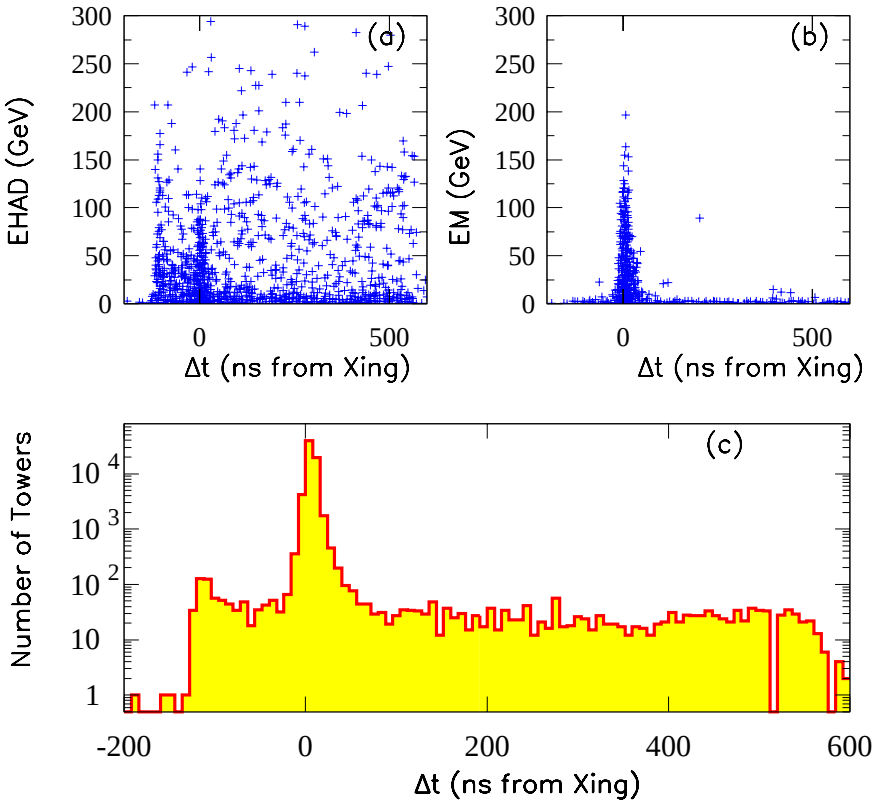

Figure C.1: EHAD(a) and EM(b) tower energy versus timing and timing distribution (c)for all central towers.

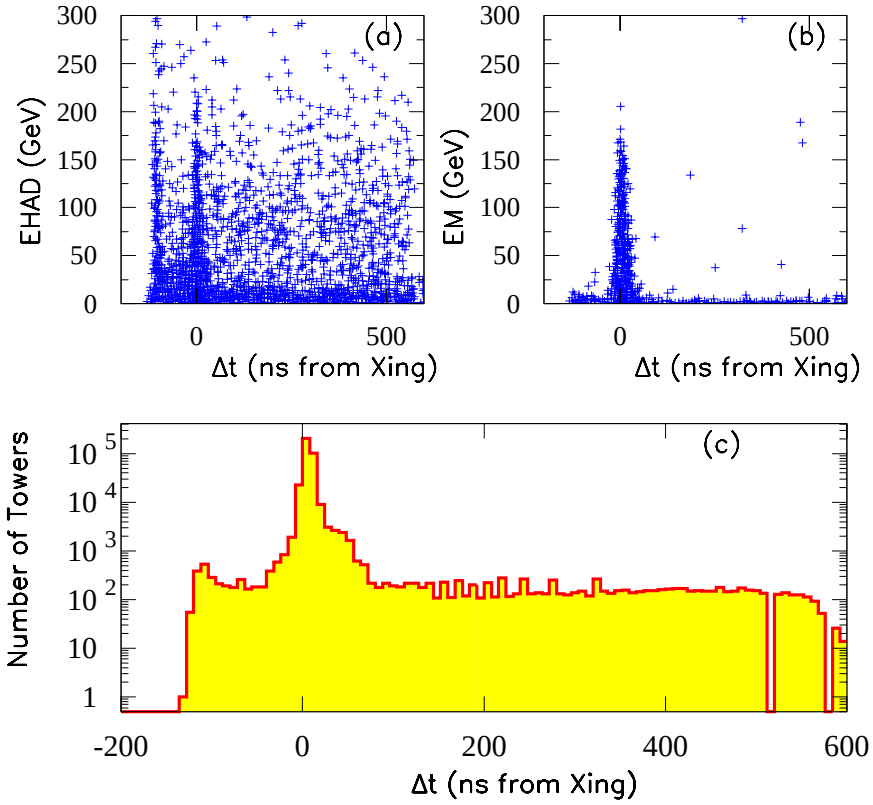

Figure C.2: (a) EHAD and (b) EM tower energy versus timing and (c) timing distribution for all End Wall towers.

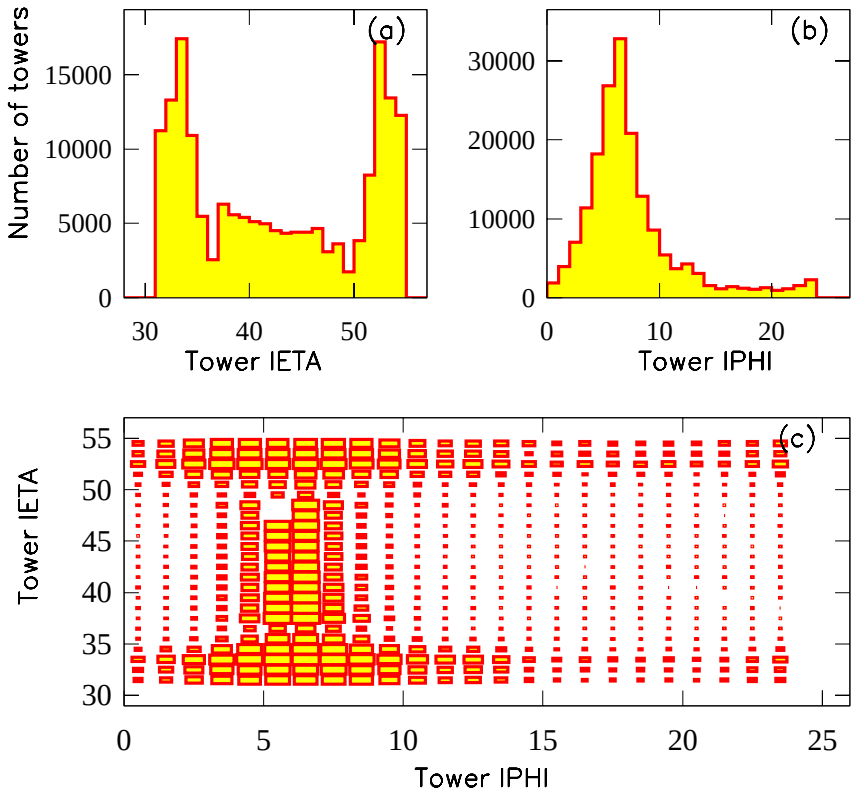

Figure C.3: For events falling in the $EOT > 10\ GeV$, $NOT > 20$ region: (a) Tower IETA, (b) Tower IPHI, (c) Tower IETA vs IPHI .

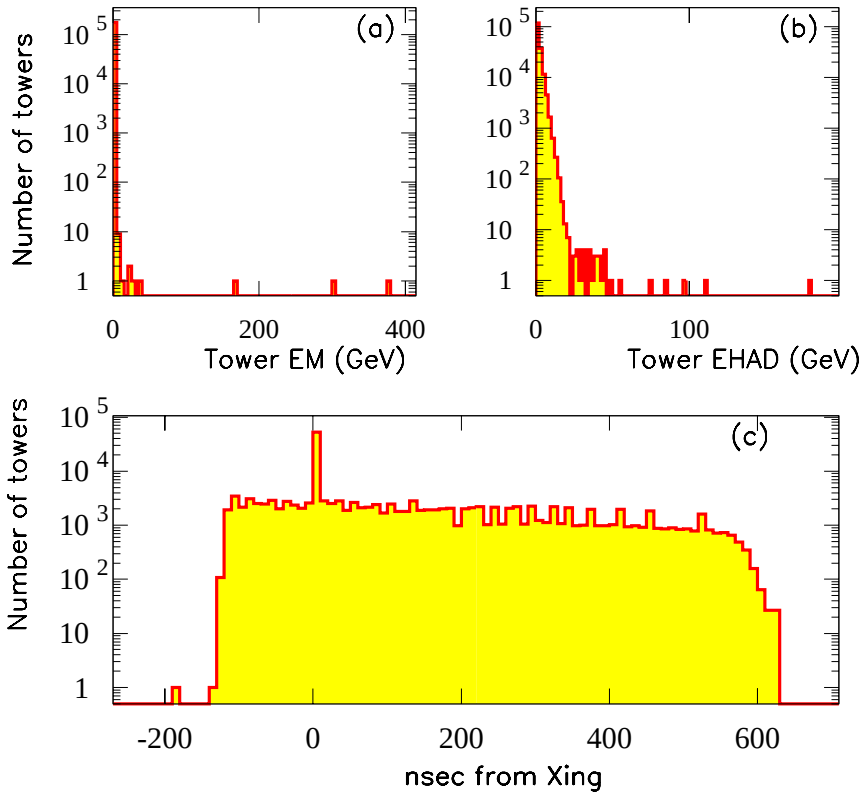

Figure C.4: For events falling in the $EOT > 10\ GeV$, $NOT > 20$ region: a) Tower EM, b) Tower EHAD, c) Tower time distribution.

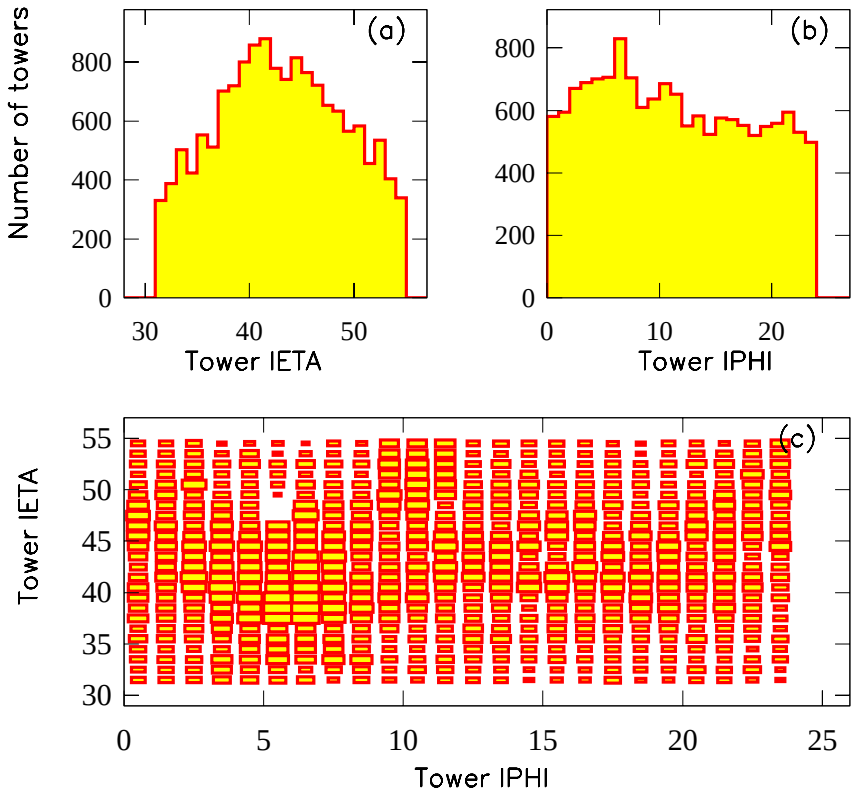

Figure C.5: For events falling in the $EOT > 10\ GeV\ , 5 < NOT < 20$ region: (a) Tower IETA, (b) Tower IPHI, (c) Tower IETA vs IPHI.

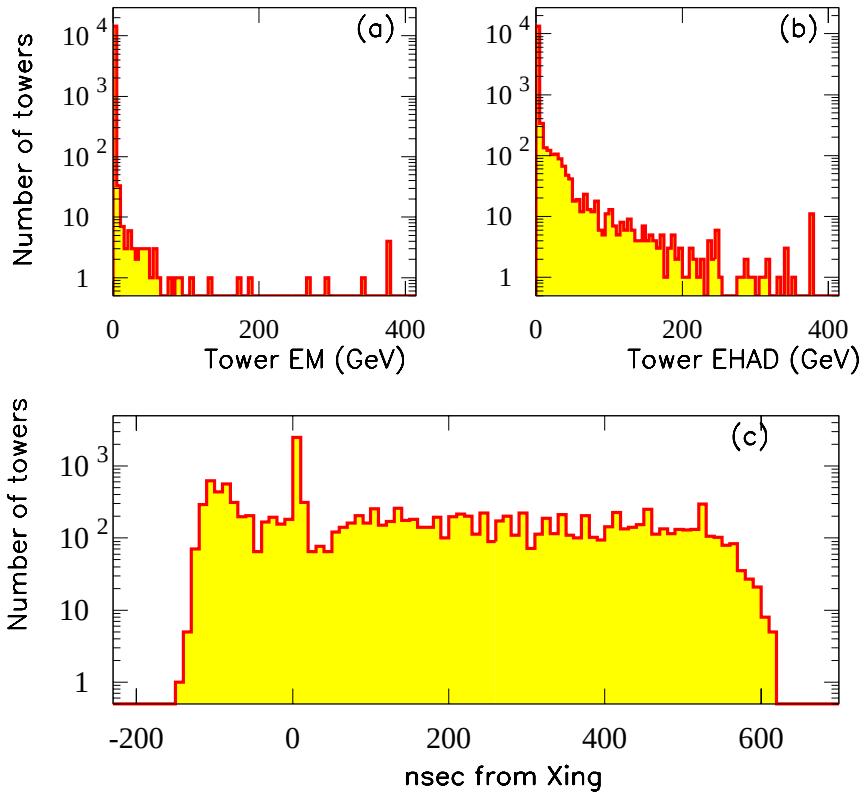

Figure C.6: For events falling in the $EOT > 10\ GeV\ , 5 < NOT < 20$ region: (a) Tower EM, (b) Tower EHAD, (c) Tower time distribution.

IPHI plot peaking at the 90 degrees crack (Figure C.5(a),(b)), remaining Main Ring events are identified. The tower hadronic and electromagnetic energy distributions, as well as the timing of the TDCs, (Figure C.6) identifies this region as background comprised mostly of cosmic rays which shower in the electromagnetic (EM) calorimetry, in-time cosmic rays as well as well as Main Ring events and problematic cable-crate noise events. Some of these events are hand-scanned and events with large isolated energy deposition are found which are consistent with *bremßtrahlung* from cosmic ray muons.

Region III: EOT > 10 GeV ; NOT < 5

From the corresponding plots for this region (Figures C.7 & C.8), it is determined that this is an Out-of-Time background region comprised mostly from cosmic rays. In the timing distribution the deep at -30 ns is a selection bias.

Region IV: EOT $\leq$ 10 GeV ; NOT $\leq$5

The tower topology as well as the tower hadronic and electromagnetic energy as given in Figures C.9, & C.10 suggest that this region is the non-fake $\not\!\!E_T$ region.

C.2 Residual Background after Stage 2 of Pre-Selection

Two methods are used to calculate the residual background in region 3 in Figure 4.14 of Chapter 4:

- **METHOD A**

  Consider regions 1, 3 and 4 to be comprised of 100% background. The back-

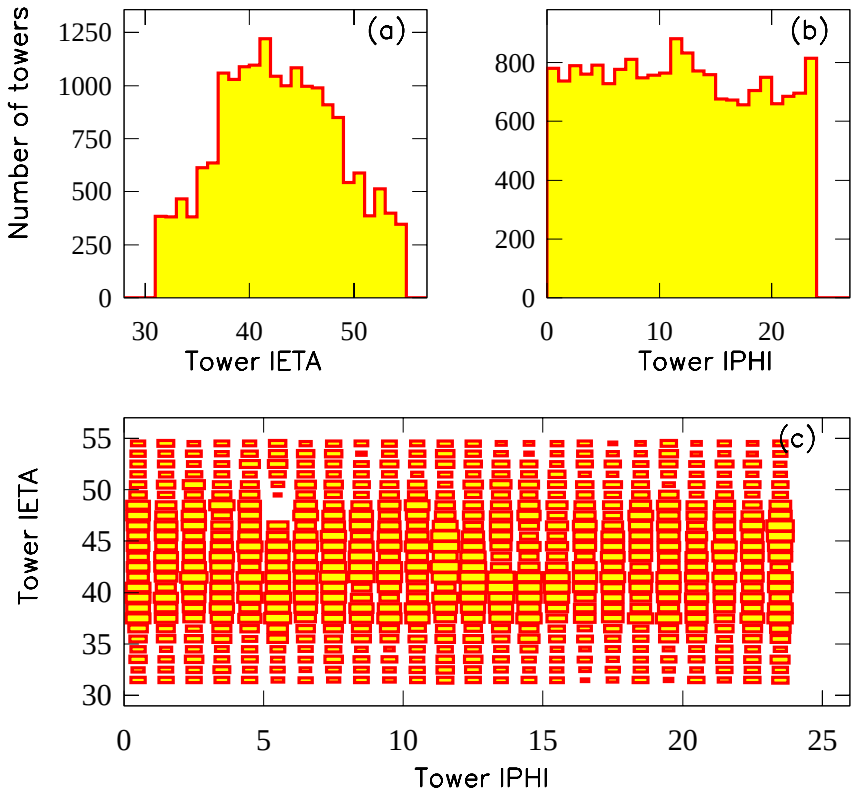

Figure C.7: For events falling in the $EOT > 10GeV$, $NOT < 5$ region: (a) Tower IETA, (b) Tower IPHI, (c) Tower IETA vs IPHI.

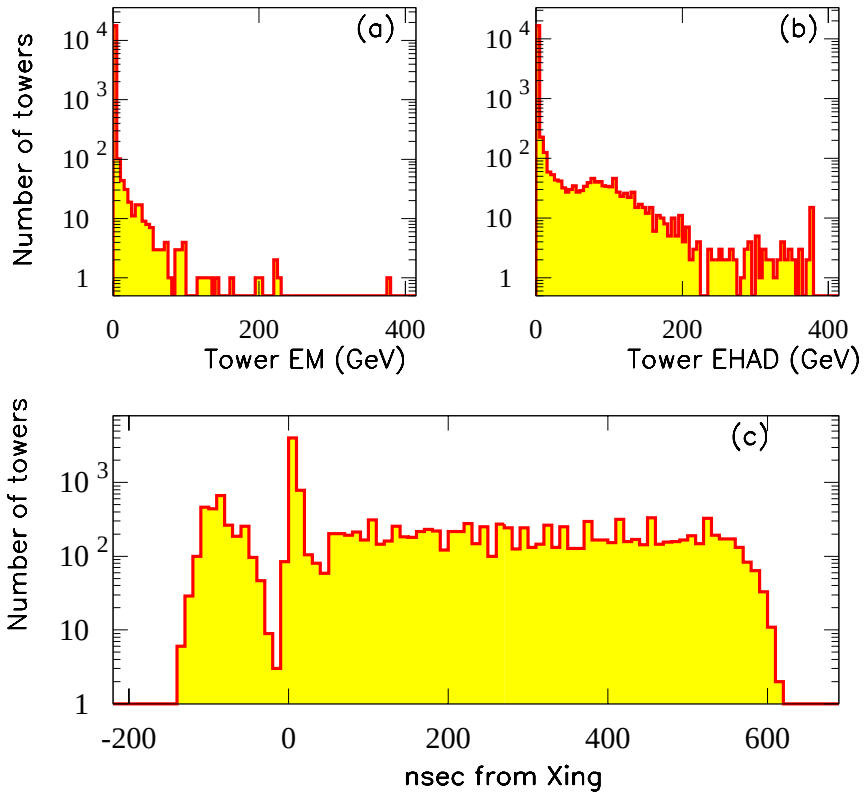

Figure C.8: For events falling in the $EOT > 10\ GeV$, $NOT < 5$ region: (a) Tower EM, (b) Tower EHAD, (c) Tower time distribution.

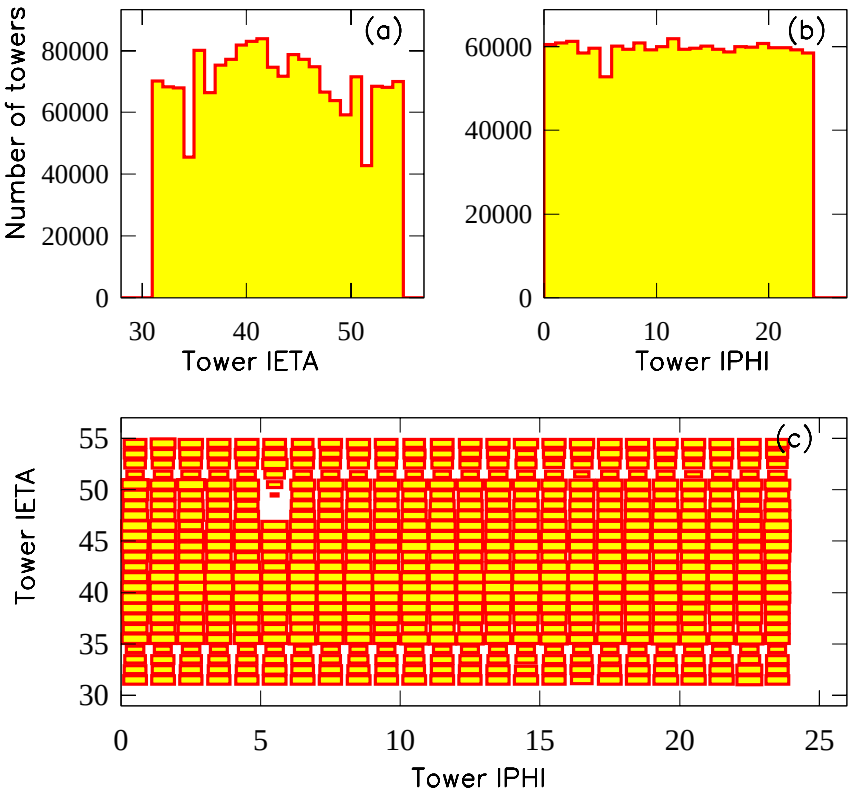

Figure C.9: For events falling in the $EOT \leq 10\ GeV$, $NOT \leq 5$ region: (a) Tower IETA, (b) Tower IPHI, (c) Tower IETA vs IPHI.

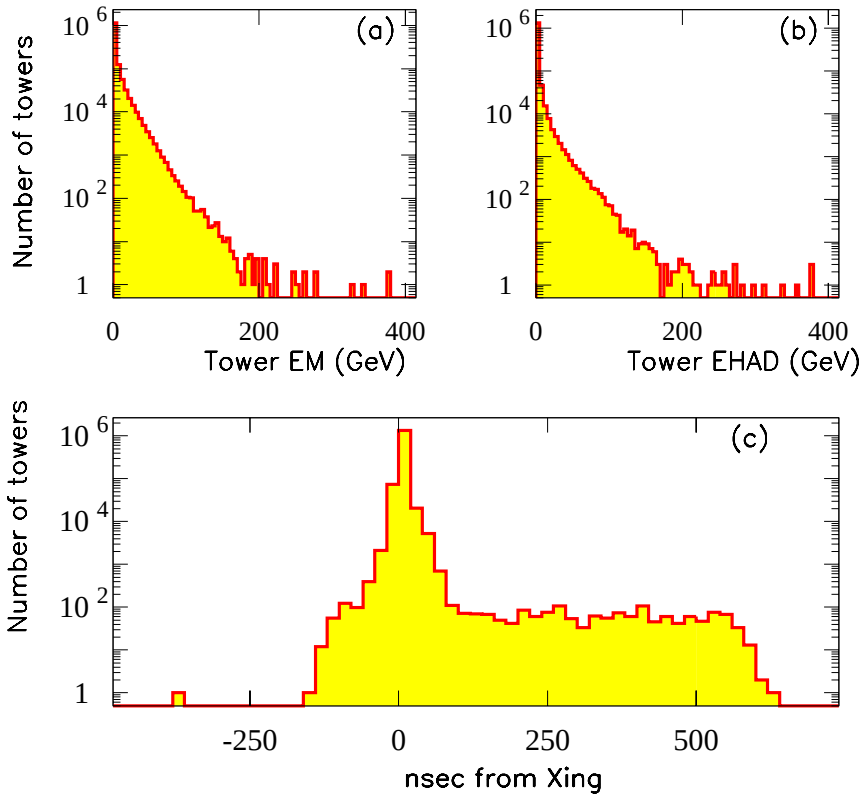

Figure C.10: For events falling in the $EOT \leq 10\ GeV$, $NOT \leq 5$ region: a) Tower EM, b) Tower EHAD, c) Tower time distribution.

ground in region 3 is given by:

$$BGR_3 = \frac{N_2}{N_1} \times N_4 \tag{C.1}$$

where N_i is the number of events falling on the corresponding region i.

- **METHOD B**

  This method considers regions 2 and 3 to contain both real $\not\!\!E_T$ and fake $\not\!\!E_T$ events. Dijet events are selected in the JET50 sample and in a Monte Carlo QCD simulation sample referred to as MCQCD50.[1] If N_{dij}^{JET50} is the number of dijets in the data and $N_{dij}^{MCQCD50}$ in the Monte Carlo then the normalization to the data is

$$\alpha = N_{dij}^{JET50}/N_{dij}^{MCQCD50} \tag{C.2}$$

  In the JET50 sample with the requirement of one central jet, let the events that fall in region 2 be N_2^{JET50}. Let in the MCQCD50 sample the events with $ECHF < 0.175$ be $N_2^{MCQCD50}$. The number of real $\not\!\!E_T$ events in region 2 is $(\alpha \times N_2^{MCQCD50})$. The number of background events in region 2 in the JET50 data sample is

$$BGR_2^{JET50} = N_2^{JET50} - (\alpha \times N_2^{MCQCD50}) \tag{C.3}$$

  In the XOXB (MET) data sample (before Stage 1), the events in regions 1 and

[1] Generator HERWIG 5.6 (2 to 2 inclusive), PDF:MRSG ,$|\eta|$ parton < 4.2, P_T generated parton > 40 GeV, E_T simulated (QFL′) leading cluster > 50 GeV.

4 are considered to be all background events:

$$N_1^{XOXB} = BGR_1^{XOXB} N_4^{XOXB} = BGR_4^{XOXB} \tag{C.4}$$

For regions 2 and 3 the number of events observed are composed of real $\not\!\!E_T$ and background events:

$$N_2^{XOXB} = S_2^{XOXB} + BGR_2^{XOXB} \tag{C.5}$$

$$N_3^{XOXB} = S_3^{XOXB} + BGR_3^{XOXB} \tag{C.6}$$

With the assumption that

$$\frac{BGR_2^{JET50}}{N_1^{JET50}} = \frac{BGR_2^{XOXB}}{N_1^{XOXB}}, \tag{C.7}$$

$$\frac{N_1^{XOXB}}{N_4^{XOXB}} = \frac{BGR_2^{XOXB}}{BGR_3^{XOXB}} \tag{C.8}$$

the residual background in region 3 is calculated.

The EOUT requirement is varied to calculate the systematic uncertainty introduced by the two methods in the four regions. The residual background in region 3 is found to be invariant (within statistical uncertainty) with respect to the Out-of-Time energy requirement for EOUT $>$ 2 GeV. The systematic uncertainty introduced by the Out-of-Time requirement for $EOUT \geq 10$ is 0.04% for both methods. For the two different methods and for EOUT $\geq$ 10, the percentage of residual background in region 3 is:

$$BGR_3^{[A]} = (0.73 \ \pm \ 0.026(stat.) \ \pm \ 0.04(syst))\% \tag{C.9}$$

$$BGR_3^{[B]} = (0.49 \ \pm \ 0.022(stat.) \ \pm \ 0.04(syst))\% \tag{C.10}$$

Unconstrained averaging is used to combine the two methods ([76]); assuming they are uncorrelated [2]:

$$BGR_3^{[AB]} = (.61 \ \pm \ .12)\% \tag{C.11}$$

C.3 Validation of Event Charge Fraction in the Monte Carlo

To calculate the efficiency of the Stage 2 requirements, it is necessary to compare the ECHF variable between data and Monte Carlo. The JET50 data sample and the corresponding Monte Carlo QCD sample (MCQCD50) are used. A tracking degradation algorithm which is described in Chapter 3 is applied on the Monte Carlo to simulate tracking inefficiencies in the data. The ECHF in the data and Monte Carlo before and after the CTC tracking degradation is shown in Figure C.11(a). In C.11(b), the E_T of the leading jet is compared between the JET50 data and the MCQCD50 Monte Carlo. The Monte Carlo is fit to the data using the shape of the ECHF distribution from the JET50 data background regions 1 & 4 as a template. Figure C.12(a) shows the combined ECHF background template from regions 1 & 4 in the JET50 sample. Figure C.12(b) shows the ECHF in the MCQCD50 Monte Carlo. Also in Figure C.12 the data and the fit using a log likelihood method are shown. The mean of the ECHF in the Monte Carlo in the region between 0.25 and 1.1 is 0.645 ± 0.0012 and in the data 0.63 ± 0.001 . The fit validates the ECHF distribution comparison between the data and Monte Carlo. The level of agreement

[2] p.10 [76] with the scale factor on the uncertainty as suggested in the Reference.

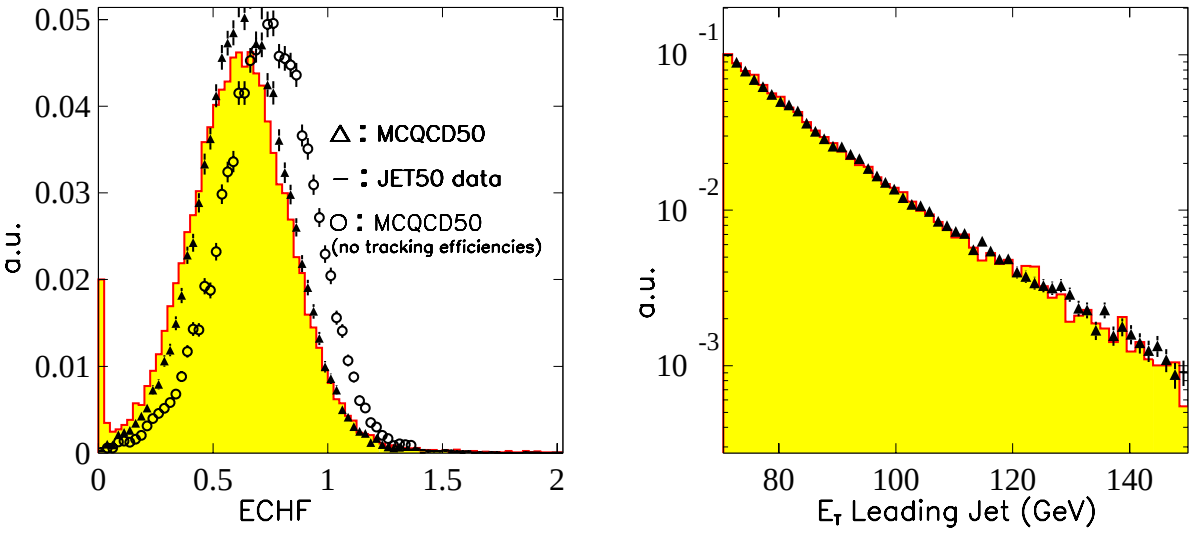

Figure C.11: (a) Comparison of ECHF between data and Monte Carlo. (b) Leading jet E_T spectrum comparison between data and Monte Carlo.

with the Monte Carlo is also shown using the distribution of the $\sum |\vec{P}_T|$ of the tracks, and the distribution of the number of tracks used to compute the ECHF in the data and in the Monte Carlo (Figure C.13).

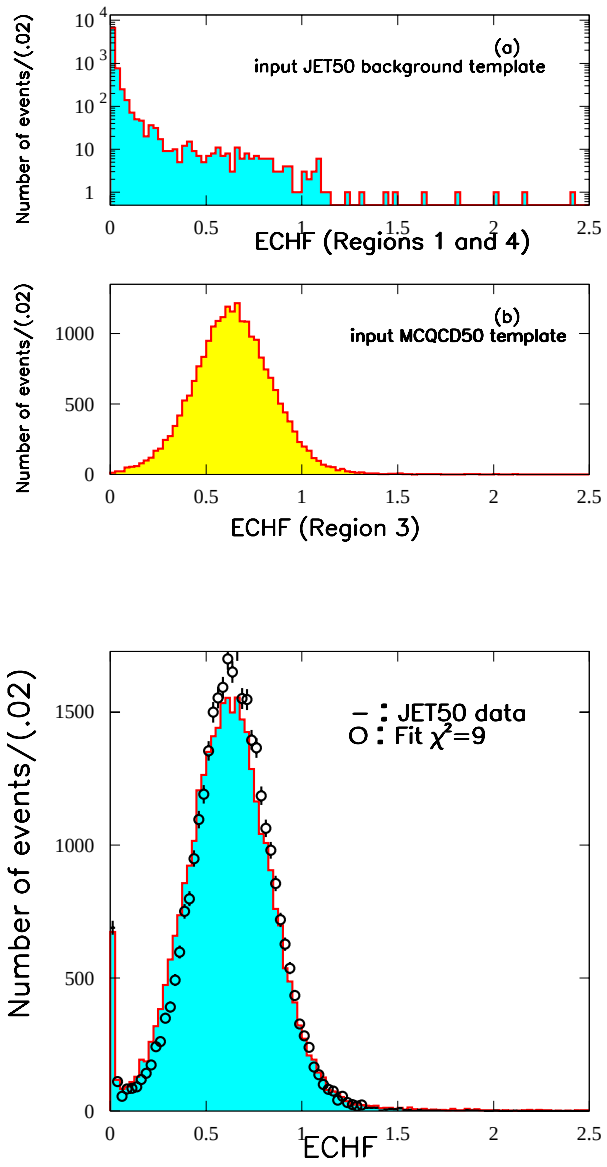

Figure C.12: top: (a) Input background ECHF template. (b) Input signal ECHF template. bottom: ECHF JET50 data and fit.

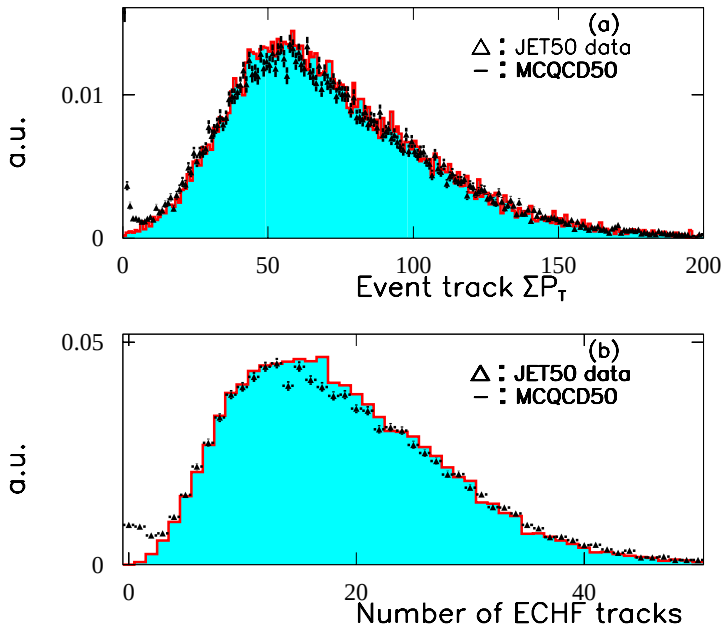

Figure C.13: Comparison between JET50 data and MCQCD50 Monte Carlo of (a) Track $\sum |\vec{P}_T|$ distribution. (b) Number of tracks distribution.

Appendix D

Run1B Jet20, Jet50 and MET* Level 2 Trigger Efficiencies

The measurement of the L2 JET20 trigger efficiency using the second jet in the JET20 data sample, of the L2 JET50 trigger efficiency using the JET20 data and of the L2 (MET_35_TEX_2_NOT_GAS.or.MET_35_TWO_JETS)(≡ MET*) trigger using the JET50 data sample is discussed. The Missing Energy + Jets analysis is using the EXOB_MET_30_COSFLT L3 trigger data sample which is fed by the L2 MET_35_TEX_NOT_GAS, MET_35_TWO_JETS trigger and the L2 JET triggers. The L2 MET* trigger efficiency needs to be measured and folded in the signal Monte Carlo. The L2 JET20 and JET50 trigger efficiencies need to be folded into the QCD Monte Carlo for multijet background. Assuming a fixed efficiency p the probability of an event passing the trigger is p and of failing is (1-p). For T events passing and F events failing, the probability of observing T and F for a given value of p is the binomial probability :

$$B(T;(T+F),p) = \left(\begin{array}{c} T+F \\ \\ T \end{array} \right) p^T (1-p)^F \tag{D.1}$$

This is the product of probabilities of each event, p^T for the successes and $(1-p)^F$ for the failures. To get the best estimate of the efficiency the above expression is maximized with respect to p. Equivalently the logarithm of it is maximized i.e.

$$\begin{aligned} \frac{d \log B}{dp} &= \frac{T}{p} - \frac{F}{1-p} = 0 \\ p &= \frac{T}{T+F} \end{aligned}$$

For an analytic form for the probability density $f(x,\theta)$ and observations

$$x_1, x_2, ...x_K, x_{K+1}, ...x_M$$

where (θ represents the set of parameters needed to solve for, x is the $\not{E}_T$ or the E_T (or whatever variable the efficiency is calculated as a function of), 1 through K are the events that are successful and K+1 through M are the failures then the joint probability density or likelihood, assuming independence of the x's is:

$$\mathcal{L} = \prod_{i=1}^{K} f(x_i,\theta) \prod_{i=K+1}^{M} (1 - f(x_i,\theta)) \tag{D.2}$$

Minimizing the $-\log \mathcal{L}$ with respect to the unknown parameters θ, θ is solved for and an analytic expression for the efficiency is obtained. The expression for f used is the

Sample	JET20	JET50
requirement	N_{events}	N_{events}
Trigger	455083	324267
Baseline	261955	114486

Table D.1: JET20/JET50 trigger and baseline samples' event content. The samples are used for trigger efficiency measurements.

product of two normal frequency [1] functions:

$$f(\not\!\!E_T, THR1, SLP1, THR2, SLP2, PLT) = PLT * FREQ(\frac{\not\!\!E_T(E_T) - THR1}{SLP1}) * FREQ(\frac{\not\!\!E_T(E_T) - THR2}{SLP2}) \quad \text{(D.3)}$$

D.1 JET20, JET50 Data Samples

The JET20/JET50 with the requirement of the corresponding trigger are reprocessed according to the highest $\sum |\vec{P}_T|$ vertex and the data Pre-Selection requirements are applied (Chapter 4). In addition, 2 jets of 15 GeV are required in the event. For the purposes of this discussion the obtained samples are referred to as baseline samples . The reduction of the samples is shown in Table D.1.

[1] $FREQ(x) = \frac{1}{\sqrt{2\pi}} \int_{\infty}^{x} e^{-\frac{1}{2}t^2}\ dt$ computed by rational Chebyshev [104] approximation.

JET20	Trigger	Baseline	*plusL2*	2nd jet passes L2 E_T threshold
N_{events}	455083	261955	161956	57446

Table D.2: JET20 data sample reduction and measurement of the L2 JET20 trigger efficiency using the second jet.

D.2 Measurement of the L2 JET20 trigger efficiency

On the baseline JET20 data sample the additional requirements (referred to as *plusL2*) are applied:

- 1 offline jet of 30 GeV,
- The E_T measured at L2, L2_E_T of the second highest L2 E_T cluster not be zero, and
- Instantaneous Luminosity $> 1\text{x}10^{32}$ cm^{-2}s^{-1}

To determine the JET20 trigger efficiency we then select the events with a second L2 cluster of L2_E_T> 20 GeV according to the trigger threshold. Figure D.1 shows the offline E_T of the second leading cluster before and after the L2 JET20 trigger threshold requirement is applied to the second leading cluster (L2_E_T> 20 GeV). By minimization of the negative log likelihood the trigger efficiency is parametrized as shown in Table D.3. The efficiency curve is shown in Figure D.1.

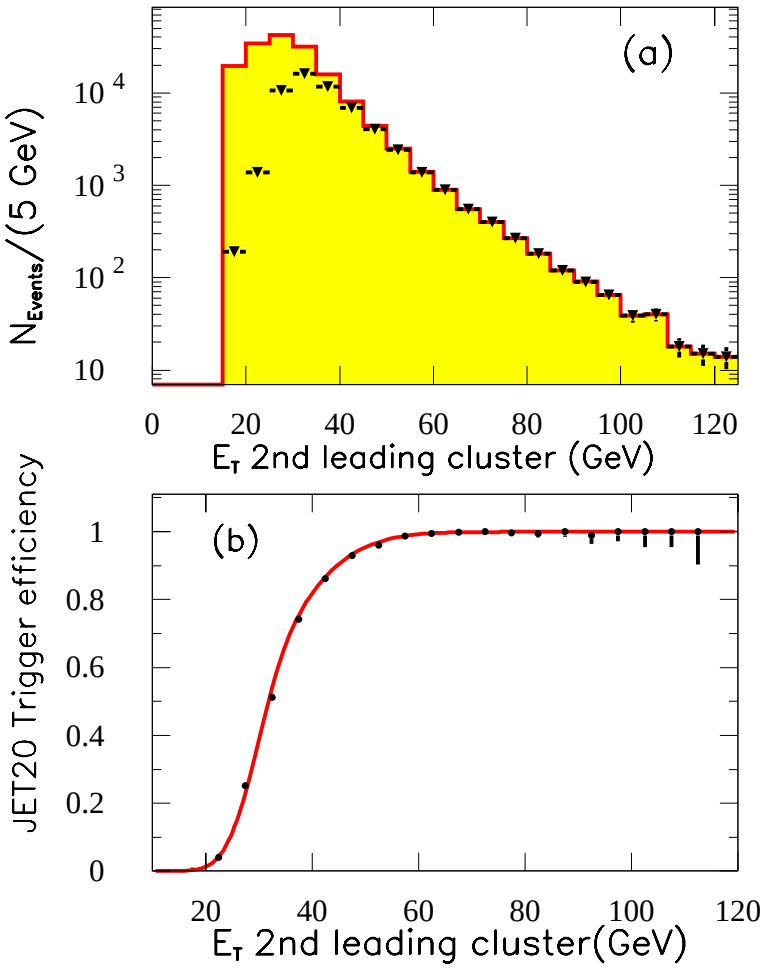

Figure D.1: (a) 2nd leading cluster offline E_T before (histogram) and after (points) the L2 JET20 trigger threshold is applied on the 2nd leading cluster. (b) JET20 trigger efficiency. The points are the data and the curve is the parameterization.

Parameter	THR1	SLP1	THR2	SLP2	PLT
Fit Value	27.92	13.06	27.78	4.63	0.998
Negative	0.49	0.42	0.19	0.07	0.001
Positive	0.45	0.45	0.19	0.07	0.0008
Parabolic	0.44	0.41	0.18	0.07	0.0009

Table D.3: Parameterization of the JET20 trigger efficiency using the second leading jet in the JET20 data. The parameters are those in expression D.3.

JET20	(Trigger)	(Baseline)	(*plusL2*)	set L2 JET50 bit
N_{events}	455083	261955	179496	8799

Table D.4: The JET20 sample reduction used to measure the JET50 trigger efficiency.

D.3 Measurement of the L2 JET50 trigger efficiency

The additional requirements are applied (*plusL2*) to the baseline JET20 data sample. To determine the JET50 trigger efficiency, the events that set the L2 JET50 trigger bit are selected as shown in Table D.4. In Figure D.2 the offline E_T of leading cluster is overlayed with the offline E_T of the leading cluster of the events that set the L2 JET50 trigger bit. The parameters determined with the unbinned likelihood fit are given in Table D.5. The efficiency curve is shown in Figure D.2 (b).

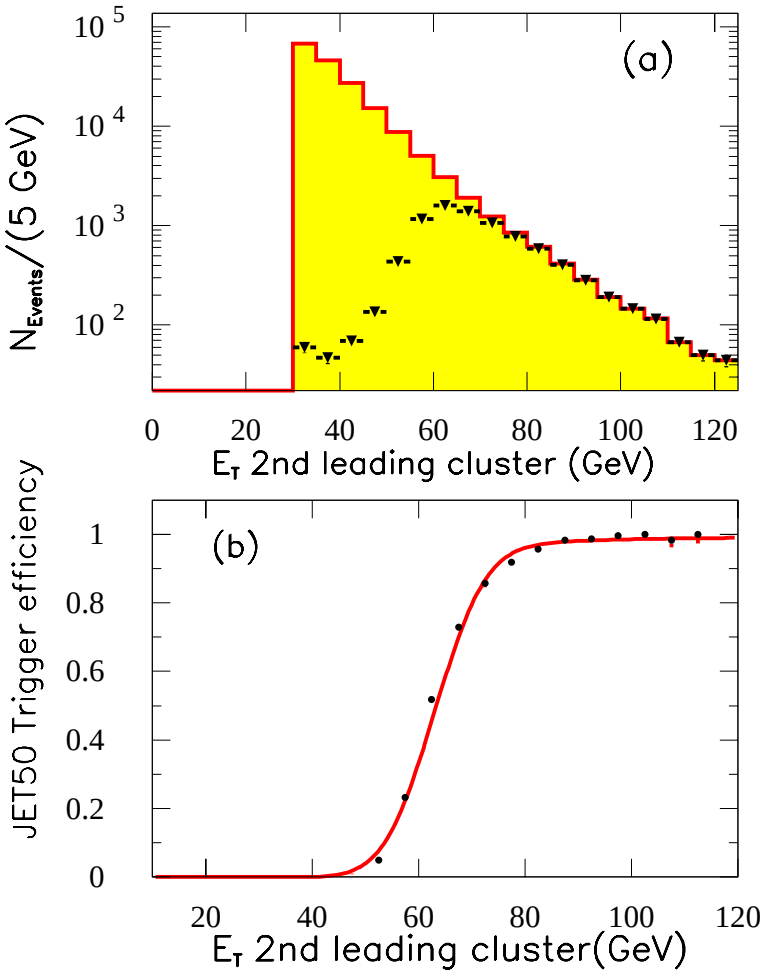

Figure D.2: (a) Leading jet E_T before (shade) and after (points) the L2 JET50 trigger requirement is applied. (b) JET50 trigger efficiency. The points are the data and the curve is the parameterization.

Parameter	THR1	SLP1	THR2	SLP2	PLT
Fit Value	62.77	7.5	none	38.84	0.993
Negative	0.15	0.08	-	3.77	0.0045
Positive	0.15	0.08	-	2.19	0.0034
Parabolic	0.14	0.08	-	2.4	0.004

Table D.5: Parameterization of the JET50 trigger efficiency using JET20 data. "none" indicates that the likelihood fit is over-constrained with 5 parameters and prefers a 4 parameter fit. The parameters are those in expression D.3.

JET50	Trigger	Baseline	set L2 MET* bits
N_{events}	324267	114486	18284

Table D.6: JET50 data reduction for the MET* trigger efficiency measurement.

D.4 Measurement of the MET* trigger efficiency with JET50 data

The baseline selection on the JET50 sample and the additional requirement of the MET* trigger requirement is shown in Table D.6. Figure D.3 shows the $\not\!\!E_T$ distribution of the JET50 events before (shaded) and after (points) the MET* trigger

Parameter	THR1	SLP1	THR2	SLP2	PLT
Fit Value	31.141	17.83	21.9	9.75	0.993
Negative	1.58	1.2	1.63	0.3	0.003
Positive	1.11	1.54	1.63	0.3	0.003
Parabolic	1.19	1.23	1.47	0.3	0.003

Table D.7: Parameterization of the MET* trigger efficiency using JET50 data. The parameters are those in expression D.3.

requirement. The parameterization of the efficiency is given in Table D.7. The efficiency curve is shown in Figure D.3(b).

D.5 Goodness of the fit / MC Pseudo-experiments

The validity of the log likelihood fits is studied by randomly drawing from the E_T or $\not\!\!E_T$ distribution of the data and creating 500 Monte Carlo samples. Each of these is of exactly the same size as the corresponding data sample. The same fitting procedure is applied to each of these Monte Carlo data samples. If the hypothesis for the fit is accurate the means of the parameter distributions of these 500 samples are expected be (within their statistical error which is the $\sigma/\sqrt{500}$) equal to the corresponding parameter from the fit to the real data. The σ of these distributions is the statistical error on the parameters of the fit on the real data. In Figure D.4 the results of the 500 fits performed on the Monte Carlo data samples for the case of the MET* trigger efficiency using the JET50 data sample is shown. By comparing the means and σ values of the parameters between the pseudo-experiments as given in Figures D.4, D.5 and D.6 and the fit to the data as given in Tables D.7, D.5, D.3, fits are judged to be trustworthy. The JET20, JET50 trigger parameterization is used in the QCD Monte Carlo for the background calculation to the multijet plus missing energy study. The MET* trigger efficiency is folded in all the signal process Monte Carlo samples. The MET* trigger efficiency is also parametrized using the JET20, JET70, SUMET135 QCD samples [105]. A 2% systematic uncertainty is obtained from the plateau value of the different parameterizations for $\not\!\!E_T >$ 70 GeV. Within uncertainties, the results of these trigger studies on the L2 MET and JET20/JET50 triggers are in agreement with previous studies ([106], [107]) at CDF.

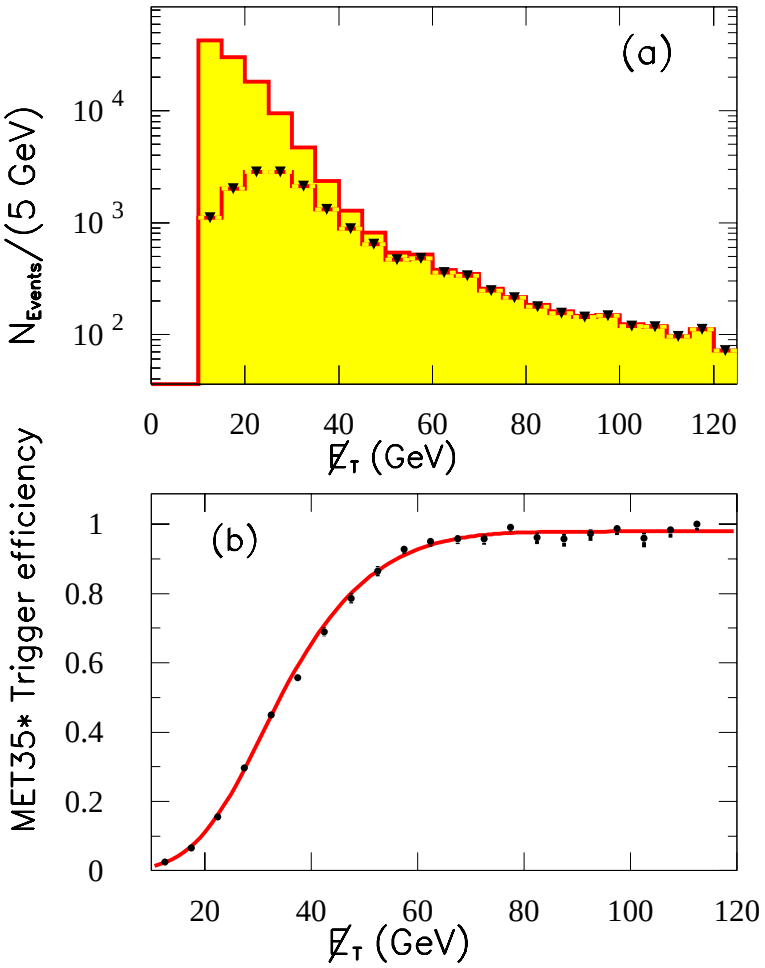

Figure D.3: (a) $\not\!\!E_T$ before (shaded) and after (points) the L2 MET* trigger requirement in the JET50 data (b) MET* trigger efficiency.

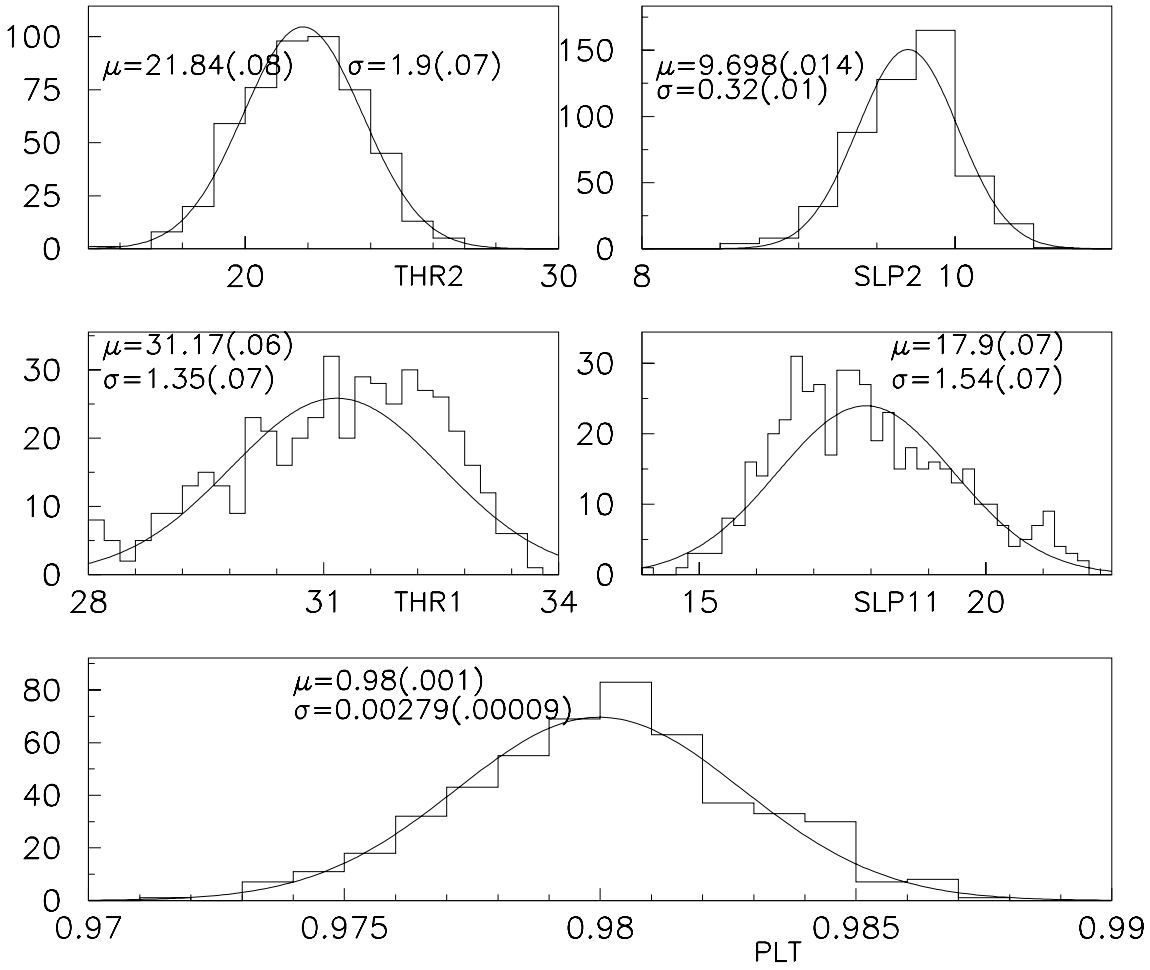

Figure D.4: Monte Carlo pseudo-experiment results to establish the goodness of the MET* trigger efficiency fit using JET50 data . The means and sigmas of the distributions of the parameters of the fits for 500 pseudo-experiments agree with the parameters and their errors from the fit to the real data. The error on the means is the $\sigma/\sqrt{N}$.

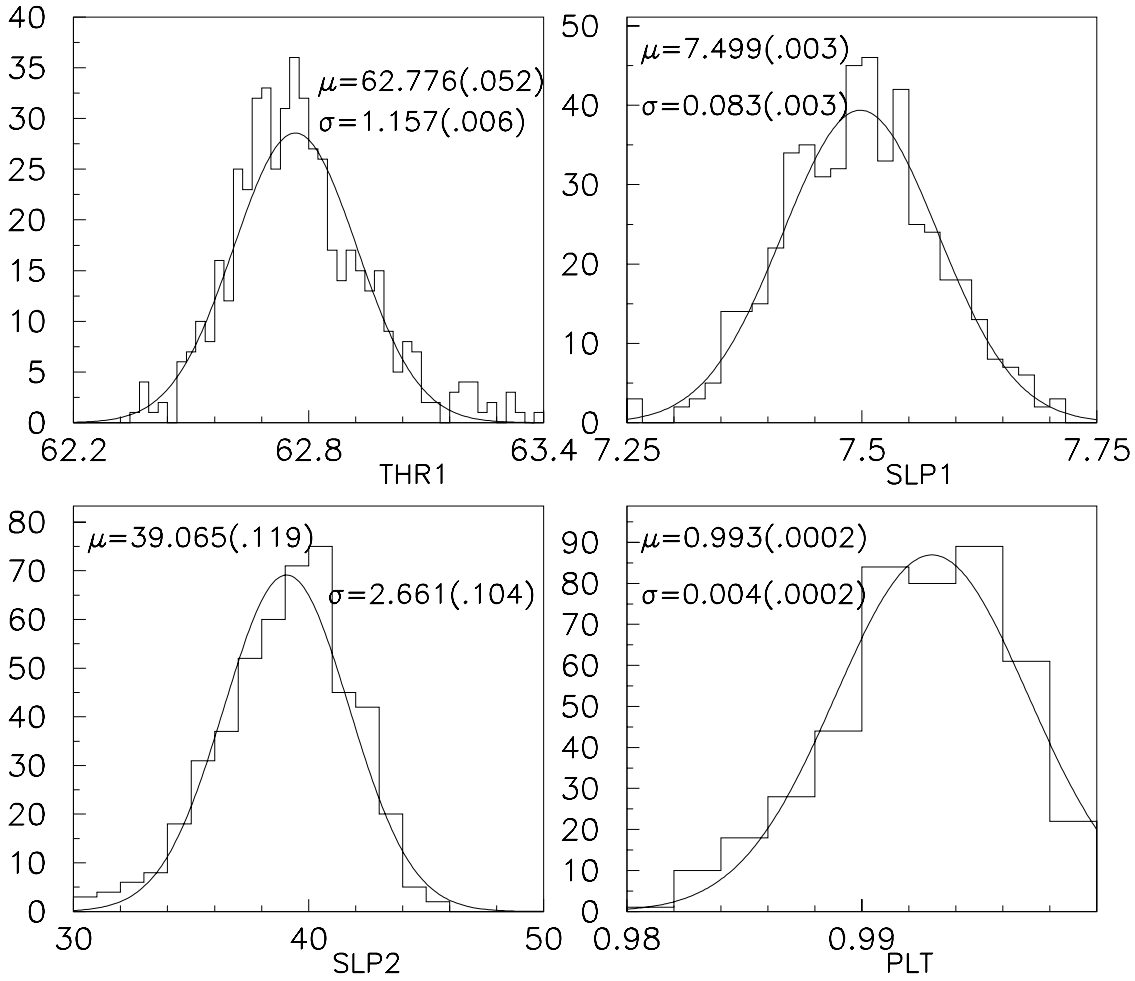

Figure D.5: Monte Carlo pseudo-experiment results to establish the goodness of the fit of the JET50 trigger efficiency using the JET20 data. The means and sigmas of the distributions of the parameters of the fits for 500 pseudo-experiments agree with the parameters and their errors from the fit to the real data. The errors on the means is the $\sigma/\sqrt{N}$.

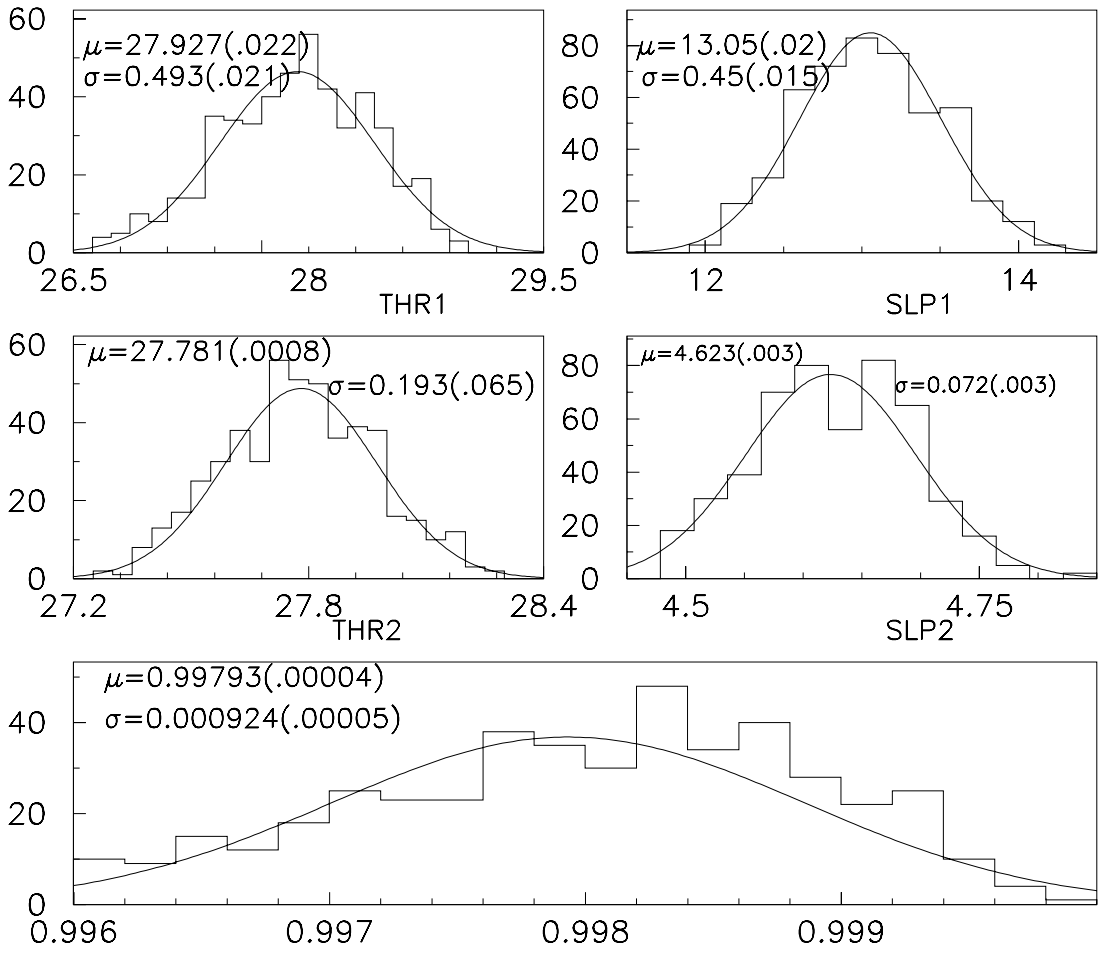

Figure D.6: Monte Carlo pseudo-experiment results to establish the goodness of the fit of the JET20 trigger efficiency using the second jet in the JET20 data. The means and sigmas of the distributions of the parameters of the fits for 500 pseudo-experiments agree with the parameters and their errors from the fit to the real data. The errors on the means is the $\sigma/\sqrt{N}$.

Appendix E

Validation of the Kinematics in the Enhanced Leading Order Monte Carlo $W/Z+$ jets Predictions

E.1 Z+jets

The kinematic distributions are compared between the $Z+$ jets data sample and the Monte Carlo samples. Results from the comparison of VECBOS+HERPRT+QFL $Z+ \geq$ 1 jet (using renormalization and fragmentation scale $Q^2 = M_Z^2 + {P_T}_Z^2$) to the data in the inclusive 1, 2 multiplicity bins validate kinematically the Enhanced Leading Order predictions in the Z+1 jets generated Monte Carlo. VECBOS+HERPRT+QFL $Z+ \geq 2$ jets is compared to the data in the inclusive 2, 3 multiplicity bins to validate the Enhanced Leading Order predictions (ELO) in the Z+2 jets generated Monte Carlo. The purpose is to be able to trust the Enhanced Leading Order simulation in predicting the additional jet bin kinematics and in particular those that are relevant

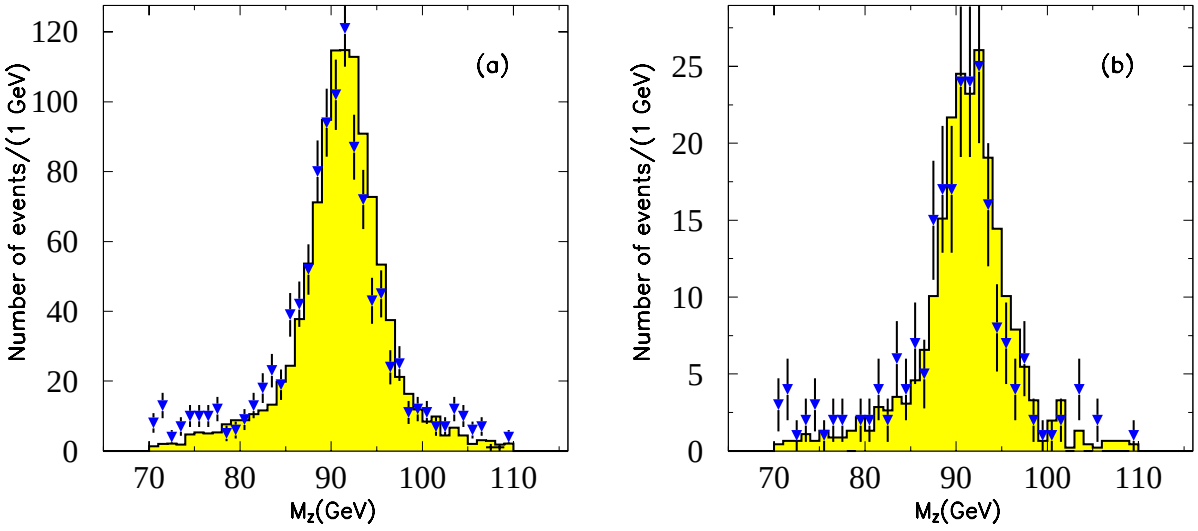

Figure E.1: Z mass in inclusive jet multiplicity bins 1 and 2 as predicted in $Z \rightarrow ee+ \geq 1$ jet Enhanced LO Monte Carlo (histogram) compared with data (points).

to the $\not\!\!E_T+ \geq$3 jets analysis. The following variables are compared: **a.** the dielectron invariant mass, **b.** the P_T of the Z boson constructed using the dielectron $\sum \vec{E}_T$, **c.** the P_T of the Z boson constructed using the $\sum \vec{E}_T$ of the jets, **d.** the jet E_T and η spectrum, **e.** the $\not\!\!E_T$ spectrum and **f.** "$\nu\not\!\!E_T$", a quantity defined by adding the electron energies to the the $\not\!\!E_T$ (to emulate the $Z \rightarrow \nu\nu + N$ jets process in the data). In all the comparisons, the Monte Carlo is directly normalized to the data in the corresponding multiplicity bin.

VECBOS/HERPRT/QFL$'$ $Z \rightarrow ee+ \geq 1$ **jet versus** $Z \rightarrow ee+ \geq 1$ **jet data (Multiplicity Bin 1 Predicting Bin 2)**

- **a.** Z mass in the inclusive 1 and 2 jet bins. The comparisons between data and Monte Carlo (generated at multiplicity bin 1) are shown in Figure E.1.

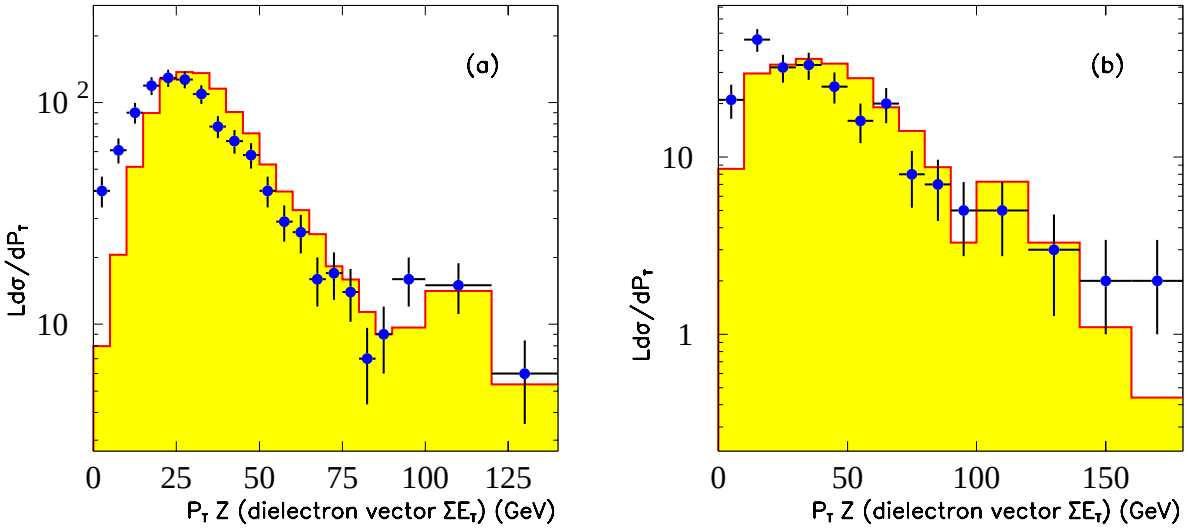

Figure E.2: Z $P_T$in inclusive jet multiplicity bins 1 (a) and 2 (b) as predicted in $Z \rightarrow ee+ \geq 1$ jet Enhanced LO Monte Carlo (histogram) compared with data (points). The Z P_T is the $\sum \vec{E}_T$ of the electrons

- **b.** The P_T of the Z boson constructed using the dielectron $\sum \vec{E}_T$ in the inclusive 1 and 2 jet bins. The comparisons between data and Monte Carlo are shown in Figure E.2.

- **c.** The P_T of the Z boson constructed using the jet $\sum \vec{E}_T$ in the inclusive 1 and 2 jet bins. The comparisons between data and Monte Carlo (generated in multiplicity bin 1) are shown in Figure E.3.

- **d.** The E_T and η of the leading jet and second leading jet. The comparisons between data and Monte Carlo (generated in multiplicity bin 1) are shown in Figure E.4.

- **e.** The $\not\!\!E_T$ in the inclusive 1 and 2 jet bins comparison between data and $Z \rightarrow ee+ \geq 1$ jet Enhanced LO Monte Carlo is shown in Figure E.5.

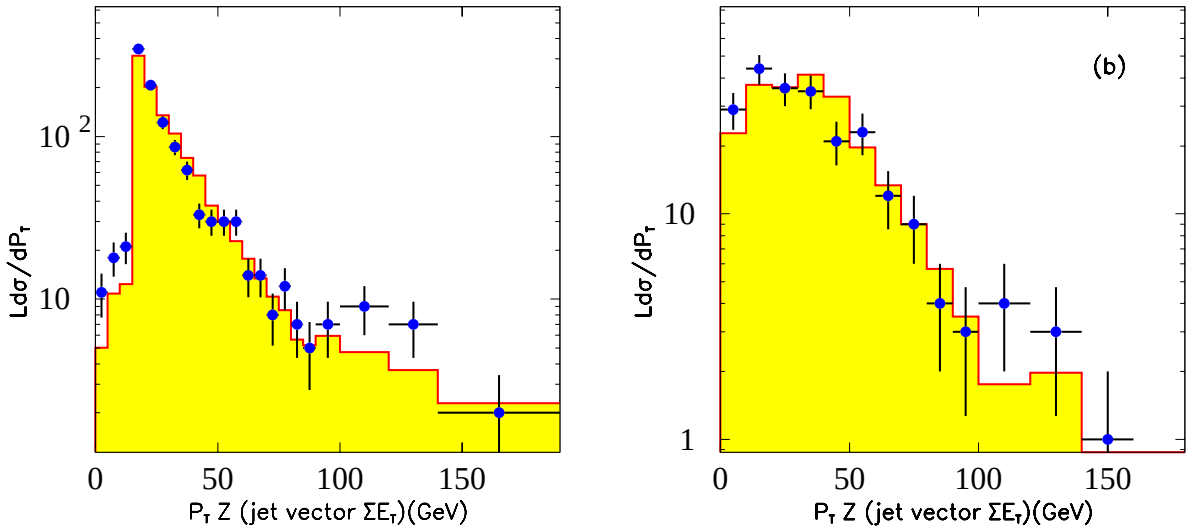

Figure E.3: Z P_T in inclusive jet multiplicity bins 1 (a) and 2 (b) as predicted in $Z \rightarrow ee+ \geq 1$ jet Enhanced LO Monte Carlo (histogram) compared with data (points). The Z P_T is the $\sum \vec{E}_T$ of the jets.

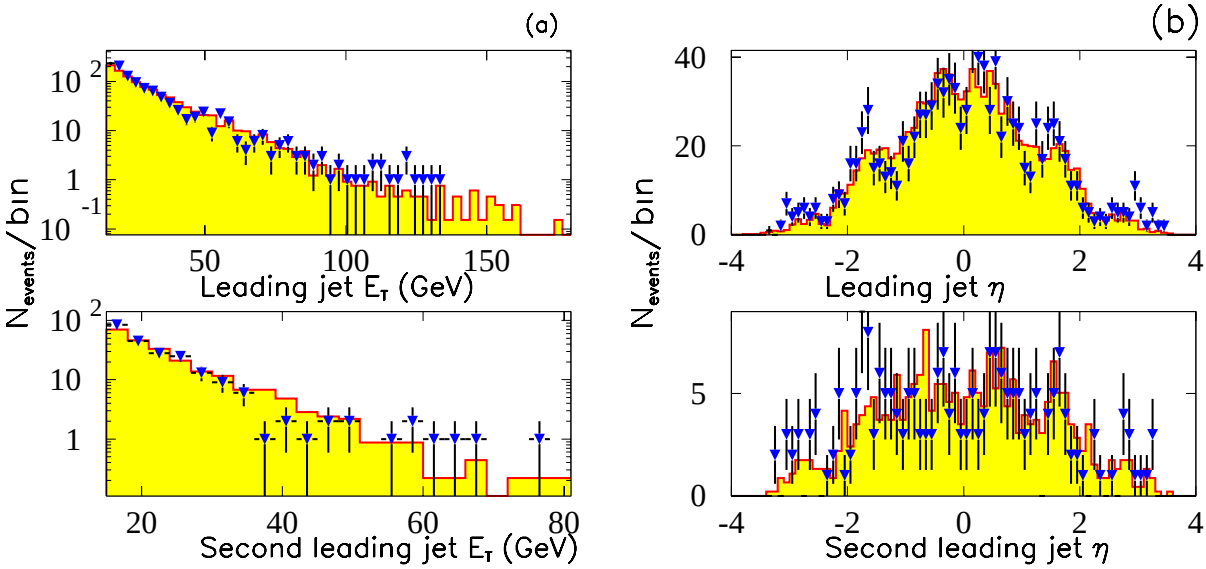

Figure E.4: Comparison of the leading (up) and second leading (down) jet (a) E_T and (b) η between the data (points) and $Z \rightarrow ee+ \geq 1$ jet Enhanced LO Monte Carlo (histogram).

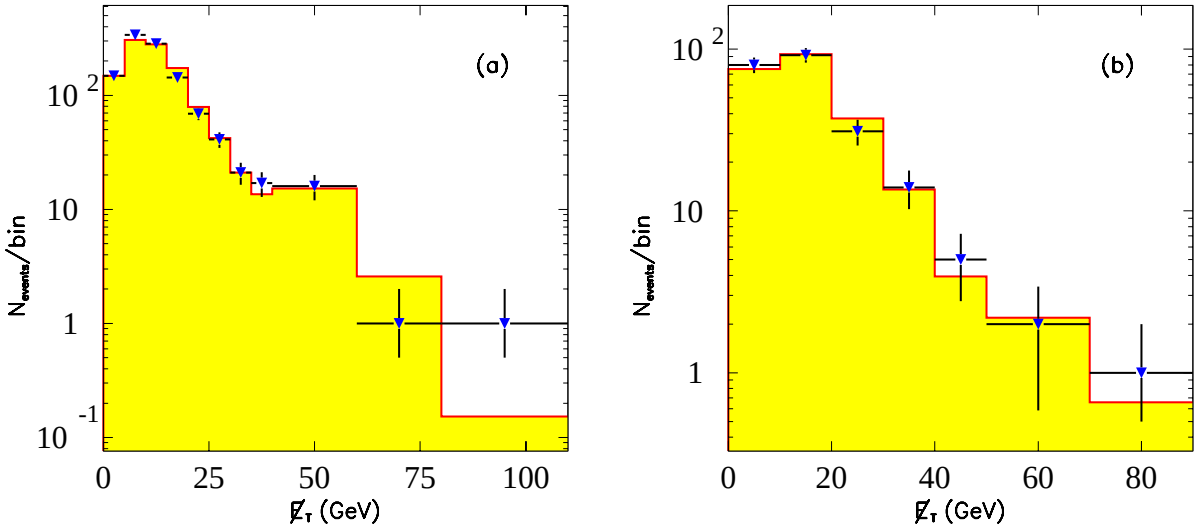

Figure E.5: $\not\!\!E_T$ in inclusive jet multiplicity bins 1 (a) and 2 (b) as predicted in $Z \rightarrow ee+ \geq 1$ jet Enhanced LO Monte Carlo (histogram) compared with data (points).

- **f.** The $\nu\not\!\!E_T$ in the inclusive 1 and 2 jet bin comparison between data and $Z \rightarrow ee+ \geq 1$ jet Enhanced Leading Order Monte Carlo are shown in Figure E.6.

VECBOS/HERPRT/QFL' $Z \rightarrow ee+ \geq 2$ **jets versus** $Z \rightarrow ee+ \geq 2,3$ **jets Data (Jet Multiplicity Bin 2 Predicting Bin 3)**

- **a.** The P_T of the Z boson constructed using the dielectron $\sum \vec{E}_T$ in the inclusive 2 and 3 jet bins comparison between data (points) and $Z \rightarrow ee+ \geq 2$ jets Enhanced LO Monte Carlo (histogram) is shown in Figure E.7.

- **b.** The P_T of the Z boson constructed using the jet $\sum \vec{E}_T$ in the inclusive 2 and 3 jet bins comparison between data and $Z \rightarrow ee+ \geq 2$ jets ELO Monte Carlo is shown in Figure E.8.

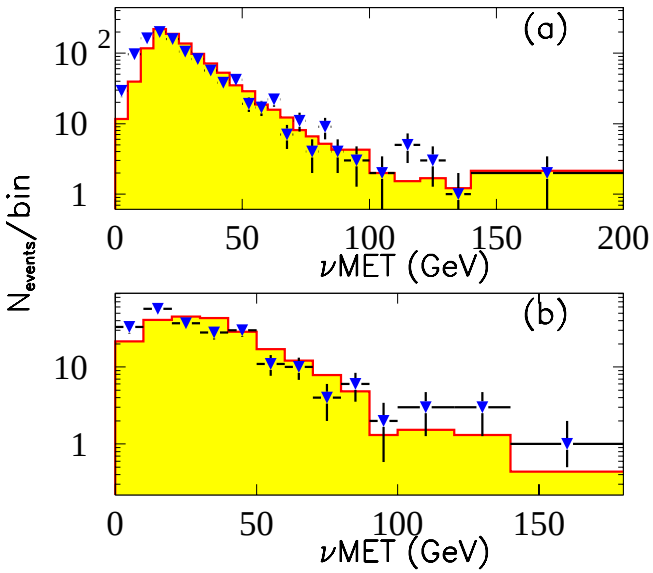

Figure E.6: $\nu\not\!\!E_T = \vec{\not\!\!E}_T + \sum \vec{E}_{T\,dielectron}$ in inclusive jet multiplicity bins 1 (a) and 2 (b) as predicted in $Z \rightarrow ee+ \geq 1$ jet Enhanced LO Monte Carlo (histogram) compared with data (points).

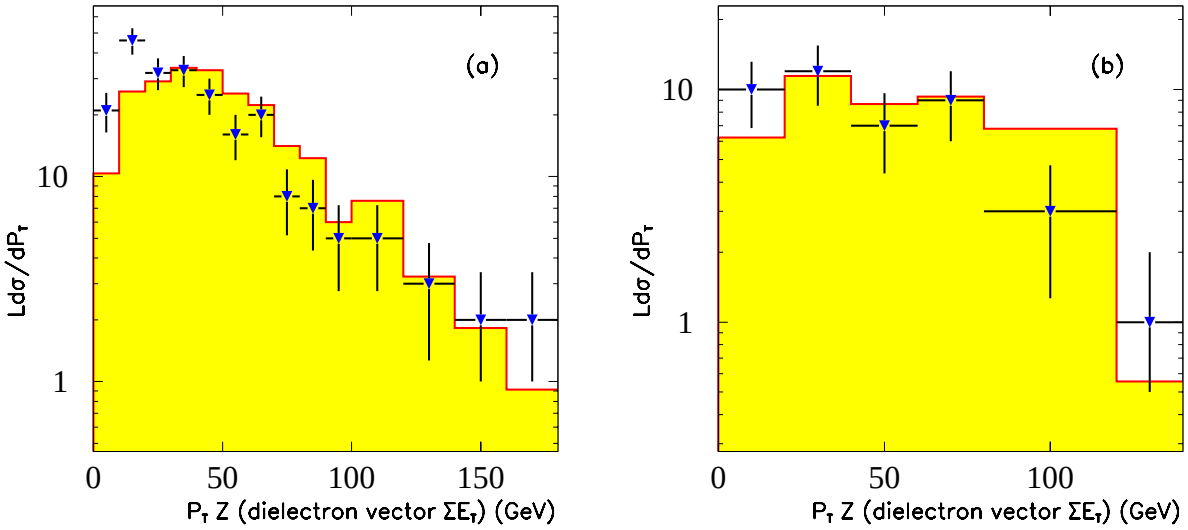

Figure E.7: Z P_T in inclusive jet multiplicity bins 2 (a) and 3 (b) as predicted in $Z \rightarrow ee+ \geq 2$ jet Enhanced LO Monte Carlo (histogram) compared with data (points). The Z P_T is the $\sum \vec{E}_T$ of the electrons.

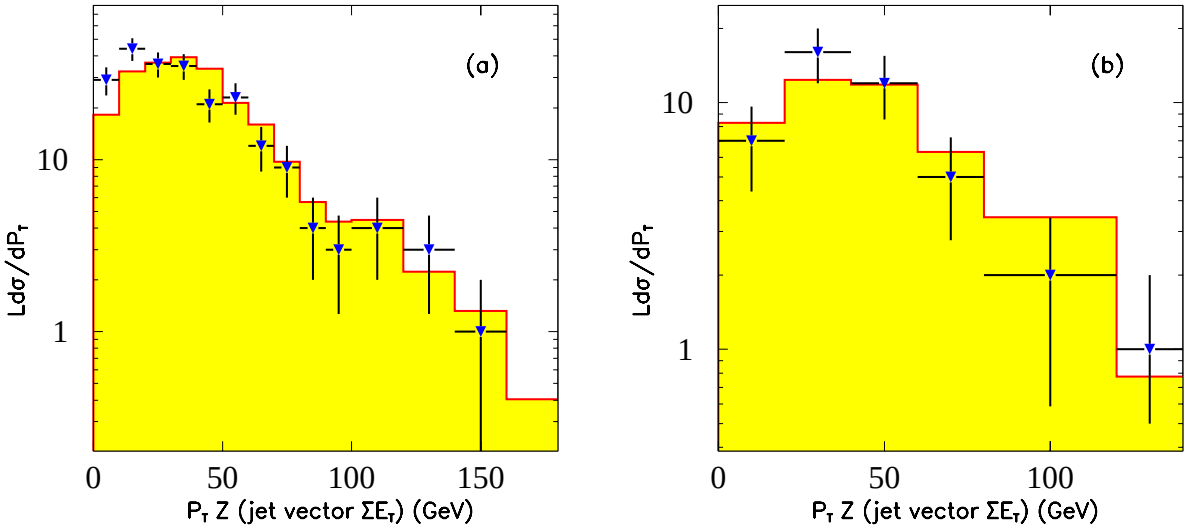

Figure E.8: Z P_T in inclusive jet multiplicity bins 2 (a) and 3 (b) as predicted in $Z \rightarrow ee+ \geq 2$ jets Enhanced LO Monte Carlo (histogram) compared with data (points). The Z P_T is the $\sum \vec{E}_T$ of the jets.

- **c.** The E_T of the second leading and third leading jet comparisons between data and $Z \rightarrow ee+ \geq 2$ jets Enhanced Leading Order Monte Carlo is shown in Figure E.9.

- **d.** The $\not\!\!E_T$ in the inclusive 2 and 3 jet bins comparison between data and $Z \rightarrow ee+ \geq 2$ jets Enhanced LO Monte Carlo is shown in Figure E.10.

- **e.** The $\nu\not\!\!E_T$ in the inclusive 2 and 3 jet bin comparison between data and $Z \rightarrow ee+ \geq 2$ jets Enhanced Leading Order Monte Carlo are shown in Figure E.11.

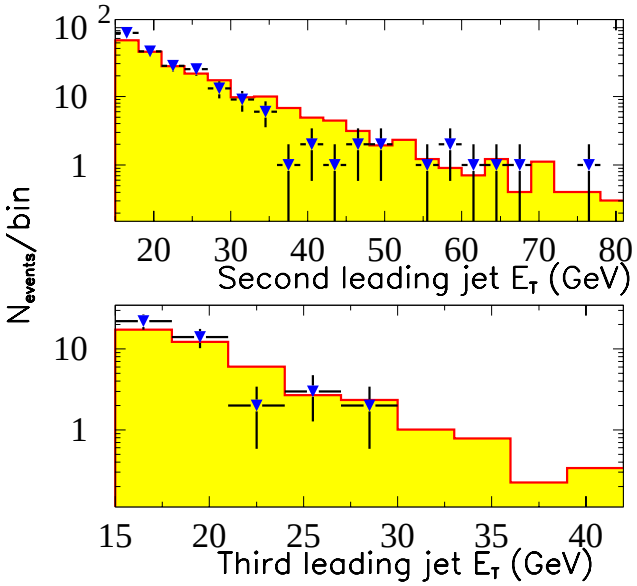

Figure E.9: Comparison of the second leading (up) and third leading (down) jet E_T between the data (points) and $Z \rightarrow ee+ \geq 2$ jets Enhanced LO Monte Carlo (histogram).

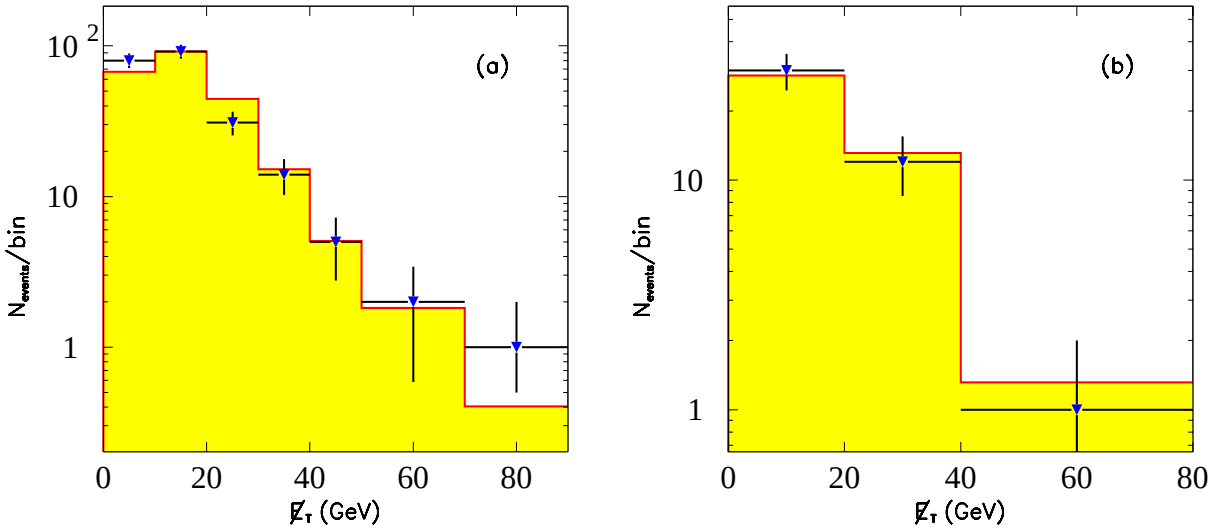

Figure E.10: $\not\!\!E_T$ in inclusive jet multiplicity bins 2 (a) and 3 (b) as predicted in $Z \rightarrow ee+ \geq 2$ jets Enhanced LO Monte Carlo (histogram) compared with data (points).

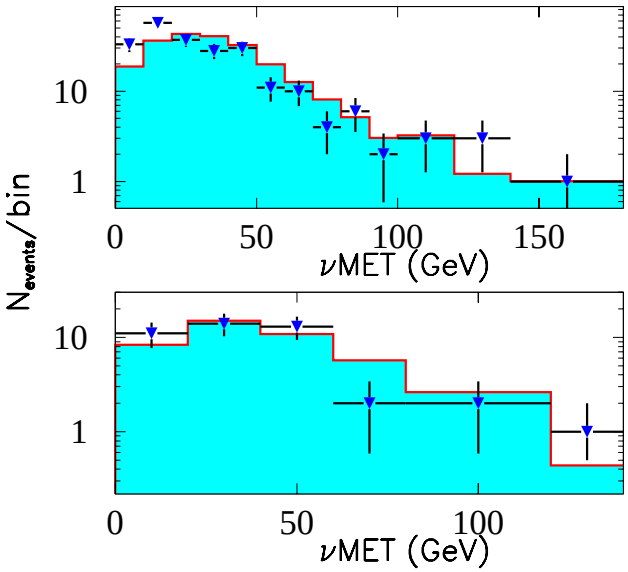

Figure E.11: $\nu\not\!\!E_T = \vec{\not\!\!E}_T + \sum \vec{E}_{T\,dielectron}$ in inclusive jet multiplicity bins 2 (a) and 3 (b) as predicted in $Z \to ee+ \geq 2$ jets Enhanced LO Monte Carlo (histogram) compared with data (points).

A note on The Low Z P_T Non-Perturbative Region

The discrepancy in the low Z P_T region in the comparison between data and Monte Carlo is due to a convolution of the calculation of the spectrum in that regime and the P_T resolution in the data. A correct description of this region requires the resummation of multiple gluon emission, which is calculated in perturbative QCD in the form of Sudakov (Appendix F) form factors. In the muon [32] case where the P_T resolution is better at low P_T , the agreement is better compared to the electron case where the E_T resolution is worse at low E_T . The slope of the distributions at the high P_T region are in agreement, the relevant region for the high $\not\!\!E_T$ $+jets$ search.

E.2 W+jets

In the selection of W events where the boson decays leptonically, apart from identifying the final state lepton in the event, a energetic neutrino that causes a large energy imbalance is required. Dilepton events with an invariant mass > 2 GeV (Drell-Yan) are removed. Z events, selected as discussed in Chapter 5, are also removed. A $\not\!\!E_T$ requirement of 20 GeV is applied. Figure E.12(a) shows the $\not\!\!E_T$ distribution in the inclusive electron + ≥ 1 jet data sample and (b) in the inclusive muon + ≥ 1 jet sample. There are two components in the $\not\!\!E_T$ spectrum: the low fast dropping exponential from the QCD background events that arises from detector resolution and from Z events where an electron or muon is lost. The peak at around 40 GeV is consistent with the neutrino coming from a leptonic W decay. The $\not\!\!E_T \geq$ 20 GeV requirement eliminates a large fraction of the QCD background. There is an ambiguity in the determination of the mass of the W since an invariant mass for the $l\nu$ pair

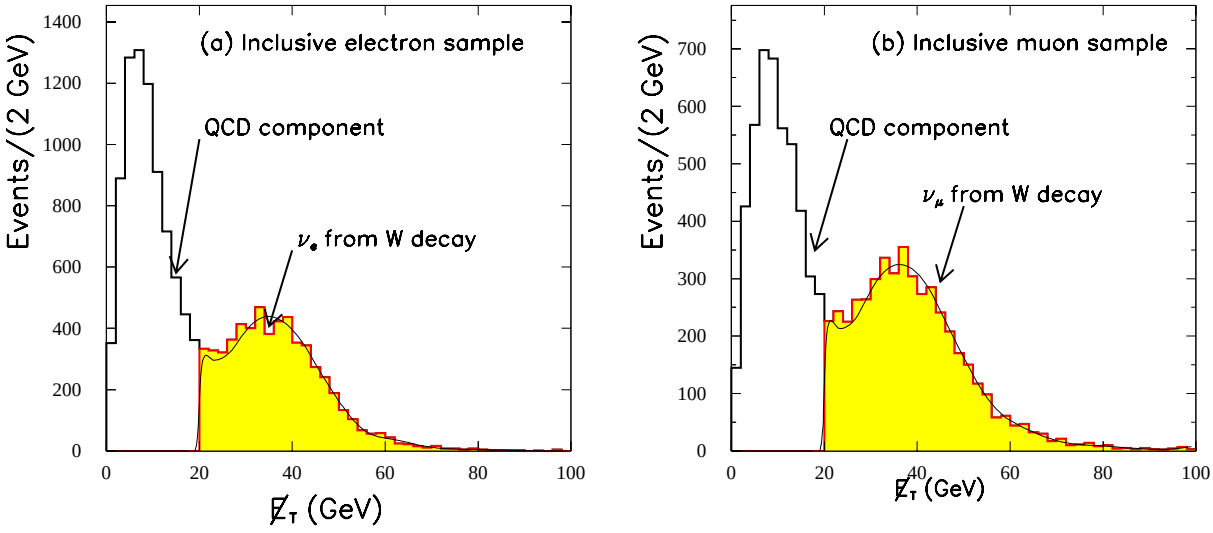

Figure E.12: $\not\!\!E_T$ distribution in (a) the inclusive data sample of isolated electrons + $\geq$1 jets, (b) the inclusive data sample of isolated muons + $\geq$1 jets.

cannot be directly reconstructed: only the transverse missing energy is attributed to the ν. Some unidentified longitudinal momentum will always be lost down the beam pipe. The transverse energy spectra of both leptons in the decay have end-points at around 40 GeV, which suggests a decay of an 80 GeV/c^2 mass object. Consider the leptonic decay of the W at rest, $P_{T(l)} = \frac{1}{2} M_W \sin\theta$. The transverse momentum distribution is given by

$$\frac{d\sigma}{dP_{T(l)}} = \frac{d\sigma}{d\cos\theta}\frac{d\cos\theta}{dP_{T(l)}} = \frac{d\sigma}{d\cos\theta}\left(\frac{2P_{T(l)}}{M_W}\right)\left(\frac{1}{4}M_W^2 - P_{T(l)}^2\right)^{-1/2} \tag{E.1}$$

The last factor is peaked at $P_{T(l)} = \frac{1}{2} M_W$. This peak is smeared by the width and transverse motion of the W. The transverse mass is less sensitive to the longitudinal

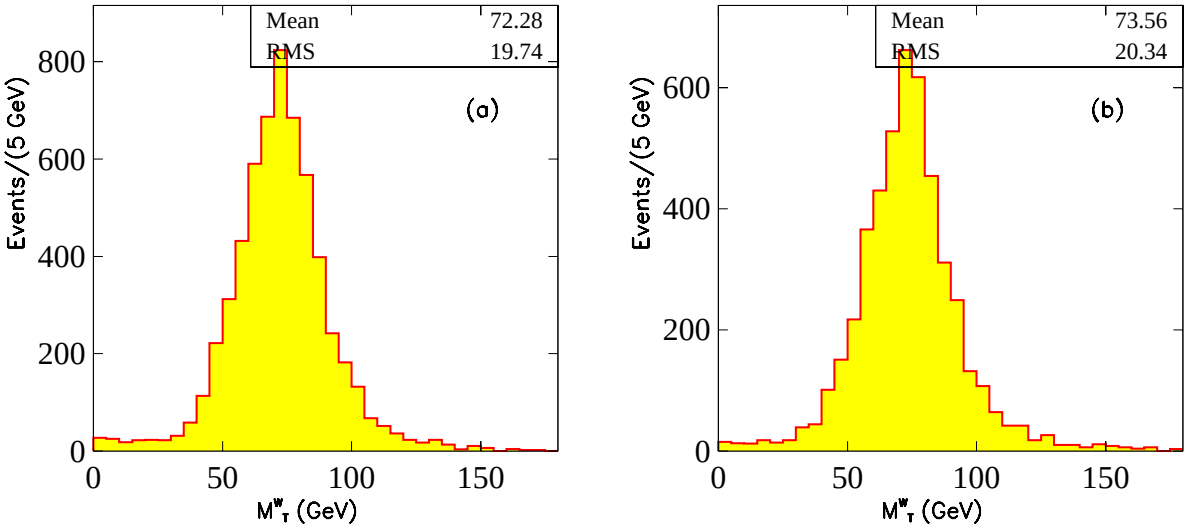

Figure E.13: W boson transverse mass distribution in (a) the inclusive sample of isolated electrons + $\geq$1 jets, (b) the inclusive sample of isolated muons + $\geq$1 jets.

motion of the W. The W transverse mass is defined as:

$$M_W^2 = (E_{T(l)} + E_{T(\nu)})^2 - (\vec{P}_{T(l)} + \vec{P}_{T(\nu)})^2 \simeq 2P_{T(l)}P_{T(\nu)}(1 - \cos\phi) \qquad \text{(E.2)}$$

where ϕ is the azimuthal separation between the charged lepton and the neutrino. Figure E.13 shows the W mass in the inclusive electron plus 1 jet (a) and muon plus 1 jet (b) data samples respectively. The comparisons of the transverse mass between data and Enhanced LO Monte Carlo $W \to l\nu$ + $\geq$ 2 jets, + $\geq$ 3 jets predictions are shown in Figures E.14 & E.15 for the electronic and muonic Ws respectively. The same comparisons are shown for the $\not\!\!E_T$ spectrum in Figures E.16 & E.17 for the electrons and muons respectively.

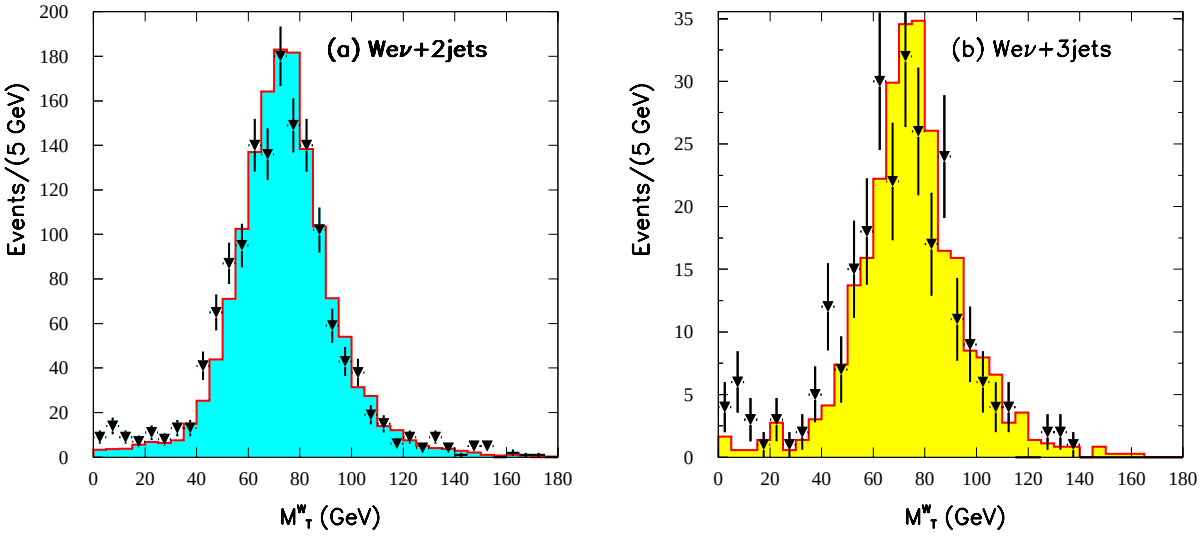

Figure E.14: W boson transverse mass distribution in data (points) and Enhanced LO Monte Carlo $W \to e\nu + \geq 2$ jets (histogram) in the (a) inclusive 2 jet multiplicity and (b) 3 jet multiplicity bin.

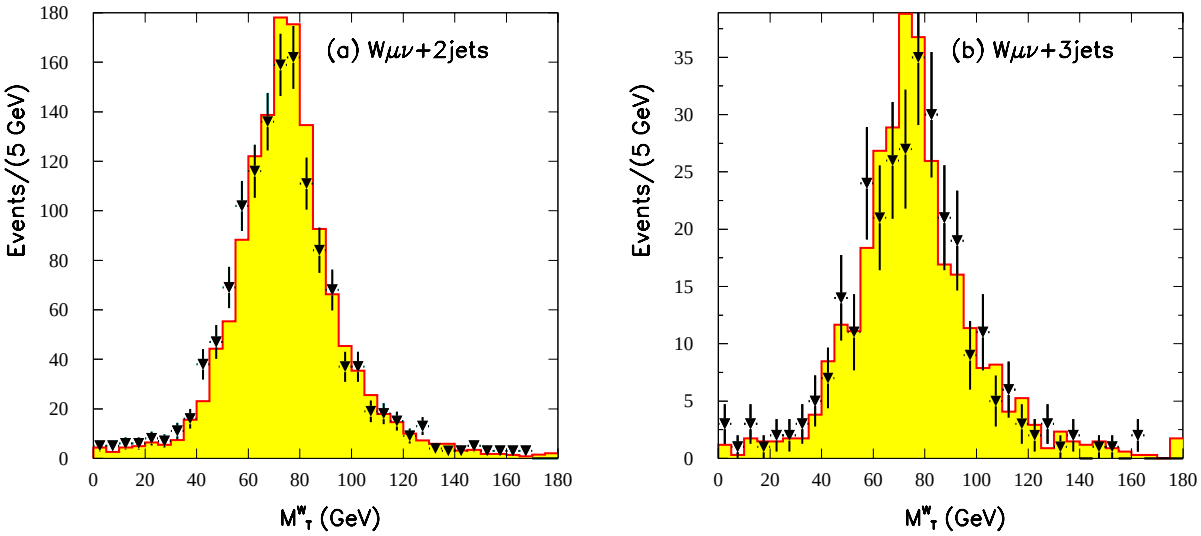

Figure E.15: W boson transverse mass distribution in data (points) and Enhanced LO Monte Carlo $W \to \mu\nu + \geq 2$ jets (histogram) in the (a) inclusive 2 jet multiplicity and (b) 3 jet multiplicity bin.

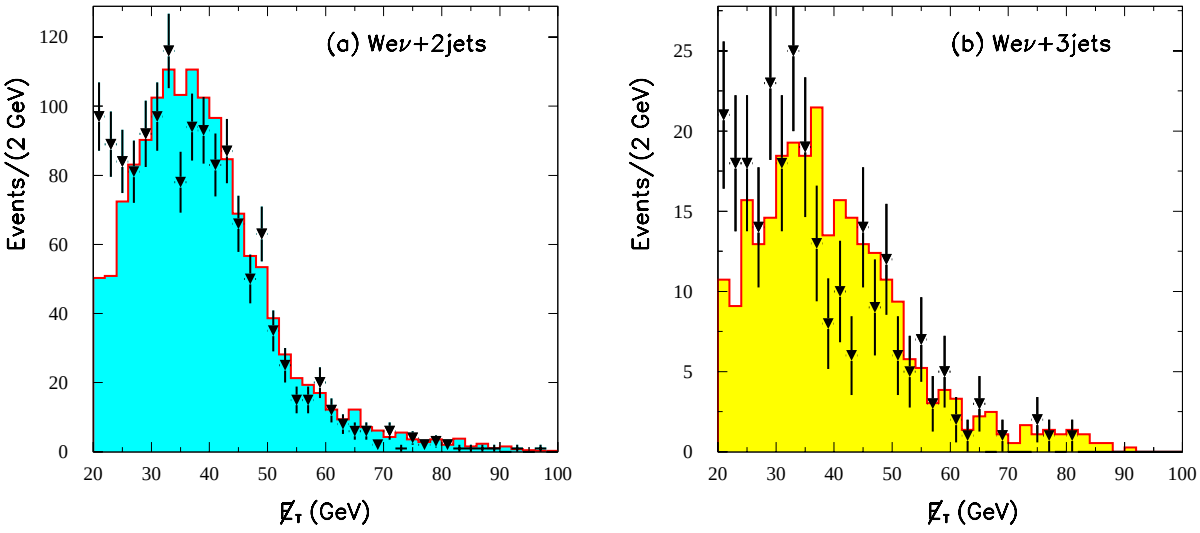

Figure E.16: $\not\!\!E_T$ distribution in data (points) and Enhanced LO Monte Carlo $W \rightarrow e\nu + \geq 2$ jets (histogram) in the (a) inclusive 2 jet multiplicity and (b) 3 jet multiplicity bin.

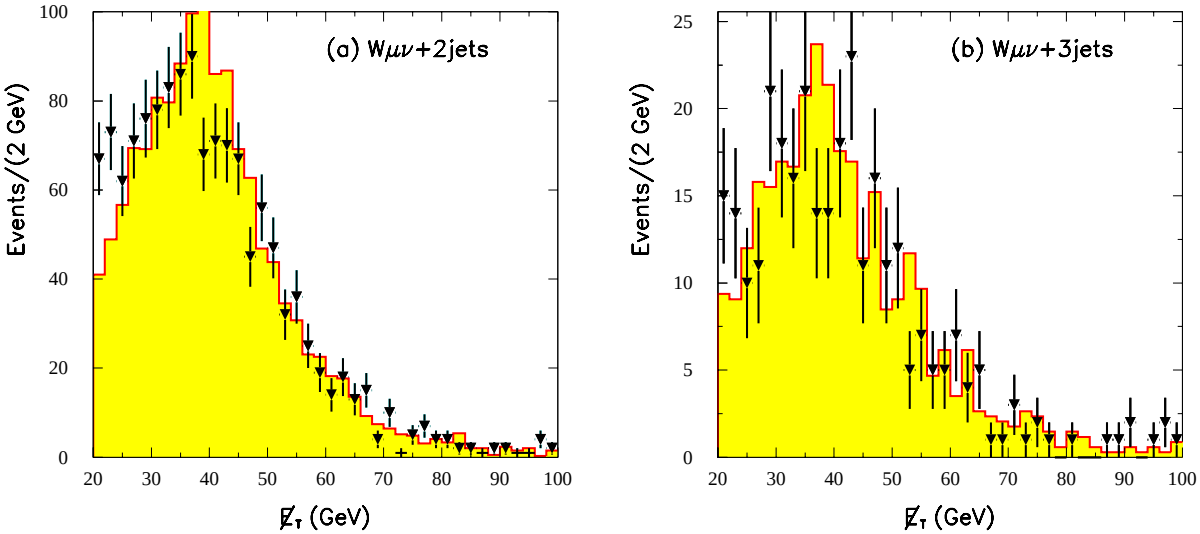

Figure E.17: $\not\!\!E_T$ distribution in data (points) and Enhanced LO Monte Carlo $W \rightarrow \mu\nu + \geq 2$ jets (histogram) in the (a) inclusive 2 jet multiplicity and (b) 3 jet multiplicity bin.

Appendix F

Jet Physics, Quantum Chromodynamics

F.1 Naive Parton Model

Jet physics began with deeply inelastic scattering at SLAC in the late 1960s. Among the discoveries was that of *scaling* the fact that the inclusive differential cross section for (Figure F.1)

$$e(k) + N(p) \rightarrow e(k') + X \tag{F.1}$$

that is

$$\frac{d^2\sigma}{d\Omega dk^{0\prime}} \tag{F.2}$$

is expressed as a function of a single kinematic variable, x

$$x = \frac{Q^2}{2M\nu} \tag{F.3}$$

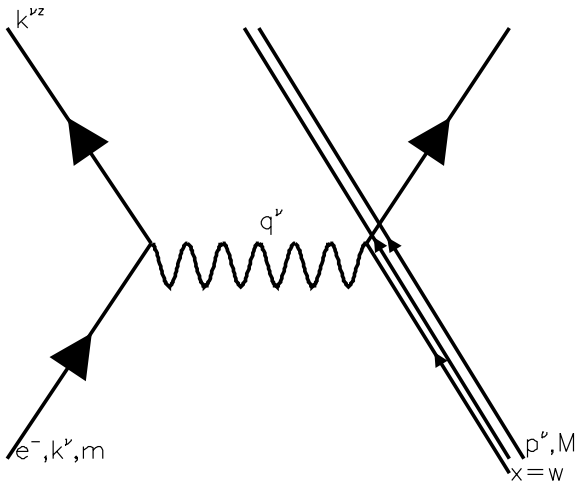

Figure F.1: Deeply Inelastic Scattering.

with M the mass of the proton, ν the electron energy loss and Q^2 the change in the electron four momentum. Q^2 is an index of how hard the collision is. In the Feynman parton model the proton is pictured as an ensemble of quasi-free massless, point like particles. In a frame where the proton has infinite momentum the electron interacts with a parton which carries a momentum fraction w of the proton and the two scatter with the rest of the proton recoiling. For a massless parton

$$k' = (k+q)^2 = q^2 + 2k \cdot q \tag{F.4}$$

$$k = wP \tag{F.5}$$

$$P \cdot q = M\nu \tag{F.6}$$

$$w = -\frac{q^2}{2P \cdot q} = \frac{Q^2}{2M\nu} = x \tag{F.7}$$

Parton models are described in terms of a)functions which give the momentum distribution of the partons, b)a hard scattering process, c)a way to form stable par-

ticles off the outgoing partons. The first and last are characterized by much larger time than the hard scattering reaction.

The formation of jets is predicted in the parton model. The partons are thought of as quasi-free particles within the nucleon but the forces between them grow large as they tend to separate; the nucleon is stable itself. The recoiling parton leaves a trail of particles (the jet) formed by the energy in the stretching field lines between parton pairs. The P_T flow in a hard scattering event lies in an angular region around the recoiling parton. The momentum of particles in the jet transverse to the jet axis is small and the angular extent of the jet grows smaller as its total P_T increases. In hadron-hadron collisions the same ideas hold. The two colliding nucleons are highly relativistic. The colliding partons carry momentum fractions x_1 and x_2 with probability determined by the hadrons' parton momentum distribution functions. The center of mass energy of the two partons and the total longitudinal momentum P_l are

$$\hat{s} = x_1 x_2 E_{beam}, \qquad P_l = (x_1 - x_2) E_{beam} \tag{F.8}$$

The first clusters of back to back hadronic jets were observed in e^+e^- collisions at SPEAR [109], [110]. ISR at CERN also reported jet production [111] and UA2 [112] showed that the "jettiness" of the event increased with the P_T in the event. The hadronic collider experiments also found that along with the jets there was an *underlying event* created by the proton remnant which behaved qualitatively as a *Minimum Bias* collision typical of less energetic collisions. This was a model. The theory is Quantum Chromodynamics.

F.2 Quantum Chromodynamics: Summary

Quantum Chromodynamics gives an additional degree of freedom called *color* to the Gell-Mann quarks and uses the associated local gauge symmetry to provide the dynamics. The Lagrangian density is

$$L_{QCD} = -\frac{1}{2}TrG_{\mu\nu} + \sum_{i=1}^{n_f} \bar{q}_i(i\gamma^\mu D_\mu - m_i)q_i \tag{F.9}$$

where

$$G_{\mu\nu} = \partial_\mu A_\nu - \partial_\nu A_\mu - ig[A_\mu, A_\nu], D_\mu q_k = (\partial_\mu - igA_\mu)q_k, A_\mu = \sum_{\alpha=1}^{8} A_\mu^\alpha \lambda^\alpha/2 \tag{F.10}$$

The matter fields are the quarks. They are four component Dirac spinors with flavor (up, down,strange, charm, top, bottom) and color (1,2,3 for blue, red, green) indices. The flavor indices are neglected in the above expressions as they are not affected by the QCD interactions. The gauge fields (A_μ) are the gluons, which being vectors, carry Lorentz indices and color indices. The quark and gluon fields have kinetic energy. The gluon kinetic energy is antisymmetric on its Lorentz indices: there is no explicit mass terms for the gluons. There are three- and four-point gluon couplings. The term with the covariant derivative describes the quark gluon interaction. There is an explicit mass term for the quarks. Generally the mass of the quarks is taken to be zero.

The Lagrangian is invariant under local gauge transformations. Important aspects of QCD become apparent when the theory is renormalized. Renormalization relieves the theory from unphysical infinities when calculating Feynman diagrams. It also shows how field theory changes with the momentum scale of the particles involved.

The renormalization program introduces a redundant momentum scale μ. Physics processes cross sections are calculated in term of the momentum scale and the other parameters of the theory. The basic parameters of the theory, such as coupling constants, change with the momentum scale and the measurable cross sections do not depend on the redundant momentum scale. The scale dependence of the QCD strong coupling constant depends on only one parameter in the leading order approximation:

$$a_s(Q^2) = \frac{12\pi}{(33 - 2f)\ln(Q^2/\Lambda^2)} \tag{F.11}$$

f is the number of flavors of fermions of mass less than $Q/2$ and Λ is the fundamental scale parameter of QCD. The unrenormalized theory had no such fundamental parameter. Λ describes how quickly the coupling constant changes with the momentum scale. For high momentum transfer the coupling constant goes to zero but it is large for values of the momentum transfer close to Λ. The falling of the coupling constant with Q^2 is called *asymptotic freedom*, and this is the major reason perturbation theory (which requires a small coupling constant to expand about) can be applied to high Q^2 processes. For $Q^2 \sim \Lambda^2$ the above expression is not be to be believed: $a_s(Q^2)$ becomes very large and the perturbative approach behind the expression breaks down. Λ can be thought of as the energy scale at which the strong interactions really become strong, *i.e.* the confining forces set in. In terms of distance the confining region of the strong forces is about 1 fm suggesting a value of Λ of about 200 MeV.

At very high Q^2 the individual quarks are probed in the proton and ultimately the sea quarks and antiquarks as well as gluons. As the Q^2 becomes larger the quarks probed are very likely to have radiated a gluon. In the naive parton model the scaling behavior is a kinematic result. To zeroth order in a_s the *structure functions*

F_1 and F_2 which describe the two parts of the hadron tensor do not depend on the momentum scale. Applying the calculation at a higher Q^2 the dynamics are changing. The momentum fraction of the quark taken from the proton is the same but there is a probability of gluon *bremßtrahlung* and the longitudinal momentum of the quark has to be degraded. In the calculation the quark needs a small mass so that divergences are controlled. The result is that at higher Q^2 the leading order calculation is inadequate and the inclusion of next-to-leading order (first order in a_s) corrections is resulting in a logarithmic dependence on Q^2 (scaling is violated). The quark momentum distributions evolve according to the Altarelli-Parisi expression

$$\frac{dq(x,Q2)}{d(lnQ^2)} = \frac{a_s(Q^2)}{2\pi}\int_x^1 \frac{dw}{w}[q(w,Q^2)P_{qq}(\frac{x}{w}) + g(w,Q^2)P_{qg}(\frac{x}{w})] \tag{F.12}$$

$P_{qq}(z) = \frac{4}{3}(\frac{1+z^2}{1-z})$ is the probability that a quark having radiated a gluon is left with a fraction z of its original momentum (which is already a fraction w of the hadron momentum). This probability is high for large momentum fractions: high momentum quarks lose energy by radiating gluons. The tendency is that the distribution function will get smaller at large x and larger at small x. The singularity at z=1 is the infrared divergence and is associated with the emission of a soft gluons. $P_{qg}(z)$ is the probability that a gluon splits into a quark with momentum fraction z and an antiquark with momentum fraction 1-z. These probability functions are called *splitting functions*. The structure functions F_1 and F_2 can be related to sums of the quark distribution functions in electron-nucleon deeply inelastic scattering. By measuring differential cross sections for different hadronic targets and employing isospin symmetry arguments, information about the individual distribution functions is obtained. Measurement shows that quarks and antiquarks carry only half of the

proton's momentum.

Determining the distribution functions of the gluons is more difficult because none of the traditional lepton probes interact with gluons. The absence of antiquarks beyond a certain value of x indicates that there are no gluons with momentum fraction that high or higher, since all antiquarks in the proton came from gluon splitting into $q\bar{q}$ pairs. By measuring the antiquark distribution functions and their change with Q^2 the gluon distribution function can be solved for.

The calculation of the distribution functions is an iterative process. Starting at a Q^2 the first order change is calculated for a slightly higher Q^2, and the new $q(x, Q^2)$ is used as a starting point in the next iteration. The Altarelli-Parisi equations are not used to determine how the momentum is shared at any Q^2 but rather how if the sharing is measured in one experiment at one value of Q^2 it can be used to describe the sharing at a different Q^2.

F.2.1 Final/Initial State Radiation and Fragmentation

During the final state shower, time-like partons produced in the initial state shower and the hard scattering radiate until their invariant mass is so small that perturbation theory can no longer be applied. The calculation is a classical approximation that considers each radiation as an independent process. The infrared radiation is incorporated in HERWIG (soft gluon interference). *Final state evolution* is an attempt to describe the formation of a parton cascade , a quantum mechanical process, in classical terms. In the calculation of the Feynamn graph, the kinematics and branchings are specified and an amplitude is calculated. In a shower Monte Carlo the process is reversed. The probabilities are given and all the kinematics and topology are generated. In this specific sense, evolution refers to the choice of the invariant mass squared

of the parton, often called *virtuality* of the parton. The *Sudakov form factor* which represents the probability that a parton a which originates with invariant mass Q has evolved without branching from Q^2 down to t is used in the final state evolution:

$$d\Delta(t, Q_0^2) = -\frac{dt}{t}\Delta_\alpha(Q^2, Q_0^2)\sum_b \int dz \frac{\alpha_s}{2\pi} P_{ba}(z) \tag{F.13}$$

The parton shower proceeds by generating a random number R between 0 and 1 and solving $\Delta(Q^2, t) = R$ for t. If t is less than Q_0^2, the perturbative cutoff, there is no branching. Otherwise there is branching with energy fraction given by the splitting function. Each parton is assigned a momentum fraction z and a tentative virtuality, $(1-z)t$, and the process is repeated on each of the partons.

In ISAJET z is not the momentum fraction carried away by the radiated particle but the light cone energy fraction $z = \frac{E'+P'_L}{E+P_L}$. The perturbative cutoff is 6 GeV and to study the systematic uncertainty due to the final state radiation in this analysis the cutoff is varied.

The initial state shower is simulated in a manner very similar to the final one. The initial parton with a low virtuality (near the perturbative cutoff) as it radiates time-like partons becomes more space-like until it reaches the hard scattering Q^2 scale where it is not necessary that the the fundamental kinematic condition $x_1 x_2 = \frac{M^2}{s}$ is met. The solution to this problem [113] is to generate the shower in a backward manner with the space-like partons evolving back down to their mass shell by radiating time-like partons. *Fragmentation* refers to end of the jet formation where the colored partons turn themselves under the action of the strong force into color singlet hadrons. Associated with each parton is a fragmentation function $D_h^k(z)$ which is the probability of finding a hadron of type h with momentum fraction z in a jet of type

k. The fragmentation function is assumed universal. An up-quark jet is the same in any process that involves up-quark outgoing parton. A splitting function $f_h^k(z)$ is at any stage of the fragmentation the probability that the type k jet produces a hadron h with momentum fraction z. The fragmentation function is

$$D(z) = f(z) + \int_z^1 f(1-z')D(\frac{z}{z^{prime}})\frac{dz'}{z'} \tag{F.14}$$

The Field-Feynman quark-jet algorithm [114] uses $f(z)$ to generate the flavors and momentum fraction of the first $q\bar{q}$ meson. It gives it a small transverse momentum, and a spin. The procedure is repeated for all quarks until they have energy less than a specified cut (usually the pion mass). The unmatched quarks are assembled into hadrons by an ad hoc mechanism. Gluons are replaced by a $q\bar{q}$ pair. Since each jet chain conserves momentum but does not conserve energy, the kinematics of the event are rescaled. To study the systematic uncertainty due to the initial state modeling in ISAJET, the initial evolution is omitted and the results are compared with the nominal evolution scheme.

F.3 QCD-improved parton model

To summarize, jet production at the Tevatron $p\bar{p}$ collisions can be described as a series of phases each characterized by a particular value of Q^2.

- Protons and antiprotons are characterized by 900 GeV energy and by quark and gluon distribution functions, which at some low value of Q^2 describe how the hadron's momentum is shared among its constituents.

- The colliding partons go through initial state evolution, described by the Altarelli-

Parisi equations. By radiating time-like partons (with mass larger than the rest mass) they tend to become space-like(with mass less than the rest mass). The time-like partons will take part in the final state shower. The space-like partons can not radiate real particles. The sum of the 4-momenta of the colliding space-like partons which travel in opposite directions, is time-like. The masses squared of the space-like particles which take part in the hard collision are a generally of the same order as their center of mass energy, but negative.

- The hard-scattering of quasi-free partons described by a QCD matrix element squared follows the initial state evolution. Two or more scattered partons emerge from the hard collision with positive mass. The probability of the scattering is proportional to a_s^n where n is the number of scattered partons.

- The scattered partons and the time-like partons radiated in the initial state shower take part in the final state shower where by successive radiation, all particles return to their mass shell. At high values of Q^2, the dynamics of the shower are well described by perturbative QCD.

- Below a certain cutoff the strong coupling constant is too large to trust perturbative calculation. Phenomenological models are used to describe the final stages of the evolution and the formation of hadrons, known as fragmentation or hadronization.

A review of QCD tests in $p\bar{p}$ can be found in Reference [115].

F.3.1 Multijet Monte Carlo generation

There are two basic approaches in generating basic QCD processes. In the first approach there is no initial or final state evolution and no production of final state

particles. The parton momentum functions are evolved to the proper Q^2 using the Altarelli-Parisi equation but the time-like particles that would be produced are ignored. 2, 3, and 4 jet events are produced separately and all processes must be calculated in the same order for the cross sections to be well-behaved order by order in a_s. With increasing center of mass energy more P_T is available for the production of distinguishable jets and the relative probability for example for 4-jet production relative to 2-jet production grows. The third order calculation is not adequate. To include four jets the 2-jet, 3-jet cross section has to be calculated to order a_s^4. Monte Carlo programs which include initial and final state showers based on the Altarelli-Parisi equations avoid this problem. ISAJET generates a parton shower each branch of which appears with probability $a_s \ln Q^2$ where Q^2 refers to the mass of the parton that radiates. This leading log procedure sums all terms of form $a_s^n \ln^n Q^2$ for all n and this is generating a *multijet-like* production process. The artificial distinction between n and $n+1$ jet events is blurred.

In this analysis the data are used to normalize QCD and W/Z QCD associate production. Shower Monte Carlo programs (HERWIG, VECBOS+HERPRT) are employed to simulate these processes.

F.4 VECBOS, HERPRT

Who is this VEC-BOS anyway? I discovered QCD. ..

Giudo Altarelli, top announcement seminar, CERN, 1994

VECtor BOSon is a leading order Monte Carlo for inclusive production of a W-boson plus up to 4 jets or a Z-boson plus up to 3 jets in hadron colors. The correlations of the vector boson decay fermions with the rest of the event are built in.

VECBOSemploys the multidimensional integration routine VEGAS to calculate the production cross sections. The total cross section for m-jet production in the QCD improved parton model can be expressed as

$$\sigma_m(s) = \sum_{final} \sum_{i,j} \int ... \int d\Phi_m dx_1 dx_2 \{ f_i^{H_1}(x_1, Q^2) f_j^{H_2}(x_2, Q^2) (\frac{d\hat{\sigma_m}(x_1 x_2 s)}{d\Phi_m})_{i,j,final} \}. \tag{F.15}$$

The integrals are carried out over the parton momentum fractions x_1 and x_2 and the available phase space Φ_m at $\hat{s} = x_1 x_2 s$, the center-of-mass energy at parton level. The matrix element squared summed over helicities and color is incorporated within the partonic cross section $\hat{\sigma}_m(\hat{s})$ and scales as g^{2m} where g is the running coupling constant. $\Phi_m(\hat{s})$ represents the phase space volume for a final state of m massless particles with an invariant mass squared $\hat{s}$ and can be written

$$\Phi_m(\hat{s}) = \frac{(\pi/2)^{m-1} \hat{s}^{m-2}}{(m-1)!(m-2)!} \tag{F.16}$$

The integration element over the phase space term is

$$d\Phi_m = \frac{1}{\Phi_m(\hat{s})} \delta^4 (\sum_{total} P_i) \prod_{final} (\frac{d^3 \vec{P}_i}{2P_i^0}). \tag{F.17}$$

The matrix elements implemented in VECBOS [25] are calculated using the Weyl-van der Waerden spinor calculus as well as recursive techniques when there are three or more gluons in a process and the helicity amplitudes calculations become complex. Before the generation, VECBOS identifies the regions of phase space where the integrand has the largest value using importance sampling. This significantly increases the efficiency of the event unweighting. [25]. The VECBOS output consists of the

four momenta of final state partons and the event weight. The production cross section is the sum of the event weights in the sample. The final state partons are not tagged as gluons or quarks since the calculation is carried out by summing over all possible states. All the colored partons are assumed to be indistinguishable. HERPRT [25] is used to randomly assign flavors and color flows to the final state partons calculated with VECBOSby sampling all allowed Feynman diagrams for the process in question. HERPRT employs HERWIG [26] for the gluon shower evolution (Initial (ISR) and Final (FSR) state), the formation of clusters, hadronization, heavy flavor and unstable hadron decays and the soft underlying event. It is assumed that there are only two types of partons, quarks and gluons, which is justified by charge conjugation conservation and that the light quarks are massless objects. HERWIG uses the Gribov-Pipatov-Altarelli-Parissi splitting functions which describe the breaking of a parton of type a into partons of type b, when the momentum transfer Q^2 is increased.

Appendix G

From the Standard to the Super-Models of Particle Physics

"Let me stress that I do not believe
that the standard theory will long survive
as a correct and complete picture of physics"
Shelly Glashow, Stockholm 1979

G.1 Within and Beyond Standard Model

The Standard Model [45], is considered to be a low energy effective theory of a yet more fundamental theory which is not well formulated as of now. To date there is very strong experimental confirmation of the Standard Model up to several hundred GeV energy range and several possible extensions have been ruled out. There are unanswered principle questions within the Standard Model and questions arising from hypothetical frameworks beyond the Standard Model that motivate particle physics experiments today. The source of electroweak symmetry breaking, whether an

observable light Higgs boson exists and whether it is connected with supersymmetry breaking at the electroweak scale, what is the supersymmetric particle spectrum and how the symmetry is broken are such questions. If supersymmetry is not the case, then what other strong interaction exists? What is the source of the neutrino masses if the neutrinos are confirmed to be massive? What kind of new particles may make up a significant dark matter component? What is the underlying physics that might explain the cosmological baryon asymmetry and the cosmological constant? Is gravity quantized and are there extra dimensions?

The Standard Model is given in terms of at least 19 parameters: 3 gauge couplings $g_{1,2,3}$ and 1 CP-violating non-perturbative vacuum angle θ_3, 6 quark and 3 charged-lepton masses with 3 charged weak mixing angles and 1 CP-violating phase δ, and 2 parameters (μ, λ) or (m_H, m_W), to characterize the Higgs sector. More parameters are required to accommodate non-accelerator observations. Neutrino masses [117] and mixing introduce at least 7 parameters: 3 masses, 3 mixing angles and 1 CP-violating phase.

Table G.1 summarizes the quantum number assignments of the fermions under the standard $SU(3)_C \times SU(2)_L \times U(1)_Y$ gauge group. The assignments are such that the theory is gauge invariant at the quantum level and all anomalies cancel. The hypercharges($Y/2 = Q - I_3$) are a priori independent of the $SU(3) \times SU(2)_L$ assignments, and quantized in the unit of 1/6 to ensure neutrality of bulk matter (measured at a precision of 10^{-21} [76]).

The standard $SU(3)_C \times SU(2)_L \times U(1)_Y$ gauge group is constructed by three seemingly unrelated gauge groups and has anomaly-free particle content in a non trivial way. The essential ingredient in the Standard Model is the electroweak symmetry breaking. In Table G.2, the bosonic particle content of the Standard Model is

shown. The gauge multiplets are necessary consequences of the gauge theories, and they appear natural. They all carry spin 1, except for one spinless multiplet: the Higgs doublet

$$\begin{pmatrix} H^+ \\ H^0 \end{pmatrix} \tag{G.1}$$

which is introduced for the purpose of breaking the electroweak symmetry $SU(2)_L \times U(1)_Y \to U(1)_{\mathrm{QED}}$ [116]. The Higgs potential

$$V = \mu^2 |H|^2 + \lambda |H|^4, \tag{G.2}$$

(where $v^2 = \langle H \rangle^2 = -\mu^2/2\lambda = (175\ \mathrm{GeV})^2$) is arranged in a way to break the symmetry without any microscopic explanations.

In the Standard Model there is a seemingly unnecessary threefold repetition of generations. The fermions have a mass spectrum which stretches over almost with six orders of magnitude between the electron and the top quark. Considering the recent evidence for neutrino oscillations, which suggest a mass of the third-generation neutrino of about 0.05 eV^2 [117], the mass spectrum is stretching over 13 orders of magnitude.

G.2 Energy - Distance scale of the Standard Model

A search for physics beyond the Standard Model implies probing at shorter distances than the distance scale of the Standard Model itself. The distance scale of the Standard Model is given by the size of the Higgs boson condensate $v = 175$ GeV. In natural units, it gives the distance scale of $d = \hbar c/v = 0.8 \times 10^{-16}$ cm. By asserting that the Standard Model is valid down to a smaller distance scale than d it is expected

$\begin{pmatrix} \nu'_e \\ e \end{pmatrix}_L^{-1/2}$	$\begin{pmatrix} \nu'_\mu \\ \mu \end{pmatrix}_L^{-1/2}$	$\begin{pmatrix} \nu'_\tau \\ \tau \end{pmatrix}_L^{-1/2}$	e_R^{-1}	μ_R^{-1}	τ_R^{-1}
$\begin{pmatrix} u \\ d' \end{pmatrix}_{L,g}^{1/6}$	$\begin{pmatrix} c \\ s' \end{pmatrix}_{L,g}^{1/6}$	$\begin{pmatrix} t \\ b' \end{pmatrix}_{L,g}^{1/6}$	$u_{R,g}^{2/3}$ $d_{R,g}^{-1/3}$	$c_{R,g}^{2/3}$ $s_{R,g}^{-1/3}$	$t_{R,g}^{2/3}$ $b_{R,g}^{-1/3}$
$\begin{pmatrix} u \\ d' \end{pmatrix}_{L,r}^{1/6}$	$\begin{pmatrix} c \\ s' \end{pmatrix}_{L,r}^{1/6}$	$\begin{pmatrix} t \\ b' \end{pmatrix}_{L,r}^{1/6}$	$u_{R,r}^{2/3}$ $d_{R,r}^{-1/3}$	$c_{R,r}^{2/3}$ $s_{R,r}^{-1/3}$	$t_{R,r}^{2/3}$ $b_{R,r}^{-1/3}$
$\begin{pmatrix} u \\ d' \end{pmatrix}_{L,b}^{1/6}$	$\begin{pmatrix} c \\ s' \end{pmatrix}_{L,b}^{1/6}$	$\begin{pmatrix} t \\ b' \end{pmatrix}_{L,b}^{1/6}$	$u_{R,b}^{2/3}$ $d_{R,b}^{-1/3}$	$c_{R,b}^{2/3}$ $s_{R,b}^{-1/3}$	$t_{R,b}^{2/3}$ $b_{R,b}^{-1/3}$

Table G.1: The fermionic particle content of the Standard Model. The primes on the neutrinos indicate that the mass eigenstates are rotated by the Maki-Nakagawa-Sakata [118] mass matrix as the primes on the down-quarks in the quark isodoublets indicate rotation by the Cabbibo-Kobayashi-Mascawa [119] matrix. The subscripts g, r, b refer to the color of QCD and the superscripts to the electric charge.

W^1, W^2, H^+, H^-	$\longrightarrow$	W^+, W^-
$W^3, B, \mathrm{Im}(H^0)$	$\longrightarrow$	γ, Z
$g \times 8$		
$\mathrm{Re}H^0$	$\longrightarrow$	H

Table G.2: The bosonic particle content of the Standard Model.

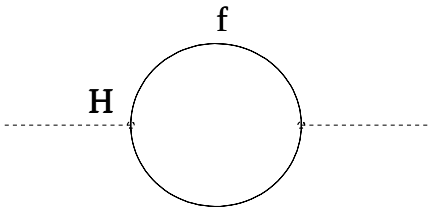

Figure G.1: Quantum corrections to the m^2_{Higgs}.

that new physics will appear at shorter distances.

Applying the Standard Model to a distance scale shorter than d a serious theoretical problem arises which is outlined below. In the Standard Model, the Higgs potential given by expression G.2. Because perturbative unitarity requires that $\lambda < 1$, $-\mu^2$ is of the order of $(100\ \mathrm{GeV})^2$ [120]. However, the mass squared parameter μ^2 of the Higgs doublet receives enormous quantum corrections from the virtual effects [121] of every particle which couples directly or indirectly to the Higgs field. In Figure G.1 a correction to m_H^2 from a loop containing a Dirac fermion f with mass m_f is shown. If the Higgs field couples to f with a term in the Lagrangian $-\lambda_f H \overline{f} f$, then the Feynman diagram in Figure G.1 yields a correction

$$\Delta m_H^2 = \frac{|\lambda_f|^2}{16\pi^2}\left[-2\Lambda_{\mathrm{UV}}^2 + 6m_f^2 \ln(\Lambda_{\mathrm{UV}}/m_f) + \ldots\right]. \tag{G.3}$$

Λ_{UV} is an ultraviolet momentum cutoff used to regulate the loop integral and is

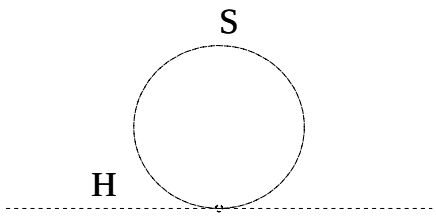

Figure G.2: Quantum corrections to the m^2_{Higgs}.

interpreted as the energy scale at which new physics enters to alter the high-energy behavior of the theory. Each of the leptons and quarks of the Standard Model play the role of f; for quarks, (G.3) is be multiplied by 3 to account for color. The largest correction comes when f is the top quark with $\lambda_f \approx 1$. If $\Lambda_{\rm UV}$ is of order M_{Planck}, the correction to m^2_H is 30 orders of magnitude larger than its expected physical mass. The problem can be alternately phrased as a problem of the experimental prediction of a small m^2_H : the theoretically natural m^2_H including the virtual corrections is closer to M^2_{Planck} than the experimentally favored value[1]. There is a contribution similar to the one in expression (G.3) from the virtual effects of any arbitrarily heavy particles which might exist. For a heavy complex scalar particle S with mass m_S which couples to the Higgs with a Lagrangian term $-\lambda_S|H|^2|S|^2$ the Feynman diagram in Figure

[1]Combining all the precision electroweak data the Higgs is expected to have mass $m_H = 76^{+79}_{-67}$GeV which corresponds to $m_H < 235$ GeV at the 95% confidence level (a conservative error ± 0.0009 in $\alpha_{em}(m_Z)$ is used and the analysis allows for unknown higher-loop uncertainties [122].)

G.2 gives a correction

$$\Delta m_H^2 = \frac{\lambda_S}{16\pi^2}\left[\Lambda_{\rm UV}^2 - 2m_S^2\ln(\Lambda_{\rm UV}/m_S) + \ldots\right]. \tag{G.4}$$

If a physical interpretation of $\Lambda_{\rm UV}$ is rejected and the loop integral is dimensionally regularlized (instead of using a momentum cut off) there will be no $\Lambda_{\rm UV}^2$ piece. Still the term proportional to m_S^2 is not be eliminated without the physically unjustifiable tuning of a counter-term specifically for that purpose. So m_H^2 is sensitive to the masses of the *heaviest* particles that H couples to; if m_S is very large, its effects on the Standard Model do not decouple, but instead make it very difficult to understand why m_H^2 is so small. If the Higgs boson is a fundamental particle either no heavy particles exist which couple (even indirectly or weakly) to the Higgs scalar field or some striking cancellation occurs between the contributions to Δm_H^2.

The systematic cancellation of contributions to Δm_H^2 is realized by introducing a supersymmetry that relates the fermions with the bosons. The relative minus sign between the fermion loop and boson loop contributions to Δm_H^2 in expressions (G.3), (G.4) shows that with such a symmetry that relates fermions with bosons, the cancellations are unavoidable.

The amelioration of the quadratic divergences is allowing the extrapolation from the Electroweak to the Planck scale and provides a motivation for supersymmetry as well as a motivation for supersymmetry breaking at the $\sim$ TeV energy scale. The "hierarchy" of these distant energy scales is understood and the masses of the sparticless are naturally constrained at the electroweak scale making the framework directly testable at the present and near future collider energies.

A supersymmetry transformation turns a bosonic state into a fermionic state, and

vice versa. The operator Q which generates such transformations is an anticommuting spinor, with

$$Q|\text{Boson}\rangle = |\text{Fermion}\rangle; \qquad Q|\text{Fermion}\rangle = |\text{Boson}\rangle. \tag{G.5}$$

Spinors are intrinsically complex objects, so $Q^\dagger$ (the hermitian conjugate of Q) is also a symmetry generator. Because Q and $Q^\dagger$ are fermionic operators, they carry spin angular momentum 1/2, *i.e.* supersymmetry must be a space-time symmetry. The possible forms for such symmetries in an interacting quantum field theory are restricted by the Haag-Lopuszanski-Sohnius extension of the Coleman-Mandula theorem [2]. For realistic theories which, like the Standard Model, have chiral fermions (*i.e.*, fermions whose left- and right-handed pieces transform differently under the gauge group) and the possibility of parity-violating interactions, this theorem implies that the generators Q and $Q^\dagger$ must satisfy an algebra of anticommutation and commutation relations with the schematic form

$$\{Q, Q^\dagger\} = P^\mu \ (a) \qquad \{Q, Q\} = \{Q^\dagger, Q^\dagger\} = 0 \ (b) \qquad [P^\mu, Q] = [P^\mu, Q^\dagger] = 0 \ (c) \tag{G.6}$$

where P^μ is the momentum generator of space-time translations. The of P^μ on the right-hand side expression G.6(a) transforms as a spin-1 object under Lorentz boosts and rotations, while Q and $Q^\dagger$ on the left-hand side each transform as spin-1/2 objects.

The single-particle states of a supersymmetric theory fall naturally into irreducible representations of the supersymmetry algebra which are called *supermultiplets*. Each supermultiplet contains both fermion and boson states, which are commonly known as *superpartners* of each other. By definition, if $|\Omega\rangle$ and $|\Omega'\rangle$ are members of the same

supermultiplet, then $|\Omega'\rangle$ is proportional to some combination of Q and $Q^\dagger$ operators acting on $|\Omega\rangle$, up to a space-time translation or rotation. The (mass)^2 operator $-P^2$ commutes with the operators Q, $Q^\dagger$, and with all space-time rotation and translation operators, so it follows that particles which inhabit the same irreducible supermultiplet must have equal eigenvalues of $-P^2$ and therefore equal masses.

The supersymmetry generators $Q, Q^\dagger$ also commute with the generators of gauge transformations, *i.e.* particles in the same supermultiplet must also be in the same representation of the gauge group and have the same electric charges, weak isospin, and color degrees of freedom.

Each supermultiplet contains an equal number of fermion and boson degrees of freedom. In a supersymmetric extension of the Standard Model, each of the known fundamental particles must therefore be in either a chiral or gauge supermultiplet and have a superpartner with spin differing by 1/2 unit. Only chiral supermultiplets can contain fermions whose left-handed parts transform differently under the gauge group than their right-handed parts. All of the Standard Model fermions (the known quarks and leptons) have this property, so they are members of chiral supermultiplets. The names for the spin-0 partners of the quarks and leptons are constructed by adding an "s", which is short for scalar. Thus generically they are called *squarks* and *sleptons*. The left-handed and right-handed pieces of the quarks and leptons are separate two-component Weyl fermions with different gauge transformation properties in the Standard Model, so each must have its own complex scalar partner. The symbols for the squarks and sleptons are the same as for the corresponding fermion, but with a tilde used to denote the superpartner of a Standard Model particle. For example, the superpartners of the left-handed and right-handed parts of the electron Dirac field are called left- and right-handed selectrons, and are denoted $\widetilde{e}_L$ and $\widetilde{e}_R$.

Names		spin 0	spin 1/2	$SU(3)_C,\ \ SU(2)_L, (1)_Y$
squarks, quarks	Q	$(\widetilde{u}_L\ \ \widetilde{d}_L)$	$(u_L\ \ d_L)$	$(\ \mathbf{3},\ \mathbf{2}\ ,\ \frac{1}{6})$
($\times$3 families)	$\overline{u}$	$\widetilde{u}^*_R$	$u^\dagger_R$	$(\ \overline{\mathbf{3}},\ \mathbf{1},\ -\frac{2}{3})$
	$\overline{d}$	$\widetilde{d}^*_R$	$d^\dagger_R$	$(\ \overline{\mathbf{3}},\ \mathbf{1},\ \frac{1}{3})$
sleptons, leptons	L	$(\widetilde{\nu}\ \ \widetilde{e}_L)$	$(\nu\ \ e_L)$	$(\ \mathbf{1},\ \mathbf{2}\ ,\ -\frac{1}{2})$
($\times$3 families)	$\overline{e}$	$\widetilde{e}^*_R$	$e^\dagger_R$	$(\ \mathbf{1},\ \mathbf{1},\ 1)$
Higgs, higgsinos	H_u	$(H^+_u\ \ H^0_u)$	$(\widetilde{H}^+_u\ \ \widetilde{H}^0_u)$	$(\ \mathbf{1},\ \mathbf{2}\ ,\ +\frac{1}{2})$
	H_d	$(H^0_d\ \ H^-_d)$	$(\widetilde{H}^0_d\ \ \widetilde{H}^-_d)$	$(\ \mathbf{1},\ \mathbf{2}\ ,\ -\frac{1}{2})$

Table G.3: Chiral supermultiplets in the Minimal Supersymmetric Standard Model.

The "handedness" does not refer to the helicity of the selectrons (they are spin-0 particles) but to that of their superpartners. In the Standard Model the neutrinos are always left-handed, so the sneutrinos are denoted generically by $\widetilde{\nu}$, with a possible subscript indicating which lepton flavor they carry: $\widetilde{\nu}_e$, $\widetilde{\nu}_\mu$, $\widetilde{\nu}_\tau$. The complete list of the squarks is $\widetilde{q}_L$, $\widetilde{q}_R$ with $q = u, d, s, c, b, t$. The gauge interactions of each of these squark and slepton field are the same as for the corresponding Standard Model fermion; for instance, a left-handed squark like $\widetilde{u}_L$ will couple to the W boson while $\widetilde{u}_R$ will not. There are two Higgs supermultiplets, with $Y = \pm 1/2$. Because of the structure of supersymmetric theories, only a $Y = +1/2$ Higgs chiral supermultiplet can have the Yukawa couplings necessary to give masses to charge $+2/3$ up-type quarks (up, charm, top), and only a $Y = -1/2$ Higgs can have the Yukawa couplings necessary to give masses to charge $-1/3$ down-type quarks (down, strange, bottom) and to the charged leptons. The corresponding $SU(2)_L$-doublet complex scalar fields are H_u and H_d respectively. The weak isospin components of H_u with $T_3 = (+1/2,\ -1/2)$ have electric charges 1, 0 respectively, and are denoted $(H^+_u,\ H^0_u)$. Similarly, the $SU(2)_L$-doublet complex scalar H_d has $T_3 = (+1/2,\ -1/2)$ components $(H^0_d,\ H^-_d)$.

Names	spin 1/2	spin 1	$SU(3)_C$, $SU(2)_L$, $U(1)_Y$
gluino, gluon	$\widetilde{g}$	g	(**8**, **1** , 0)
winos, W bosons	$\widetilde{W}^{\pm}$ $\widetilde{W}^0$	$W^{\pm}$ W^0	(**1**, **3** , 0)
bino, B boson	$\widetilde{B}^0$	B^0	(**1**, **1** , 0)

Table G.4: Gauge supermultiplets in the Minimal Supersymmetric Standard Model.

The neutral scalar that corresponds to the physical Standard Model Higgs boson is in a linear combination of H_u^0 and H_d^0;

The vector bosons of the Standard Model belong in gauge supermultiplets. Their fermionic superpartners are generically referred to as *gauginos*. The $SU(3)_C$ color gauge interactions of QCD are mediated by the gluon, whose spin-1/2 color-octet supersymmetric partner is the gluino. The electroweak gauge symmetry $SU(2)_L \times U(1)_Y$ is associated to the spin-1 gauge bosons W^+, W^0, W^- and B^0 and to the spin-1/2 superpartners $\widetilde{W}^+, \widetilde{W}^0, \widetilde{W}^-$ and $\widetilde{B}^0$, called *winos* and *bino*. After electroweak symmetry breaking, the W^0, B^0 gauge eigenstates mix to give mass eigenstates Z^0 and γ. The corresponding gaugino mixtures of $\widetilde{W}^0$ and $\widetilde{B}^0$ are called zino ($\widetilde{Z}^0$) and photino ($\widetilde{\gamma}$); if supersymmetry were unbroken, they would be mass eigenstates with masses m_Z and 0. Table G.4 summarizes the gauge supermultiplets of a minimal supersymmetric extension of the Standard Model. The chiral and gauge supermultiplets in Tables G.4 & G.3 make up the particle content of the Minimal Supersymmetric Standard Model (MSSM). The most obvious and interesting feature of this theory is that none of the superpartners of the Standard Model particles has been discovered. If supersymmetry were unbroken, then there would have to be selectrons $\widetilde{e}_L$ and $\widetilde{e}_R$ with masses exactly equal to $m_e = 0.511$ MeV/c^2. A similar statement applies to each of the other sleptons and squarks, and there would also have to be a massless gluino and photino.

These particles would have been extraordinarily easy to detect long ago. Clearly, *supersymmetry is a broken symmetry* in the vacuum state chosen by nature.

A very important clue as to the nature of supersymmetry breaking can be obtained by returning to the motivation provided by the hierarchy problem. Supersymmetry introduced two complex scalar fields for each Standard Model Dirac fermion, which is just what is needed to enable a cancellation of the quadratically divergent ($\Lambda_{\rm UV}^2$) pieces of expressions (G.3) and (G.4). This sort of cancellation requires that the associated dimensionless couplings should be related (e.g. $\lambda_S = |\lambda_f|^2$). The necessary relationships between couplings occur in unbroken supersymmetry. Unbroken supersymmetry guarantees that the quadratic divergences in scalar squared masses vanish to all orders in perturbation theory.[2] If broken supersymmetry is still to provide a solution to the hierarchy problem, then the relationships between dimensionless couplings which hold in an unbroken supersymmetric theory must be maintained. Otherwise, there would be quadratically divergent radiative corrections to the Higgs scalar masses of the form

$$\Delta m_H^2 = \frac{1}{8\pi^2}(\lambda_S - |\lambda_f|^2)\Lambda_{\rm UV}^2 + \ldots . \tag{G.7}$$

This led to the consideration of "soft" supersymmetry breaking. The effective Lagrangian of the MSSM can be written in the form

$$\mathcal{L} = \mathcal{L}_{\rm SUSY} + \mathcal{L}_{\rm soft}, \tag{G.8}$$

where $\mathcal{L}_{\rm SUSY}$ preserves supersymmetry invariance, and $\mathcal{L}_{\rm soft}$ violates supersymme-

[2] A simple way to state this, is to note that unbroken supersymmetry requires the degeneracy of scalar and fermion masses. Radiative corrections to fermion masses are known to diverge at most logarithmically, so the same must be true for scalar masses in unbroken supersymmetry.

try but contains only mass terms and couplings with *positive* mass dimension. Soft supersymmetry breaking might seem like a rather arbitrary requirement. If the large mass scale associated with the soft terms is denoted $m_{\rm soft}$, the additional non-supersymmetric corrections to the Higgs scalar (mass)^2 must vanish in the $m_{\rm soft} \to 0$ limit, so by dimensional analysis they cannot be proportional to $\Lambda_{\rm UV}^2$. More generally, minimal supersymmetric models maintain the cancellation of quadratically divergent terms in the radiative corrections of all scalar masses, to all orders in perturbation theory. The corrections also cannot go like $\Delta m_H^2 \sim m_{\rm soft} \Lambda_{\rm UV}$, because in general the loop momentum integrals always diverge either quadratically or logarithmically, not linearly, as $\Lambda_{\rm UV} \to \infty$. So they must be of the form

$$\Delta m_H^2 = m_{\rm soft}^2 \left[\frac{\lambda}{16\pi^2} \ln(\Lambda_{\rm UV}/m_{\rm soft}) + \ldots \right]. \tag{G.9}$$

Here λ is representative of dimensionless couplings, and the ellipses stand both for terms which are independent of $\Lambda_{\rm UV}$ and for higher loop corrections (which depend on $\Lambda_{\rm UV}$ through powers of logarithms).

Since the mass splittings between the known Standard Model particles and their superpartners are just determined by the parameters $m_{\rm soft}$ appearing in $\mathcal{L}_{\rm soft}$, expression (G.9) indicates that the superpartner masses cannot be too huge. Otherwise the successful cure for the hierarchy problem is lost since the $m_{\rm soft}^2$ corrections to the Higgs scalar (mass)^2 would be unnaturally large compared to the electroweak breaking scale of 175 GeV. The top and bottom squarks and the winos and bino give especially large contributions to $\Delta m_{H_u}^2$ and $\Delta m_{H_d}^2$, but the gluino mass and all the other squark and slepton masses also feed in indirectly, through radiative corrections to the top and bottom squark masses. Furthermore, in most viable models of super-

symmetry breaking the superpartner masses do not differ from each other by more than about an order of magnitude. Using $\Lambda_{\rm UV} \sim M_{Planck}$ and $\lambda \sim 1$ in equation (G.9), it is found that $m_{\rm soft}$, and therefore the masses of at least the lightest few superpartners, should be at the most about 1 TeV or so, in order for the MSSM scalar potential to provide a Higgs vacuum expectation value (VEV) resulting in m_W, m_Z = 80.4, 91.2 GeV/c^2 without miraculous cancellations. Many studies have been done on this "naturalness" [49, 50, 52, 53] issue of the sparticle masses. Experimentally, most of the superpartners of the Standard Model particles are too heavy to have been discovery so far. All of the particles in the MSSM which have already been discovered have something in common; they would necessarily be massless in the absence of electroweak symmetry breaking. In particular, the masses of the $W^{\pm}, Z^0$ bosons and all quarks and leptons are equal to dimensionless coupling constants times the Higgs VEV $\sim$ 175 GeV, while the photon and gluon are required to be massless by electromagnetic and QCD gauge invariance. All of the undiscovered particles in the MSSM have exactly the opposite property, since each of them can have a Lagrangian mass term in the absence of electroweak symmetry breaking. For the squarks, sleptons, and Higgs scalars this follows from a general property of complex scalar fields that a mass term $m^2|\phi|^2$ is always allowed by all gauge symmetries. For the higgsinos and gauginos, it follows from the fact that they are fermions in a real representation of the gauge group. If supersymmetry is correct, one neutral Higgs scalar boson should be lighter than about 150 GeV/c^2 [61] and should be discovered soon.

The superpartners listed in Tables G.3 & G.4 are not necessarily the mass eigenstates of the theory. This is because after electroweak symmetry breaking and supersymmetry breaking effects are included, there can be mixing between the electroweak gauginos and the higgsinos, and within the various sets of squarks and sleptons and

Higgs scalars which have the same electric charge. The one exception is the gluino, which is a color octet fermion and therefore does not have the appropriate quantum numbers to mix with any other particle. Most of what is unknown about the MSSM is absorbed in $\mathcal{L}_{\text{soft}}$. The structure of supersymmetric Lagrangians allows very little arbitrariness: all of the dimensionless couplings and all but one mass term in the supersymmetric part of the MSSM Lagrangian correspond directly to some parameter in the ordinary Standard Model which has already been measured by experiment. For example, the supersymmetric coupling of a gluino to a squark and a quark is determined by the QCD coupling constant α_S.

In contrast, the supersymmetry-breaking part of the Lagrangian contains many unknown parameters and a considerable amount of arbitrariness. Each of the mass splittings between Standard Model particles and their superpartners corresponds to terms in the MSSM Lagrangian which are purely supersymmetry-breaking in their origin and effect. These soft supersymmetry-breaking terms can also introduce a large number of mixing angles and CP-violating phases not found in the Standard Model. In the context of a general renormalizable theory, possible soft supersymmetry-breaking terms in the Lagrangian are

$$\begin{aligned}\mathcal{L}_{\text{soft}} = &-\frac{1}{2}\left(M_\lambda\ \lambda^a\lambda^a + \text{c.c.}\right) - (m^2)^i_j \phi^{j*}\phi_i \\ &- \left(\frac{1}{2}b^{ij}\phi_i\phi_j + \frac{1}{6}a^{ijk}\phi_i\phi_j\phi_k + \text{c.c.}\right),\end{aligned} \tag{G.10}$$

and

$$\mathcal{L}_{\text{soft}} = -\frac{1}{2}c_i^{jk}\phi^{*i}\phi_j\phi_k + \text{c.c.} \tag{G.11}$$

They consist of gaugino masses M_λ for each gauge group, scalar (mass)^2 terms $(m^2)^j_i$

and b^{ij}, and (scalar)^3 couplings a^{ijk} and c_i^{jk}. Soft mass terms for the chiral supermultiplet fermions are redundant because they can always be absorbed into a redefinition of the superpotential and the terms $(m^2)_i^j$ and c_i^{jk}. It has been shown rigorously that a softly-broken supersymmetric theory with $\mathcal{L}_{\rm soft}$ as given by expression (G.10) is indeed free of quadratic divergences in quantum corrections to scalar masses, to all orders in perturbation theory [123].

The superpotential for the MSSM is given by

$$W_{\rm MSSM} = \overline{u}\mathbf{y_u}QH_u - \overline{d}\mathbf{y_d}QH_d - \overline{e}\mathbf{y_e}LH_d + \mu H_u H_d \,. \qquad \text{(G.12)}$$

The objects H_u, H_d, Q, L, $\overline{u}$, $\overline{d}$, $\overline{e}$ appearing in expression (G.12) are chiral superfields corresponding to the chiral supermultiplets in Table **??**, The dimensionless Yukawa coupling parameters $\mathbf{y_u}, \mathbf{y_d}, \mathbf{y_e}$ are 3×3 matrices in family space. The gauge [$SU(3)_C$ color and $SU(2)_L$ weak isospin] and family indices are suppressed.

The μ term in equation (G.12) is the supersymmetric version of the Higgs boson mass in the Standard Model. It is also seen in expression (G.12) why both H_u and H_d are needed in order to give Yukawa couplings, and masses, to all of the quarks and leptons. The Yukawa matrices determine the masses and CKM mixing angles of the ordinary quarks and leptons, after the neutral scalar components of H_u and H_d get VEVs. Since the top quark, bottom quark and tau lepton are the heaviest fermions in the Standard Model, it is often useful to make an approximation that only the $(3,3)$ family components of each of $\mathbf{y_u}$, $\mathbf{y_d}$ and $\mathbf{y_e}$ are important:

$$\mathbf{y_u} \approx \begin{pmatrix} 0 & 0 & 0 \\ 0 & 0 & 0 \\ 0 & 0 & y_t \end{pmatrix}; \qquad \mathbf{y_d} \approx \begin{pmatrix} 0 & 0 & 0 \\ 0 & 0 & 0 \\ 0 & 0 & y_b \end{pmatrix}; \qquad \mathbf{y_e} \approx \begin{pmatrix} 0 & 0 & 0 \\ 0 & 0 & 0 \\ 0 & 0 & y_\tau \end{pmatrix}. \qquad \text{(G.13)}$$

In this limit, only the third family and Higgs fields contribute to the MSSM superpotential. It is instructive to write the superpotential in terms of the separate $SU(2)_L$ weak isospin components [$Q_3 = (t\, b)$; $L_3 = (\nu_\tau\, \tau)$; $H_u = (H_u^+\, H_u^0)$; $H_d = (H_d^0\, H_d^-)$; $\overline{u}_3 = \overline{t}$; $\overline{d}_3 = \overline{b}$; $\overline{e}_3 = \overline{\tau}$], so:

$$W_{\rm MSSM} \approx y_t(\overline{t}tH_u^0 - \overline{t}bH_u^+) - y_b(\overline{b}tH_d^- - \overline{b}bH_d^0) - y_\tau(\overline{\tau}\nu_\tau H_d^- - \overline{\tau}\tau H_d^0) + \mu(H_u^+ H_d^- - H_u^0 H_d^0). \qquad \text{(G.14)}$$

Since the Yukawa interactions y^{ijk} in a general supersymmetric theory must be completely symmetric under interchange of i, j, k, the $\mathbf{y_u}$, $\mathbf{y_d}$ and $\mathbf{y_e}$ imply not only Higgs-quark-quark and Higgs-lepton-lepton couplings as in the Standard Model, but also squark-Higgsino-quark and slepton-Higgsino-lepton interactions. In a similar way, the existence of all the other quark and lepton Yukawa couplings in the superpotential (G.12) leads not only to Higgs-quark-quark and Higgs-lepton-lepton Lagrangian terms as in the ordinary Standard Model, but also to squark-higgsino-quark and slepton-higgsino-lepton terms, and scalar quartic couplings [(squark)^4, (slepton)^4, (squark)^2(slepton)^2, (squark)^2(Higgs)^2, and (slepton)^2(Higgs)^2]. The decay and especially production processes for superpartners in the MSSM are typically dominated by the supersymmetric interactions of gauge-coupling strength The couplings of the Standard Model gauge bosons (photon, $W^\pm$, Z^0 and gluons) to the MSSM particles are determined completely by the gauge invariance of the kinetic terms in the Lagrangian. The gauginos also couple to (squark, quark) and (slepton, lepton) and (Higgs, higgsino) pairs with strengths proportional to the QCD and the electroweak gauge couplings. The winos only couple to the left-handed squarks and sleptons, and the (lepton, slepton) and (Higgs, higgsino) pairs do not couple to the gluino.

The bino couplings for each (scalar, fermion) pair are also proportional to the weak hypercharges Y.

G.2.1 R-parity

The superpotential (G.12) is minimal in the sense that it is sufficient to produce a phenomenologically viable model. There are other terms that could be written down which are gauge-invariant and analytic in the chiral superfields, but are not included in the MSSM because they violate either baryon number (B) or total lepton number (L). The possible existence of such terms might seem disturbing, since B- and L-violating processes have not yet been observed experimentally. The most obvious experimental constraint comes from the non-observation of proton decay, which would violate both B and L by 1 unit. B and L conservation can be postulated in the MSSM by adding a new symmetry which has the effect of eliminating the possibility of B and L violating terms in the renormalizable superpotential. This new symmetry is called "R-parity" [48].

$$R = (-1)^{3(\mathrm{B}-\mathrm{L})+2s} \tag{G.15}$$

Particles within the same supermultiplet do not have the same R-parity. The R-parity assignment is phenomenologically useful because all of the Standard Model particles and the Higgs bosons have even R-parity ($R = +1$), while all of the squarks, sleptons, gauginos, and higgsinos have odd R-parity ($R = -1$). The R-parity odd particles are known as "supersymmetric particles" or "sparticles". If R-parity is exactly conserved, then there can be no mixing between the sparticles and the $R = +1$ particles. Furthermore, every interaction vertex in the theory contains an even number of $R = -1$ sparticles. This has three important consequences:

- The lightest sparticle with $R = -1$, called the "lightest supersymmetric particle" or LSP, must be absolutely stable. If the LSP is electrically neutral, it interacts only weakly with ordinary matter, and it makes an attractive candidate [47] for the non-baryonic dark matter which seems to be required by cosmology.

- Each sparticle other than the LSP must eventually decay into a state which contains an odd number of LSPs (usually just one).

- In collider experiments, sparticles can only be produced in even numbers (usually two-at-a-time).

In this analysis the MSSM is considered to conserve R-parity.

G.2.2 Soft supersymmetry breaking in the MSSM

To complete the description of the MSSM, the specification of the soft supersymmetry breaking terms is necessary

$$\begin{aligned}
\mathcal{L}_{\rm soft}^{\rm MSSM} = & -\frac{1}{2}\left(M_3 \widetilde{g}\widetilde{g} + M_2 \widetilde{W}\widetilde{W} + M_1 \widetilde{B}\widetilde{B}\right) + \text{c.c.} \\
& -\left(\widetilde{\overline{u}}\,\mathbf{a_u}\,\widetilde{Q} H_u - \widetilde{\overline{d}}\,\mathbf{a_d}\,\widetilde{Q} H_d - \widetilde{\overline{e}}\,\mathbf{a_e}\,\widetilde{L} H_d\right) + \text{c.c.} \\
& -\widetilde{Q}^\dagger\,\mathbf{m_Q^2}\,\widetilde{Q} - \widetilde{L}^\dagger\,\mathbf{m_L^2}\,\widetilde{L} - \widetilde{\overline{u}}\,\mathbf{m_{\overline{u}}^2}\,\widetilde{\overline{u}}^\dagger - \widetilde{\overline{d}}\,\mathbf{m_{\overline{d}}^2}\,\widetilde{\overline{d}}^\dagger - \widetilde{\overline{e}}\,\mathbf{m_{\overline{e}}^2}\,\widetilde{\overline{e}}^\dagger \\
& - m_{H_u}^2 H_u^* H_u - m_{H_d}^2 H_d^* H_d - (b H_u H_d + \text{c.c.})\,. \qquad \text{(G.16)}
\end{aligned}$$

In equation (G.16), M_3, M_2, and M_1 are the gluino, wino, and bino mass terms. The second line in (G.16) contains the (scalar)^3 couplings [of the type a^{ijk} in (G.10)]. Each of $\mathbf{a_u}$, $\mathbf{a_d}$, $\mathbf{a_e}$ is a complex 3×3 matrix in family space, with dimensions of (mass).

They are in one-to-one correspondence with the Yukawa coupling matrices in the superpotential. The third line of equation (G.16) consists of squark and slepton mass terms of the $(m^2)^j_i$ type in equation (G.10). Each of $\mathbf{m^2_Q}$, $\mathbf{m^2_{\overline{u}}}$, $\mathbf{m^2_{\overline{d}}}$, $\mathbf{m^2_L}$, $\mathbf{m^2_{\overline{e}}}$ is a 3×3 hermitian matrix in family space. The last line of (G.16) includes the supersymmetry-breaking contributions to the Higgs potential; $m^2_{H_u}$ and $m^2_{H_d}$ are (mass)^2 terms of the $(m^2)^j_i$ type, while b is the only (mass)^2 term of the type b^{ij} in equation (G.10) which can occur in the MSSM. Schematically,

$$M_1,\ M_2,\ M_3,\ \mathbf{a_u},\ \mathbf{a_d},\ \mathbf{a_e} \ \sim\ m_{\rm soft}; \tag{G.17}$$

$$\mathbf{m^2_Q},\ \mathbf{m^2_L},\ \mathbf{m^2_{\overline{u}}},\ \mathbf{m^2_{\overline{d}}},\ \mathbf{m^2_{\overline{e}}},\ m^2_{H_u},\ m^2_{H_d},\ b\ \sim\ m^2_{\rm soft} \tag{G.18}$$

with a characteristic mass scale $m_{\rm soft}$ which should not be much larger than 10^3 GeV. The expression (G.16) is the most general soft supersymmetry-breaking Lagrangian of the form (G.10) which is compatible with gauge invariance and R-parity conservation.

Unlike the supersymmetry-preserving part of the Lagrangian, $\mathcal{L}^{\rm MSSM}_{\rm soft}$ introduces many new parameters which were not present in the ordinary Standard Model. A count [56] reveals that there are 105 masses, phases and mixing angles in the MSSM Lagrangian which cannot be rotated away by redefining the phases and flavor basis for the quark and lepton supermultiplets, and which have no counterpart in the ordinary Standard Model. Supersymmetry *breaking* appears to introduce a tremendous arbitrariness in the Lagrangian. If the squark and slepton (mass)^2 matrices are each proportional to the 3×3 identity matrix in family space (or equivalently stated, are *flavor blind*):

$$\mathbf{m^2_Q} = m^2_Q\mathbf{1};\quad \mathbf{m^2_{\overline{u}}} = m^2_{\overline{u}}\mathbf{1};\quad \mathbf{m^2_{\overline{d}}} = m^2_{\overline{d}}\mathbf{1};\quad \mathbf{m^2_L} = m^2_L\mathbf{1};\quad \mathbf{m^2_{\overline{e}}} = m^2_{\overline{e}}\mathbf{1}. \tag{G.19}$$

then all squark and slepton mixing angles are rendered trivial, because squarks and sleptons with the same electroweak quantum numbers will be degenerate in mass and can be rotated into each other. Supersymmetric contributions to Flavor Changing Neutral Currents processes in such an idealized limit are very small, modulo the mixing due to $\mathbf{a_u}$, $\mathbf{a_d}$, $\mathbf{a_e}$. Adding the assumption that the (scalar)^3 couplings are each proportional to the corresponding Yukawa coupling matrix

$$\mathbf{a_u} = A_{u0}\,\mathbf{y_u}; \qquad \mathbf{a_d} = A_{d0}\,\mathbf{y_d}; \qquad \mathbf{a_e} = A_{e0}\,\mathbf{y_e}. \tag{G.20}$$

ensures that only the squarks and sleptons of the third family can have large (scalar)^3 couplings. Large CP-violating effects are avoided with the assumption that the soft parameters do not introduce new complex phases. Then the only CP-violating phase in the theory is the CKM phase found in the ordinary Yukawa couplings. These conditions make up a weak version of what is often called the assumption of *soft-breaking universality*.

The soft-breaking universality relations (or stronger versions of them) are presumed to be the result of some specific model for the origin of supersymmetry breaking, even though there is considerable diversity as to what the specific model should actually be. They are indicative of an underlying simplicity or symmetry of the Lagrangian at some very high energy scale Q_0, which is the "input scale". If this Lagrangian is used to compute masses and cross-sections and decay rates for experiments at ordinary energies near the electroweak scale, the results involve large logarithms of order $\ln(Q_0/m_Z)$ coming from loop diagrams.

Large logarithms are resummed using renormalization group (RG) equations, by treating the couplings and masses appearing in the Lagrangian as "running" parame-

ters. The soft-breaking universality conditions are interpreted as boundary conditions on the running soft parameters at the RG scale Q_0 which is very much higher than direct experimental probes. The soft parameters, the superpotential parameters, and the gauge couplings are RG-evolved down to the electroweak scale

At the electroweak scale, expressions (G.19) and (**??**) do no longer hold. However, RG corrections due to gauge interactions respect (G.19) and (**??**), while RG corrections due to Yukawa interactions are quite small except for couplings involving the top squarks and possibly the bottom squarks and tau sleptons. In particular, the (scalar)^3 couplings should be quite negligible for the squarks and sleptons of the first two families. Furthermore, RG evolution does not introduce new CP-violating phases.

One hint that such a program can succeed is the apparent unification of gauge couplings in the MSSM [124]. The 1-loop RG equations for the Standard Model gauge couplings g_1, g_2, g_3 are given by

$$\frac{d}{dt}g_a = \frac{1}{16\pi^2}b_a g_a^3 \qquad \Rightarrow \qquad \frac{d}{dt}\alpha_a^{-1} = -\frac{b_a}{2\pi} \qquad (a = 1, 2, 3) \tag{G.21}$$

where $t = \ln(Q/Q_0)$ with Q the RG scale. In the Standard Model, $b_a^{\rm SM} = (41/10, -19/6, -7)$, while in the MSSM one finds instead $b_a^{\rm MSSM} = (33/5, 1, -3)$. The latter set of coefficients are larger because of the virtual effects of the extra MSSM particles in loops. In terms of the conventional electroweak gauge couplings g and g' with $e = g\sin\theta_W = g'\cos\theta_W$, then $g_2 = g$ and $g_1 = \sqrt{5/3}g'$. The quantities $\alpha_a = g_a^2/4\pi$ have the property that their reciprocals run linearly with RG scale at one-loop order. In Figure G.3 the RG evolution of the α_a^{-1} is compared between the Standard Model (dashed lines) and the MSSM (solid lines). Unlike the Standard Model, the MSSM

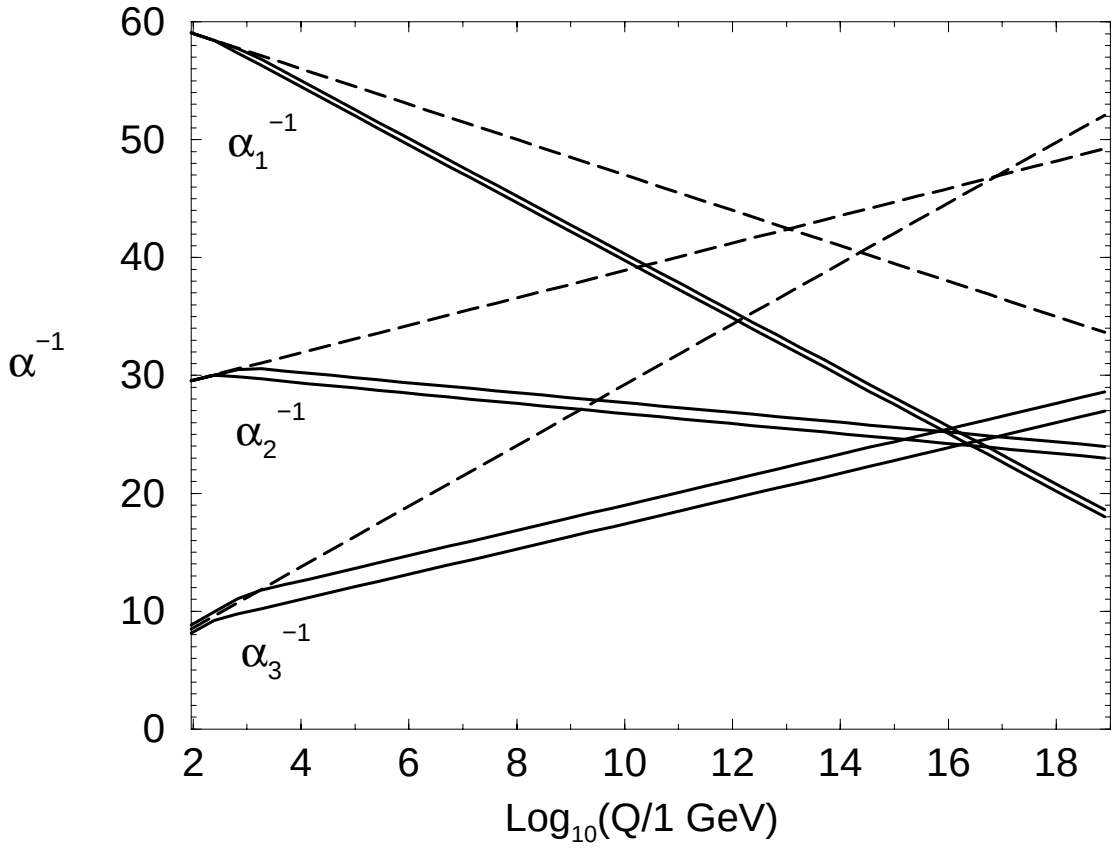

Figure G.3: RG evolution of the inverse gauge couplings $\alpha_a^{-1}(Q)$ in the Standard Model (dashed lines) and the MSSM (solid lines). In the MSSM case, $\alpha_3(m_Z)$ is varied between 0.113 and 0.123, and the sparticle mass thresholds between 250 GeV and 1 TeV. Two-loop effects are included [2].

includes just the right particle content to ensure that the gauge couplings can unify, at a scale $M_{GUT} \sim 2 \times 10^{16}$ GeV. While the apparent unification of gauge couplings at M_U could be just an accident, it may also be a strong hint in favor of a grand unified theory (GUT) or superstring models, which predict gauge coupling unification below M_{Planck}.

The one-loop RG equations for the three gaugino mass parameters in the MSSM are determined by the same quantities $b_a^{\rm MSSM}$ which appear in the gauge coupling RG expressions. (G.21):

$$\frac{d}{dt} M_a = \frac{1}{8\pi^2} b_a g_a^2 M_a \qquad (b_a = 33/5, 1, -3) \tag{G.22}$$

for $a = 1, 2, 3$. The three ratios M_a/g_a^2 are each constant (RG-scale independent) up to small two-loop corrections. In minimal supergravity models:

$$M_a(Q) = \frac{g_a^2(Q)}{g_a^2(Q_0)} m_{1/2} \qquad (a = 1, 2, 3) \tag{G.23}$$

at any RG scale $Q < Q_0$, where Q_0 is the input scale which is presumably nearly equal to M_{Planck}. Since the gauge couplings are observed to unify at $M_{GUT} \sim 0.01 M_{Planck}$, it is expected that $g_1^2(Q_0) \approx g_2^2(Q_0) \approx g_3^2(Q_0)$ and

$$\frac{M_1}{g_1^2} \approx \frac{M_2}{g_2^2} \approx \frac{M_3}{g_3^2} \tag{G.24}$$

at any RG scale, up to small two-loop effects and possibly larger threshold effects near M_{GUT} and M_{Planck}. The common value in equation (G.24) is also equal to $M_{1/2}/g_{GUT}^2$ in minimal supergravity models, where g_{GUT} is the unified gauge coupling at the input scale and $M_{1/2}$ is the common gaugino mass.

G.3 The relative yields of $\tilde{q}\overline{\tilde{q}}$, $\tilde{q}\tilde{q}$, $\tilde{g}\tilde{g}$ and $\tilde{q}\tilde{g}$ final states for the points generated in this analysis.

The pie plots for the relative yields for all the points used in the analysis are given in the graphs following. "Msq" is the squark mass and "Mglss" is the gluino mass. The first set of graphs correspond to the MSSM signal points in regions C and D and the second to the mSUGRA signal points in regions A and B.

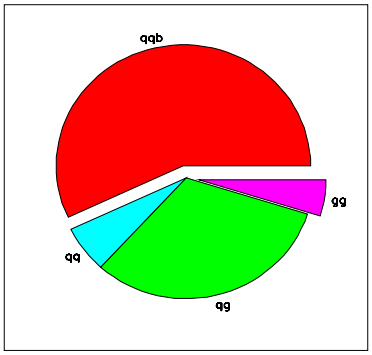

Msq 220 Mgls 250

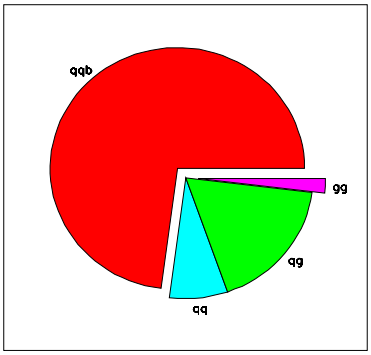

Msq 225 Mgls 300

squark–antisquark production
squark–squark production
squark–gluino production
gluino–gluino production

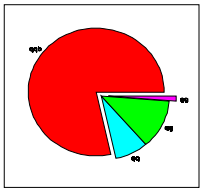

Msq 225 Mgls 325

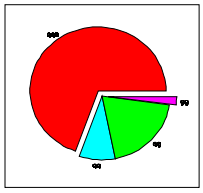

Msq 200 Mgls 275

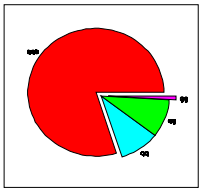

Msq 200 Mgls 325

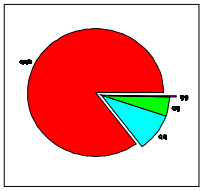

Msq 200 Mgls 370

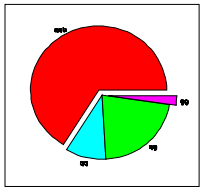

Msq 175 Mgls 250

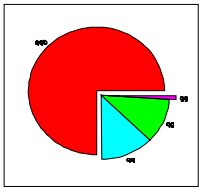

Msq 150 Mgls 275

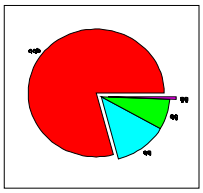

Msq 150 Mgls 300

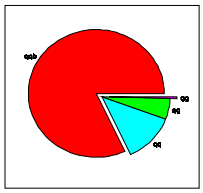

Msq 150 Mgls 325

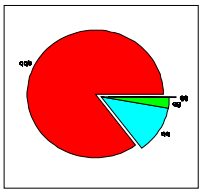

Msq 150 Mgls 370

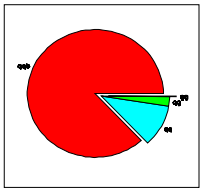

Msq 180 Mgls 400

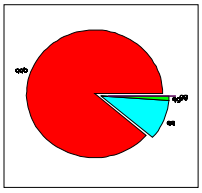

Msq 180 Mgls 450

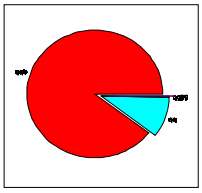

Msq 160 Mgls 500

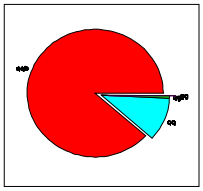

Msq 150 Mgls 450

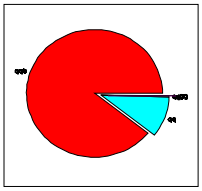

Msq 150 Mgls 500

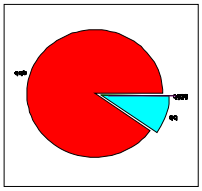

Msq 150 Mgls 550

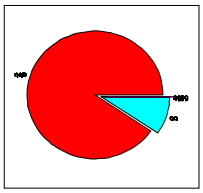

Msq 150 Mgls 570

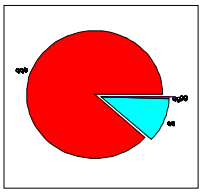

Msq 130 Mgls 450

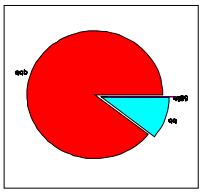

Msq 130 Mgls 500

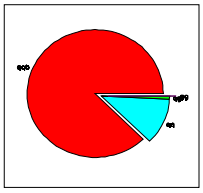

Msq 110 Mgls 400

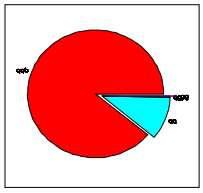

Msq 110 Mgls 450

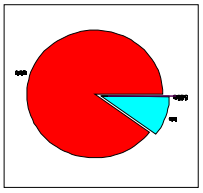

Msq 105 Mgls 500

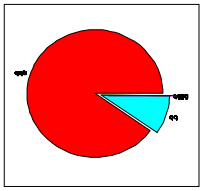

Msq 120 Mgls 550

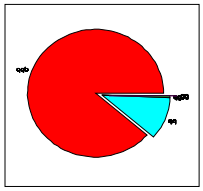

Msq 90 Mgls 400

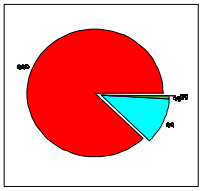

Msq 95 Mgls 370

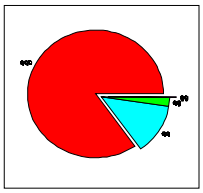

Msq 100 Mgls 325

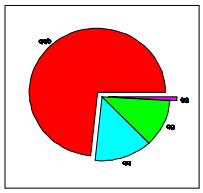

Msq 125 Mgls 250

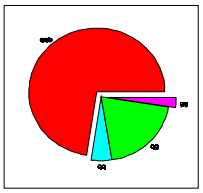

Msq 275 Mgls 325

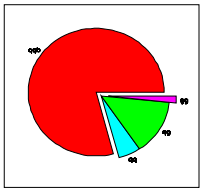

Msq 275 Mgls 350

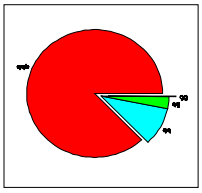

Msq 200 Mgls 400

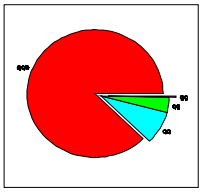

Msq 225 Mgls 400

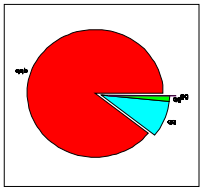

Msq 200 Mgls 450

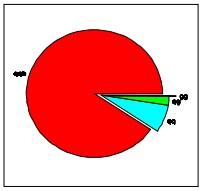

Msq 250 Mgls 450

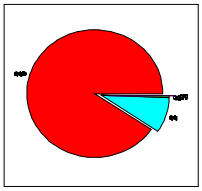

Msq 200 Mgls 500

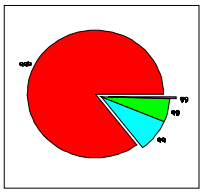

Msq 225 Mgls 375

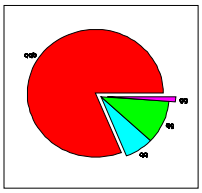

Msq 250 Mgls 350

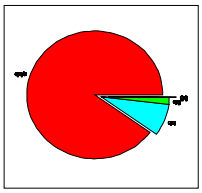

Msq 225 Mgls 450

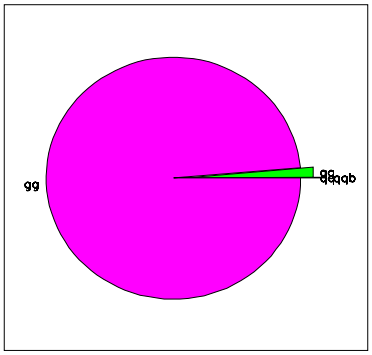

Msq 480 Mgls 181

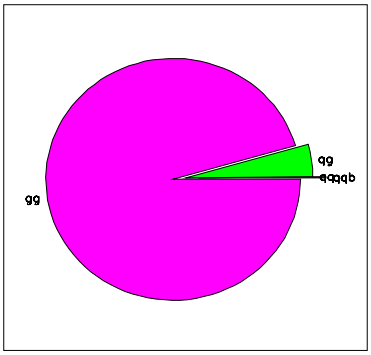

Msq 469 Mgls 237

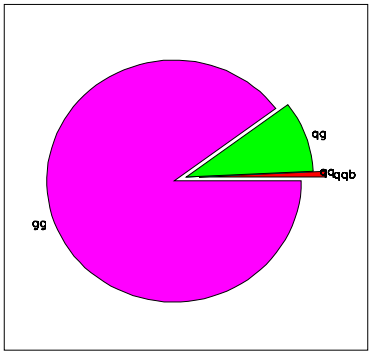

Msq 425 Mgls 237

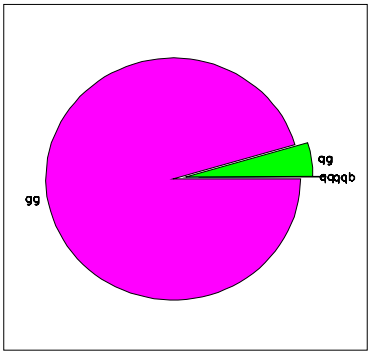

Msq 409 Mgls 179

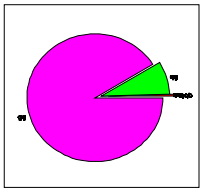

Msq 370 Mgls 177

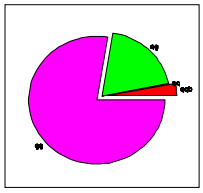

Msq 379 Mgls 235

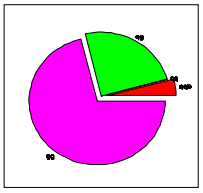

Msq 330 Mgls 204

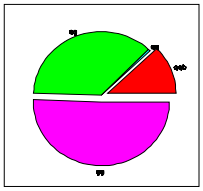

Msq 320 Mgls 230

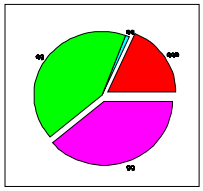

Msq 300 Mgls 230

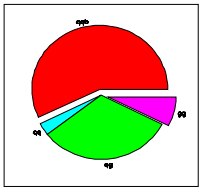

Msq 299 Mgls 300

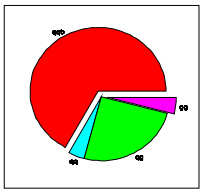

Msq 295 Mgls 319

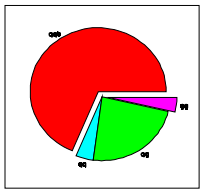

Msq 288 Mgls 319

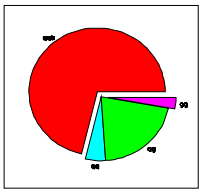

Msq 274 Mgls 318

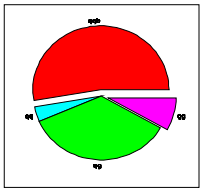

Msq 275 Mgls 275

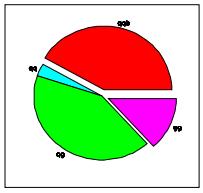

Msq 263 Mgls 247

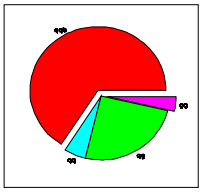

Msq 256 Mgls 292

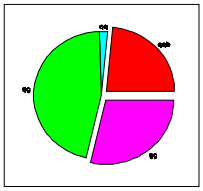

Msq 260 Mgls 212

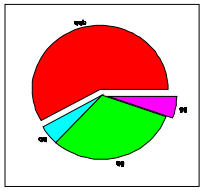

Msq 251 Mgls 270

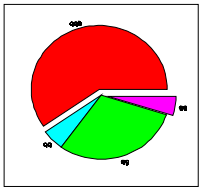

Msq 244 Mgls 269

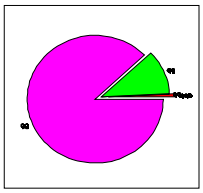

Msq 310 Mgls 146

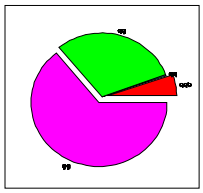

Msq 277 Mgls 173

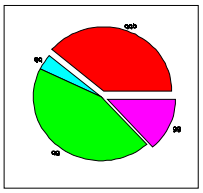

Msq 231 Mgls 220

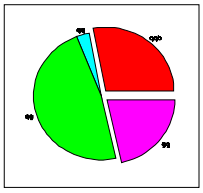

Msq 226 Mgls 197

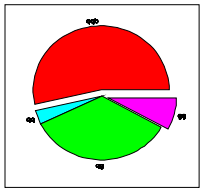

Msq 280 Mgls 280

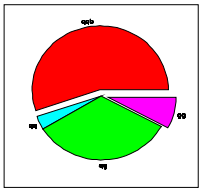

Msq 290 Mgls 290

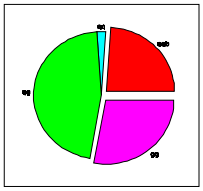

Msq 256 Mgls 210

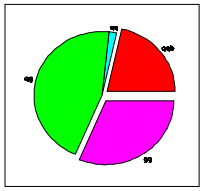

Msq 263 Mgls 210

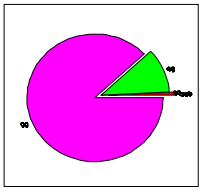

Msq 368 Mgls 191

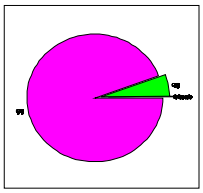

Msq 413 Mgls 193

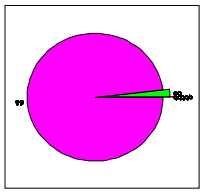

Msq 478 Mgls 195

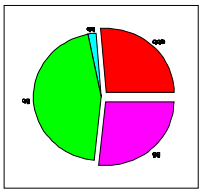

Msq 274 Mgls 227

Appendix H

Analysis Variables and Optimization

H.1 E_T Leading Jet, Second Leading Jet, $\not\!\!E_T$ H_T .

The $N_{signal}/\sqrt{N_{background}}$ as a function of a) the leading jet E_T, b) the second leading jet E_T, c) the $\not\!\!E_T$ and d) the H_T for two representative signal points are shown in Figures H.1, H.2, H.3 & H.4. The required values used in the analysis of $E_{T1} \geq 70$ GeV, and $E_{T2} \geq 30$ GeV are efficient for the signal detection.

H.2 Indirect Lepton Veto validation

In the high P_T lepton sample $W \to e\nu_e$ and $W \to \mu\nu_\mu$ events are selected. The same selection is applied in the Monte Carlo. Data and Monte Carlo is compared after applying each of the indirect lepton veto criteria separately and both. The results for the W decaying into electrons are shown in Figure H.5 and in table H.1. The corresponding muon results are shown in figure H.6 and in table H.2. The tracking

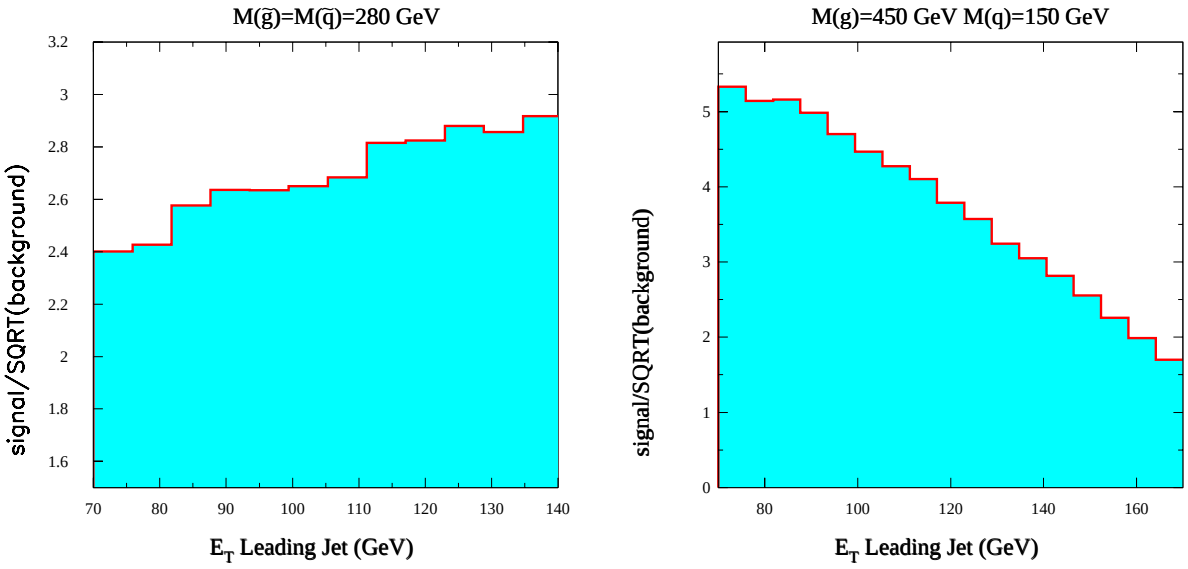

Figure H.1: Signal/SQRT(background)(E_{T1}) for two signal points.

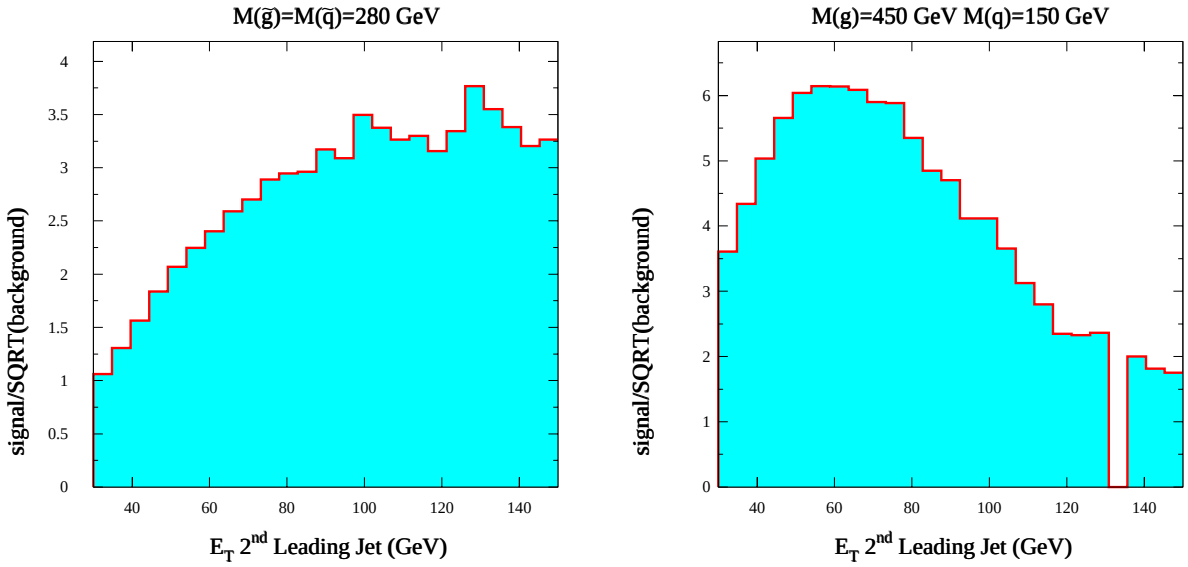

Figure H.2: Signal/SQRT(background)(E_{T2}) for two signal points.

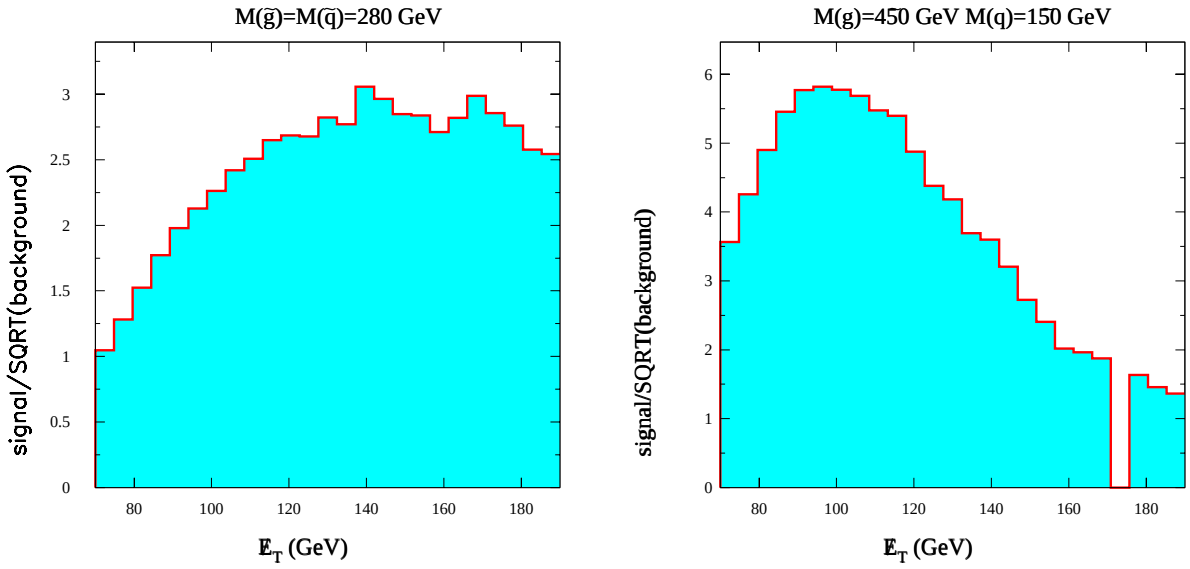

Figure H.3: Signal/SQRT(background)($\not\!\!E_T$) for two signal points.

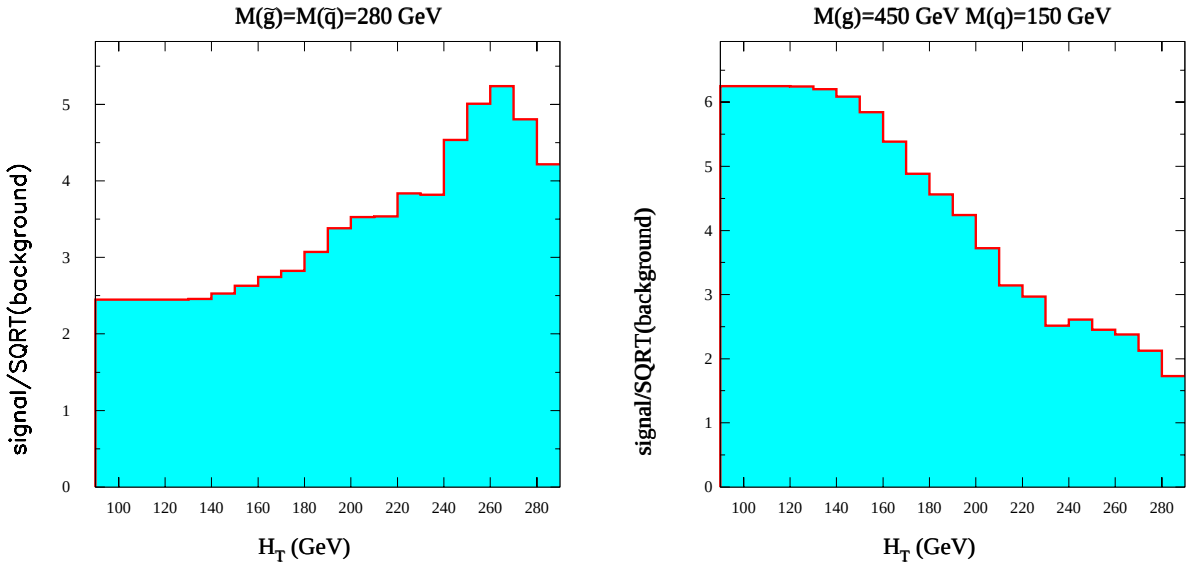

Figure H.4: Signal/SQRT(background)(H_T) for two signal points.

	$We\nu$+3j	track isolation	EMF	both
	N_{events}			
data	1442	141	174	30
MC	1442	140	181	21
MC=VECBOS+HERPRT+QFL $W(\rightarrow e\nu_e)$+jets				

Table H.1: Indirect Lepton Veto requirements validation with $W(\rightarrow e\nu_e)$+ jets data and Monte Carlo : Predictions are in agreement with the data. The cumulative rejection efficiency of the requirements is 98%.

	$W\mu\nu$+3j	track isolation	EMF	both
	N_{events}			
data	304	23	291	22
MC	304	35	285	34
MC=VECBOS+HERPRT+QFL $W(\rightarrow \mu\nu_\mu)$+jets				

Table H.2: Indirect Lepton Veto requirements validation with $W(\rightarrow \mu\nu_\mu)$+ jets data and Monte Carlo: Predictions are in agreement with the data. The cumulative rejection efficiency of the requirements is 93%.

isolation requirement in examined in the JET data and QCD Monte Carlo predictions. In Figure H.7 the QCD predictions are normalized to the JET data for all $\not\!\!E_T$ values and the Isolated Track multiplicity is shown for the data and the predictions. The comparison is shown before and after the $\not\!\!E_T$ 70 GeV requirement is applied.

H.3 $\delta\phi_{min}$ study and optimization

$\delta\phi_{min}$ is the minimum ϕ between any jet and the $\not\!\!E_T$. The requirement $\delta\phi_{min} < 0.3$ rad is rejecting residual QCD background from mismeasured jets. In Figure H.8 the optimization for this variable is shown for two representative points in the SUSY parameter space. In Figures H.9 the $\delta\phi_{min}$ distribution is shown for the QCD back-

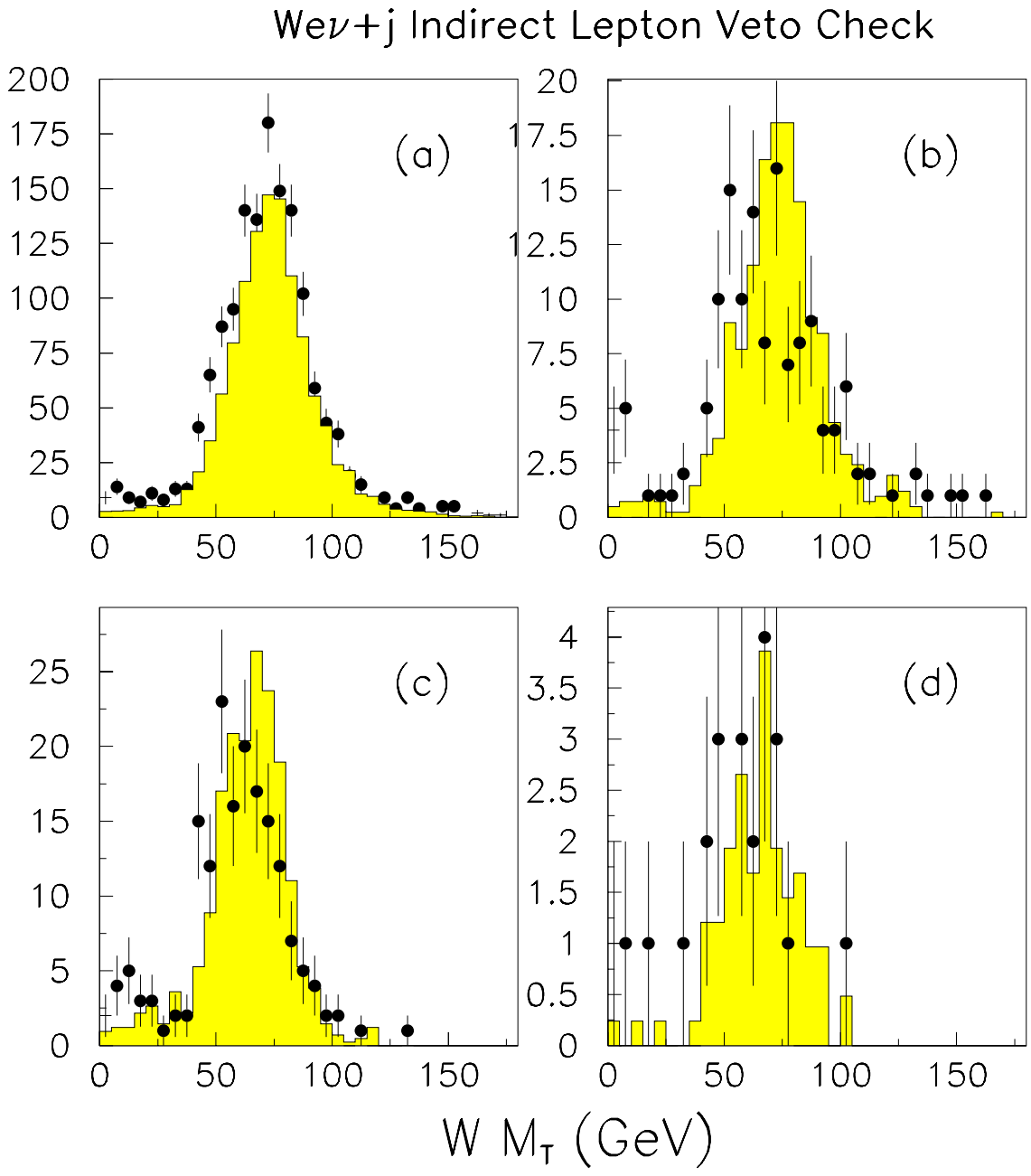

Figure H.5: Points is data, histogram is VECBOS+QFL' $W \to e\nu_e$+jets (a) $W \to e\nu_e$ (here the electron counts as jet) - MC normalized to data, (b) track isolation criterion applied, (c) EMF criterion applied (d) both indirect lepton veto criteria applied. In (b) through (d) the normalization derived from (a) is used. (Table H.1.)

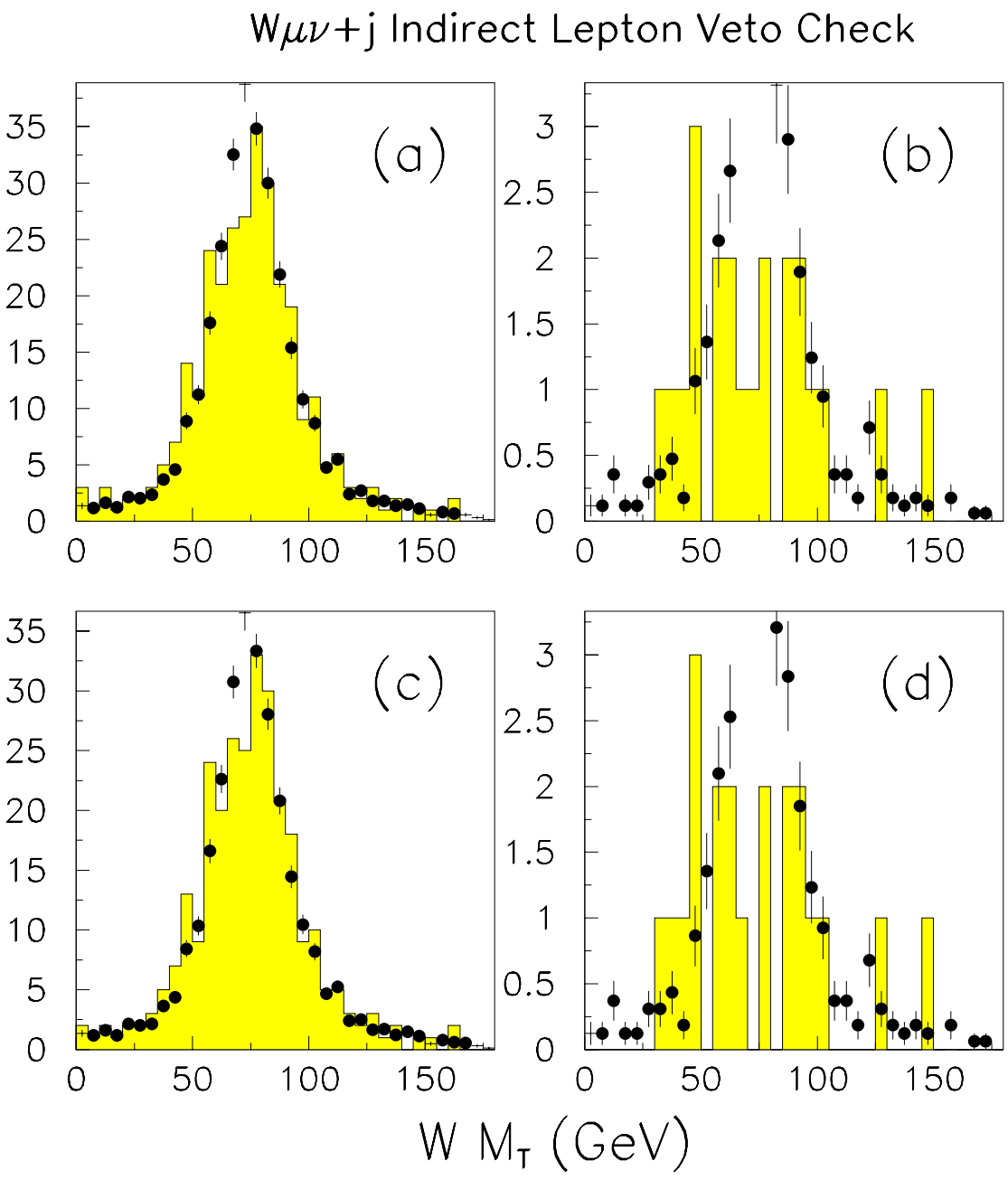

Figure H.6: Points is data, histogram is VECBOS+QFL′ $W \rightarrow \mu\nu_\mu + \geq 3$ jets (a)$W \rightarrow \mu\nu_\mu$ - MC normalized to data, (b) track isolation criterion applied (c) EMF criterion applied (d) both indirect lepton veto criteria applied. In (b) through (d) the normalization is derived from (a). (Table H.2.)

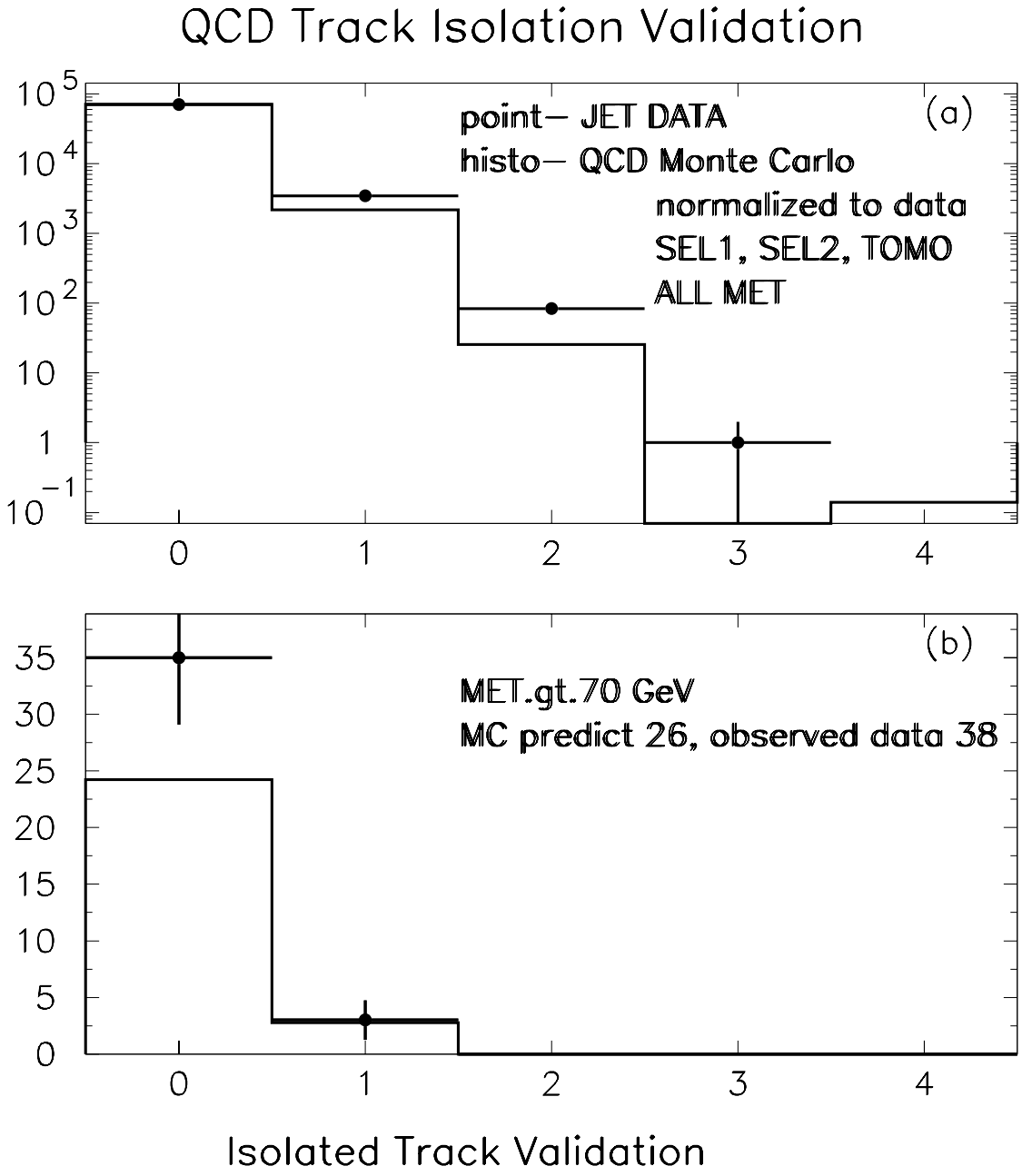

Figure H.7: Points is data, histogram is HERWIG+QFL2-to-2. (a) N_{trk}^{iso} in data and Monte Carlo before any $\not\!\!E_T$ rrequirement (b) After the $\not\!\!E_T \geq$ 70 GeV requirement. Normalization derived from (a). N_{trk}^{iso} bin 0 events enter in the blind box.

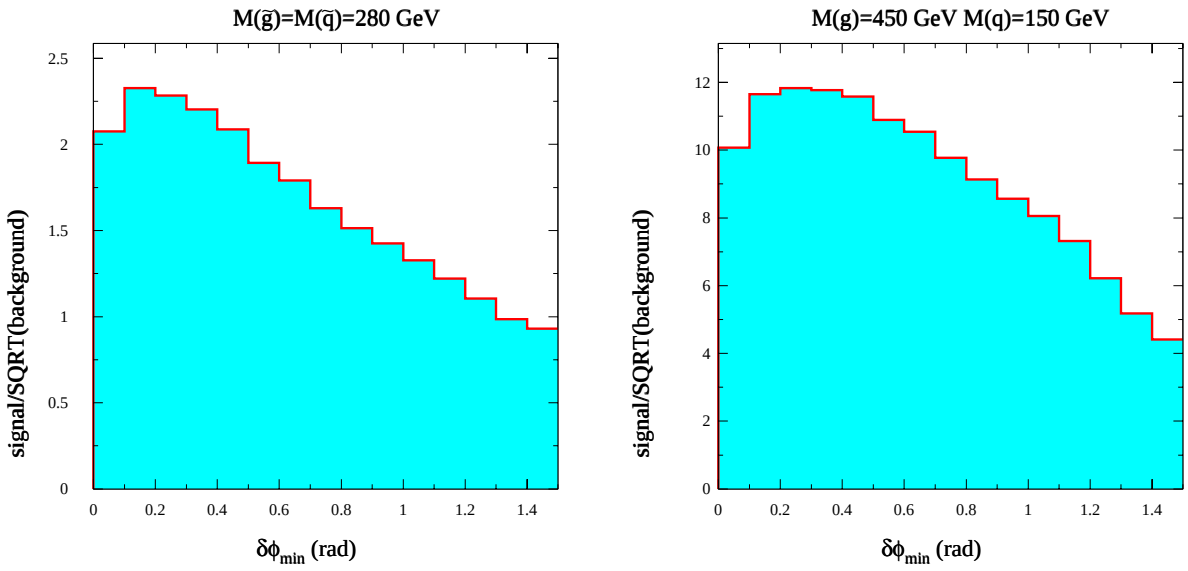

Figure H.8: Signal/SQRT(background)($\delta\phi_{min}$) for two signal points.

ground before the fiducial requirements are applied. As expected the mismeasurements are peaking at ϕ close to the $\phi(\not\!\!E_T)$. The same distribution is shown after the fiducial requirements are applied which tend to flatten the $\delta\phi_{min}$ distribution. The step at 0.5 rad is exactly the *tomographic* requirement for the second and third jets that fall into uninstrumented regions and are aligned in ϕ with the $\not\!\!E_T$ vector. At higher $\not\!\!E_T$ the effect is pronounced because the relative rate of mismeasurements is higher. The same distributions are shown for the representative point in the SUSY parameter space in Figures H.10 & H.10.

H.4 Shapes around the Box

Figures H.12 through H.17 present the results of the comparisons between the data and the Standard Model predictions in the remaining bins around the Blind Box.

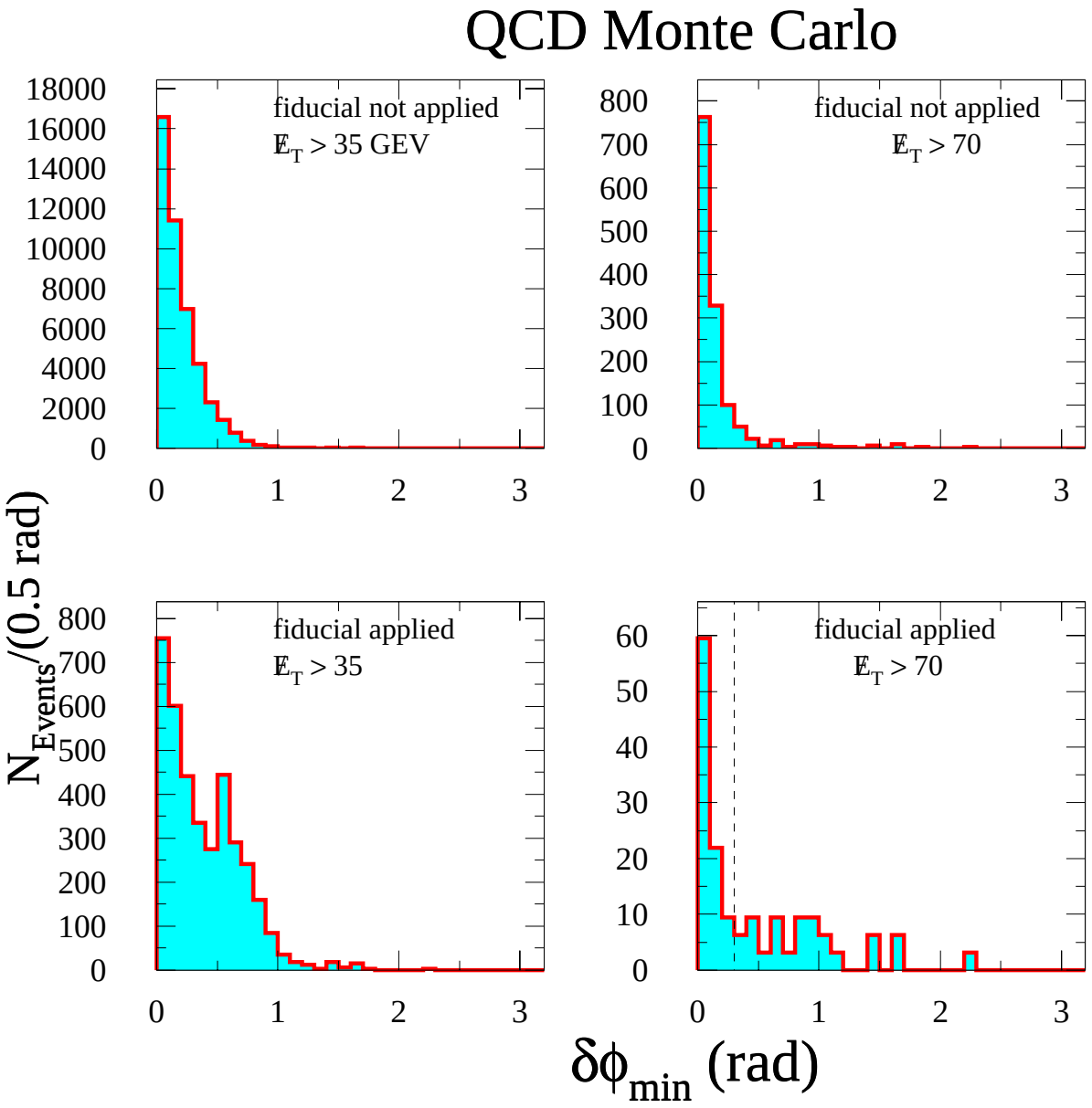

Figure H.9: QCD simulation: $\delta\phi_{min}$ variable before and after the fiducial requirements for $\not\!\!E_T >$ 35 GeV and $\not\!\!E_T >$ 70 GeV.

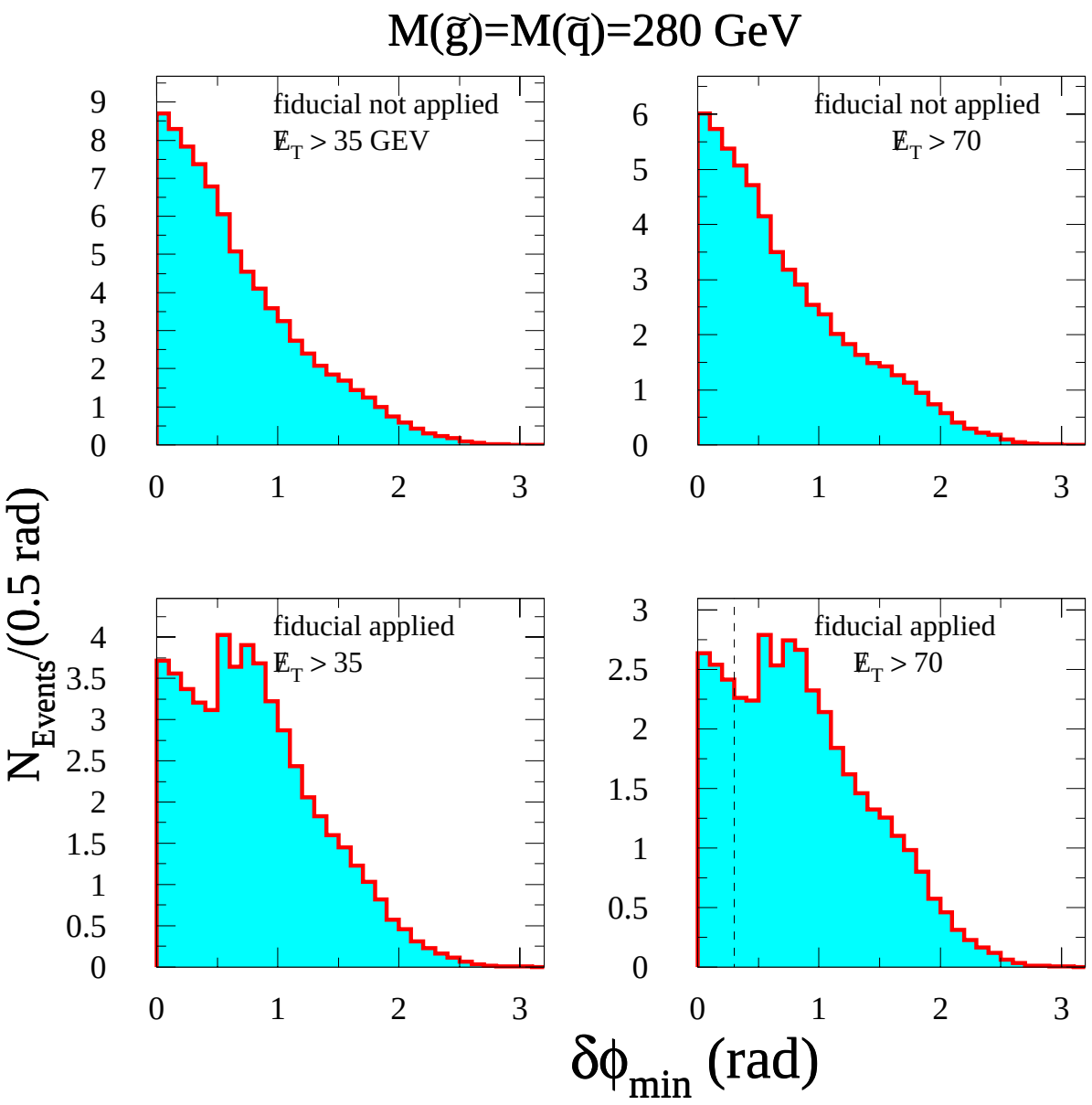

Figure H.10: $\delta\phi_{min}$ variable before and after the tomography+2d-$\delta\phi$ requirements for $\not\!\!E_T >$ 35 GeV and $\not\!\!E_T >$ 70 GeV.

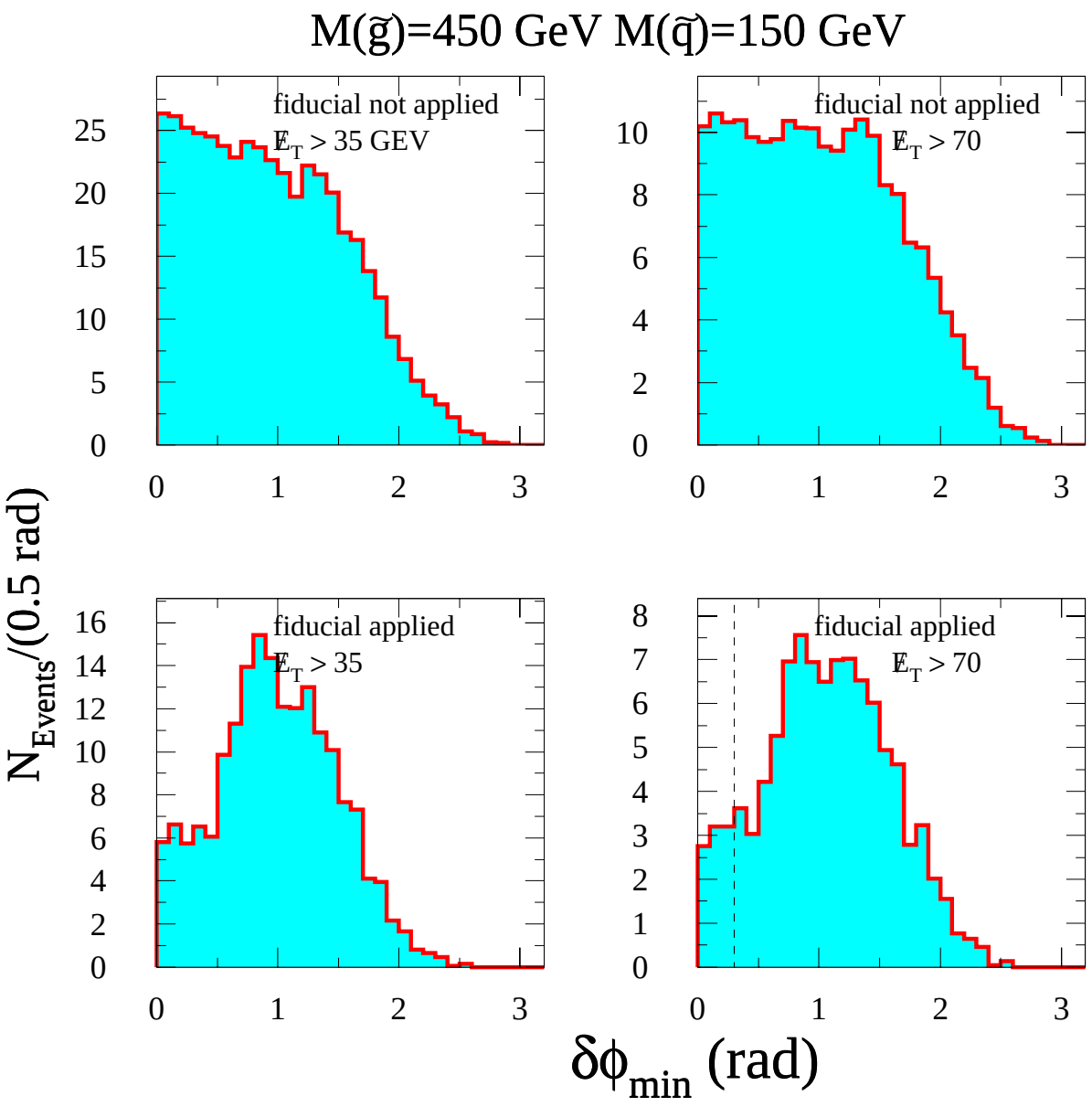

Figure H.11: $\delta\phi_{min}$ variable before and after the tomography+2d-$\delta\phi$ requirements for $\not\!\!E_T >$ 35 GeV and $\not\!\!E_T >$ 70 GeV.

Figures H.26 through H.29 show the events display of a few events passing all the analysis requirements.

H.4.1 $\not\!\!E_T$, H_T optimization in the signal space

Figures H.18 through H.25 present the optimization for representative points in regions A,B,C and D of the $m_{\tilde{q}}$–$m_{\tilde{g}}$ space. The curves marked b_i in region A are points that initially (regions B and C were studied before A and D) were thought to belong in the general region B. Upon study of representative points of all regions, kinematically these points were found to belong to region A. The optimization changed slightly. *A posteriori* the decision ought to be made whether to keep the initial optimization which was not optimal or to whether to correct it. The latter was chosen given that only the Monte Carlo is used to optimize the requirements for the SUSY regions. Neither the initial blind box definition, nor the analysis final results is affected by this.

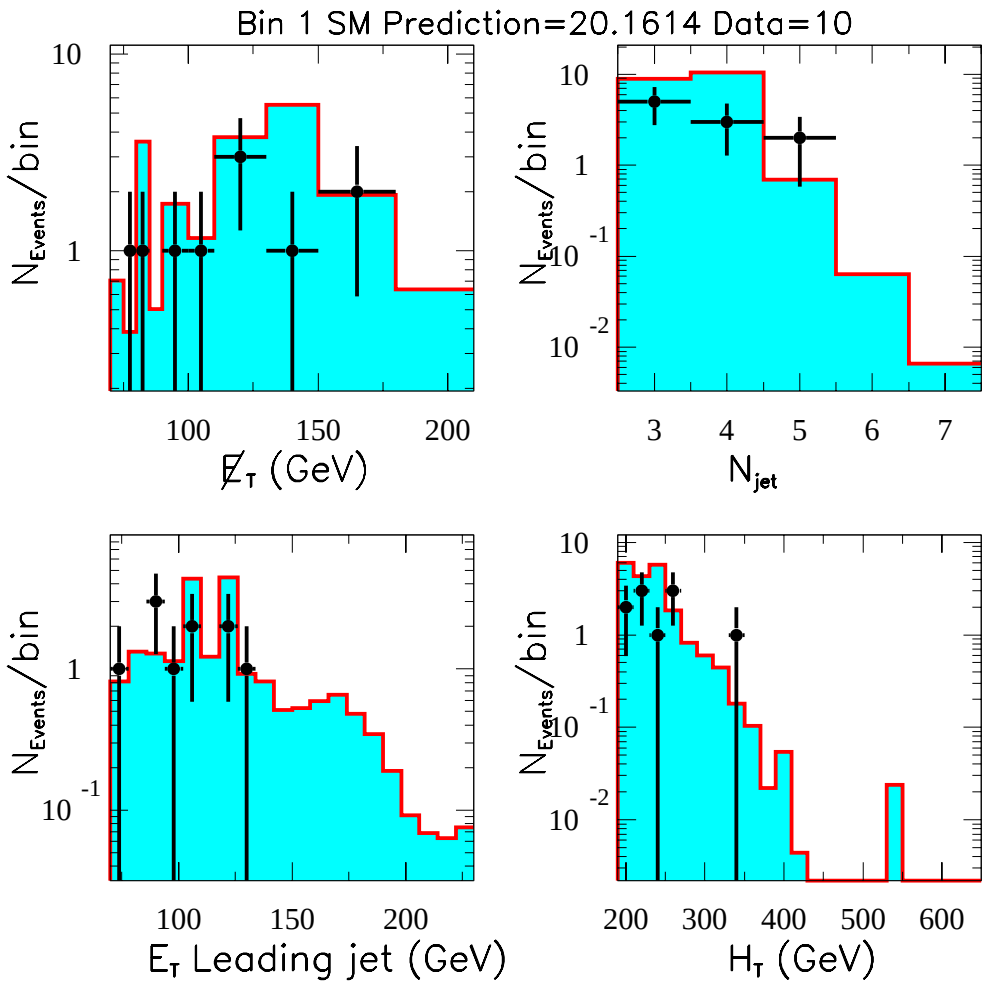

Figure H.12: Comparison of Standard Model prediction and data in bin 1.

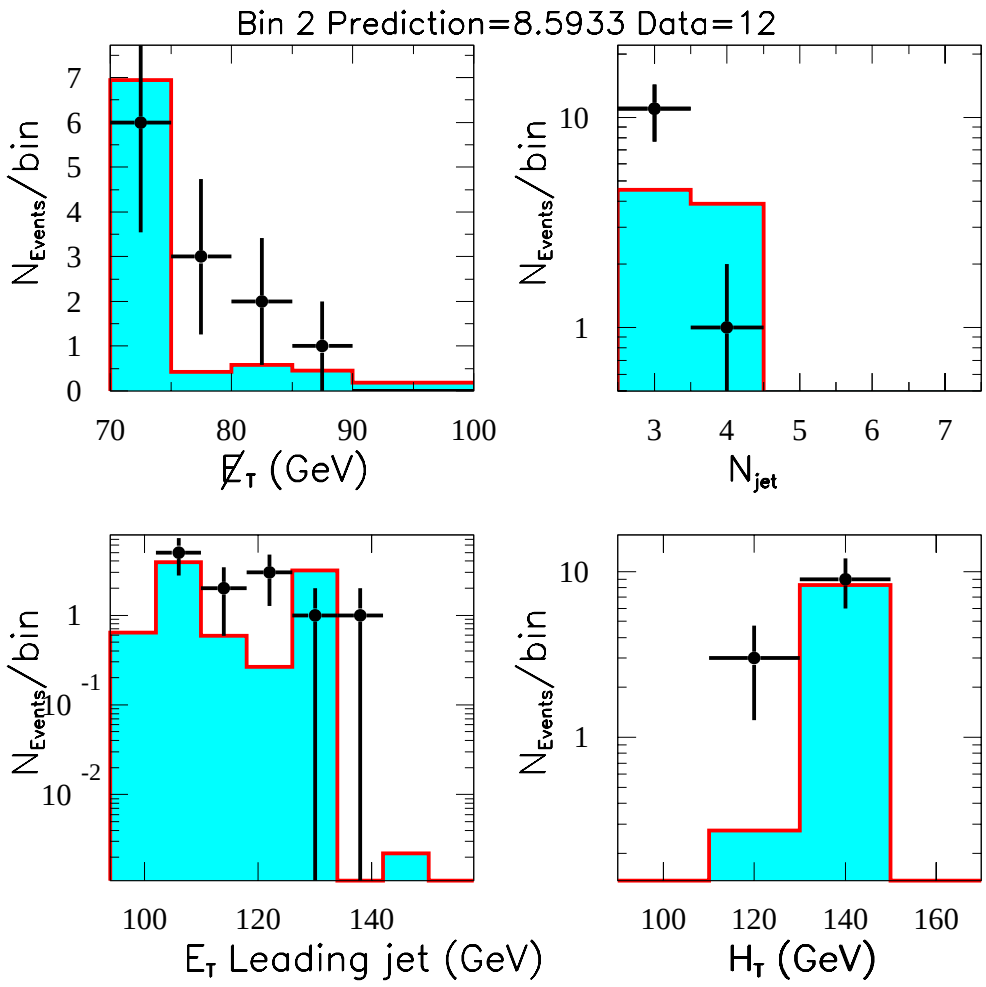

Figure H.13: Comparison of Standard Model prediction and data in bin 2.

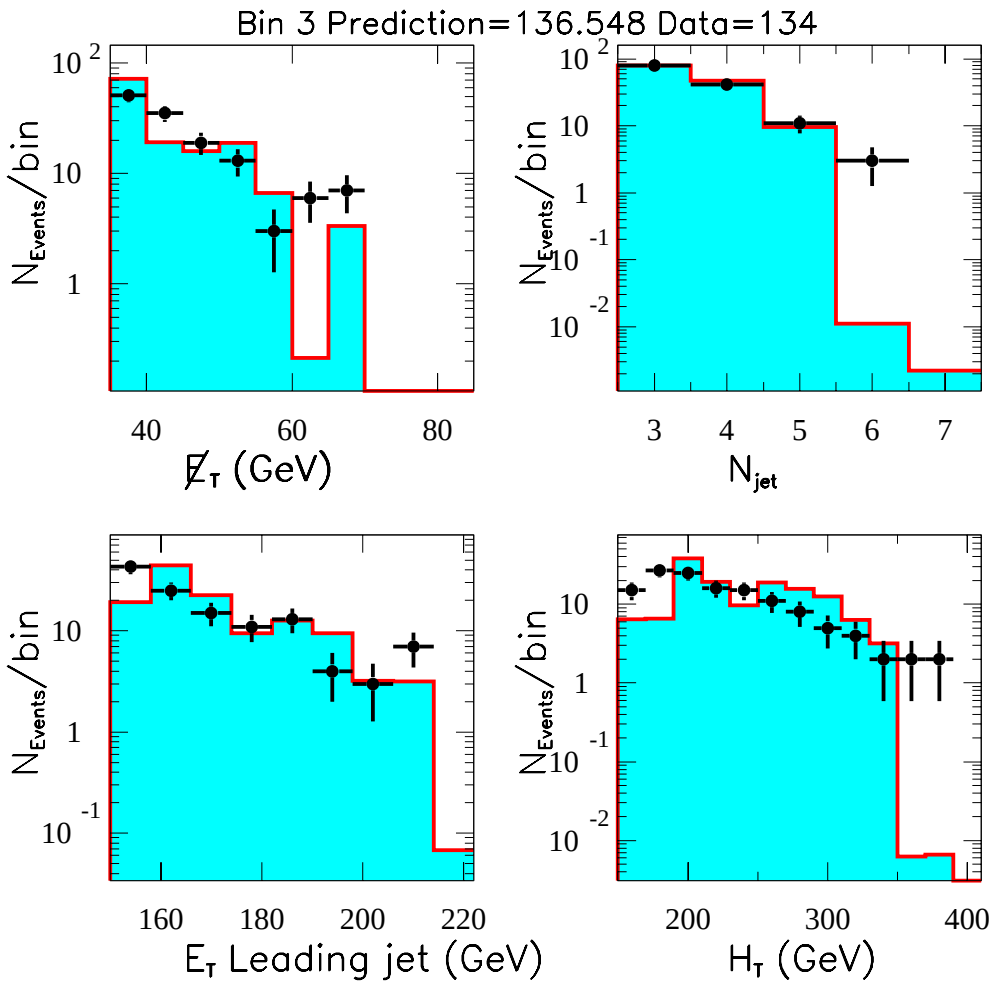

Figure H.14: Comparison of Standard Model prediction and data in bin 3.

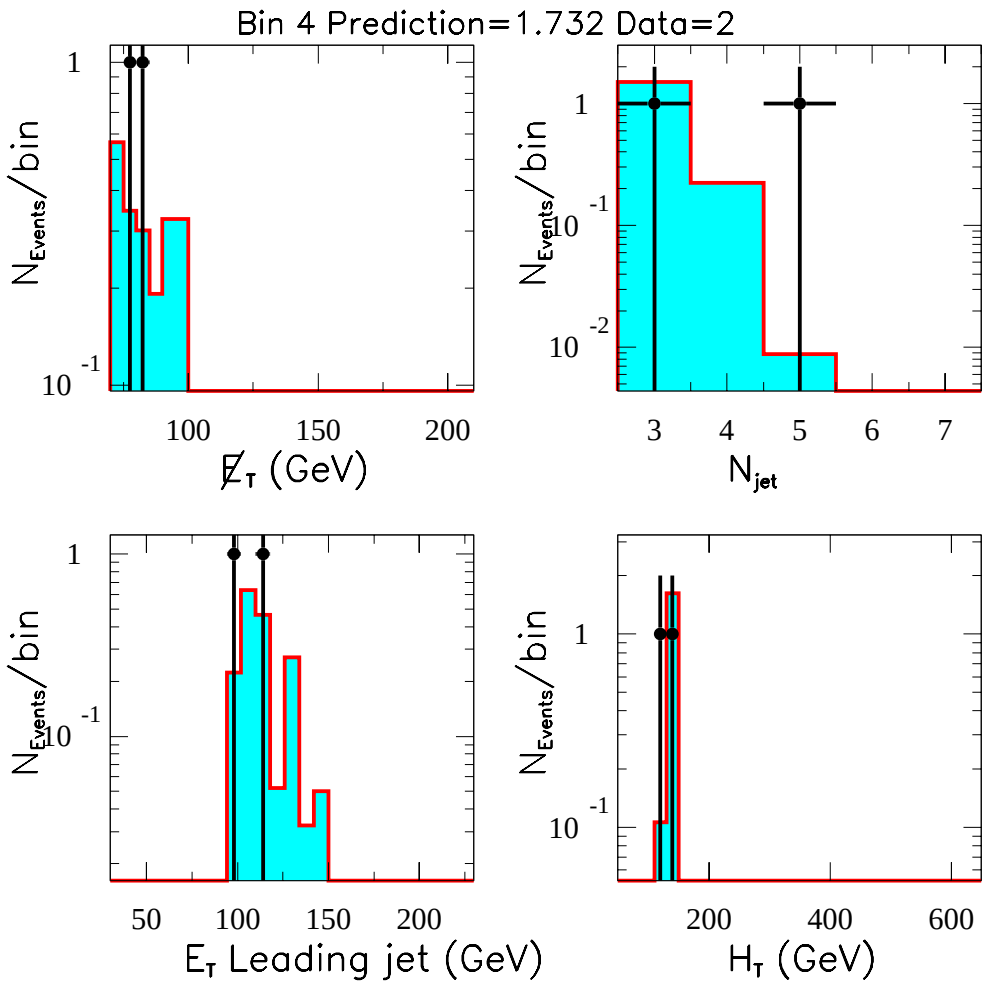

Figure H.15: Comparison of Standard Model prediction and data in bin 4.

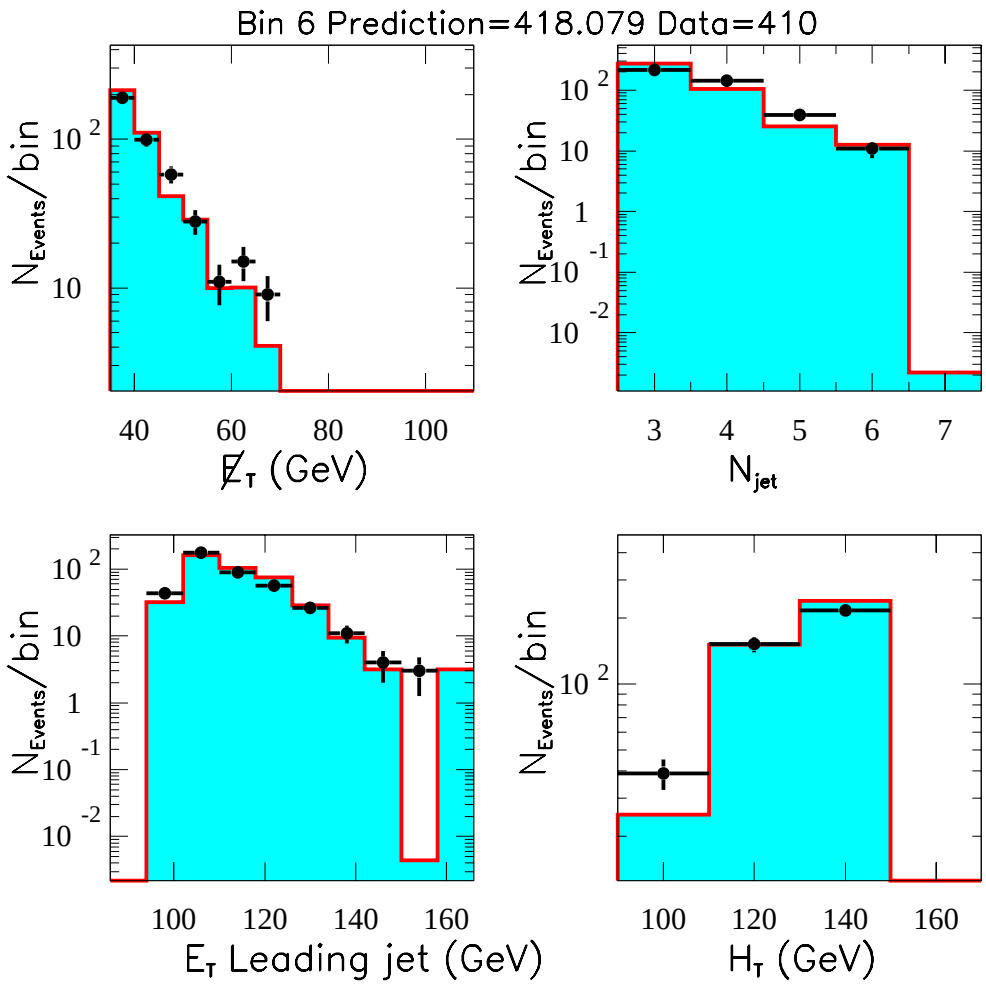

Figure H.16: Comparison of Standard Model prediction and data in bin 6.

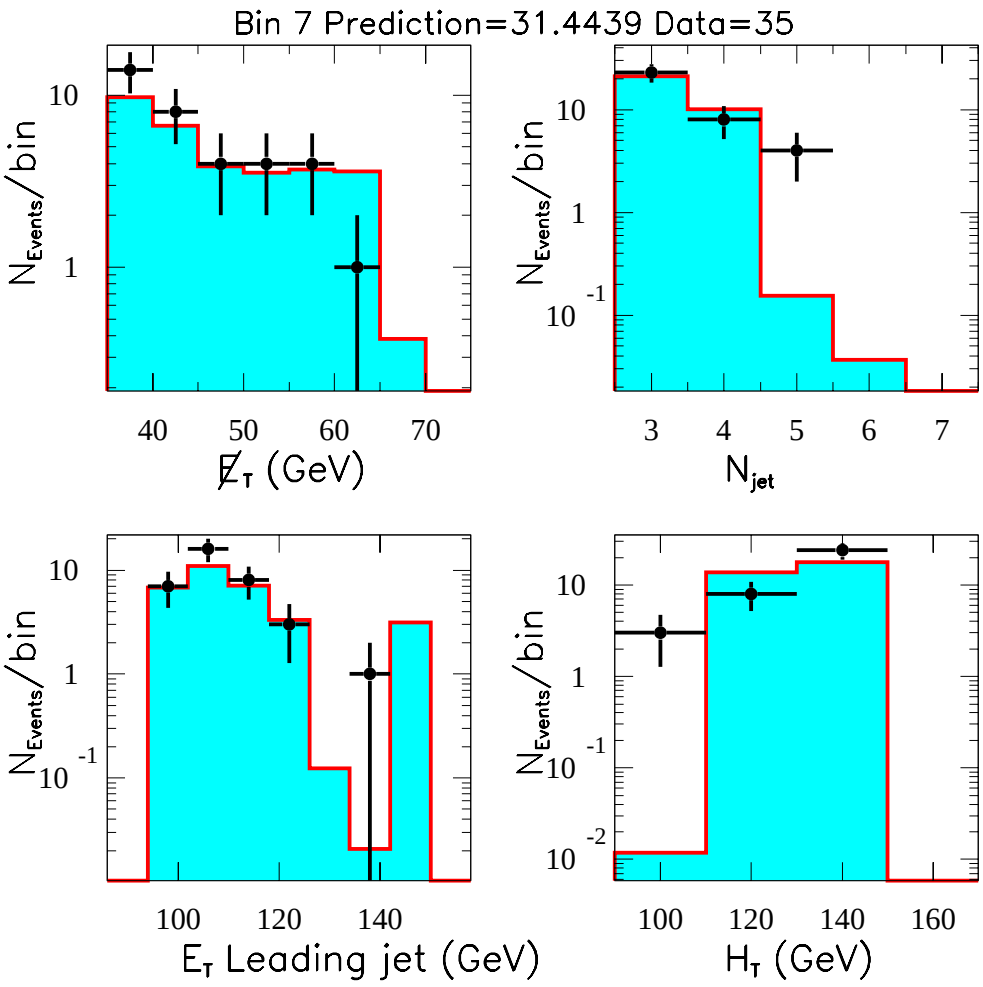

Figure H.17: Comparison of Standard Model prediction and data in bin 7.

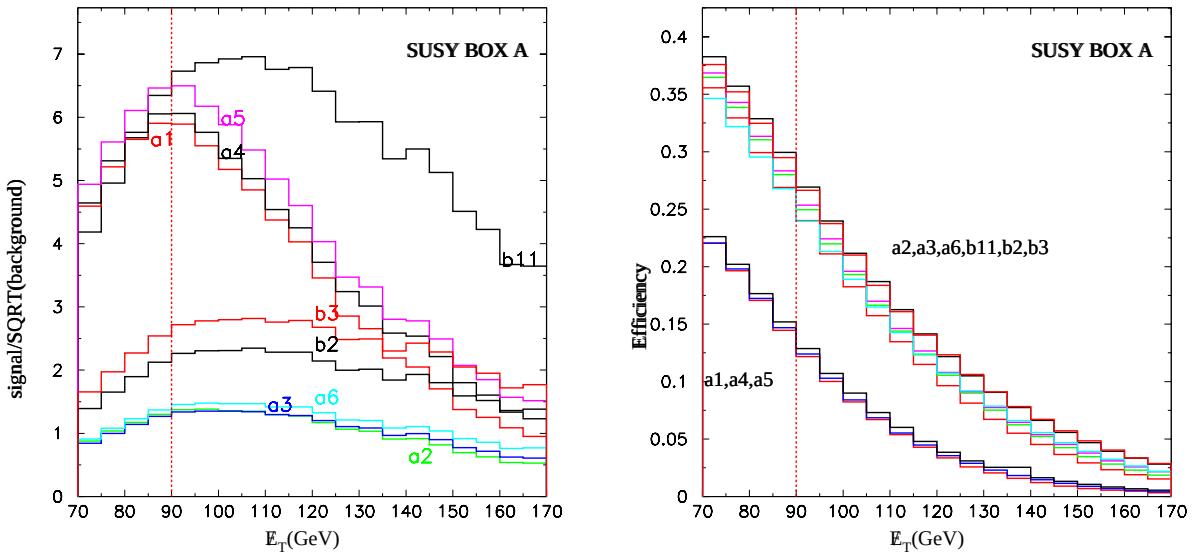

Figure H.18: $\not\!\!E_T$ Optimization Box A.

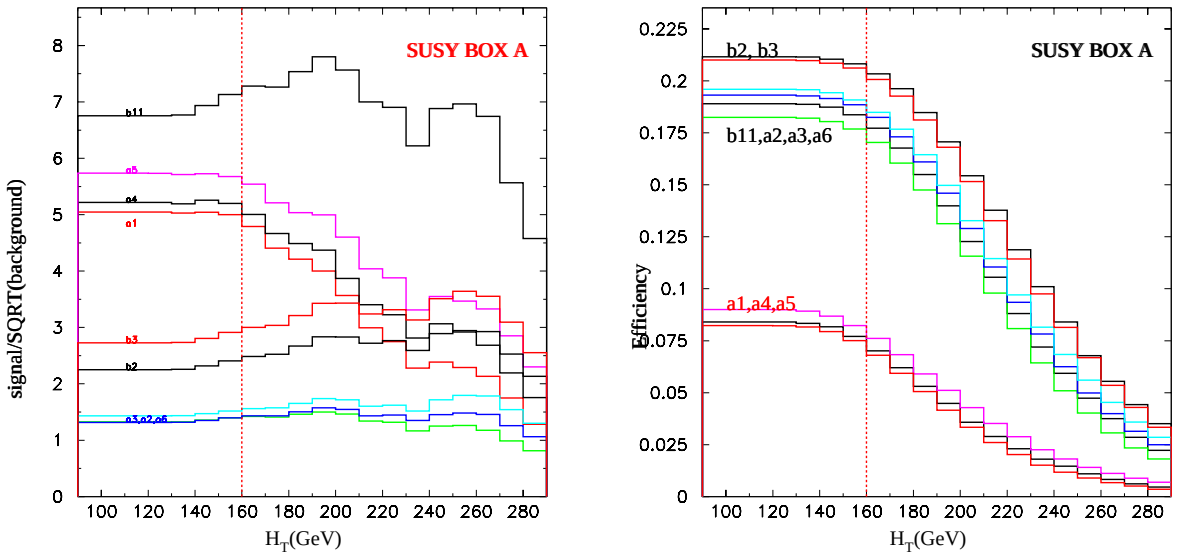

Figure H.19: H_T Optimization Box A.

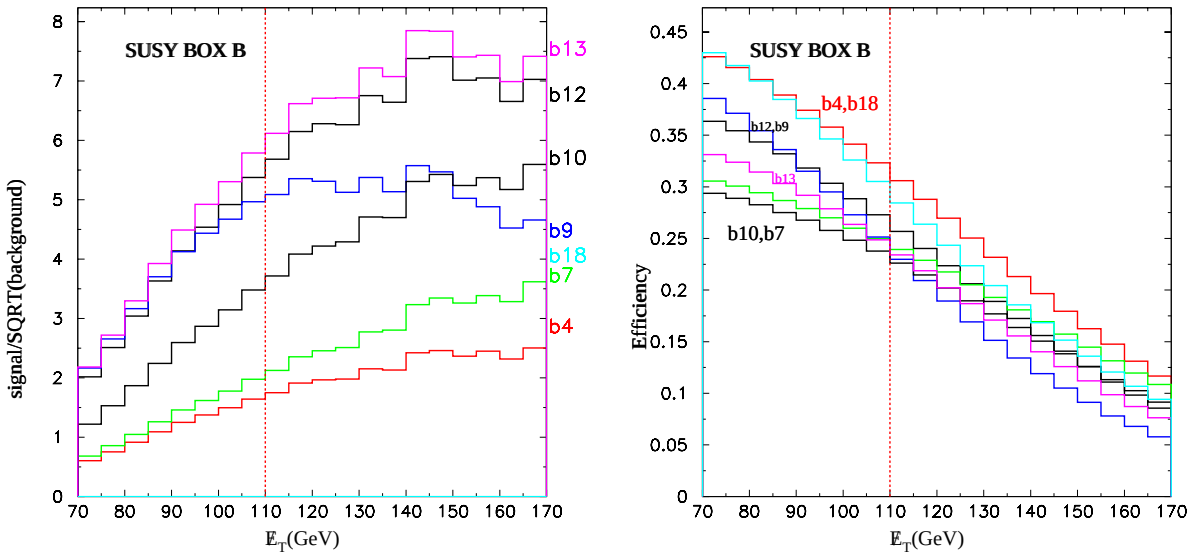

Figure H.20: $\not\!\!E_T$ Optimization Box B.

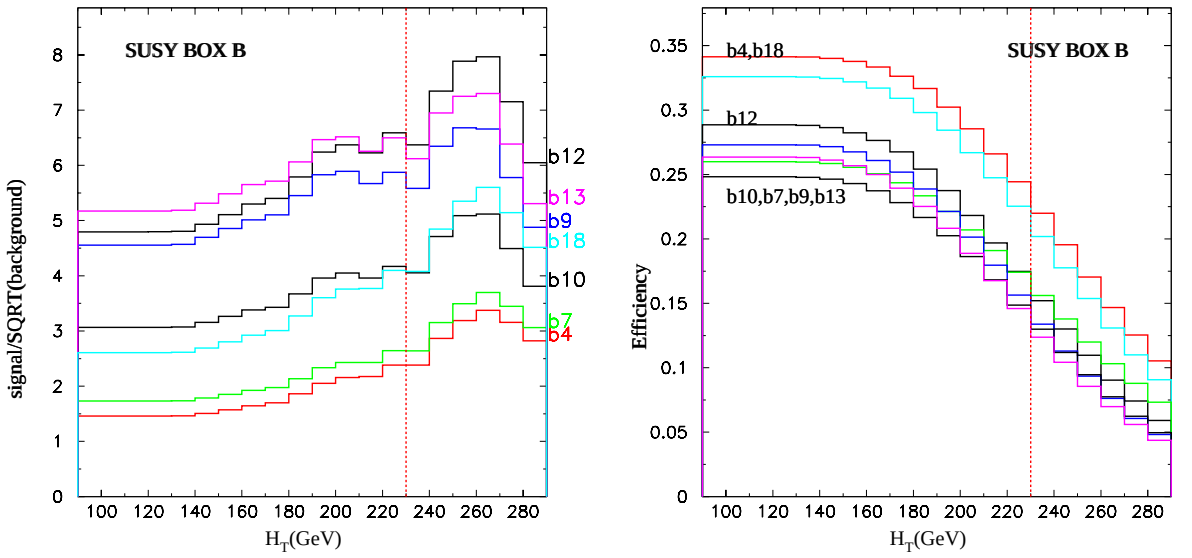

Figure H.21: H_T Optimization Box B.

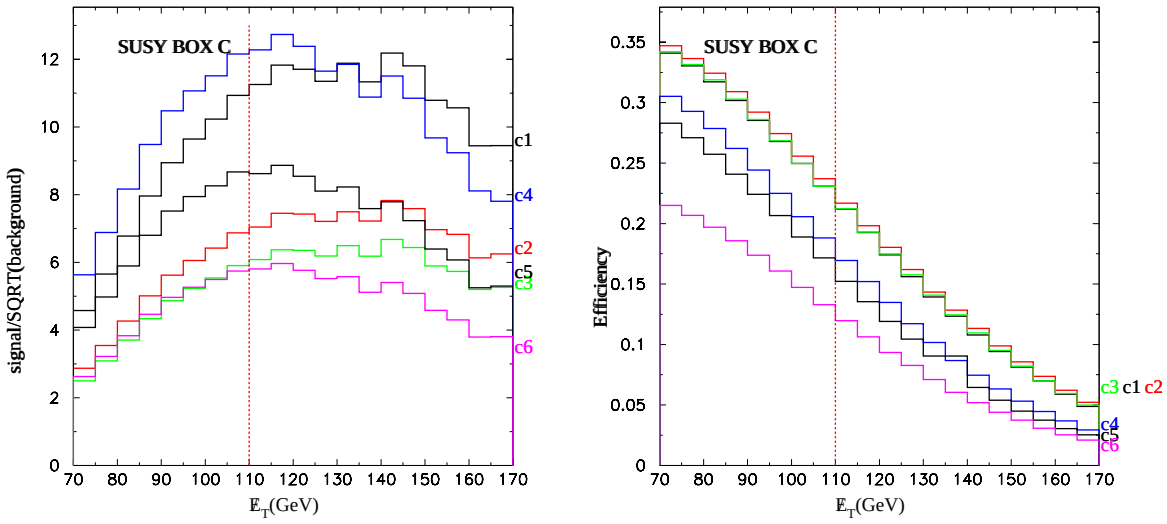

Figure H.22: $\not\!\!E_T$ Optimization Box C.

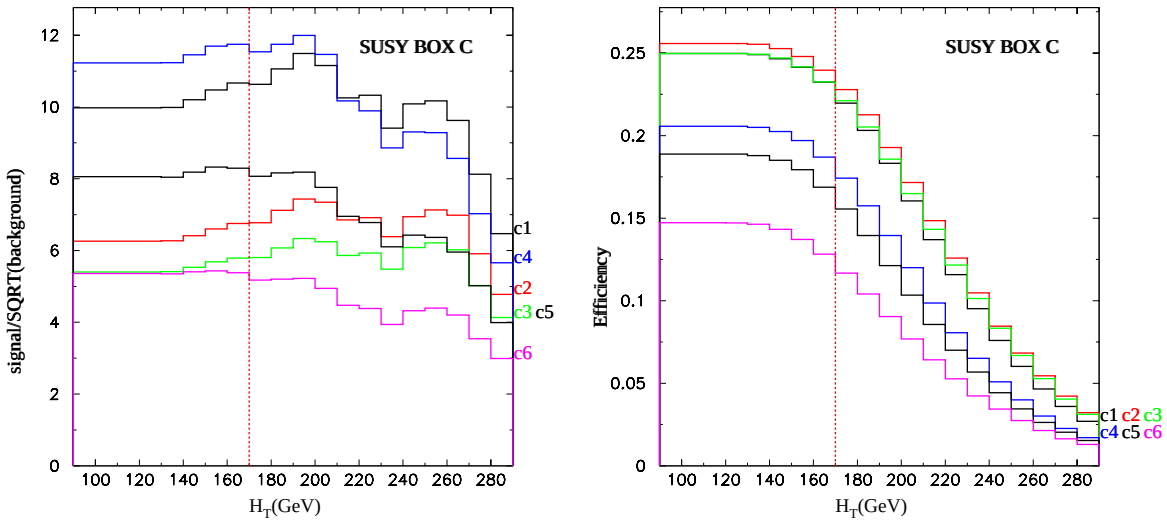

Figure H.23: H_T Optimization Box C.

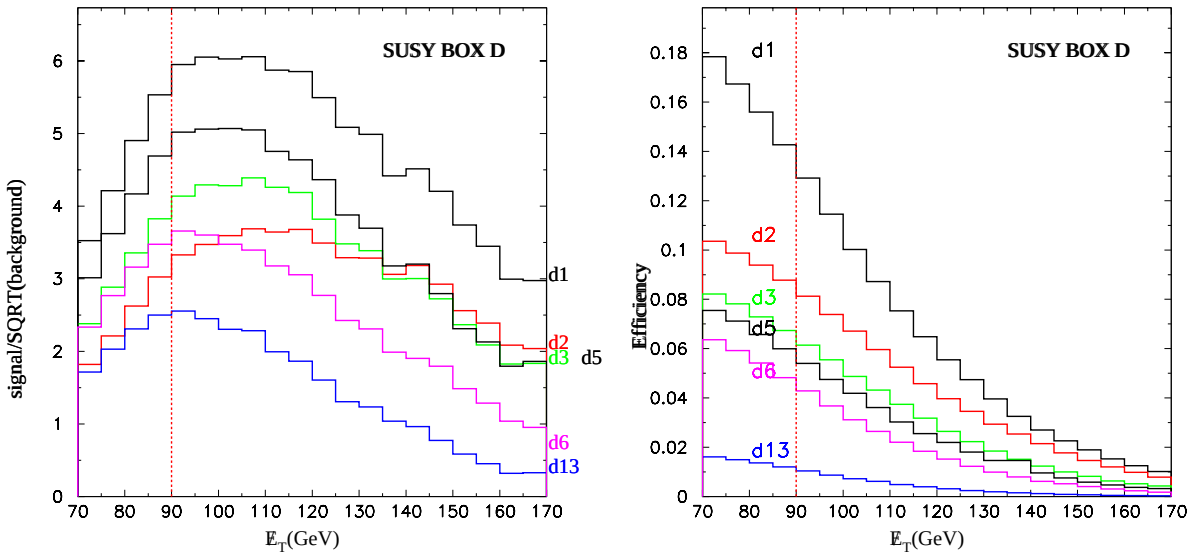

Figure H.24: $\not\!\!E_T$ Optimization Box D.

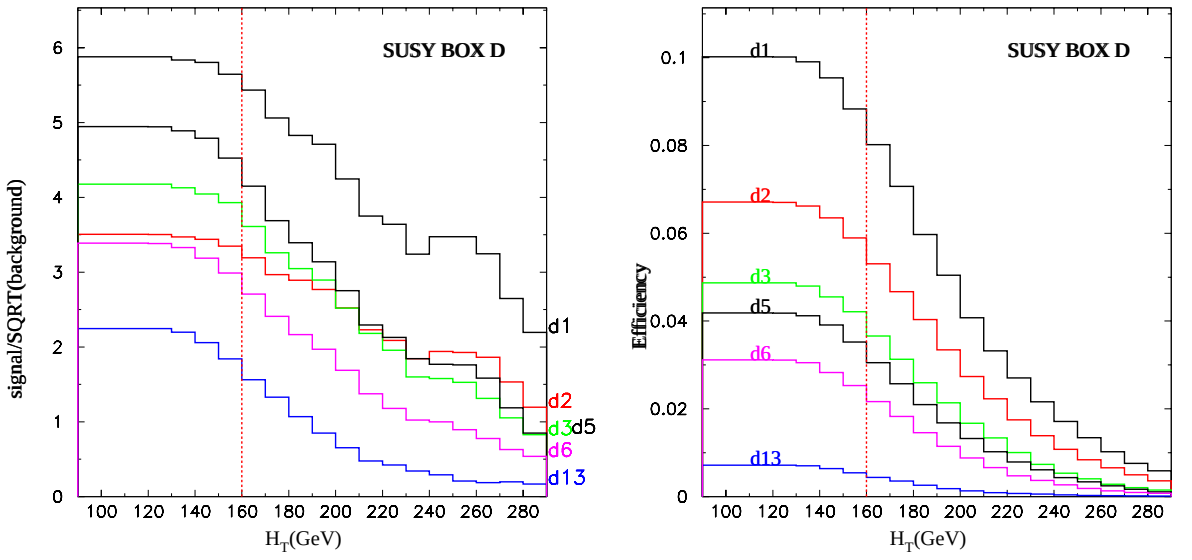

Figure H.25: H_T Optimization Box D.

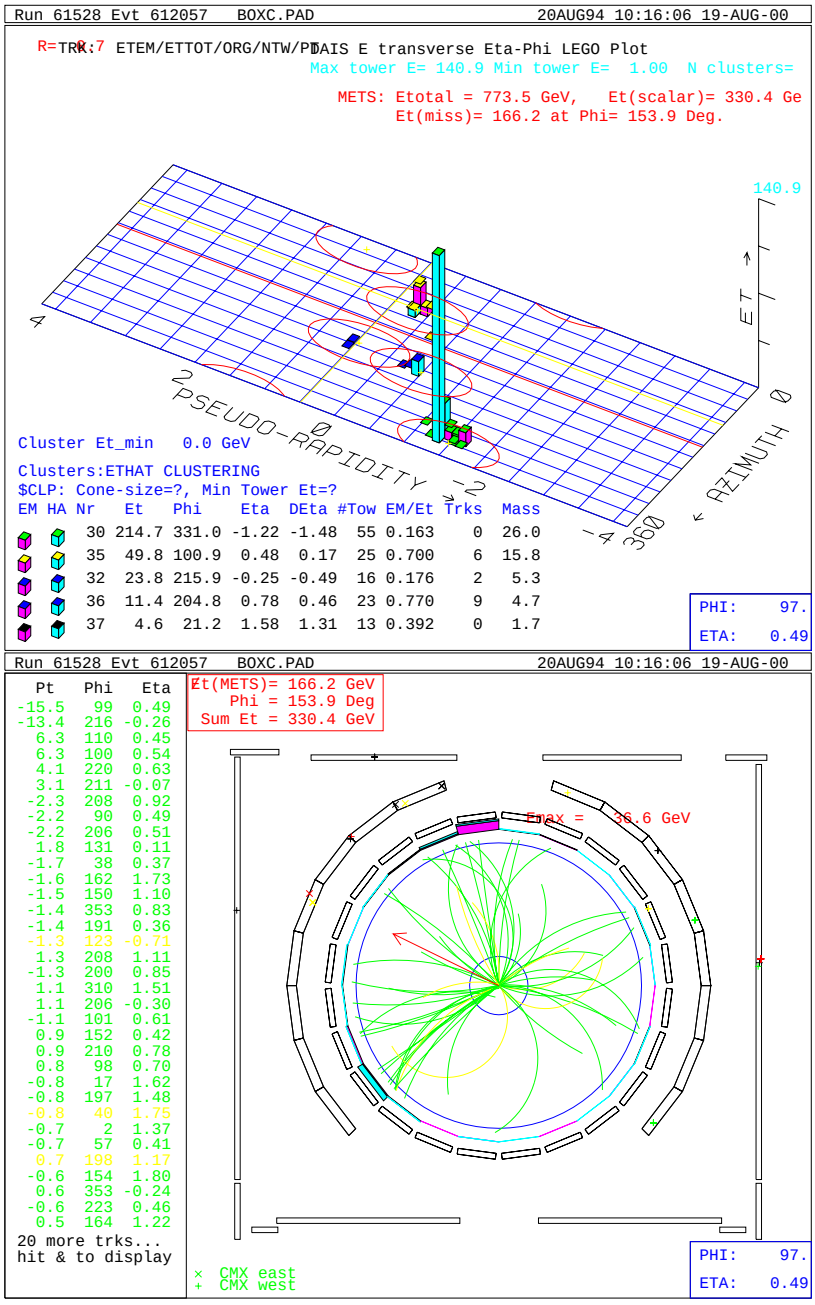

Figure H.26: (Top) LEGO (Bottom) CTC Event Display of candidate event.

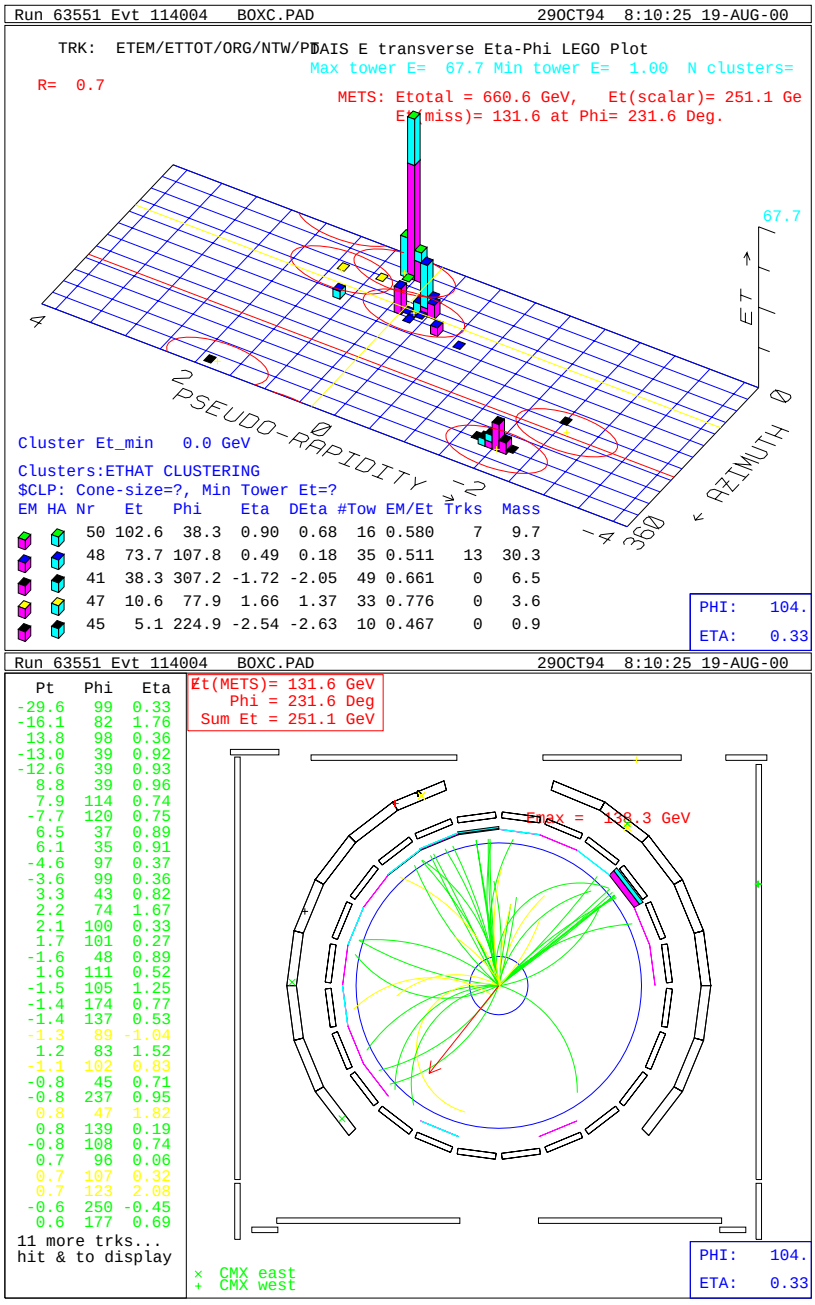

Figure H.27: (Top) LEGO (Bottom) CTC Event Display of candidate event.

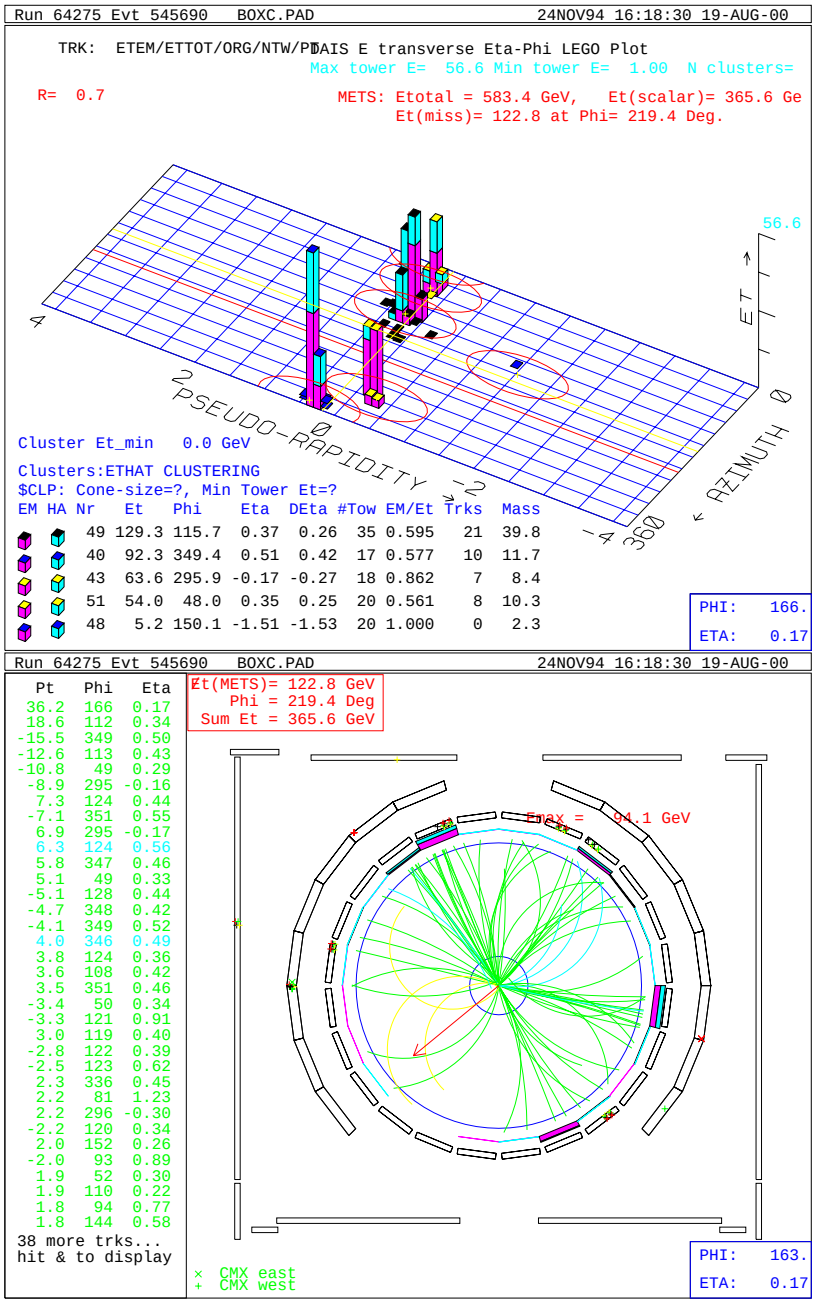

Figure H.28: (Top) LEGO (Bottom) CTC Event Display of candidate event.

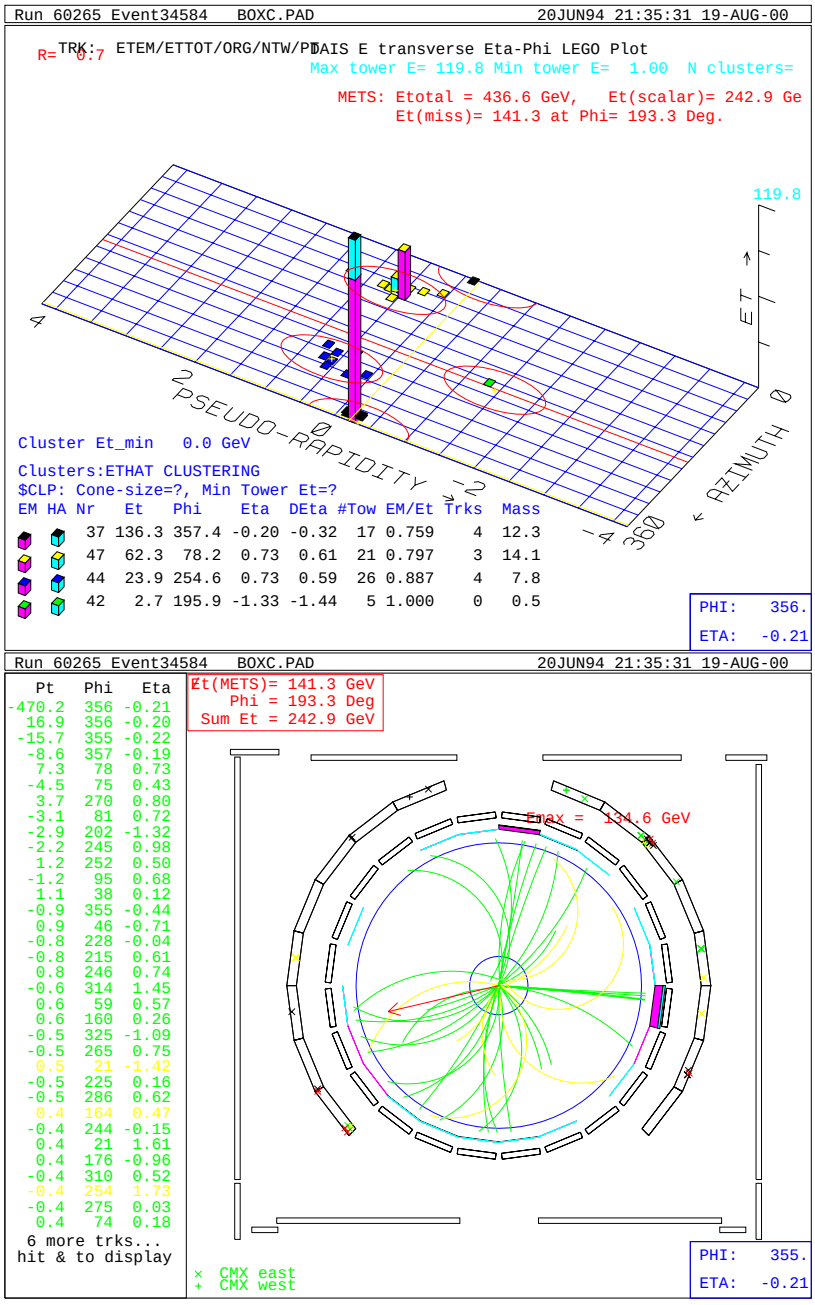

Figure H.29: (Top) LEGO (Bottom) CTC Event Display of candidate event.

Bibliography

[1] A.V. Tollestrup, *The Fermilab Tevatron Project*, FERMILAB-TM-0880, 29, (1979).

L.C. Teng, *The Fermilab Tevatron*, FERMILAB-TM-1044, Orbis Scientiae, (1981).

[2] S. Coleman and J. Mandula, *All Possible Symmetries of the S Matrix*, Phys. Rev. **159**, 1251 (1967).

R.Haag, J. Lopuszanski and M.Sohnius, *All Possible Generators of Supersymmetries of the S Matrix*, Nucl. Phys. **B 88**, 257, (1975).

P. Ramond, *Dual Theory for Free Fermions*, Phys. Rev. **D 3**, 2415 (1971).

A. Neveu and J.H. Schwarz, *Factorizable Dual Model of Pions*, Nucl. Phys **B 31**, 86 (1971).

J.Wess and J. Bagger, *Supersymmetry and Supergravity*, Princeton University Press, Princeton NJ, (1992).

G.G. Ross, *Grand Unified Theories*, Addison-Wesley, (1985).

P.G.O. Freund, *Introduction to Supersymmetry*, Cambridge University Press, (1986).

P.P. Srivastava, *Supersymmetry and Superfields*, Adam-Hilger, Bristol England, (1986).

R.N. Mohopatra, *Unification and Supersymmetry: Frontiers of Quark-Lepton Physics*, Springer-Verlag, New York (1992).

R. Arnowitt, A. Chamseddine and P. Nath, *Applied N=1 Supergravity*, World Scientific, Singapore, (1984).

H.P. Nilles, *Supersymmetry, Supergravity and Particle Physics*, Phys. Rept. **110** 1, (1984).

H. Haber, *Introductory Low-Energy Supersymmetry*, TASI-92 Lectures, eds J.Harvey and J. Polchinski, World Scientific, (1993).

P. Ramond, *Introductory Lectures on Low Energy Supersymmetry*, TASI-94 Lectures, hep-th/9412234 (1994).

S.Martin, *A Supersymmetry Primer*, Perspectives on Supersymmetry, ed G. Kane, World Scientific, Singapore, (1998).

J.D. Lykken, *Introduction to Supersymmetry*, TASI-96 Lectures, hep-th/9612114 (1996). R. Barbieri, S. Ferrara and C. A. Savoy, *Gauge Models With Spontaneously Broken Local Supersymmetry*, Phys. Lett. **B119**, 343, (1982).

L. Hall, J. Lykken and S. Weinberg, *Supergravity As The Messenger Of Supersymmetry Breaking*, Phys. Rev. **D27** (1983) 2359.

[3] R. Markeloff, *An Analysis of Monojet Data in ppbar Collisions at* $\sqrt{s}$ *= 1.8 TeV*, University of Winsconsin, Ph.D. thesis, unpublished, (1994).

[4] The D0 Collaboration, *Measurement of the Top Quark Pair Production Cross Section in* $p\bar{p}$ *Collisions*, Phys. Rev. Lett.**79**, 1203, (1997).

[5] T. Affolder *et al.*, The CDF Collaboration, *Search for Higgs Bosons Produced in Association with a Vector Boson in* $p\bar{p}$ *Collisions at* $\sqrt{s}$*=1.8 TeV* to be published, Phys. Rev. Lett., (2000).

[6] T. Affolder *et al.*, The CDF Collaboration, *Search for Scalar Top and Scalar Bottom Quarks in p anti-p Collisions at* $\sqrt{s}$ *= 1.8 TeV*,Phys. Rev. Lett.**85**, 5704, (2000).

[7] T. Affolder *et al.*, The CDF Collaboration, *Search for Second and Third Generation Leptoquarks Including Production via Technicolor Interactions in p anti-p Collisions at* $\sqrt{s}$ *= 1.8 TeV*, FERMILAB-PUB-00/073-E, submitted to Phys. Rev. Lett.March 31, (2000).

[8] T. Affolder *et al.*, The CDF Collaboration, *Limits on Gravitino Production and New Processes with Large Missing Transverse Energy in p anti-p Collisions at* $\sqrt{s}$ *= 1.8 TeV*, FERMILAB-PUB-00/064-E, Submitted to Phys. Rev. Lett., March 17, (2000).

[9] M. Acciari *et al.*, The L3 Collaboration, *Search for Low Scale Gravity Effects in e+e- Collisions at LEP*, Phys. Lett. **B464**, 135, (1999).

[10] The CDF Collaboration, *The CDF Detector: An Overview*, *Nucl.Instrum. and Methods* **A** 271,387, (1988).

[11] KTeV collaboration, *Observation of Direct CP Violation in K_S,L to* $\pi\pi$ *Decays*, Phys. Rev. Lett.**83** 22, (1999).

[12] NOMAD Collaboration (J. Altegoer *et al.*), *A Search for* $\nu_\mu \to \nu_\tau$ *oscillations using the NOMAD detector*, Phys. Rev. Lett.**B431**, (1998).

[13] A. Vaitaitis *et al.*, *Search for Neutral Heavy Leptons in a High-Energy Neautrino Beam*, Phys. Rev. Lett. **83**,4943 (1999).

J. Formaggio, *et al.*, *Search for a 33.9-MeV/*c^2 *Neutral Patricle in Pion Decay*, Phys. Rev. Lett. **84** 4043, (2000).

[14] D.Perkins, *Introduction to High Energy Physics*, (Addison-Wesley Publishing Company), (1987).

[15] S. D. Holmes, *Achieving high luminosity in the Fermilab tevatron* FERMILAB-CONF-91-141, (1991).

[16] F. Abe *et al.*, The CDF Collaboration, *Measurement of sigma B(W→ e nu) and sigma B(Z0 → e+ e-) in p anti-p Collisions at* $\sqrt{s}$ *= 1.8 TeV*, Phys. Rev. Lett.**76**, 3070(1996).

[17] F. Abe *et al.*, The CDF Collaboration, *Measurement of the antiproton-proton total cross section at* $\sqrt{s}$ *=546 and 1800 GeV*, Phys. Rev. D **50**, 5550, (1994).

[18] D.Hennessy, A. Beretvas, *Luminosity of CDF*, CDF internal publication 4721, to be published in Nucl.Instrum. and Methods, (2000).

[19] D. Amidei *et al.*, *The SVX*, Nucl.Instrum. and Methods **A** 350, 73, (1994).

[20] G.Sciacca *et al*, *SVX-': The New CDF silicon vertex detector*, FERMILAB-CONF-94/205-E (1994).

[21] F. Abe *et al.*, The CDF Collaboration, *Study of four-jet events and evidence for double parton interactions in pp-bar collisions at* $\sqrt{s}$ *=1.8 TeV*, Phys. Rev. D **47**, 4857, (1994).

[22] T. Affolder *et al.*, The CDF Collaboration, *Measurement of the W Boson Mass with the Collider Detector at Fermilab*, submitted to Phys. Rev. D July 26, (2000).

[23] F.K.Ptohos, *Measurement of the* $t\bar{t}$ *cross section using heavy flavor tags in inlusive W + 3 jet events*, Ph.D thesis Harvard University, unpublished, (1998).

[24] M. Gold, *Identification of Cnversion Electron Pairs*, CDF internal publication 913, (1989).

D. Gerdes, , *Study of Conversion Removal for the Lepton + Jets Sample* CDF internal publication 2903, (1994).

[25] F. A. Berends, W. T. Giele, H. Kuijf, and B. Tausk, *On the Production of a W and Jets at Hadron Colliders*, Nucl. Phys.**357**, 32, (1991).

[26] G. Marchesini , B.R. Webber , G. Abbiendi, I.G. Knowles, M.H. Seymour, L. Stanco, *HERWIG Version 5.9*, hep-ph/9607393 (1996).

G. Marchesini and B. R. Webber, *Monte Carlo Simulation of General Hard Processes with Coherent QCD Radiation* Nucl. Phys.**310**, 461, (1988).

[27] T. Sjöstrand, *PYTHIA 5.6 and JETSET 7.3: Physics and Manual*, Report No. CERN-TH-6488/92 (1992).

(http://wwwcn.cern.ch/asdoc/pythia_html3/pythia57.html), PYTHIA V5.6 is used.

[28] M. Shapiro *et al.*, *A User's guide to QFL*, CDF internal publication 1810, (1992).

[29] H. Baer *et al*, *ISAJET 7.37: A Monte Carlo Event Generator for pp, $\bar{p}p$, and e^+e^- Interactions*, hep-ph/9804321. Bug fixes from later versions are incorporated.

[30] A. Caner, A. Mukherjee, A. Yagil, *Tracking Efficiency for Soft Lepton Tagging*, CDF internal publication 2363 (1993).

[31] G. Unal, *Tracking efficiency and SVX b-tag efficiency*, CDF internal publication 3563, (1996).

[32] M. Spiropulu and J. Huth, *On the determination of the V plus jets background to the MET plus jets search* CDF internal publication 4512, (1998).

[33] V. D Barger and R. J. N. Phillips, *Collider Physics, Frontiers in Physics*, Addison-Wesley (1997).

[34] W. Giele *et al. On the production of a W and jets at hadron colliders*, Nuc. Phys. **357** (1991).

http://fnth02.fnal.gov/people/giele/vecbos.html

M. L. Mangano, *The Unweighting of Matrix Element Monte Carlos*, CDF internal publication 1665, (1992).

M. L. Mangano, J. Benlloch, A. Caner and T. Rodrigo, *On Transforming Partons Into Jets: HERPRT, a new Interface*, CDF internal publication 1823, (1991).

[35] F. Abe *et al.*, The CDF Collaboration, *Measurement of the production and muonic decay rate of W and Z bosons in p anti-p collisions at* $\sqrt{s}$ *= 1.8 TeV* Phys. Rev. Lett.**69**, 28, (1992).

[36] R. Bonciani *et al.*, *NLL resummation of the heavy-quark hadroproduction cross-section*, Nucl. Phys. **B529**,424 (1998).

[37] T. Stelzer, Z. Sullivan and S. Willenbrock, *Single-top-quark production via W-gluon fusion at next-to-leading order* Phys.Rev **D56**, 5919, (1997).

M. C. Smith and S. Willenbrock, *QCD and Yukawa Corrections to Single-Top-Quark Production via q qbar* $\rightarrow$ *t bbar* Phys.Rev.D **D54**, 6696, (1996).

T. Tait C. P. Yuan, *The phenomenology of single top quark production at the Fermilab Tevatron* hep-ph/9710372 (1997).

[38] J. Ohnemus and J. F Owens, *An Order alpha-s calculation of hadronic Z Z production*, Phys. Rev. **D43** 3626, (1991).

J. Ohmenus, *An Order alpha-s calculation of hadronic W+- Z production*, Phys. Rev. **D44**, 3477, (1991).

J. Ohmenus, *An Order alpha-s calculation of hadronic W- W+ production*, Phys. Rev. **D44**, 1403, (1991).

[39] E. Buckley-Geer, *Measurement of the fully corrected* $\Sigma {E_T}^{jet}$ *cross-section using the full RunI data sample*, CDF Internal document 3995, (1997).

[40] E. Buckley-Geer, *Measurement of the fully corrected* ΣE_T *cross-section at the Fermilab Proton-Antiproton Collider*, CDF Internal publication 3119 (1996).

[41] Apollinari *et al.*, *Heavy flavor content of jets in the data and in Herwig simulations*, CDF Internal publication 4115, (1999).

[42] CDF Run-II Trigger Group, *Run-II Trigger Table and Datasets Plan*, CDF internal publication 4718, (2000).

[43] R. Field and D. Stuart, *Min-Bias Data: Jet Evolution and Event Shapes*, CDF internal publication 5067 (1999).

[44] F. Abe *et al.*, The CDF Collaboration, *Properties of Photon Plus Two-Jet Events in p anti-p Collisions at* $\sqrt{s} = 1.8$ *TeV*, Phys. Rev. **D** (1997), FERMILAB-PUB-97/106-E.

[45] S. L. Glashow, *Partial Symmetries of Weak Interactions*, Nucl. Phys.**22** 588,(1961)

S. Weinberg, *A Model of Leptons*, Phys. Rev. Lett.**19** 1264,(1967)

A. Salam, *Gauge Unification of Fundamental Forces* Proc. 8th Nobel Symposium, Stockholm, (1979).

[46] J. Ellis, Perspectives in High Energy Physics, 3rd Latin American Symposium on High-Energy Physics, hep-ph/0007161 (2000).

[47] H. Goldberg, *Constraint on the photino mass from cosmology* Phys. Rev. Lett. **50**, 1419 (1983).

J. Ellis, J. Hagelin, D.V. Nanopoulos, K. Olive, and M. Srednicki, *Supersymmetric relics from the big bang*, Nucl. Phys. **B238**, 453, (1984).

[48] R. Farrar and P. Fayet, *Bounds On R Hadron Production From Calorimetry Experiments*, Phys. Lett. **B79**, 442 (1978).

[49] E. Gildener, *Gauge Summetry Hierarchies*, Phys. Rev. **D14**, 1667, (1976)

E.Gildener and S. Weinberg, *Symmetry Breaking and Scalar Bosons*, Phys. Rev. **D13**, 3333, (1976)

L. Maiami, Proceedings of the Summer School of Gif-Sur-Yvette (1980)

M. Veltman, *The Infrared- Ultraviolet Connection*, Acta Phys. Polon. **B12**, 437, (1981)

S. Dimopoulos and S. Raby, *Supercolor*, Nucl. Phys. **B192**, 353, (1981)

E. Witten, *Dymanical Breaking of Supersymmetry*, Nucl. Phys. **B188**, 513, (1981)

S. Dimopoulos and H. Georgi *Softly Broken Supersymmetry and SU(5)*, Nucl. Phys. **B193**, 150, (1981).

[50] R. Barbieri and G.F. Giudice, *Upper Bounds on Supersymmteric Particle Masses*, Nucl. Phys. **B306** 63, (1988).

[51] S. Dimopoulos and G.F. Giudice, *Naturalness Constraints in Supersymmetric Theories with Non-Universal Soft Terms*, Phys. Lett. **B357**, 573, (1995).

[52] G. Anderson, D. Castano, *Naturalness and superpartner masses or when to give up on weak scale supersymmetry*, Phys.Rev. D52, 1693, (1995).

[53] M. Bastero-Gil, G. L. Kane and S. F. King *Fine Tuning Constraints on Supergravity Models*, hep-ph/9910506 (1999)

G. L. Kane and S .F. King, *Naturalness Implications of LEP results*, Phys. Lett. **B451** 113, (1999) and references therein.

[54] J.L.Feng, K.T.Matchev and T. Moroi, *Naturalness Re-Examined : Implications for Supersymmetry searches*, Proceedings of PASCOS'99, Lake Tahoe, December 10-16, 1999

J. L. Feng, K. T. Matchev and T. Moroi, *Multi-TeV Scalars are Natural in Minimal Supergravity*, Phys. Rev. Lett. **84** 2322, (2000)

J. Bagger, J. Feng, N. Polonsky, *Naturally Heavy Scalars in Supersymmetric Grand Unified Theories*, Nucl. Phys. **B563**, 3, (1999).

[55] K. R Dienes and C. Kolda, *Twenty Open Questions in Supersymmetric Particle Physics*, 'Perspectives on Supersymmetry', ed. by G. Kane, published by World Scientific (1997).

[56] S. Dimopoulos and D. Sutter, *The Supersymmetric Flavor Problem*, Nucl. Phys. **B452**, 496, (1995).

[57] H.E. Haber and G.L. Kane, *The search for supersymmetry: Probing Physics Beyond the Standard Model*, Phys. Rep **117**,75, (1985)

[58] J.F. Gunion and H.E. Haber, *Higgs Bosons In Supersymmetric Models. 1.*, Nucl. Phys. **B272**, 1, (1986)

J.F. Gunion and H.E. Haber, *Higgs Bosons In Supersymmetric Models. 2. Implications For Phenomenology*, Nucl. Phys. **B278**, 449, (1986)

J.F. Gunion and H.E. Haber, *Higgs Bosons In Supersymmetric Models. 3. Decays Into Neutralinos And Charginos*, Nucl. Phys. **B307**, 445, (1988).

[59] S. Weinberg, *The Quantum Theory of Fields*, Cambridge University Press, and References therein, (1996).

[60] V. Barger, M. S. Berger, and P. Ohmann *Supersymmetric particle spectrum*, Phys. Rev. **D49**, 4908, (1994).

[61] G. L. Kane, C. Kolda and J. D. Wells, *Calculable upper limit on the mass of the lightest Higgs boson in any perturbatively valid supersymmetric theory*, Phys. Rev. Lett. **70**, 2686, (1993)

J.R. Espinosa and M. Quiros, *Upper bounds on the lightest Higgs boson mass in general supersymmetric Standard Models*, Phys. Lett.B**302**, 51, (1993) and references therein.

[62] S.P. Martin and M.T. Vaughn, *Regularization dependence of running couplings in softly broken supersymmetry*, Phys. Lett. B**318**, (1993).

[63] D. Pierce and A. Papadopoulos, *The Complete radiative corrections to the gaugino and Higgsino masses in the minimal supersymmetric model*, Nucl. Phys. **B430**, 278, (1994)

D. Pierce and A. Papadopoulos, *Radiative corrections to neutralino and chargino masses in the minimal supersymmetric model*, Phys. Rev. **D50**, 565, (1994).

[64] L.E. Ibanez and C. Lopez, *N=1 Supergravity, The Weak Scale and the Low-Energy Particle Spectrum*, Nucl. Phys. **B233**, 511, (1984).
L. E. Ibanez, C. Lopez and C. Munoz, *The Low-Energy Supersymmetric Spectrum According to N=1 Supergravity GUTS*, Nucl. Phys. **B256**, 218, (1985).

[65] V. Barger, C. E. M. Wagner, *Report of the SUGRA Working Group for Run II of the Tevatron, et al.* hep-ph/0003154, (2000).

[66] W. Beenakker,R. Hopker,M. Spira, ,P. M. Zerwas, *Squark and Gluino Production at Hadron Colliders*, Nucl. Phys. **B492**, 51, (1997).

[67] M. Gluck and W. Vogelsang, *Polarized prompt photon production in high-energy polarized e p collisions*, Z. Phys. **C53**, 695, (1992).

[68] M. Spira, personal communication.

[69] M. Spira,PROSPINO NLO cross section calculation program, *http://www.desy.de/ spira/prospino/*

[70] F. Abe *et al.*, The CDF Collaboration, The mu tau and e tau Decays of Top Quark Pairs Produced in ppbar Collisions at $\sqrt{s}$=1.8 TeV, Phys. Rev. Lett.79, 3585, (1997)

[71] M. Gallinaro and M. Hohlmann, *Search for Charged Higgs Using Tau Dileptons*, CDF internal publication 4336, (1997).

[72] F.Ptohos, $t\bar{t}$ *cross section at CDF* Procs. of Intl. Europhysics Conf. on High Energy Physics (EPS-HEP99) edited by K. Huitu, H. Kurki-Suonio, J.Maalampi, published by IOP Publishing (Bristol, UK), 637, (2000).

[73] A. D. Martin, R. G. Roberts, and W. J. Stirling *Pining Down the Glue in the Proton*, Phys. Lett. **B354**, 155, (1995).

[74] H.L. Lai *et al.*, CTEQ-Coll., *Global QCD Analysis and the CTEQ Parton Distributions*, Phys. Rev. **D51**, 4763, (1995)

[75] A. D. Martin, W. J. Stirling and R. G. Roberts, *New information on parton distributions*, Phys. Rev. **D47**, 867, (1993).

[76] C. Caso *et al.*, *Review of Particle Physics*, Particle Data Group Eur. Phys. J. **C3**, 781, (1998).

[77] J. Conway and K. Maeshima, *Poisson Upper Limits Incorporating Uncertainties in Acceptance and Background*, CDF internal publication, 4476, (1999)

[78] C. Albajar *et al.*,The UA1 Collaboration, *Events With Large Missing Transverse Energy At The CERN Collider (Paper 3): Mass Limits On Supersymmetric Particles*, Phys. Lett. **B198**, 261, (1987).

[79] J. Alitti *et al.*, The UA2 Collaboration, *A Search For Squark And Gluino Production At The CERN Anti-P P Collider*, Phys. Lett. **B235**, 363, (1990).

[80] P. Abreu *et al.*, The DELPHI Collaboration, *Search For Scalar Quarks In Z0 Decays*, Phys. Lett. **B247**, 148, (1990).

[81] T. Affolder *et al.* The CDF Collaboration, *Test of enhanced leading order QCD in W boson plus jets events from 1.8-TeV anti-p p collisions*, FERMILAB-PUB-00-196-E, Submitted to Phys. Rev. (2000).

[82] F. Abe *et al.*, The CDF Collaboration, *Limits On The Masses Of Supersymmetric Particles From 1.8-Tev P Anti-P Collisions*, Phys. Rev. Lett. **62**, 1825 (1989).

[83] Ia Iashvili, *MSSM SUSY Searches at LEP2*, Talk presented at 35th Rencontres de Moriond: ElectroWeak Interactions and Unified Theories, Les Arcs, hep-ex/0007001, 2000.

[84] F. Abe *et al.* The CDF Collaboration, *Search for squarks and gluinos from anti-p p collisions at* $\sqrt{s}$ *= 1.8-TeV*, Phys. Rev. Lett. **69**, 3439, (1992).

[85] S. Abachi *et al.*, The D0 Collaboration, *Search for squarks and gluinos in p anti-p collisions at* $\sqrt{s}$*= 1.8-TeV*, Phys. Rev. Lett. **75**, 618, (1995).

[86] F. Abe *et al.*, The CDF Collaboration, *Search for Gluinos and Squarks at the Fermilab Tevatron Collider*, Phys. Rev. **D56**, R1357, (1997).

[87] B. Abbott *et al.*, The D0 collaboration, *Search for Squarks and Gluinos in Events Containing Jets and a Large Imbalance in Transverse Energy*, Phys.Rev.Lett. **83**, 4937, (1999).

[88] S. Van Der Meer, *Stochastic Cooling In The Cern Anti-Proton Accumulator.* IEEE Trans. Nucl. Sci. **28**, 1994, (1981)

[89] S. Coleman and D. J. Gross, *Price Of Asymptotic Freedom*, Phys. Rev. Lett. **31**, 851, (1973).

[90] S. Rosier-Lees, *LEP SUSY Working Group Status Report*, LEPC, *http://lepsusy.web.cern.ch/lepsusy/*, (2000).

[91] S. Martin, *Phenomenological implications of Supersymmetry Breaking Mechanisms*, DPF, *http://www.dpf2000.org/BSM1.htm#ses1* (2000).

[92] G. Anderson, H. Baer, C. Chen and X. Tata, *The reach of Fermilab Tevatron upgrades for SU(5) supergravity models with non-universal gaugino masses*, Phys. Rev. **D61**, 095005, (2000) [hep-ph/9903370].

[93] A. Conolly and D. Stuart, *Search for Long-lived Charged MAssive Particles in Run 1B*, CDF internal publication 4180, (2000) and References therein.

[94] N. Arkani-Hamed, S. Dimopoulos and G. Dvali, *The hierarchy problem and new dimensions at a millimeter* Phys. Lett. **B429**, 263, (1998)

[95] E. A. Mirabelli, M. Perelstein and M. E. Peskin, *Collider signatures of new large space dimensions*, Phys. Rev. Lett. **82**, 2236 (1999)

[96] K. Burkett and M. Spiropulu, *Missing Energy Signature from Kaluza-Klein Graviton Emission With Run IB Data*, CDF Internal Publication 5151, (1999).

[97] S. Van Der Meer, *Stochastic Cooling*, Helv. Phys. Acta **59**, 906, (1986).
S. Van Der Meer, *Stochastic Cooling And The Accumulation Of Anti-Protons*, Rev. Mod. Phys. **57**, 689, (1985).

[98] A. V. Tollestrup and G. Dugan, *Elementary Stochastic Cooling*, FERMILAB-TM-1227

[99] W. Kells, J. Marriner, R. J. Pasquinelli and S. Mtingwa, *Performance of Tevatron I core stochastic cooling systems*, 12th Particle Accelerator Conference (PAC), Washington, (1987).

[100] D. Boussard, *Advanced Cooling Techniques: Stochastic Cooling Of Bunches In High-Energy Colliders* Frontiers of particle beams* 269, South Padre Island (1986).

[101] V. Visnjic, *Betatron stochastic cooling in the debuncher: Present and future*, FERMILAB-TM-1845.

[102] Details about the Tevatron Operation and parameters can be found at *http://www-bd.fnal.gov/tevatron/*.

[103] S. Kuhlmann, J. Yoh, *Filtering Jet Backgrounds in the CDF Central Detector*, CDF internal publication 548, (1987)

S. Kuhlman, A. F. Garfinkel, *Performance of Hadron TDC*, CDF internal publication 482, (1987).

[104] W.J. Cody, *Rational Chebyshev approximations for the error function*, Math. Comp. **22** 631,(1969); CERNLIB writeup at *http://consult.cern.ch/shortwrups/c301/top.html*.

[105] M. Spiropulu, *Run1B Jet20, Jet50 and MET35* trigger efficiencies* CDF internal publication 5152, (1999).

[106] L. Groer, C.Loomis, *Run 1B MET_35 Trigger Efficiency*, CDF internal publication 3532 (1997).

[107] M. Okabe, *Measurement of the strong coupling alpha_s using two jet cross section from Run IB*, CDF internal publication 4138, (1998).

[108] John Wahl, *R Acceptances and Systematics*, CDF internal publication 4599, (1998).

[109] R. F. Schwitters *et al.*, *Azimuthal asymmetry in Inclusive Hadron Production by e^+e^- Annihilation*, Phys. Rev. Lett.**35**, 1320, (1975).

[110] G.G Hanson *al.*, *Evidence for Jet Structure in Hadron Production by e^+e^- Annihilation*, Phys. Rev. Lett.**35**, 1609, (1075).

[111] P. Darriylat, *Large Transverse Momentum Processes*, Annual Review of Nuclear and Particle Science, vol.30 ,159, (1980).

[112] P. Bagnaia *et al.*, *Measurement of very large transverse momentum jet production at CERN $p\bar{p}$ collider*, Phys. Rev. Lett., **B138** , 430, (1984).

[113] T. Sjöstrand, *A Model for Initial Parton Showers*, Phys. Rev. Lett.**175B**, 321, (1985).

[114] R. D. Field, R .P. Feynman, *A Paramterization of The Properties of Quark Jets*, *Nucl. Phys.* **B136**, 1, (1978).

[115] J. Huth and M. Mangano *QCD Tests in Proton Antiproton Collisions*, Annu. Rev. Part. Sci. **43**, 585, (1993).

[116] C. Quigg, *Gauge Theories of the Strong, Weak and Electromagnetic Interactions*, (Benjamin-Cummings, Reading, (1983).

[117] The Super-Kamiokande Collaboration, *Evidence for oscillation of atmospheric neutrinos*, Phys. Rev. Lett. **81**, 1562, (1998).

[118] Z. Maki, M. Nakagawa and S. Sakata, *Remarks On The Unified Model Of Elementary Particles*, Prog. Theor. Phys. **28**, 870 (1962).

[119] M.Kobayashi and T.Maskawa, *CP Violation In The Renormalizable Theory Of Weak Interaction*, Prog. Theor. Phys. **49**, 652 (1973); N Cabbibo Phys. Rev. Lett. **10** 531, (1961).

[120] B.W. Lee, C. Quigg and H.B. Thacker, *Weak Interactions At Very High-Energies: The Role Of The Higgs Boson Mass*, Phys. Rev.**D16**, 1519, (1977).

[121] M. Veltman, , *Second Threshold in Weak Interactions*, Acta Phys. Pol. **B8**, 475, (1977).

[122] For the most recent results, LEP Electroweak Working Group *http://lepewwg.web.cern.ch/LEPEWWG/*

[123] L. Girardello and M. T. Grisaru, *Soft Breaking Of Supersymmetry*, Nucl. Phys. **B194**, 65 (1982).

[124] P. Langacker, *Precision Tests Of The Standard Model*, in Proceedings of the PASCOS90 Symposium, Eds. P. Nath and S. Reucroft, (World Scientific, Singapore 1990).

J. Ellis, S. Kelley, and D. Nanopoulos, *Probing the desert using gauge coupling unification*, Phys. Lett. **B260**, 131, (1991).

U. Amaldi, W. de Boer, P. H. Frampton, H. Furstenau and J. T. Liu, *Consistency checks of grand unified theories*, Phys. Lett. **B281**, 374, (1992).